ANALYTICAL AND EXPERIMENTAL STUDIES OF STRUCTURAL HEALTH MONITORING OF NONLINEAR VISCOUS DAMPERS

by

Raymond Walter Wolfe

A Dissertation Presented to the
FACULTY OF THE GRADUATE SCHOOL
UNIVERSITY OF SOUTHERN CALIFORNIA
In Partial Fulfillment of the
Requirements of the Degree
DOCTOR OF PHILOSOPHY
(CIVIL ENGINEERING)

August 2002

Copyright 2002   Raymond Walter Wolfe

UNIVERSITY OF SOUTHERN CALIFORNIA
THE GRADUATE SCHOOL
UNIVERSITY PARK
LOS ANGELES, CALIFORNIA 90007

This dissertation, written by

.....*RAYMOND   WALTER   WOLFE*.....

under the direction of h.i.s...... Dissertation Committee, and approved by all its members, has been presented to and accepted by The Graduate School, in partial fulfillment of requirements for the degree of

DOCTOR OF PHILOSOPHY

....
Dean of Graduate Studies

Date ....*6/28/02*........

DISSERTATION COMMITTEE

....
Chairperson

....

....

Dedication

This dissertation is dedicated to the memory of Walter Hinds Doty, my grandfather. His words of inspiration provided the impetus to continue forth and complete this effort. He used to say "You can take away a man's job, his fortunes and dignity, but you can never steal his education."

ii

Acknowledgements

I would like to extend a special thanks to my wife Laura of nearly 12 years, without whom I would have never had the strength to complete this work. She patiently and unselfishly stood beside me as I spent countless hours at class or studying for exams. Her technical expertise helped solve many of the seemingly insurmountable problems faced through the course of my studies. I am indebted to her for allowing the opportunity to pursue this dream.

Special thanks are also extended to my brother Richard Henry Aaron Wolfe, who reviewed this document for grammatical correctness and provided moral support on may occasions.

To all my family and friends who accepted the fact that my academic pursuit reduced the time we had to share and enjoy, thank you for being there and never giving up, and thank you for your support. I would not have had the strength to complete this without your support and love.

To Dr. Masri for his guidance and support over the past five years, thank you for the opportunities you have provided.

To Dr. Wellford and Dr. Redekopp, my dissertation committee members, thank you for your time, wisdom and support.

To Dr. Hany J. Farran, my Master's thesis advisor and mentor at the California Polytechnic University, Pomona, thank you for pushing me to reach new heights.

Table of Contents

List of Tables

ix

LIST OF FIGURES

X

xvi

Abstract

Viscous dampers are integral components in the implementation of structural control retrofit strategies on several new and retrofitted bridges throughout the world. Due to the significance of the role played by the dampers in the retrofit schemes, it is imperative that some of the hurdles impeding the field implementation of structural health monitoring applications in conjunction with such dampers be investigated and resolved.

The goals of the research reported herein were to conduct analytical and experimental studies to evaluate a promising strategy for structural health monitoring of nonlinear viscous dampers. The sequence of analytical and experimental studies performed was designed to illuminate the numerous challenging technical issues encountered in the characterization of the physical phenomena exhibited by structural damper components. Nonparametric and parametric algorithms were investigated to determine their suitability to field applications in detecting potential system degradation under the influence of noise pollution. Statistical tools such as probability density functions, root-mean-square error analysis, data normalization and curve-fitting techniques were employed in ascertaining the effectiveness and sensitivities of the various algorithms. It is found that the structural health monitoring techniques investigated in this study offer the potential for being useful tools in detecting and quantifying relatively small changes in the system being monitored.

1.0 Introduction

1.1 Motivation

In recent times, with the ever increasing assimilation of high density population centers, particularly in earthquake prone regions such as the Pacific Rim, more emphasis has been placed on the ability of engineered structures to withstand seismic excitations. Today, engineers and scientists have the ability to physically measure and model dynamic phenomena with increasing accuracy, as computer data acquisition, processing, control, storage capacity and simulation tools are continually improved.

One of the main concerns of engineers today is not only the design but also the assessment, analysis and retrofitting of existing structures. Economically, it is not feasible to demolish and reconstruct most structures that are determined to be below acceptable seismic standards. Thus, engineers must develop retrofit strategies designed to incorporate modifications to existing structural parameters, thereby enabling a given structure to behave in a manner consistent with current design philosophy.

Large-scale dampers are being specified for incorporation into several toll bridge retrofit strategies. The reasons are obvious; energy dissipative devices such as dampers reduce adjoining member design demands, thereby allowing subsequent reduction in member sizes ... and yielding dramatic weight and cost savings. As

1

such, dampers are integral components of these structures; the failure of even one can portend potentially catastrophic system failure. Given the critical nature of the damper elements to the success of retrofit strategies being implemented on these large-span structures, a means of evaluating their health is imperative.

At the present time, engineers are uncertain as to how to approach the problem of evaluating the structural integrity of the viscous dampers, particularly those being placed in service on several toll structures throughout the State of California ("State"). The current practice involves removing dampers from service for testing and evaluation … and then reinstalling or replacing them as necessary. The obvious downside to this approach is the economic burden of maintaining such a program. A related problem arises from the potential for damage during removal/installation, transit and testing. Without the luxury of proven alternatives, such as health monitoring systems, the above must necessarily be coordinated on a periodic basis.

Structural health monitoring has received much attention from researchers in the past decade. While the merits of numerous signature-based nondestructive evaluation (NDE) approaches continue to be investigated, health monitoring methods that do not require *a priori* knowledge of a structure are advantageous, as they offer the ability to detect unforeseen failure modes. Hence, the motivation for model-based inverse methods based on system identification theory is obvious.

2

A typical scheme utilized in structural health monitoring algorithms is the model updating approach. This approach relies on measured data collected from prescribed instrumentation to continually update the stiffness distribution of a simulation model of the system under investigation. System degradation is predicated on stiffness variations revealed in the measured data. Predetermined threshold crossings defining specific failure modes are used to identify failure potential. In general, though, the model updating approach presents an ill-conditioned, non-unique, inverse problem. The primary sources of the difficulties presented by this approach are measurement noise and modeling errors.

A number of papers have been published on various analytical techniques. Many of these papers are cited herein, with reference listings. In this fashion, the interested reader can further acquaint himself/herself with the intricate details of these tools as well as the power and promise presented by each. Additionally, examples depicting the applicability of these tools to experimental data provide further insight into the existing state of research in this important field; several such examples are included in the reference material, again for the benefit of the reader. The challenge of this research, then, is not in developing analytical tools but, rather, it is in the selection, optimization, calibration and evaluation of those extant, from the perspective of quality assurance needs.

3

1.2 Background

Caltrans is currently implementing a $4 billion statewide seismic retrofit program (Wolfe and Wahbeh, 2000). The main focus remaining in this program is six of the seven major State toll bridges, the Vincent Thomas Bridge being recently completed. One of these toll structures, the retrofit of the San Francisco-Oakland Bay Bridge (SFOBB), is currently under construction, providing data for this research.

The SFOBB carries Interstate 80 over the San Francisco Bay eight and one quarter miles, connecting the cities of San Francisco and Oakland (reference Figure 1.1). The structure is divided into East Bay and West Bay crossings, also known as the East and West Spans. The former, with four separate structure types, is scheduled for replacement beginning next year. The West Crossing is currently being retrofit and has numerous large viscous dampers incorporated into the retrofit strategy.

The West Bay Crossing is comprised of concrete approach spans at both ends. A continuous truss spans from the San Francisco anchorage to the cable bent, nearly 900 feet in length. Trademark back-to-back suspension spans, centered on a 450-foot high vertical cantilever pier in the middle of the bay and crossing from San Francisco to Yerba Buena Island, comprise the West Bay Crossing (reference Figure 1.2). At 10,303 feet (1.95 miles) long, this crossing includes two suspension structures (East and West) as well as a continuous span and center and island

4

anchorages. Both the East and West suspension bridges are nearly identical in

length, at 4,630 feet; the West suspension bridge is merely 11 feet longer.

Figure 1.1. Site map

The retrofit design of the West Spans of the SFOBB incorporates one hundred (100)

dampers. Specification of these dampers was crucial to the success of the design in

meeting stipulated criteria. Other retrofit designs implementing viscous dampers

include the interim retrofit of the SFOBB East Spans, the Vincent Thomas

Suspension Bridge in San Pedro and the Coronado Bay Bridge in San Diego. In

each case, the design team was similarly challenged to properly specify the damper

elements. While a considerable body of work exists to assist in solving damper

5

specification problems, the choice of which of the techniques to use remains a problem. Until now, no comprehensive evaluation of these techniques had been completed; nor had the best techniques been selected and optimized for application, complicating the design efforts.
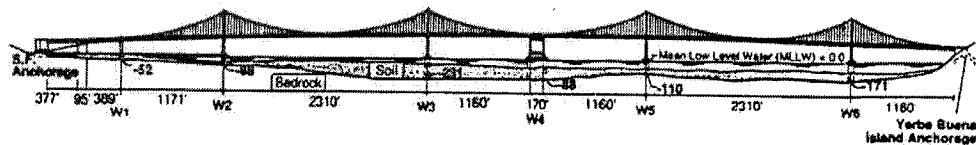
Figure 1.2. West Crossing elevation, SFOBB

1.3 Research Objectives

The research contained herein attempts to quantify the class of problems associated with viscous dampers, specifically as they are applied to retrofit strategies on large bridge structures, such as the West Spans of the SFOBB. Health monitoring techniques are evaluated and optimized for application to damper elements in an effort to facilitate *in situ* evaluation of their continued ability to perform as designed.

The main objective of this research is to develop an optimized set of analytical tools that can be implemented in the field to monitor the health of the damper elements. This research will utilize prototype and proof test data, coupled with possible broadband data to fully characterize the dynamics of the dampers, as a means of selection and optimization of the set of analytical tools, parametric and nonparametric, previously developed. Additional simulations and testing are being

6

performed currently on the campus of the University of Southern California to further quantify the most promising analytical tools for detecting slight variations in damper performance which might portend failure.

It is important to note that the analytical tools presented herein, do not require extensive *a priori* knowledge of the damper mechanisms. Quite the contrary, while the parametric tools require limited knowledge to allow system equation estimation, the nonparametric tools do not require any knowledge of the system, utilizing instead input excitation with judiciously chosen output data to analytically model the system characteristics. Additionally, these methods do not require external forcing functions, beyond system calibration, to reliably detect subtle changes in the system's dynamics. It is these subtle data shifts, captured in the first and second moment descriptions of the data, which, when acquired and analyzed in continuous, real-time mode, provide invaluable insight to the health of a system.

This study will focus on optimizing structural health monitoring algorithms for specific application in field analysis. Actual implementation will require minimal additional efforts and instrumentation.

7

2.0 Literature Survey

Before launching into the detail of this research, it is important to assess that which has been done before. Of the multitude of papers published on this topic, many were reviewed; several warrant brief discussion. As such, this section provides a chronological summary of key research directly and peripherally linked to the examination embodied in this research. Topics included range from simulation efforts to experimental studies, with selection predicated on health monitoring and system identification techniques. A more in-depth listing of relevant papers is included in alphabetic order in the references.

Masri and Caughey (1979) develop a nonparametric identification technique utilizing system state variables of nonlinear systems to describe the system characteristics in terms of orthogonal functions. A main advantage to nonparametric algorithms lies in their inherent ability to represent systems without *a priori* assumptions of the system model. The approach discussed has the further advantage of being able to successfully model hysteretic systems, which often pose difficulties with other nonparametric simulation algorithms. They report rapid convergence rates with minimal execution time and storage requirements. Finally, this technique is largely insensitive to data noise pollution.

Masri, Miller, Sassi, and Caughey (1984) present an approximate method of system equation order reduction, utilizing conventional condensation techniques. This

8

method is shown effective for the nonparametric identification of reduced-order model generalized nonlinear restoring forces. They demonstrate the ability to reduce the order of discrete multi-degree-of-freedom (mdof) dynamic systems, which possess arbitrary nonlinear characteristics.

Makris and Constantinou (1990) propose a fractional derivative Maxwell model. Said model was developed and calibrated from experimentally observed dynamic characteristics. They report reasonable agreement between the predictions derived from the simulation algorithm as compared with experimental results.

Constantinou and Symans (1992) present results from a series of component tests on viscous dampers to determine mechanical characteristics, frequency and temperature dependencies. They develop a mathematical model to describe the macroscopic behavior of the dampers from empirical results.

Raghavendrachar and Aken (1992) discuss the application of impact testing on a three-span reinforced concrete bridge relating to structural identification, health monitoring and damage detection. Impact testing is performed on the structure to facilitate damage detection and identification. They note that identification algorithms relying on frequency shifts and few mode shapes are not adequate to detect subtle system damage. They propose quantifying the structure flexibility with modal testing utilizing multi-reference testing.

9

Masri, Chassiakos and Caughey (1993) discuss the application of artificial neural networks to the identification of nonlinear dynamic systems. In this paper, the authors demonstrate the effectiveness of neural networks for dynamic system simulation modeling of nonlinear structural systems. As a test case, they simulate a damped Duffing oscillator, given a deterministic excitation. The simulation model incorporates a three-layer, feedforward neural network, which is shown to be adequate for characterization of the internal force in the damped Duffing oscillator.

Soong (1986-1994) investigates the feasibility of viscoelastic dampers as integral control mechanisms in large civil engineering structures. Analytical and simulation techniques for assessing the impact of viscoelastic dampers in civil engineering structures subjected to seismic loading are evaluated. Results are compared to those acquired from extensive experiments.

Taylor and Constantinou (1994) utilize experimental results to demonstrate the validity and significant energy dissipation capabilities of viscous dampers. They report substantial displacement and inter-story drift reductions, as well as inertial force reduction in certain favorable conditions. The degree of frequency (DOF) insensitivity of dynamic systems with viscous dampers is discussed. Experimental tests were performed on dampers with nonlinear viscous characteristics and marked

10

insensitivity to temperature variations. One tested damper had a stroke of +/- 600 mm and an output force of approximately 1500 kN.

Aiken and Kelley (1995) report results from reduced-scale damper testing as performed for the Golden Gate Bridge Seismic Rehabilitation Project. Their stated primary research goals were to evaluate damper energy dissipation and wear characteristics. The dampers were excited by multiple-cycle, constant velocity displacement loads at varying amplitudes and frequencies as well as sinusoidal displacements.

Masri, Nakamura, Chassiakos and Caughey (1996) present a neural network-based approach for the detection of structural characteristic changes of undefined structural systems. The approach relies on training the dynamic structural characteristics of a "healthy" structure. Subsequently, the trained network is fed the vibration excitation simultaneously experienced by the structure; the difference between the simulation and actual structure outputs are compared to an allowable error deviation. Hence, a simple error comparator defines the "health" of the structure. Damage detection is thus facilitated by threshold evaluations. This is a very promising technique for the application proposed.

A discussion of ambient vibration measurements is presented by Abe et al (1996). Ambient vibration data is captured and analyzed from Japan's "Hakucho Bridge",

located in the windy and seismically active northern region of that country. The identification scheme employs statistical means of analysis. Captured data is integrated using the random decrement method to cancel random measurement components, leaving the free vibration response of the system for modal analysis (Ibrahim, et al, 1977).

Liu and Sun (1997) develop an intelligent monitoring system for a bridge using neural networks. In the study, a truck of constant mass is driven across the bridge at a constant speed. The monitoring system, comprised of several back-propagation neural networks, measures minimum and maximum elongation of the bridge and evaluates its current condition. The study concludes that the monitoring system is an effective means of detecting damage in bridges.

Park, Reich and Alvin (1997) investigate three approaches that use relative changes in localized flexibility properties to detect structural damage. The approaches evaluated are a free-free substructural flexibility method, a deformation-based flexibility method, and a strain-basis flexibility method. The three approaches are applied to a model ten-story building, an experimental bridge, and a hybrid experimental-simulated engine structure. The research shows that while all three methods are effective in determining damage locations, the strain-base substuctural flexibility method is the most desirable.

12

Vanik and Beck (1997) present a continual on-line Bayesian probabilistic structural health monitoring method. This method can be useful in detecting small degrees of damage over long periods of time. Test results using 2-DOF and 10-DOF shear structure models are presented.

Katafygiotis and Lam (1997) also propose a Bayesian probabilistic approach for damage detection. In this research, damage is quantified through a set of damage parameters. These parameters are treated as random variables, and their probability density functions are estimated, allowing a probabilistic estimate of damage. Ultimately, damage is expressed as a finite set of damage modes, which can be ranked according to their relative probabilities.

Al-Khalidy, et al (1997) use wavelet analysis to detect fatigue damage in structures. The structures are modeled as linear single-degree-of-freedom (sdof) oscillators. The work shows that detection of fatigue signals are affected by sampling rate, signal-to-noise ratio and the vanishing moments of the wavelets used. External noise degrades the ability to detect the impulsive signals. High sampling frequency is preferable when small noise levels are present while low sampling frequency is suggested with higher noise levels.

Quantitative non-destructive evaluation and probabilistic monitoring are discussed by Achenbach, et al (1997) as complementary tools for determining structural

13

reliability. The paper presents techniques and instrumentation for flaw detection, including laser based ultrasonics, neural networks and integrated microsensors. In addition, condition monitoring is studied as an assessment of residual structural reliability.

Gaul and Sachau (1997) develop a simulation that uses active damping to control the dynamics of flexible lightweight space structures. Nonlinear transfer behavior, often observed in the joints of large space systems, is controlled by adapting contact pressure. Pizoelectric elements are used in bolted connections to achieve the desired joint pressure. Simulation studies show that greater damping performance is achieved through the use of active joints.

Lihua and Baoqi (1997) use a neural network approach to determine the location and strength of external forces acting on a plate structure. The structural response is measured with several pizoelectric sensors. A neural network model is used to determine an approximate relationship between the sensor output and the location of the load. Once the location is found, a second neural network uses the sensor output along with the location estimate to approximate the magnitude of the load. The advantages of the system are (1) that the structure is simple, (2) the neural network takes little time to train and (3) the algorithms converge well.

14

To control structural vibration, a neural controller structural design methodology is developed by Yang and Lee (1997). The approach combines experimental design with back-propagation neural network design such that the advantages of both methods can be integrated. Optimum neural network solutions are found in an experimental fashion, thereby eliminating the need for lengthy trial-and-error methods. In addition, design parameters can be analyzed through variance. Eight design parameters are used; and, an adaptive learning rate is employed.

Herrmann and Streng (1997) use neural networks to determine the location and magnitude of damage in two dimensional truss structures. The paper evaluates learning rules and network types as applied to the stated problem; it further discusses dimensional analysis as a tool for problem specific data preprocessing. As well, pruning algorithms, which are used to reduce neural network topologies, are studied. The authors conclude that a trained neural network can effectively locate and quantify the damage in a structural system, as long as the training patterns include a sufficient number of characteristics to distinguish the various states of the structure.

Chong (1997) presents an overview of the NDE of civil infrastructures. In addition, the paper outlines current projects and studies related to NDE, smart structures and materials.

15

Farrar and Doebling (1997) summarize their experience performing modal tests for damage detection on a large highway bridge in its undamaged and damaged states. The authors focus on lessons learned from this project as well as others.

A damage detection method based on the use of measured structural dynamic response and separation by damage type is presented by Hanagud and Luo (1997). Two types of damages are considered in the paper: delamination and stiffness loss due to impact damage, and traverse cracks. The approach combines the use of neural sub-networks with information obtained from the damaged structures.

Chassiakos, Masri, Smythe and Caughey (1998) present a method for on-line identification of hysteretic systems subjected to arbitrary dynamic excitations. They propose the use of the Bouc-Wen model as the basis of the identification scheme, leveraging its ability to capture properties of a wide class of nonlinear systems. A discrete-time linearized, parameterized estimator is derived for on-line hysteretic behavior estimation. Through simulation studies, they reveal that the proposed algorithm for on-line estimation of system behavior accurately portrays actual system response under wide-band random excitation.

Mita (1999) presents an overview and needs assessment of health monitoring technologies necessary to preclude future disasters such as that experienced in Kobe, Japan after the 1995 Hyogo-Ken Nanbu Earthquake. Discussion is offered

16

concerning recent contracts that have been awarded in Japan to develop new techniques and approaches in health monitoring and adaptive structural control techniques.

Sikorsky (1999) redefines the definition of structural health monitoring as given by Housner, et al (1997) to include locating and estimating damage severity and corresponding consequences (Sikorsky, 1999). He discusses Caltrans' efforts at developing a viable system from a corporate operations viewpoint, utilizing an expected loss formulation proposed (Sikorsky, 1997) in a previous paper by the author. Damage detection is facilitated by measuring the structure's stiffness properties following procedures outlined (Stubbs and Kim, 1996; Stubbs, et al, 1992). A simple updating algorithm is applied in comparing the measured data with that of the established baseline.

Park and Reich (1999) review two complementary model-based localized structural damage detection methods. The theoretical basis for these methods is a partitioned formulation of the equations of motion. One of the two methods reviewed is based on localized flexibility variations (Lloid and Wang, 1999; Alvina and Park, 1996). The second method utilizes invariance properties of the elemental or substructural transmission zeros (Reich and Park, 1999). Both methods employ a baseline reference structure for comparison. The damage detection algorithm for the localized flexibility approach relates the quasi-static strain output at one location to a

17

conjugate strain-based input force at another location. Comparisons of the flexibility changes along the matrix diagonal are sufficient to uniquely identify and locate damage. Damage detection based on localized transmission zeroes relies on a element-by-element comparison of the transmission zeros of a particular localized transfer function corresponding to one substructure for the reference and measured cases.

The practical issues associated with the implementation of effective health monitoring systems are discussed by Hall (1999). Concerned with the appropriate identification and subsequent development of data management systems for the purposes of health monitoring, he espouses a thorough, disciplined approach to the engineering and technical data management aspects of any viable structural health monitoring system.

Lee and Liang (1999) address several pertinent concerns inherent in bridge monitoring systems, namely, signal-to-noise ratios and the relation of measured vibrational data to damage thresholds. They propose a revised modal parameter, termed the energy transfer ratio (ETR) as a baseline signature. Next, they investigate the application of ETR to identification and damage location. Finally, they report on their successes in relation to conventional analysis.

18

Chang, et al (1999) propose an adaptive neural network method (Doebling, et al, 1996; Atalla, et al, 1998; Masri, et al, 1993; Levin and Leven, 1998; Wu, et al, 1992; Szewczyk and Hajela, 1994; Jiao, 1996; Luo and Hanagud, 1997) for structural model updating and damage detection. The method employs an improved back-propagation learning algorithm with a jump factor. A dynamic learning rate also developed and incorporated.

Helmicki, et al (1999) demonstrate the evaluation of a steel-stringer bridge through various monitoring techniques and field tests (Helmicki, et al, 1999). Their work focuses on the instrumentation, data collection and processing from a steel-stringer concrete deck composite bridge structure (HAM-126-0881) constructed in the Cincinnati, Ohio area in 1997. Measurements were acquired throughout the construction phases, allowing *in-situ* development of a health monitoring system baseline. A total of 642 channels of data are available for future health monitoring evaluation.

Catbas, et al (1999) present an overview of health monitoring for long span structures. They cite the recent retrofit activities on two bridges, the Golden Gate and SFOBB, in Northern California as examples of the need for adequate health monitoring systems to preclude abrupt disruption to the region's economic well being. Their studies actually concentrate on the Commodore Barry Bridge (CBB) spanning the Delaware River between Chester, Pennsylvania and Bridgeport, New

19

Jersey. Discussions center on the appropriate modeling of the structure for baseline development, instrumentation types and data acquisition management.

Lloyd and Wang (1999) discuss decision error minimization in probabilistic neural networks. Their approach is to apply a Monte Carlo simulation of a two dimensional neural network to determine the probability of not achieving a successful detection; i.e., a miss or false alarm. They conclude that the miss probability is dependent on the kernel density estimator window width used to characterize the training set. Additionally, they demonstrate that through implementation of a selection based, data driven criteria for h, instead of using h_{opt} as selected in the MISE sense, detection errors are not adequately impacted. Instead, they propose an algorithm which estimates the influence of the bias error using asymptotic expansions, resulting in reasonable detection rates.

A discourse on symptom based reliability is presented by Yao and Wong (1999). In this paper, they explore the merits of implementing fuzzy sets to facilitate descriptive interfacing with health monitoring systems. Issues of fatigue and as-built environmental concerns are capable of being addressed with symptom based reliability variables. This work is ongoing.

Hyland and Fry (1999) present a neural-genetic hybrid approach for structural health monitoring systems. They modify neural network theory to incorporate a series of

20

identical replicators, each competing to identify the system being analyzed. Their work in many ways emulates behavioral science research, providing "rewards" to successful replicators, by Darwinian selection criteria; *the most adaptive species prevails*. The basic premise is to arbitrarily select the synaptic weights for each replicator, then apply the system stimuli to the replicator bank. A comparator evaluates the output of each replicator, and determines the "winning" replicator, that which yields the lowest output error as compared to the system output. The other replicators retain their existing weights and continue to compete, thereby increasing system reliability and performance as these might more quickly discern and correct for changes in the system. Applications of this methodology are potentially numerous.

Time-domain parameter estimation techniques for structural damage detection are presented by Sana and Rao (1999). In short, neural network based algorithms incorporating smart actuators and sensors are discussed. A parameter identification method based on time-domain response data is employed to extract vibration signatures for damage detection. This method relies on accurate modeling of the structural system under consideration (Banks, et. al., 1996), as it is determined that the structural variations leading to damage are not well defined in a standard finite element model. The modeling method employed is shown to easily describe the piezoceramic patch interactions with the underlying structures, yielding good agreement with the experimental data. Neural networks are chosen for their

21

adaptability to complex unknown systems because of the inherent difficulties in measuring the system damping ratio, hence reducing the effectiveness and reliability of transfer function coefficients as the poles and zeros cannot be accurately placed. Limitations to this method include difficulty in modeling complex systems, detecting multiple damages and discerning delaminations, cracks, etc.

The application of wavelet analysis is studied and reported on by Hou and Noori (1999). They utilize a wavelet-based approach to discern structural damage. Structural damage is detected by locating spikes in the wavelet decomposition of the acceleration response. A major limitation to this approach, as reported, is its sensitivity to noise corruption, hence requiring a relatively large signal-to-noise ratio (SNR) for accurate detection.

Bolton, et al (1999) are concerned with methods of evaluating structural deterioration. They report on the results of a modal-based Level IV non-destructive damage detection procedure. Data collection from in-service structures was collected from drop hammer tests. The data was then processed to yield modal parameters. They report that the fundamental mode shapes were in agreement with analytical predictions; however, they also note that higher mode shapes were more complex. Additionally, the recorded data was well above the ambient noise floor created by traffic loading. An impact of 3000 lb peak over 50 ms was reported sufficient to excite all structural modes necessary for damage detection algorithms.

22

While the reported results were good, this method does rely on off-line post processing of the data, and is not applicable for on-line algorithms at present.

Shinozuka and Rejaie (2000) used correlation techniques on remotely sensed pre- and post-disaster imagery to detect damage. Camera calibration data is utilized to achieve three-dimensional representations of the imagery. Correlation between the baseline image and additional imagery collected at a later time is performed to detect changes.

Free damped vibrations of a suspension bridge are studied by Rossikhin and Shitikova (2000). The study utilizes fractional derivatives to define system damping features. The research concludes that the use of fractional derivatives in modeling viscosity yields a two-fold influence on a suspension bridge; the stabilizing effect of damping of vibration amplitudes and the destabilizing effect of unstable vibratory motions. The system is stable when the orders of the fractional derivatives governing the damping of vertical and torsional vibrations are equal. Instability of the system results when the fractional derivatives differ.

Long-term continuous, remote monitoring of bridges is discussed by Alampalli and Cioara (2000). Acceleration data due to vehicular traffic was recorded and analyzed. Fluctuations in modal frequencies due to thermal conditions were determined to set a baseline for damage detection thresholds. Estimation of variations in the modal

23

parameters of the structure were evaluated utilizing the Selective Random Decrement Technique. An alternate method, briefly discussed, is the application of the Fast Fourier Transform of the signal with a curve-fitting algorithm.

Several types of control strategies are investigated by Agrawal (2000) for the control of an electromagnetic semi-active friction damper and a semi-active stiffness damper. This study was performed with data gathered from buildings subjected to near-field earthquakes. Data from the Northridge and Kobe earthquakes was utilized. The research reveals that two of the semi-active dampers evaluated outperformed other passive and semi-active dampers.

Lopes, et al (2000) utilize neural networks to detect and locate structural damage. An external surface-bonded piezoelectric sensor/actuator excites the structure at greater than 30 kHz to facilitate structural point impedance changes. Said changes reportedly result from structural damage. Multiple sets of neural networks were developed to detect, locate and characterize structural damage through examination of variations in the measured impedance curves. In short, this method is predicated on the knowledge that structural damage is both a local phenomena and a high frequency effect.

Wavelet analysis of measured reflected signals is discussed by Lihua (2000). Electrical time domain reflectometry (ETDR) (Dowing et al, 1995) techniques are

24

improved through the application of wavelet analysis. Basically, transmission line theory is used to simulate time-domain reflection in concrete structures. Damage thresholds are established as the sensitivity of the time-domain reflection coefficient of the transmission line. Wavelet analysis is employed to preclude difficulties in identifying the arrival time of the reflected signal due to attenuation and environmental measurement noise.

Health monitoring of long-span bridges is studied by Catbas, et al (2000). The researchers focused on the applicability of numerous data recovery stations for long-span structures, concluding that present star topology systems wherein the data recovery systems are centrally located are not feasible for long-span structures. The basic premise of this paper was integrated asset management of data collection systems for bridges.

The research by Fuchs, et al (2000) reviews the applicability of utilizing a scanning laser-based displacement measurement instrument for monitoring large-scale civil structures. Data was collected from several long-span specimens at the Federal Highway Administration's (FHWA) Turner-Fairbank Highway Research Center (TFHRC) to determine the feasibility of implementing laser-based scanning systems in the field. Detailed surface profiling and long-term movement data was recorded.

Stubbs, et al (2000) present a practical methodology applicable to NDE of the structural properties of bridges. The Damage Index Method (Stubbs ,et al, 1992) utilizes changes in the modal strain energy, as stored in the pre- and post-damaged structure, as an indicator of structural damage. They state that this method is capable of locating structural damage where no baseline data is available (Stubbs and Kim, 1996).

Park, et al (2000) discuss experimental work on an impedance-based health monitoring technique for civil structures. High frequency structural excitation (30 kHz) is applied to the structure of interest through surface-bonded piezoelectric sensor/actuators to facilitate damage detection. Variations in structural impedance are used as the indication that damage has occurred. Importantly, this method is not able to predict the exact nature and size of incurred damage. Reliance on quantitative NDE techniques such as ultrasonics (UT) or eddy current (ET) may be required to facilitate more precise location and classification of damage.

A semi-active variable damping tuned liquid column damper is researched by Yalla, et al (2000). Various semi-active algorithms are compared, such as clipped optimal continuously varying and on-off approaches. Additionally, sub-optimal control strategies using LQR/LQG and fuzzy controllers for a mdof structure with the tuned liquid column dampers attached at the top story are studied.

26

A method of localized structural health monitoring on damage detection of a bridge column is demonstrated by Reich and Park (2000). The method is based on the relative changes and localized flexibility properties of the structure.

Chen (2000) investigates the effect of soil-structure interaction (SSI) on the performance of passive, semi-active and active control strategies. The research shows that SSI tends to degrade the effectiveness of control systems. This is largely due to the fact that damping is increased, causing the structure to behave like a rigid body.

Choi and Kwon (2000) developed a damage detection system for a steel truss bridge to determine the location and severity of damaged members. A finite element model of the bridge was developed and a damaged scenario was simulated. A neural network was implemented to determine the location of the most severely damaged member.

Optimal instrumentation strategies for structural health monitoring methods are presented by Paadimitridu, et al (2000). Information entropy measures of the uncertainty in modal parameter estimates are minimized to determine optimal sensor configuration. Structural model parameterization is used to facilitate input-output descriptions of the structural behavior. Bayesian statistical methods are employed to compute the information entropy of the uncertainty in the parameters of the

27

structural model. A generic algorithm is utilized to evaluate the discrete optimization problem involving minimization of the information entropy over all possible sets of sensor configurations.

Cosner (2001) examines uncertainty quantification for application in computational fluid dynamics (CFD). While interested in establishing confidence levels for CFD predictions in the design process, his work on uncertainty quantification is relevant to this effort.

Ziemianski (2001) analyzes neural network applications in damage detection problems. He concludes that Back-Propagation Neural Networks (BPNNs) can be a valuable tool in the analysis of structural damage problems.

Sikorsky, et al (2001) present a modal analysis of two adjacent structures on Route 86 in Riverside County. Interestingly, one structure is a conventionally reinforced concrete slab and the other is comprised largely of carbon and glass-fiber reinforced composite materials. Determination of system stiffness changes is accomplished by defining damage in terms of global stiffness variations. Modal analysis of field derived data sets are compared to finite element models of the structure without flaws.

28

Quantification of uncertainties inherent in physical systems is discussed by Doebling and Hemez (2001). The effects of parametric variability propagation in numerical simulations is considered in evaluating the validity of system modeling. Parametric and nonparametric uncertainties are also studied. Monte Carlo techniques are utilized in quantifying the effects of system variability. Correlation of response parameter ratios is reported.

Jin and Livingston (2001) discuss the development of an extensive health monitoring sensor network for incorporation in the new reinforced concrete Woodrow Wilson Bridge across the Potomac River. Optimization of sensor location was determined utilizing a detailed nonlinear finite element (FE) model. Member connectivity is considered in the FE evaluation. Model validation will be performed during construction phases, leading to corrections in the sensor network for final evaluation.

Vecchio and Van der Auweraer (2001) present a model-based approach to damage detection and localization. They validate their proposed methodology with experimental test data derived from a simple structure with artificially applied damage scenarios. Damage localization requires a FE model. Acquired data is processed statistically utilizing the χ^2 approach. Structural damage is quantified by comparing modal statistics to an undamaged reference case.

29

Of the papers reviewed, those which presented the neural network approach as well as approximate methodologies of system equation order reduction appear to be the most promising technologies for the intended purpose. There are numerous other papers in this burgeoning field of research. In fact, technical conferences are held worldwide with multiple papers on this very topic. One such conference is the annual IMAC, where a substantial number of technical papers are devoted to technical damage detection and health monitoring.

30

3.0 Theoretical Background

This chapter provides the major impetus to this research effort and presents a brief synopsis of the system identification approaches utilized in later sections. Current quality assurance testing specifications for dampers employed on several California bridges are presented.

3.1 SFOBB Dampers

Figure 3.1 below provides a view of a typical tandem set of dampers as proposed for implementation on the West Spans retrofit of the SFOBB.
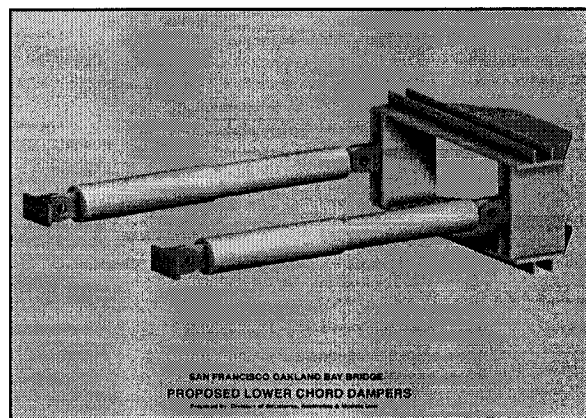
FIGURE 3.1. Typical damper

Dampers can be described by a relatively simple mathematical model, as depicted in Figure 3.2 below. This fact simplifies the development of mathematical representations of the damper system.

31

$$F(t)$$

$$g(y,\dot{y},\mathrm{T})$$

$x_1(t)$ $x_2(t)$

$x_1(t)$ $\mathrm{T}(t)$ $x_2(t)$

$x_1(t)$ $x_2(t)$
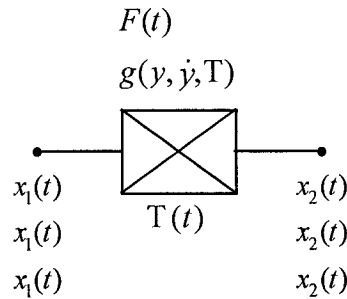
FIGURE 3.2. Descriptive mathematical model

3.2 Planned Quality Assurance Testing

The contract specifications for most dampers incorporated into State of California

highway bridges require limited testing, both at the prototype and proof levels.

These tests basically analyze the dampers at discrete frequencies. In reality, the

dampers will be exposed to numerous broadband excitations throughout their service

life. Hence, any analysis attempting to capture and quantify the dynamic

characteristics of the dampers, particularly for optimization and eventual application

of analytical NDE tools must necessarily include similar testing.

Presently, the contract specifications require the aforementioned tests to be

conducted at the newly constructed Seismic Response Modification Device Test

System (SRMD) on the campus of the University of California, San Diego. The

potential exists for the proof tests to occur at the damper manufacturing facility,

Taylor Devices Incorporated in New York, if a variance is accorded.

32

While the contract specifications clearly stipulate the testing at the prototype and proof levels, they do not broach the topic of instrumentation, opting instead to allow the test facility the leeway to propose alternatives. In reality, the degree of instrumentation is relatively minor to obtain the data required for the temperature and hysteresis specifications. In fact, a thermocouple, a force transducer and a displacement transducer are all that are needed to comply. Further discussion of instrumentation requirements for this proposal is contained in Section 4.

3.3 Development of an Accurate Mathematical Model for an Individual Damper Element

3.3.1 Technical approaches

Using one of the generic viscous dampers as shown in Figure 3.1, a sequence of experimental tests was conducted to precisely characterize the force-deformation properties of an isolated individual member. Parametric as well as nonparametric analytical approaches were employed to furnish different formats of the member's characteristics. These are discussed below.

3.3.1.1 Parametric identification approaches

Parametric identification approaches to structural health monitoring provide an important class of identification procedures. Parametric methods basically attempt to determine the value of previously identified and assigned parameters based on an assumed representation of the dynamic system under investigation. Their value

33

cannot be overestimated, as they provide analytical methodologies wherein the estimated system parameters can easily be associated with identifiable system parameters such as stiffness and damping. Hence, deviations in the identified model parameters can be traced to actual changes in the system being estimated. This allows a measured degree of identification, which may not be a precise indicator of the source of a problem, but nonetheless yields clues for system evaluation.

Parametric methods allow identification of hysteretic systems, a particularly difficult class of nonlinear structural behavior. Chassiakos, et al, 1998 presented an efficient technique to develop suitable nonlinear model(s) of varying degrees of complexity; this technique serves as the basis for the following parametric analysis. Additionally, the parametric method studied herein for the evaluation of the damper components on the retrofit of the West Spans of the SFOBB is capable of providing real-time structural monitoring. This was an important point when investigating potential on-line structural health monitoring systems.

For the dynamic system under consideration - that is, dampers - the system equation of motion is well documented. All that remains is estimating the mass, stiffness and damper coefficients. For the general case, the governing equation of motion can be represented as

$$m_2 \ddot{x}_2(t) + c_2 \dot{x}_2(t) + k_2 x(t) + m_1 \ddot{x}_1(t)$$
$$+ c_1 \dot{x}_1(t) + k x_1(t) + f_n(t) = F(t) \tag{3.1}$$

34

where the matrices, m, c and k are defined as the mass, damping and stiffness matrices, $F(t)$ is the loading matrix and $f_n(t)$ defines the nonlinear forces. Details of this equation are found in Masri, et al (1987).

3.3.1.2 Nonparametric identification approaches

While parametric methods attempt to fit experimental data to an assumed model of the dynamic system of interest, nonparametric methods yield a functional representation of the dynamic system without assumed *a priori* knowledge. Basically, nonparametric methods can be viewed as analytical tools to evaluate "black box" system characteristics. Information regarding the system input excitation and relevant output data are fed into a variety of analytical tools to yield the internal system characteristics. Such algorithms have been finely honed in the past fifteen years, resulting in tools that can replicate "black box" dynamic system responses remarkably accurately within a few data samples. Examples are depicted in the pertinent references.

The nonparametric phase of the investigation utilized two approaches:

a.) The method of Masri and Caughy (1979), whereby the effective restoring force of the element was analytically represented in terms of a doubly-indexed series of orthogonal polynomials involving appropriate basis functions that depend on the element's state variables.

35

b.)   The use of artificial neural networks consisting of three-layer

feedforward nets (Masri, et al, 1993).

As with the class of parametric models, nonparametric methods can be applied to highly nonlinear dynamic systems as easily as to linear systems. Additionally, real-time, continuous data acquisition is possible.

3.4 Parametric Studies to Evaluate Damage Pattern Signatures

In quantifying the damper system characterization, several parametric studies were performed. These studies established the various relevant influences acting on the system, thereby facilitating establishment of damage detection thresholds. As in any parametric analysis, data was collected and represented statistically.

Among the issues investigated in this task were:

1. The influence of the spectral content of the excitation on the member's behavior.

2. The variation of the member's properties with deformation
   (excitation) level.

3. The influence of the direction of excitation on the member's
   response.

4. The stationarity of the member's properties (thermal effects, wear, etc).

5. The level of uncertainty in the member's behavior.

36

4.0 Test Apparatus

4.1 Equipment Specifications

As noted previously, calibration and initial selection and optimization was undertaken in the labs on the campus of the University of Southern California. To facilitate this testing, a test stand was constructed, a hydraulic actuator sized and purchased, and a similar damper element acquired from Taylor Devices, Inc. Data acquisition and processing was performed as delineated above.

A 10-kip Taylor Devices damper was selected for testing after discussions with both Taylor and Enidine, the two damper manufacturers prequalified by Caltrans to bid to supply dampers for the seismic retrofit of the SFOBB. This selection was largely based on the fact that Taylor could provide a reasonably scaled damper with similar internal construction as compared to the full-scale dampers specified for the SFOBB retrofit. This damper was being reconfigured by Taylor Devices from a 20-kip model to meet the necessary specifications for the work discussed herein; that is, a damper force rating of 10-kips, velocity capacity of 70 ips and +/-6 inch stroke.

The next step was sizing of the actuator. An 11-kip MTS Systems actuator fitted with a 90 gpm servo valve was chosen to meet the velocity requirements of the test plan. Basically, the sizing calculations were performed as follows:

37

$$\dot{m} = 90\,gpm\,servo\,valve\,x\left(\frac{1\,\text{min}}{60\,\text{sec}}\right)x\left(\frac{1\,ft^3}{7.48\,gal}\right)x\left(\frac{1728\,in^3}{1\,ft^3}\right)$$

(4.1)

$$\dot{m} = 346.5\,in^3\,/\,\text{sec}$$

The cross-sectional area of the damper piston was simply computed as

$$Area = \frac{Force}{\text{Pr}essure} = \frac{11\,kips}{3\,kips} = 3.667\,in^2$$

(4.2)

Then, the maximum attainable velocity given the selected components was simply

$$V_{max} = \frac{\dot{m}}{A} = \frac{346.5\,in^3\,/\,\text{sec}}{3.667\,in^2} = 94.5\,ips$$

(4.3)

The maximum frequency component attainable with the specified equipment was

calculated from simple trigonometric formulas as

$$x = A\sin(2\pi f t)$$

(4.4)

$$\dot{x} = 2\pi f A\cos(2\pi f t)$$

where the maximum velocity was as computed above, $V_{max} = 94.5$ ips $= 2\pi f A$. Recall

from the damper specifications cited above that the maximum displacement is +/- 6

inches. Thus, A is equal to 6 and the maximum attainable frequency is

$$f_{max} = \frac{V_{max}}{2\pi A} = \frac{94.5\,ips}{2\pi(6\,in)} = 2.5\,hz$$

(4.5)

Reducing the displacement to ½ inch peak yields a maximum frequency of 30 Hz.

Figure 4.1 pictorially depicts the frequency/displacement relationship for the

specified test components.

38
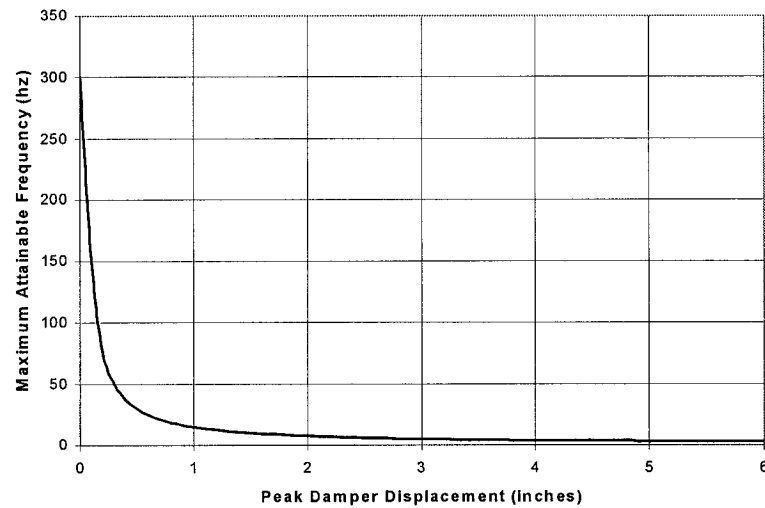
FIGURE 4.1. Damper test frequency/displacement relationship

4.2 Setup

To handle the large forces and accelerations generated in this testing a massive steel and concrete table was constructed (reference Figure 4.2).
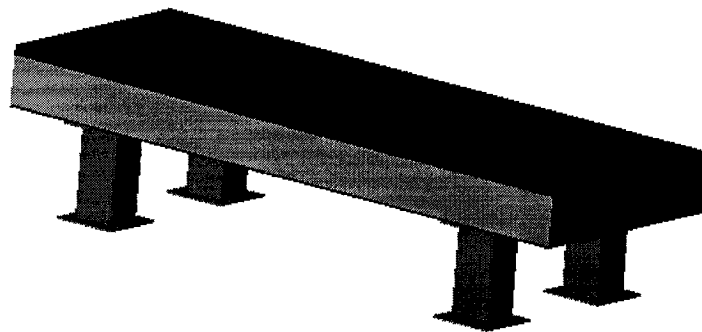
FIGURE 4.2. SolidWorks® depiction of test stand

39

Finite element modeling of the table was performed using NASTRAN®, after mesh

development in SolidWorks®. Table sizing was designed to force a natural resonant

frequency of around 50 Hz, with the actual first mode reported at 48 Hz (reference

Figure 4.3). Note that the mode shape depicted in Figure 4.4 is the seventh mode

shape. NASTRAN® reports the first six mode shapes as rigid body motions, so mode

shape number seven is the first unconstrained mode shape, often referred to as the

first mode shape in literature. Handling limitations due to existing laboratory

facilities factored heavily in the final table design. The table weight was limited to

8.2 kips, being comprised of a 9.5-inch thick concrete slab sandwiched between two

steel plates. The top plate was two inches thick, the bottom plate only one-half inch

thick.
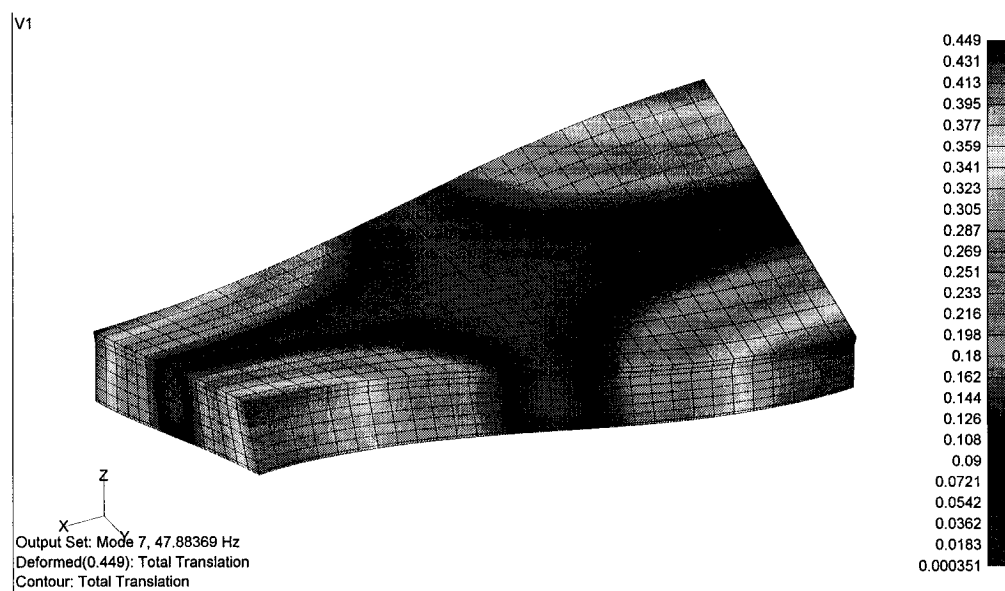
FIGURE 4.3. Table finite element results

40

5/8-inch diameter (#5) reinforcing steel studs were fillet welded in a 9.5x10-inch

pattern on each plate to ensure adequate bond to the concrete layer (reference Figure

4.4). A total of 120 reinforcing steel studs were utilized. Trunyon mounts were then

welded to the ends of the steel plates, acting as spacers for the sandwiched concrete

slab as well. The steel plates were set in a vertical plane, and concrete was placed

and vibrated in between the steel forms. The completed slab was then moved on

dollies to its final resting place on 4-8x8x1/2 TS legs located in a corner of the

basement dynamics laboratory.

View of Top and Bottom Plates

Close-up of 8x8x1/2

End View Depicting Welded Studs
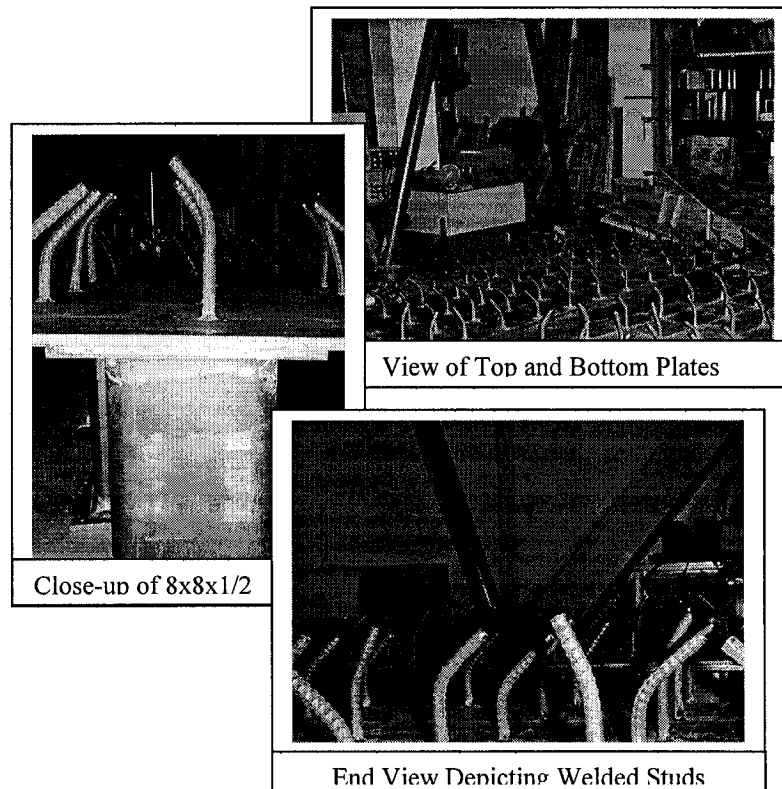
FIGURE 4.4. Construction photos

41
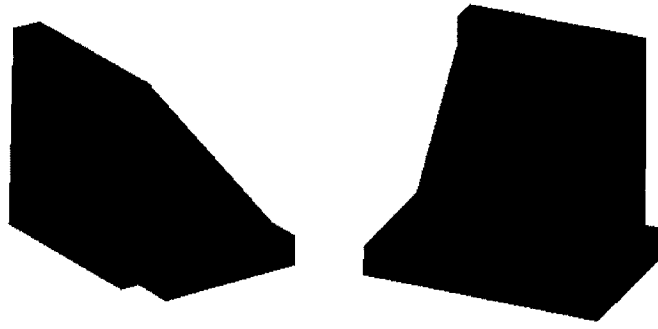
FIGURE 4.5. Table anchor blocks

The 11-kip actuator and 10-kip damper were mounted to fabricated steel anchor

blocks, which are shown in Figure 4.5. These anchor blocks are comprised of 1 and

2-inch steel plates joined with fillet welds. The anchors are designed to bolt to the

tabletop, thereby allowing flexibility with various damper sizes. The damper and

actuator components attached to the anchor blocks via bolted clevises.

The connection between the actuator and damper incorporated linear bearings to

preclude introducing moments to the damper and actuator shafts, which could lead to

premature failure of the components. This assembly was also bolted to the tabletop

to allow adjustments as warranted with new hardware. Clevises were attached to a

built-up, "T"-bracket design, 2-inch thick steel plate to mate to the linear bearings.

Completed depictions of the assembly, incorporating the actuator and damper

elements with the anchor blocks are shown in Figure 4.6. An exploded view of the

42

damper/actuator connection assembly is presented in Figure 4.7. The completed

assembly is photographed in Figure 4.8.

The noise floor introduced by the bearings was measured and recorded as shown in

Figure 4.9. At 1.59 Hz, the level of noise compared to the measured acceleration

was approximately 21%. This noise was interpreted to be within the range of 1.2-2.2

Hz.
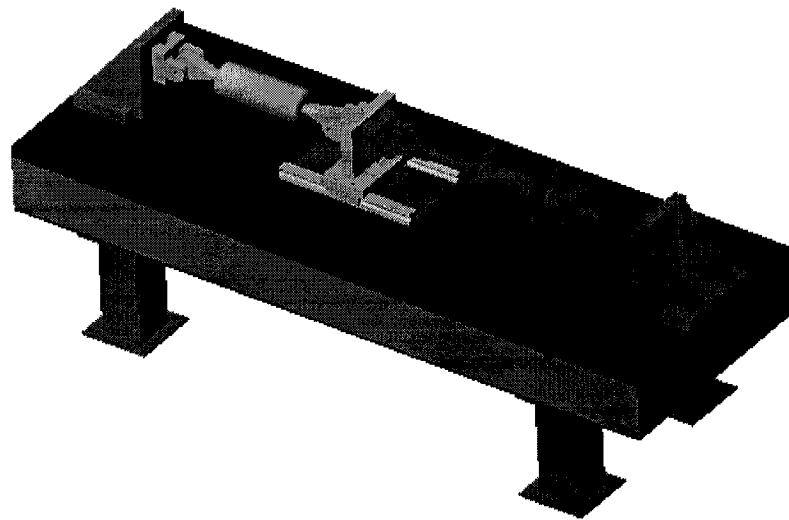
FIGURE 4.6. Completed assembly

43
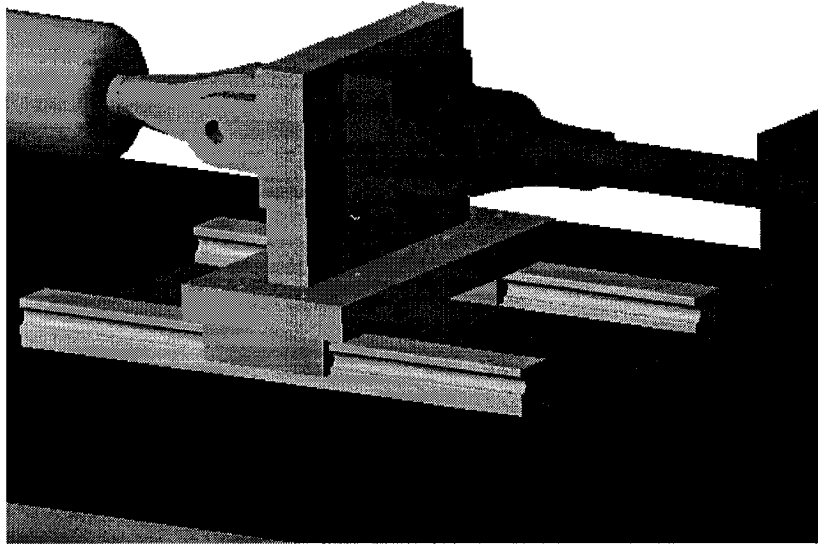
FIGURE 4.7. Actuator/damper connection
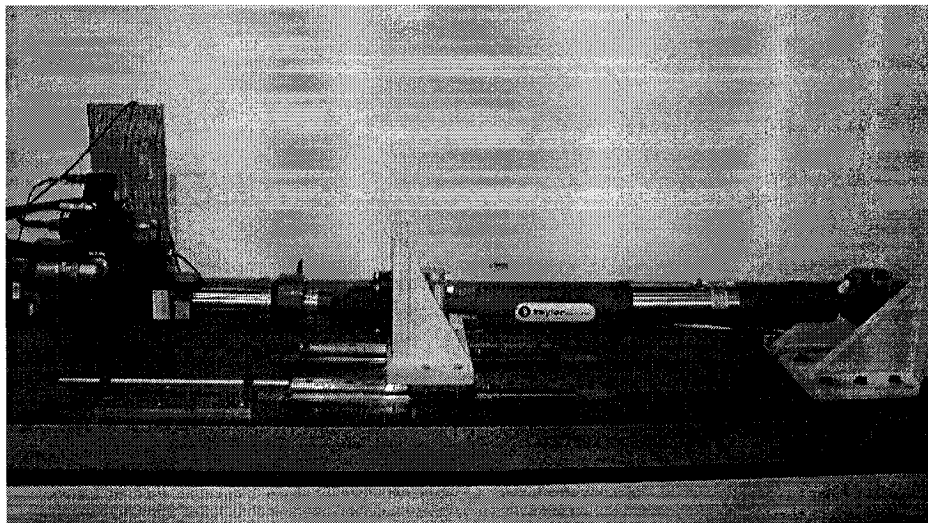
FIGURE 4.8. Photo of actual completed assembly

44
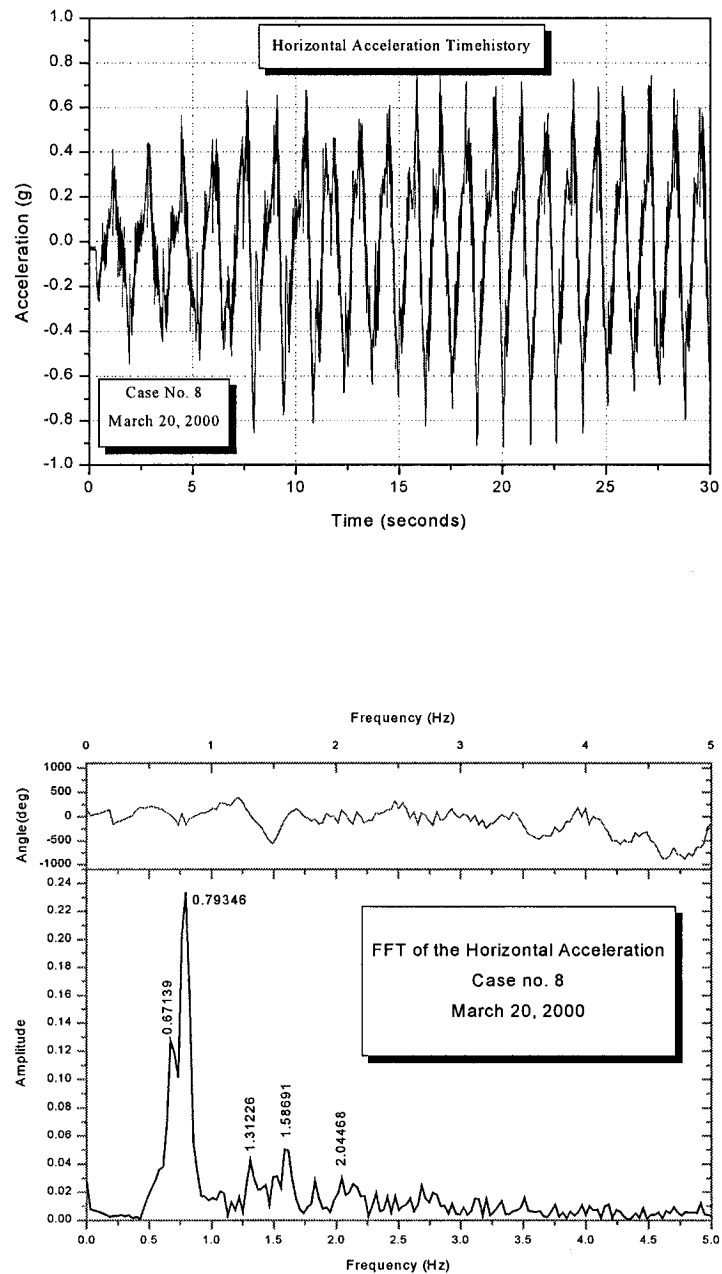
FIGURE 4.9. Measurement and analysis of bearing motion

(Upper: acceleration timehistory; Lower: acceleration frequency content)

45

Hydraulic energy to the servo valve was plumbed from the existing dual sliding tables pump located in the basement of Kaprielian Hall. A hydraulic manifold located immediately prior to the servo valve served to reduce the head losses due to compressibility concerns. The system was controlled by an existing MTS controller outfitted with a special control module. A dedicated Pentium PC running Windows NT provided data acquisition capability. The computer was networked to allow easy data transfer to the UNIX system for data storage, manipulation and processing. A simplified depiction of this setup is presented below in Figure 4.10.

FIGURE 4.10. Simplified diagram of test system

5.0 Data Collection and Processing

An important aspect of successful research programs relates to well-planned execution. Good research is not only technically accurate and focused, but also replicable. This chapter provides appropriate detail related to the planning phases of the research, including the necessary instrumentation, data collection and archiving tools utilized. Also included is a discussion of the various processing algorithms used for system parameter identification.

5.1 Instrumentation

Figure 5.1 depicts an idealized damper, detailing the location of sensors. The contract specifications for seismic retrofitting of bridges in California with viscous dampers require a thermocouple (T), a force transducer (F) and a displacement transducer (y) to collect the necessary data for the prototype and proof testing. To facilitate the additional testing proposed herein - to quantify and optimize the analytical tools for health monitoring applications - additional instrumentation was required. Basically, the addition of acceleration ($\ddot{y}$) and velocity transducers ($\dot{y}$) were necessary to identify system characteristics. Due to the relatively simple dynamical system presented by viscous dampers, a single acceleration transducer and a velocity transducer were sufficient. These instruments were optimally located, as depicted in Figure 5.1 below.

47

$$y(t) = x_2(t) - x_1(t)$$
$$\dot{y}(t) = \dot{x}_2(t) - \dot{x}_1(t)$$
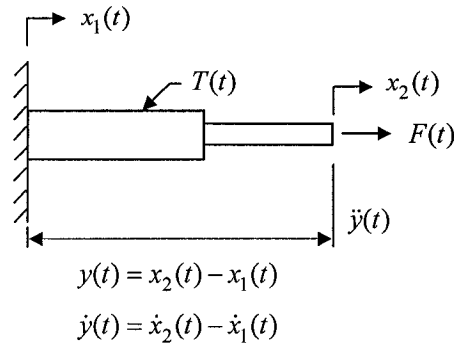
FIGURE 5.1. Typical damper

5.2 Data Collection and Storage

Data collection from experimental laboratory tests was performed utilizing a

Pentium personal computer equipped with a National Instruments® AT-MIO-16X

A/D board. A LabVIEW® program was written to facilitate data acquisition and

storage. The program features eight acquisition channels and supports multiple

output channels for control signals. Acquired data was written to a user-defined text

file, which could then be read into postprocessing routines in Fortran, MSExcel® and

Matlab®, or ported to the UNIX platform in ASCII format. A user-friendly interface

allowed selection of data acquisition rates, number of channels, channel gains,

instrumentation gain factors, channel naming conventions and data file output

conventions. Acquisition rates were between 1 and 5 kHz, to ensure capturing high

frequency data.

48

5.2.1 Data Acquisition

Engineering researchers have historically modeled the complexities of natural phenomena with reduced-order mathematical representations. Such modeling reduces complexities to manageable levels, important for real-time data processing as well as developing insight into the physical system. Acceptable levels of reduced-order model inaccuracy in replicating physical system interactions and behavior under a wide range of stimulus are defined and quantified through simulation and experimental testing.

This research attempts to model the complex dynamics of a viscous damper as an sdof system. In reality, dampers are highly nonlinear mdof systems with complex mechanical/fluid interactions. Nonlinear dynamics inherent in dampers include gap elements to model fluid/orifice interaction under reversing direction. The measured signature of highly damped systems is largely characterized by low frequency components. It is this fact that attracts the engineering profession to apply damping systems for structural seismic behavior modification. However, the design of data acquisition systems must span a broad frequency range, from nearly direct current (DC) to high frequencies to capture the nonlinear interactions contained in the high frequency range of the signal. Application of the Sampling Theorem (Kreysig, 1993) to avoid digitization errors requires the sampling frequency be greater than twice the maximum frequency component of interest in the signal being sampled.

49

To detail the effects of improper sampling or digitization, Figure 5.2 depicts three phase-plane plots of restoring force versus velocity derived from the same experimental data set. The damper was excited by a 5 Hz sinusiodal input with a 0.25 inch peak amplitude. The external damper temperature at the beginning of the test was 73.4°F, increasing to 78.2°F at the culmination of the 30 second test. The data plotted in Figure 5.2a contains sampled frequency information to 5 kHz. Figure 5.2b displays the identical phase plane representation, only the data set used is decimated by filtering, reducing the frequency content to below 1 kHz. Figure 5.2c represents the same data set decimated to 250 Hz. The phase-plane representation in Figure 5.2a is noticeably rippled throughout, with large nonlinearities evident at near-zero velocities when the system is experiencing direction reversal. The ripples in the phase diagram indicate the presence of nonlinear system dynamics captured in the higher frequency realm of the signal. These ripples are largely lost in Figure 5.2c, with only limited evidence of nonlinear system behavior, substantiating the need for higher data acquisition sampling rates to facilitate detection of subtle shifts in the dynamic behavior of a damped system. The large excursions at low force and velocities in the phase-plane plot are indicative of "dead-space" dynamics occurring in the viscous fluid/orifice interaction during direction reversal. These excursions provide a means of quantifying the orifice sizing through measurement of the length of the spike and modeling of the fluid/orifice interaction. At elevated temperatures or changing fluid viscosity, the fluid/orifice interaction will vary, thereby providing a potential gage of system degradation. Thus, the data acquisition system design is a

50

critical element in successfully capturing the system dynamics to discriminate subtle signal shifts potentially indicative of system degradation.

5.2.2 Data Storage

Data from the simulation studies, as well as from the laboratory experiments were processed and stored in ASCII format on a UNIX platform in the USC Department of Civil Engineering Research database (Wolfe, 1999). This database is a tool intended to facilitate large-scale data storage resulting from the variety of research projects undertaken at the University. Data stored in a two-dimensional ASCII array is processed and stored efficiently in the database for future reference. The database is a compilation of the efforts of various graduate students and Dr. Masri through the years, dating back to the days of the VAX system (the late 1970's through the 1980's).

The benefits associated with the utilization of the database for the storage of research data include the ability to quickly and easily retrieve user-defined segments of the data for analysis. Additionally, the user can input a forty-character descriptive text line to facilitate data definition for future reference. The data array can be n-dimensional, given that n is specified as a parameter in the source code. In addition, a variety of data analysis tools are available to facilitate this endeavor, including integration codes, statistical analysis and plotting routines. The data can also be retrieved and exported to external data analysis packages.

51
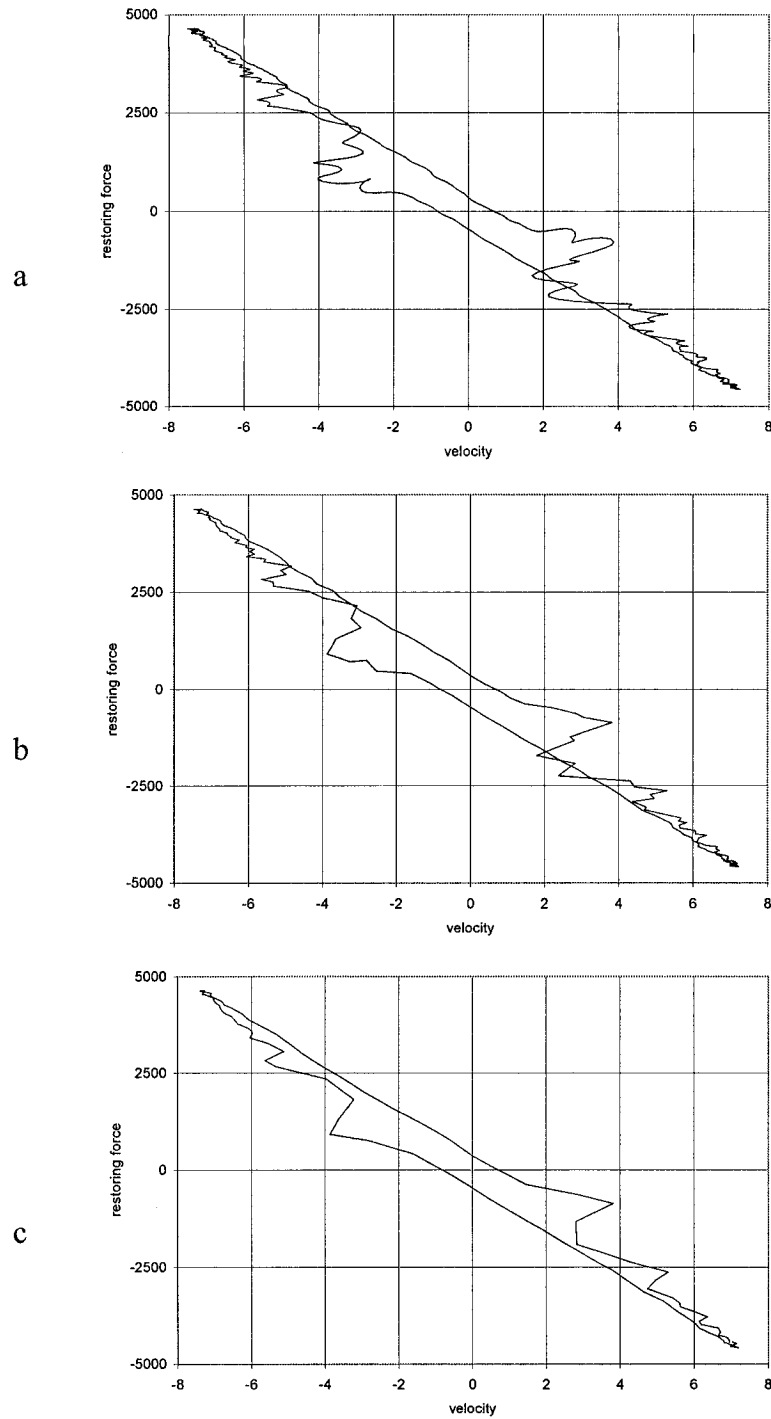
FIGURE 5.2. Restoring force vs velocity phase plots

In general, the database can accommodate an *n*-dimensional array of data for processing and storage. The data must simply be saved in ASCII format to facilitate the procedure. Vector storage names as well as the number of columns of data contained in the data array to be processed must be hard-coded into the source code prior to compilation. The present code offers the user the flexibility to add a comment description line for the set of data being processed from one input array. A parsing routine was written to preprocess the data, regardless of whether it is formatted as comma, space or tab delimited. The output of this preprocessor is data formatted in one-dimensional vectors, as required by the database.

The naming conventions used for the data collected from the instruments discussed above were as follows:

Displacement transducer	x1
Velocity transducer	xd1
Accelerometers (2 total)	xdd1, xdd2
Force transducer	force1
Thermocouples (2 total)	TC1, TC2

A naming convention for implementation with the USC UNIX-based database was necessary to handle the large quantities of data generated from both the experimental and simulation studies. First, the database allows three character descriptions in the database file names, Dxxx.FDR and Sxxx.RUF. Databases were kept for each phase

53

of the experimental and simulation testing: calibration, testing and simulation. The testing and simulation phases consisted of a series of excitations, including sinusoidal, swept sine, and stationary and nonstationary random. Excitation control parameters such as amplitude, frequency, sweep time, period and degree of nonstationarity were varied to fully characterize the system response for both the experimental and simulation studies. This was addressed in the excitation naming convention as noted below. The data channels stored within the databases followed standard engineering naming conventions as noted above.

DCAL.FDR	SCAL.RUF	calibration
DESN.FDR	SESN.RUF	experimental, sine
DESW.FDR	SESW.RUF	experimental, swept sine
DESR.FDR	SESR.RUF	experimental, stationary random
DENR.FDR	SENR.RUF	experimental, nonstationary random
DSSN.FDR	SSSN.RUF	simulation, sine
DSSW.FDR	SSSW.RUF	simulation, swept sine
DSSR.FDR	SSSR.RUF	simulation, stationary random
DSNR.FDR	SSNR.RUF	simulation, nonstationary random

5.2.3 Excitation Log

The excitation channel naming convention linked the applied excitation to the excitation log as defined herein. The six-character excitation channel was named

EXCTxx. Two examples depicting the usage of the excitation log are presented herein, one for a sinusoidal system input and the other for a random excitation.

Sinusoidal input: $F(t) = F_0 \sin(\omega t)$

EXCT01 $F_0 = 1, \omega = \omega_n$

EXCT02 $F_0 = 1, \omega = \omega_n - \delta$

EXCT03 $F_0 = 1, \omega = \omega_n + \delta$

$\vdots$ $\vdots$ $\vdots$

EXCT0m $F_0 = 2, \omega = \omega_n$

EXCT0m+1 $F_0 = 2, \omega = \omega_n - \delta$

EXCT0m+2 $F_0 = 2, \omega = \omega_n + \delta$

$\vdots$ $\vdots$ $\vdots$

random input: $F(t) = F_0$

EXCT01 $F_0 = x_1$

EXCT02 $F_0 = x_2$

$\vdots$ $\vdots$ $\vdots$ $\vdots$ $\vdots$

EXCT0m $F_0 = x_m$

$\vdots$ $\vdots$ $\vdots$ $\vdots$ $\vdots$

Note that ω_n was determined in the calibration phase, where the damper was characterized.

55

5.3 Data Processing

5.3.1 Parametric Technique

As stated previously, the parametric technique proposed by Chassiakos, et al, 1998, was investigated as a potential health monitoring tool. This method is capable of handling the problem of identification of hysteretic systems, a particularly difficult class of nonlinear structural behavior. Additionally, this method provides the ability to track variations in structural parameters real-time; thus, it is suited to the time-varying application presented herein. In the specific case of a damper element, the hysteretic nature of the inelastic restoring force precludes expressing the nonlinear force in algebraic form.
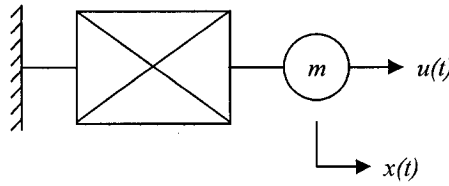
FIGURE 5.3. Typical damper

In formulating the problem, the sdof system depicted in Figure 5.3 to be identified is governed by the expression

$$m\ddot{x}(t) + r(x(t), \dot{x}(t)) = u(t) \tag{5.1}$$

where *x(t)* is defined as the system displacement, $r(x(t), \dot{x}(t))$ is the restoring force and *u(t)* is the external excitation. The mass of the system is easily estimated if unknown; in the case of the damper, the mass changes only due to loss of fluid. Both

56

the external forcing function, *u(t)*, and the system acceleration are obtained from measurements at times t_k, $k = 1,\ldots.$ The velocity and displacement, $\dot{x}(t)$ and $x(t)$, are available by direct measurement or indirectly through integration of the signal, $\ddot{x}(t)$.

For the specific case of damper elements under investigation, the restoring force, $r(x(t), \dot{x}(t))$, exhibits hysteretic characteristics. Hence, the Buoc-Wen nonlinear differential equation can be utilized to describe the restoring force as

$$r(x, \dot{x}) = z \tag{5.2}$$

$$\dot{z} = \left(\frac{1}{\eta}\right)\left[A\dot{x} - v\left(\beta|\dot{x}|\right)|z|^{n-1}z - \gamma\dot{x}|z|^{n}\right] \tag{5.3}$$

Varying the parameters, η, A, v, β, γ, and n, and the combinations therein, yields smooth hysteretic loops with differing characteristics.

The Buoc-Wen model is linearly parameterized with respect to the coefficients, *(1/η)A, (1/η) vβ, (1/η) vγ*, and nonlinearly with respect to the power, *n*. Because it is desirable to implement a linearly parameterized estimator for the on-line estimation of hysteretic systems, the model is modified as

$$\dot{z} = \left(\frac{1}{\eta}\right)\left[A\dot{x} - \sum_{n=1}^{n=N} a_n v\left(\beta|\dot{x}|\right)|z|^{n-1}z - \gamma\dot{x}|z|^{n}\right] \tag{5.4}$$

where a_n determines the contribution of *n* to the hysteresis, and *N* is chosen to be a sufficiently large integer.

57

An equivalent discrete-time model of the system was necessary, as the measurements were obtained at discrete-time intervals, Δt; for example, a 1 kHz sample rate would yield a $\Delta t = 0.001$ milliseconds. The discrete-time version of the model can be written as

$$z(k) = z(k-1) + \Delta t\left(\frac{1}{\eta}\right)A\dot{x}(k-1)$$

$$+ \Delta t\sum_{n=1}^{n=N}\left(-a_n\left(\frac{1}{\eta}\right)v\beta|\dot{x}(k-1)||z(k-1)|^{n-1}z(k-1) + a_n\left(\frac{1}{\eta}\right)v\gamma\dot{x}(k-1)|z(k-1)|^n\right)$$

(5.5)

Hence, the discrete-time linearly parameterized estimator is expressed as

$$\hat{r}(k) = z(k-1) + \theta_0(k)\dot{x}(k-1)$$

$$+ \sum_{n=1}^{n=N}\left(\theta_{2n-1}(k)|\dot{x}(k-1)||z(k-1)|^{n-1}z(k-1) + \theta_{2n}(k)\dot{x}(k-1)|z(k-1)|^n\right)$$

(5.6)

where the coefficients, $\theta_i(k)$, $i = 0,\ldots,2N$, are the estimates at time, t_k, of the corresponding coefficients from the discrete-time system equation described above; i.e., $\theta_0(k)$ is an estimate of $\Delta t(1/\eta)A$, $\theta_{2n-1}(k)$ is an estimate of $-(\Delta t)a_n(1/\eta)v\beta$ and $\theta_{2n}(k)$ is an estimate of $-(\Delta t)a_n(1/\eta)v\gamma$.

Following the established procedures of estimation theory (Ioannou, 1996), the vector of parameter estimates at time t_k is $\theta(k) = [\theta_0(k),\ \theta_1(k),\ \ldots,\ \theta_{2N}(k)]^\mathrm{T}$ and

58

$\theta^* = [\theta^*_0, \theta^*_1, \ldots, \theta^*_{2N}]^\mathrm{T}$ contains the actual values of the parameters being estimated. Next, let $\phi(k)$ be a vector containing the system measurements corresponding to each parameter in the preceding equation at each time, t_k. The estimator can then be expressed in classical form as

$$\hat{r}(k) = z(k-1) + \phi^T(k-1)\theta(k) \tag{5.7}$$

The associated estimation error is then

$$e(k) = \hat{r}(k) - r(k) = \phi^T(k-1)\theta(k) - \phi^T(k-1)\theta^* = \phi^T(k-1)\widetilde{\theta}(k) \tag{5.8}$$

where $\widetilde{\theta}(k) = \theta(k) - \theta^*$ is the $((2N+1) \times 1)$ vector of parameter errors between the actual and estimated values, θ_i.

Actual implementation of the above estimation algorithm incorporates the gradient projection adaptive law (Chassiakos, et al, 1998; Ioannou and Sun, 1996) and a least squares based adaptive law (Smythe, 1998) to obtain on-line estimates of the damper element parameters.

5.3.2 Nonparametric Techniques

5.3.2.1 Method of Masri and Caughy (1979)

In an effort to mitigate the problems associated with nonparametric identification techniques, such as greater mathematical complexity, convergence difficulties, excessive computational effort, restrictions on the dynamic systems to be evaluated and restrictions on the system excitations, a simplified method was developed by

59

Masri and Caughy (1979). This relatively straightforward approach allows the identification of a broad class of dynamic models. Through the application of regression techniques coupled with orthogonal polynomials, several advantages are realized:

1.) The technique's applicability extends to linear, nonlinear, hysteretic, nonhysteretic and self-excited systems with limit cycles.

2.) The type of probing signal utilized for system identification is virtually boundless.

3.) In the absence of *a priori* knowledge of the type and order of the nonlinearities, several of the orthogonal polynomials can be determined while the lower-order coefficients remain valid for the higher ones.

4.) The approximation error within the range of measurements can be forced to oscillate nearly equally between the limits with the application of Chebyshev polynomials.

5.) The convergence rate is vastly improved, even for nonpolynomial linearity types, reducing execution times.

Development of the procedure follows closely with that for the parametric technique; that is, starting with the sdof system illustrated in Figure 5.3, the governing equation of motion can be written as

$$m\ddot{x}(t) + r(x(t), \dot{x}(t)) = u(t) \qquad (5.9)$$

60

where $x(t)$ is defined as the system displacement, $r(x(t), \dot{x}(t))$ is the restoring force, and $u(t)$ is the external excitation. This equation can be rewritten as

$$r(x(t), \dot{x}(t)) = u(t) - m\ddot{x}(t) \tag{5.10}$$

The terms on the right-hand-side (RHS) of Equation 5.10 are known or available from measurements. Hence, the timehistory of the restoring force, $r(x(t), \dot{x}(t))$, can be computed. In general, the basis of the procedure is to estimate the real restoring force, $r(x(t), \dot{x}(t))$, by an approximate function, $\hat{r}(x(t), \dot{x}(t))$. This approximate function is expressed in terms of two-dimensional orthogonal polynomials as

$$r(x, \dot{x}) \approx \hat{r}(x, \dot{x}) = \sum_{i=0}^{m2} \sum_{j=0}^{n2} C_{ij} T_i(x') T_j(\dot{x}') \tag{5.11}$$

where the T's are defined as Chebyshev polynomials. One of the attractive attributes of Chebyshev polynomials, besides their orthogonal nature, is the fact that they yield an equi-ripple approximation within a prescribed interval of interest.

The normalized values, $x', \dot{x}'$ of x and $\dot{x}$, are defined as

$$x' = \frac{\left[x - (x_{\max} + x_{\min})/2 \right]}{\left[(x_{\max} - x_{\min})/2 \right]} \tag{5.12}$$

$$\dot{x}' = \frac{\left[\dot{x} - (\dot{x}_{\max} + \dot{x}_{\min})/2 \right]}{\left[(\dot{x}_{\max} - \dot{x}_{\min})/2 \right]} \tag{5.13}$$

The Chebyshev polynomials are defined as

$$T_n(\xi) = \cos(n \cos^{-1} \xi) \qquad -1 \le \xi \le 1 \tag{5.14}$$

which can be shown to satisfy the weighted orthogonality property

$$\int_{-1}^{1} \frac{T_n(\xi) T_m(\xi) d\xi}{\sqrt{1-\xi^2}} = \begin{cases} 0 & n \neq m \\ \pi/2 & n = m \neq 0 \\ \pi & n = m = 0 \end{cases} \qquad (5.15)$$

where $w(x) = 1/\sqrt{1-x^2}$ is the weighting function. A graphical representation of the

Chebyshev polynomials is presented in Figure 5.4.

The least-squares Chebyshev polynomial approximation, $\hat{r}(x, \dot{x})$ of $r(x, \dot{x})$, yields

coefficients, C_{ij}, as

$$C_{ij} = \begin{cases} (2/\pi)^2 \upsilon & i \text{ and } j \neq 0 \\ (2/\pi^2) \upsilon & i \text{ or } j = 0 \\ (1/\pi^2) \upsilon & i = j = 0 \end{cases} \qquad (5.16)$$

where

$$\upsilon = \int_{x=-1}^{1} \int_{y=-1}^{1} r(x,y) T_i(x) T_j(y) w(x) w(y) dx \, dy \qquad (5.17)$$

Transforming to polar coordinates yields

$$v = \int_{\theta=0}^{\pi} \int_{\phi=0}^{\pi} r(\cos^{-1} x, \cos^{-1} y) T_i(\theta) T_j(\phi) d\theta \, d\phi \qquad (5.18)$$

To facilitate numerical integration, the above is discretized as

$$v = \sum_{i=1}^{MX2} \sum_{j=1}^{NY2} r_{kl} \cos\left[i(\Delta\theta)(k-1)\right] \cos\left[j(\Delta\phi)(l-1)\right] \Delta\theta \, \Delta\phi \qquad (5.19)$$

The equally spaced increments in θ and ϕ are given by

62

$$\Delta\theta = \frac{\pi}{MX2}$$

(5.20)

$$\Delta\phi = \frac{\pi}{NY2}$$

and

$$r_{kl} = r(\cos\theta_k, \cos\phi_l)$$

$$\theta_k = (k-1)\Delta\theta \qquad 0 \le \theta \le \pi$$

(5.21)

$$\phi_l = (l-1)\Delta\phi \qquad 0 \le \phi \le \pi$$

The restoring force is computed at equally spaced intervals in θ and ϕ while the physical data are available for only a portion of the $(x, \dot{x})$ or (θ, ϕ) planes. Thus, a two-dimensional interpolation scheme is utilized to compute the restoring force.
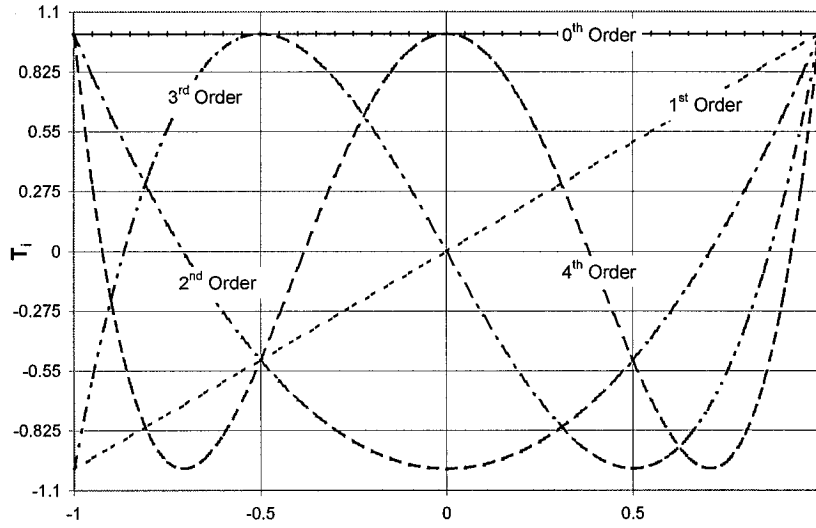
FIGURE 5.4. Chebyshev polynomials

63

The Chebyshev coefficients are directly related to the surface, $r(x,\dot{x})$, over the range $-1 \leq x' \leq 1, -1 \leq \dot{x}' \leq 1$. For the case of the linear sdof system, the restoring force is

$$r(x,\dot{x}) = m(2\zeta\omega\dot{x} + \omega^2 x) \tag{5.22}$$

where ω is the natural frequency, and ζ is the ratio of critical damping. Given the boundary constraints,

$$r(x,0) \equiv g(x) = m\omega^2 x$$

$$\tag{5.23}$$

$$r(0,\dot{x}) \equiv h(\dot{x}) = 2\zeta\omega m\dot{x}$$

it follows that

$$r(x,\dot{x}) = g(x) + h(\dot{x}) \tag{5.24}$$

Obviously, the above expression for the restoring force is simply the sum of a function of the system displacement and a function of the system velocity only.

Generalizing the above to the nonlinear case, the restoring force approximation is written as

$$r(x,\dot{x}) \approx \sum_{i=0}^{ml} a_i\, T_i(x') + \sum_{j=0}^{nl} b_j\, T_j(\dot{x}') \tag{5.25}$$

The above approximation of the restoring force is valid for locations in the $(x,\dot{x})$ - plane far removed from the measured response pairs, $(x,\dot{x})$. The coefficients a and b are Chebyshev polynomial coefficients for one-dimensional least squares experimental data fitting. The a's correspond to experimental data where $|\dot{x}| \approx 0$; the b's for $|x| \approx 0$. Hence, the coefficients are given as

64

$$r(x,0) \approx \hat{g}(x) = \sum_{i=0}^{m1} a_i T_i(x')$$

(5.26)

$$r(0,\dot{x}) \approx \hat{h}(\dot{x}) = \sum_{j=0}^{n1} b_j T_j(\dot{x}')$$

where the coefficients can be written as

$$a_0 = \frac{1}{MX1} \sum_{j=0}^{MX1-1} r(\xi_j, 0), \qquad a_k = \frac{2}{MX1} \sum_{j=0}^{MX1-1} r(\xi_j, 0) T_k(\xi_j)$$

(5.27)

$$b_0 = \frac{1}{NY1} \sum_{j=0}^{NY1-1} r(0, \xi_j), \qquad b_k = \frac{2}{NY1} \sum_{j=0}^{NY1-1} r(0, \xi_j) T_k(\xi_j)$$

Note that the abscissa variables x' and $\dot{x}'$ have been transformed by equations 5.12 and 5.13 to satisfy the range constraint on θ in the Chebyshev polynomial. The constraint that the interpolation scheme must generate equally spaced data is predicated on the following definition:

$$\xi_i = \cos\left[(2i+1)\frac{\pi}{2n}\right] \qquad i = 0,1,...,n-1$$

(5.28)

For equidistant data points, $(x,\dot{x})$, sufficiently close to measured data points, two-dimensional interpolation is adequate to estimate the value of $r(x,\dot{x})$. In general, Equation 5.25 will yield an estimate of the unknown surface at the prescribed locations.

65

5.3.2.2 Artificial Neural Network

Another nonparametric procedure employed in this study is based on the use of artificial neural networks for the identification of nonlinear systems. The advantages of neural network techniques lie in their very construction; neural networks do not perform sequential computations, as does a Von Neuman machine, being comprised of parallel nets of simpler computational components. This fact implies that neural networks contain more processing elements than a sequential machine such as the Von Neuman computer and, thus, yield a higher degree of robustness. Artificial neural networks were developed in the early 1940's to emulate the neuron in biological studies, with much of the pioneering attributed to McCulloch and Pitts (1943). Since they were developed to simulate biological cells' ability to adapt, neural networks provide an intrinsic ability to adapt to their environment. Hence, neural networks can be applied to systems where they are given a set of "training" parameters, a prescribed set of rules or inputs and outputs, and then can "learn" about the system by continuously adapting their internal parameters to simulate the training examples.

The unique simplicity of the neural network, coupled with it's inane ability to adapt to a prescribed system, has made it a preferred algorithm for numerous applications where real-time adaptation and fast processing of large data sets are required. Applications include image and speech recognition, robotics control and, more recently, system identification.

66

Neural networks are basically comprised of a replicator, which, as its name implies, simply tries to emulate the input/output characteristics of a given unknown dynamic system. The error between the net output and the unknown system response is computed, and fed back through the network, resulting in adjustments to the replicator's synaptic weights to gradually reduce the error such that it converges to an acceptable predefined threshold. Hence, the replicator becomes an artificial copy of the unknown dynamic system, yielding a model of the system for future analysis.
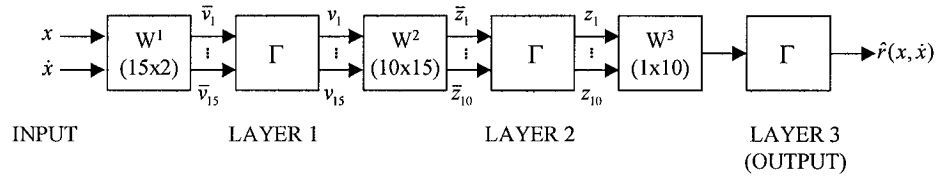
FIGURE 5.5. Multilayer feedforward neural network

As in the previous discussions, a nonlinear sdof system is illustrated in Figure 5.3. The unknown restoring force equation follows from the discussion of Equation 5.10 in the preceding sections. Again, it is assumed that the acceleration, $\ddot{x}(t)$, and input excitation, $u(t)$, are available from measurements and that the mass, m, is known or easily estimated, so that the restoring force, $r(x(t), \dot{x}(t))$, is the only unknown to be solved for in Equation 5.10.

For the case described above in Figure 5.5, the system inputs would be the measured displacement, $x(t)$, and velocity, $\dot{x}(t)$. The network output, $\hat{r}(x(t), \dot{x}(t))$, is then an

67

approximation of the restoring force, $r(x(t), \dot{x}(t))$. An example three-layer

feedforward network (Narendra and Parthasarathy, 1990) is depicted in Figure 5.5.

This net incorporates fifteen nodes in the first hidden layer, ten nodes in the second

hidden layer, requiring two inputs and yields one output. For the given problem at

hand, this network might well provide a reasonable estimation of the unknown

restoring force, given the system inputs of displacement and velocity. The network

topology is represented by various matrices designated by W^i and bias terms, b^i. For

a two-dimensional input vector , $X = [x, \dot{x}]^T$, the output of the network, $\hat{r}(x(t), \dot{x}(t))$,

is computed as

$$
\left\{
\begin{array}{ll}
\bar{v} = W^1 X + b^1; & v_i = \gamma(\bar{v}_i), \quad i = 1,\dots 15 \\[2ex]
\bar{z} = W^2 v + b^2; & z_i = \gamma(\bar{z}_i), \quad i = 1,\dots 10 \\[2ex]
\hat{r} = \gamma(W^3 z + b^3)
\end{array}
\right\}
\tag{5.29}
$$

The function, $\gamma(x)$, is typically defined as a sigmoid function as expressed in

Equation 5.30, and plotted in Figure 5.6.

$$
\gamma(x) = \frac{1}{1 + e^{-cx+d}}
\tag{5.30}
$$

The network is "trained" by presenting it with a series of discrete input vectors,

$\{[x_k, \dot{x}_k]^T\}$, and a sequence of discrete desired output vectors, $\{r_k\}$. Then, with an

initially prescribed set of weights, W^i, and biases, b^i, the input vector is propagated

forward through the network at time, t_k. The network output, $\hat{r}_k$, is computed

according to the algorithms set forth in Equation 5.29. Next, the error between the

68

network output, $\hat{r}_k$, and the desired output, r_k, is computed. Based on a prescribed error performance criterion, such as a least squares algorithm or other cost function minimization procedures, the weights and biases are adjusted to reduce the error and the process repeated until an acceptable error threshold is reached.

Evaluation of the success of the network training process is accomplished by inputting vector sequences, $\left\{ [x_\alpha, \dot{x}_\alpha]^T \right\}$, not included in those used for training. A well "trained" network should yield an output sequence, $\{\hat{r}_\alpha\}$, within acceptable tolerance as compared to the actual system output, $\{r_\alpha\} = \{r(x_\alpha, \dot{x}_\alpha)\}$.
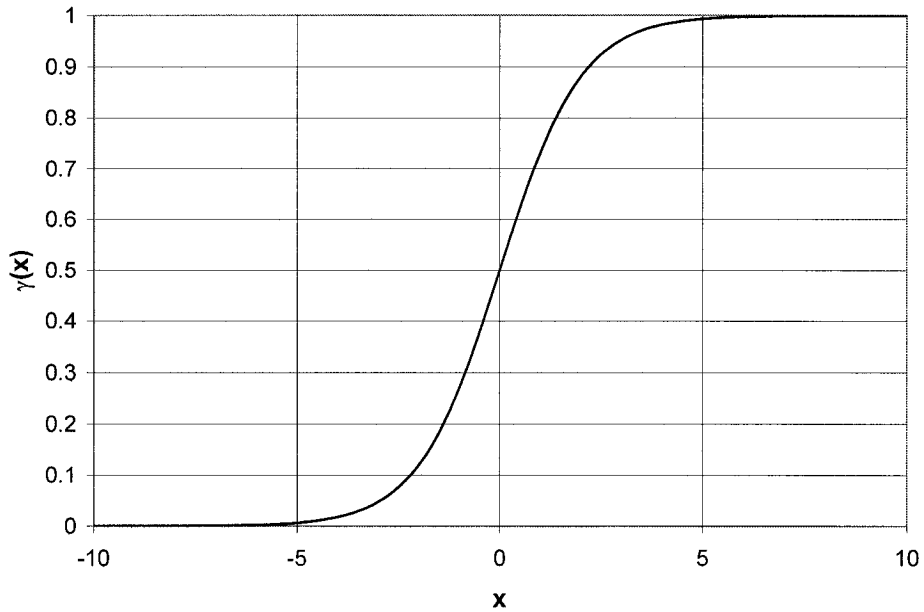
FIGURE 5.6. Sigmoid function

A detailed partial depiction of the network is given in Figure 5.7. It is important to note that the network topology, the number of layers and the number of nodes, are

69

not stipulated by any design guidelines; rather, said selection is based on experience and testing. For the given network, with fifteen hidden nodes in the first layer, ten hidden nodes in the second layer, two inputs and one output, the total number of network parameters requiring adjustment is 216. In general, the total number of parameters for adjustment in any given network can be computed as

$$n_{tot} = n_{input} \times n_{W,nodes,layer1} + n_{W,nodes,layer1} \times n_{W,nodes,layer2} +$$

$$n_{W,nodes,layer2} + \ldots + n_{bias,layer1} + n_{bias,layer2} + \ldots + n_{bias,layer n}$$

(5.31)
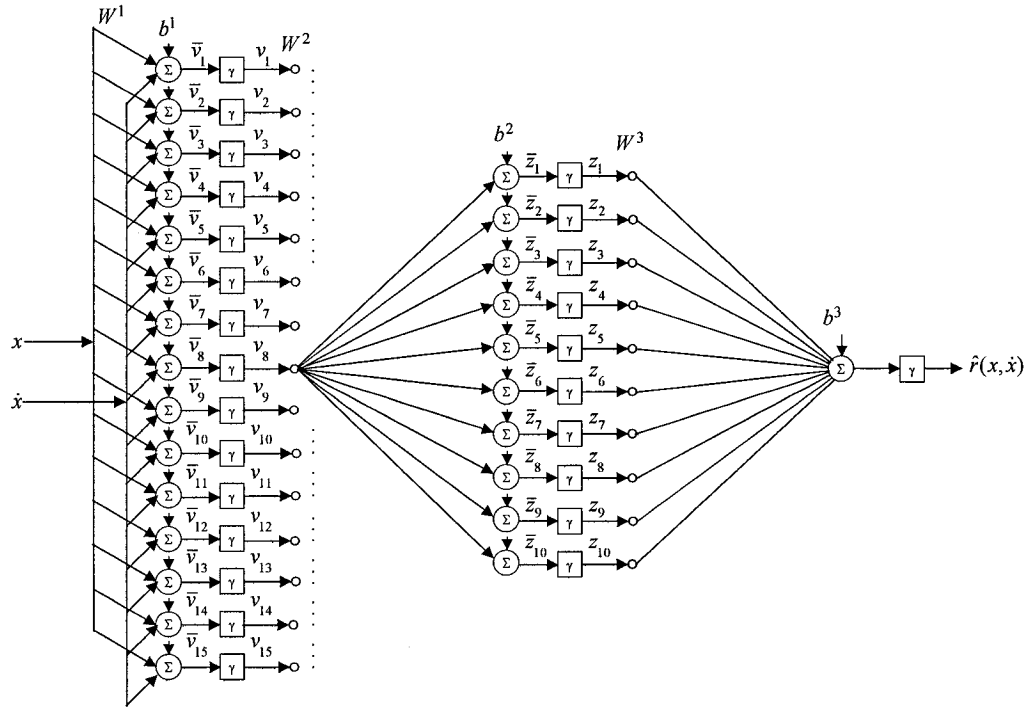
FIGURE 5.7. Detailed partial network topology

6.0 Simulation Studies

6.1 Simulation

As discussed previously, computer simulations of damper elements are crucial for the initial selection and optimization of the analytical tools necessary for real-time data processing. Simulations were carried out utilizing the nonlinear three-dimensional frame program *204.exe*, which was developed by Dr. Masri and students (Wolfe, 2000). Comparison simulations were developed using the 4th-order Runge-Kutta method in conjunction with the analytical tools described herein.

6.2 Simulations using 204.in

The *204.exe* program is a powerful three-dimensional, nonlinear finite element code, which allows the user the flexibility to add elements in a three-dimensional frame environment with nonlinear elements incorporated. An additional feature allows multiple support excitations specified. The input file, *204.in*, is designed to follow the format depicted in Figure 6.1 below.

The *204.exe* program allows user-defined integration step-size, *DT*, maximum solution time, *TMAX*, and plot time increments, *DTPLOT* (reference Figure 6.2). Hence the user has the ability to determine the resolution of the stored data for plotting purposes.

71
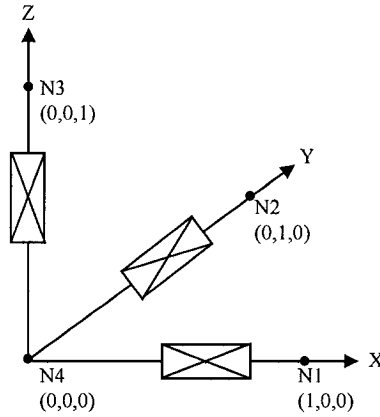
FIGURE 6.1. *204.in* model format
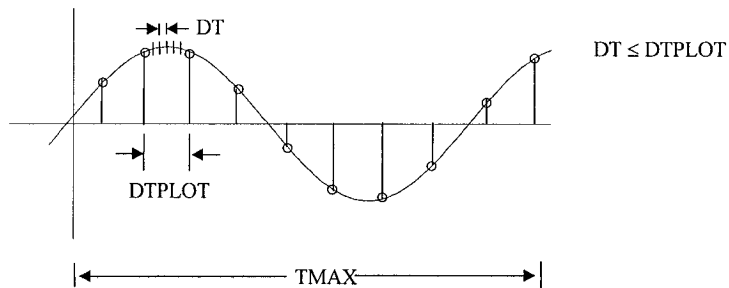
FIGURE 6.2. Data sampling

Each element prescribed in the model must be defined. The *204.exe* program allows

nine type specifications, each type delineating the number of multipliers in the

restoring force equation. For the damper problem being discussed herein, consider a

72

linear sdof system with a given mass and natural period $T = 2\pi/\omega$. The restoring

force equation is given as

$$f(x,\dot{x}) = m(2\xi\omega\dot{x} + \omega^2 x) \qquad (6.1)$$

which is easily verified from mechanics. Nonlinear damper representations such as

the Duffing and Van der Pol oscillators are discussed later.

The *204.in* input file represents the equation as

$$f(x,\dot{x}) = GP(M,1)x + GP(M,2)\dot{x} + GP(M,3)x^3 + ... \qquad (6.2)$$

where M is the element number and $GP(\,)$ is the element multiplier. Hence, a matrix

of multipliers is created based on the number of elements specified. Linear system

representations are modeled by specifying the first two elements. Nonlinear systems

require specification of additional element multipliers.

Naturally occurring measurement errors due to uncertainties and noise thresholds can

also be simulated. Data postprocessing and storage routines are identical to those

anticipated for use with the actual measured data from laboratory testing. Thus, the

simulation studies not only enable the selection and preliminary optimization of the

analytical tools for the research, but also hone the process of data manipulation.

6.2.1 Simulated Data

A free-body diagram (FBD) of the damper element reveals that there are only five

degrees of freedom (DOF) at each end. Note that a torsional moment at ends i and j

73

relies on the damper configuration, but, as a minimum, will result from the shear

stress or viscosity of the fluid.
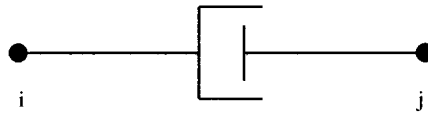
FIGURE 6.3. FBD damper model

Figure 6.4 below depicts the sdof damper as modeled in the *204.in* file.
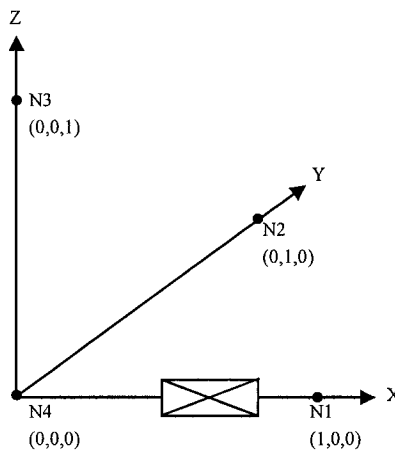
FIGURE 6.4. Single element sdof damper model

For the damper case, there are two nodes and one element, with a total of five DOF.

DT was set equal to 0.0025 seconds, *TMAX* to 50.0 seconds, and *DTPLOT* to 0.010

seconds. Element connectivity was left as given in the existing file, with the

exception that only the element between nodes 4 and 1 (N1,N4) was turned on

(reference Figure 6.4). Recall from the damper model depicted above that three

DOF exist at node 1, and two at node 4. Note that DOF's are counted similar to

local coordinates, with DOF's 1, 2, and 3 located at node 1, and DOF's 4 and 5 at

74

node 4. Springs with stiffness k = 10,000 are placed at all other DOF specified to preclude numerical instability problems in the solution.

6.2.1.1 Linear systems

For a linear sdof system with unit mass, the natural period and natural frequency are

$$T = \frac{2\pi}{\omega} = 1 \tag{6.3}$$

$$f = \frac{1}{T} = 1 \tag{6.4}$$

Thus, the natural circular frequency is $\omega = 2\pi = 6.28318$. The stiffness is then computed as $k = m\omega^2 = (6.28318)^2 = 39.478$. The coefficient of damping is

$$\zeta = \frac{c}{2\sqrt{km}} \tag{6.5}$$

which implies that $c = 2\sqrt{km}\zeta = 2\sqrt{(2\pi)^2}\zeta = 4\pi\zeta$. Thus,

$c = 12.566\zeta \mid_{\zeta=0.05} = 0.62832$. This result yields a system gain of 10, as depicted in the plots in Figure 6.5. This figure contains six plots; the excitation, acceleration, and velocity timehistories are contained in the first row from left to right. The system displacement timehistory is the first plot on the second row, with the remaining plots depicting the phase-plane relationship between the displacement and velocity, and the displacement to restoring force.

Given the above, for the single element model specified in the damper example,

75

$GP(1,1) = k = 39.478$, and $GP(1,2) = c = 0.62832$ (assuming $\zeta = 0.05$). All other

multipliers for this element are set to zero since the model is to be linear.

6.2.1.1.1 Sinusoidal excitation

A test simulation was performed using a sinusoidal input with an amplitude,

$F_0 = 39.478$, and $\omega = 2\pi$.
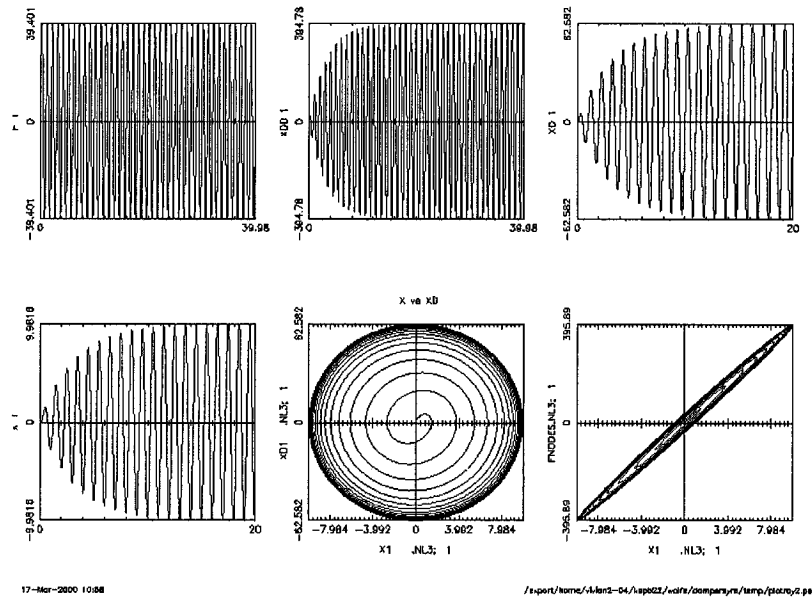
FIGURE 6.5. Noise-free sinusoidal damper data

Next, the data was corrupted with stationary, zero-mean noise having a standard

deviation of 0.05. The application of noise to the data was to simulate the noise

realized in typical data acquisition processes. Such noise is attributable to

instrumentation susceptibility, cabling interference and acquisition hardware.

76
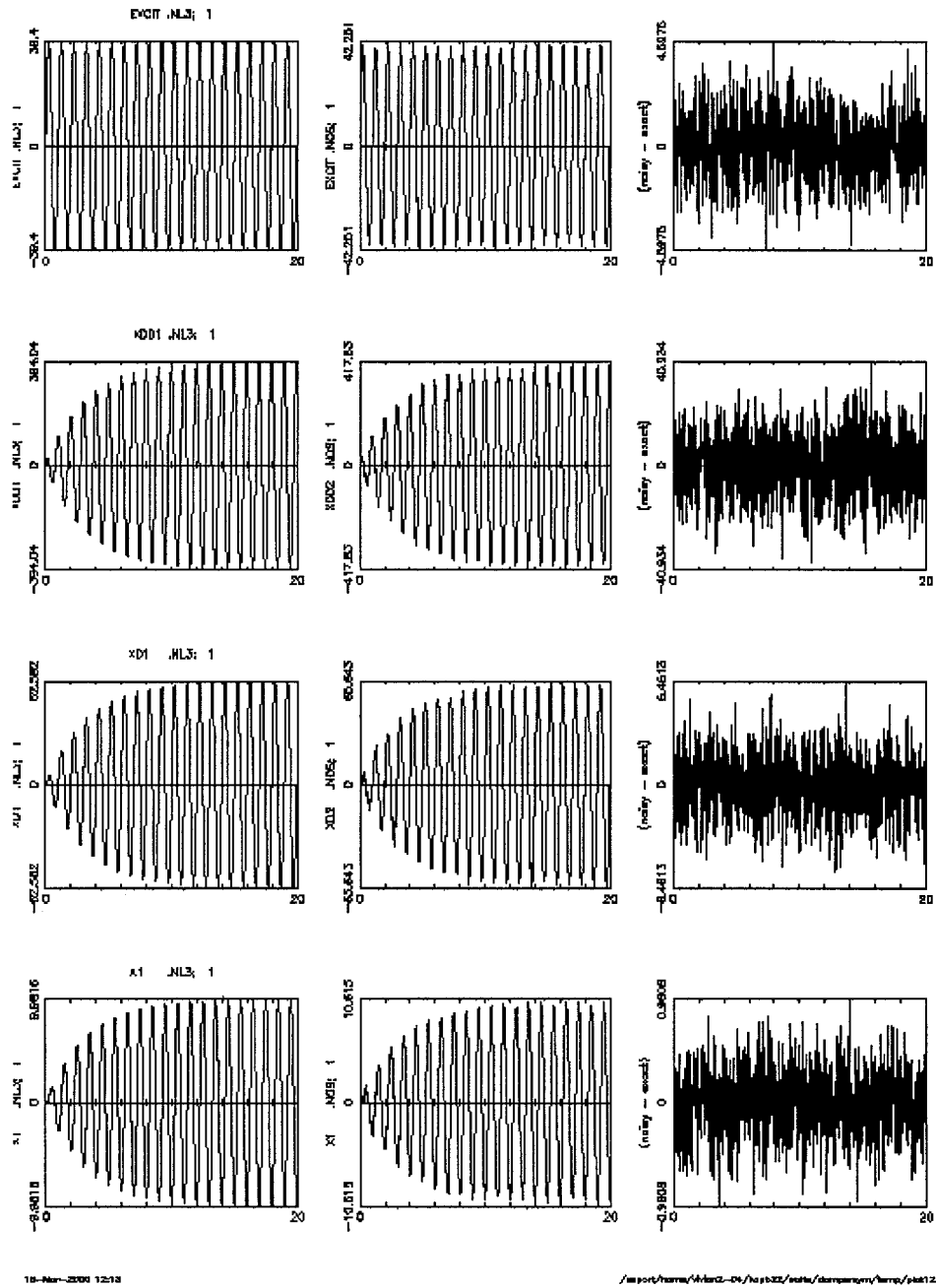
FIGURE 6.6. Noise-polluted sinusoidal damper data

77

Figure 6.6 displays three columns of plots, with the four rows depicting the excitation, acceleration, velocity, and displacement records, respectively. The first column plots the above without noise added, and hence replicates that depicted in Figure 6.5. The second column incorporates noise to the signals. The third column depicts a measure of the added noise. Figure 6.7 displays the internal element forces, following the format in Figure 6.6 as described above. Note that as there is only one element, a damper, only one row of data is plotted in Figure 6.7.
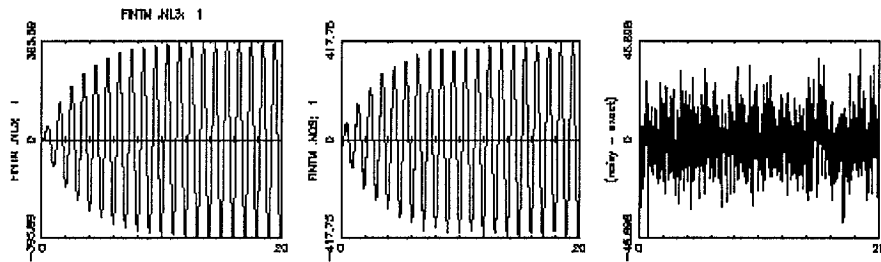
FIGURE 6.7. Noise-polluted internal element forces w/ sinusoidal excitation

In the following subsections, simulated damper input and output is presented following the format described above for Figures 6.5 through 6.7. This allows for continuity and clarity in presentation and discussion.

6.2.1.1.2 Swept-sine excitation

The simulated data developed in Section 6.2.1.1.1 incorporates a sinusoidal input. For the purposes of scientific evaluation of the parametric and nonparametric tools,

78

additional system excitation is necessary. Using the sdof model developed in the

previous section, the simulated damper is subjected to a swept-sine excitation

$$F(t) = F_0 \sin[\Omega(t)]t \tag{6.6}$$

where the variable frequency $\Omega(t)$ varies linearly between $t = 0$ and $t = T_s$ according

to the relationship

$$\Omega(t) = at + b \tag{6.7}$$

The coefficients of this equation are defined as

$$a = \frac{(\omega_2 - \omega_1)}{2T_s} \qquad b = \omega_1$$

$$\tag{6.8}$$

$$\omega_1 = \Omega_0 \qquad \omega_2 = 2\Omega(T_s) - \Omega(0)$$

where $\omega = 1$ and $T = 2\pi/\omega$. The frequency limits are chosen as $\Omega(0)/\omega = 0.5$ and

$\Omega(T_s)/\omega = 1.5$, in sweep time $T_s/T = 5$. This prescribed excitation yields the large-

amplitude motion time-history record depicted in Figure 6.8 below.
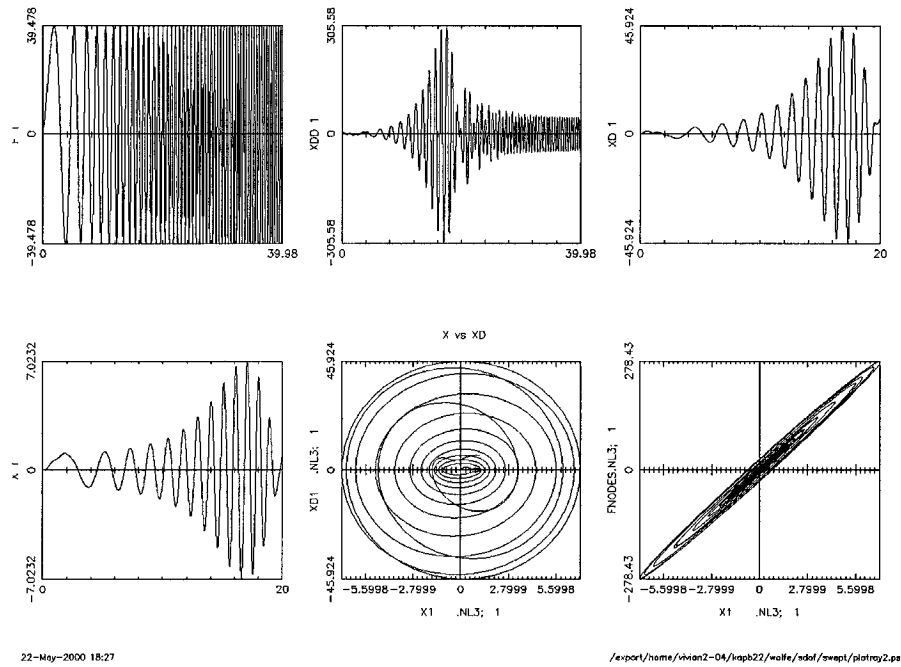
FIGURE 6.8. Noise-free swept-sine damper data

Data corruption as outlined in Section 6.2.1.1.1 above yields the following data

representation in Figures 6.9 and 6.10.
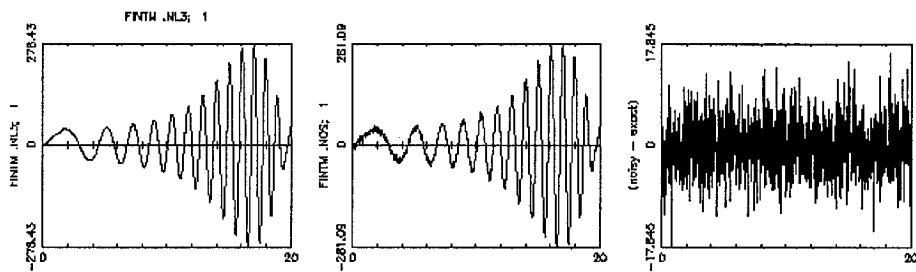
FIGURE 6.9. Noise-polluted internal element forces w/swept-sine excitation

80
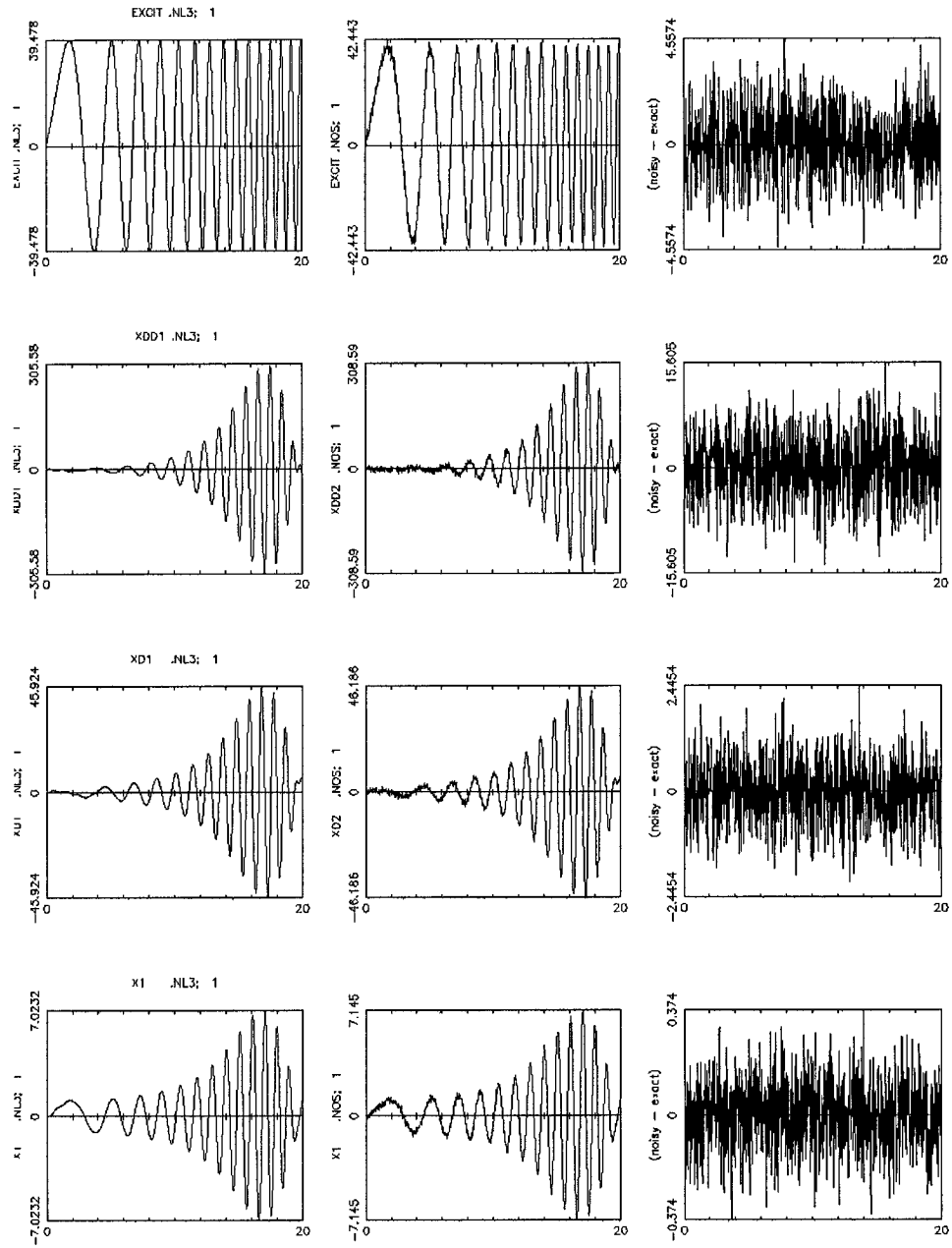
FIGURE 6.10. Noise-polluted swept-sine damper data

81

6.2.1.1.3 Stationary random excitation

The stationary random excitation function envelope was characterized by the following equation:

$$y(t) = A_1 e^{A_2 t} \tag{6.9}$$

where $A_1 = 1.0$, $A_2 = -0.05$, and the mean of the random process, $\mu = 0$, and the standard deviation was as prescribed below.

6.2.1.1.3.1 Stationary random excitation with $\sigma = 1$

Again, utilizing the model developed in Section 6.2.1.1.1, simulation data was developed with a stationary random excitation. The standard deviation was set at $\sigma = 1$ to yield a slight nonlinear system behavior. The simulated data is depicted in Figures 6.11 - 6.13.

6.2.1.1.3.2 Stationary random excitation with $\sigma = 5$

Additional stationary random excitation data was simulated with a standard deviation, of $\sigma = 5$ to yield a higher degree of system nonlinearities. This data is depicted in Figures 6.14 - 6.16 below.
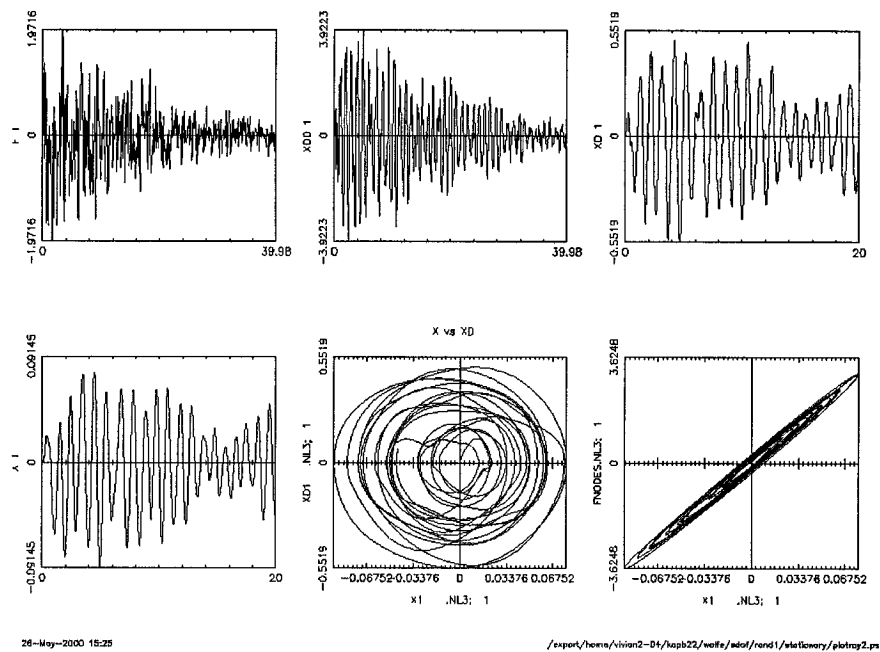
FIGURE 6.11. Noise-free stationary random ($\sigma = 1$) damper data
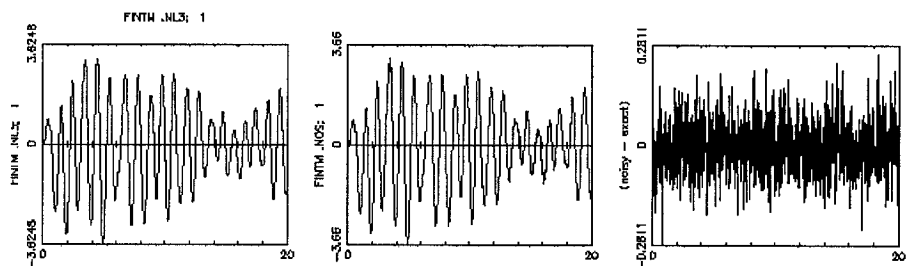
FIGURE 6.12. Noise-polluted internal element forces w/ stationary random

($\sigma = 1$) excitation

83
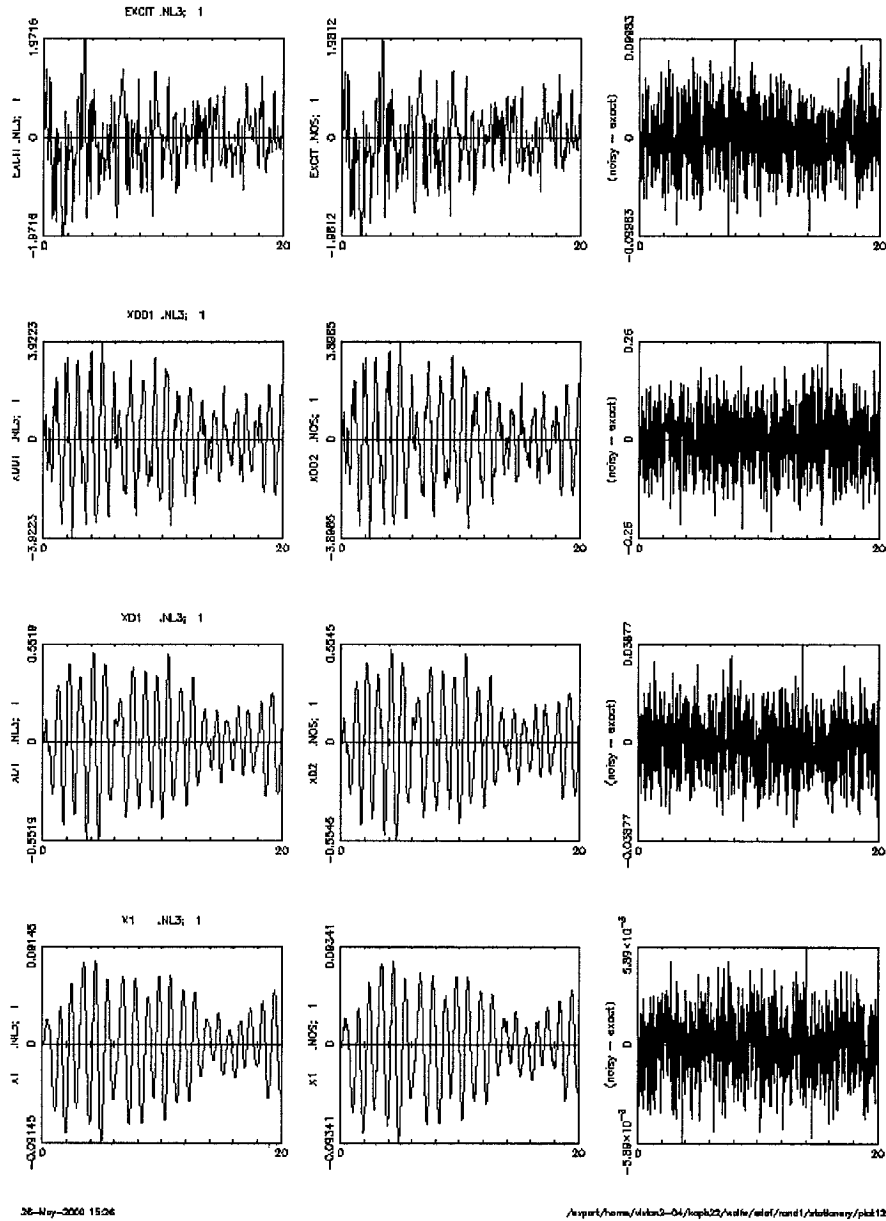
FIGURE 6.13. Noise-polluted stationary random ($\sigma = 1$) damper data
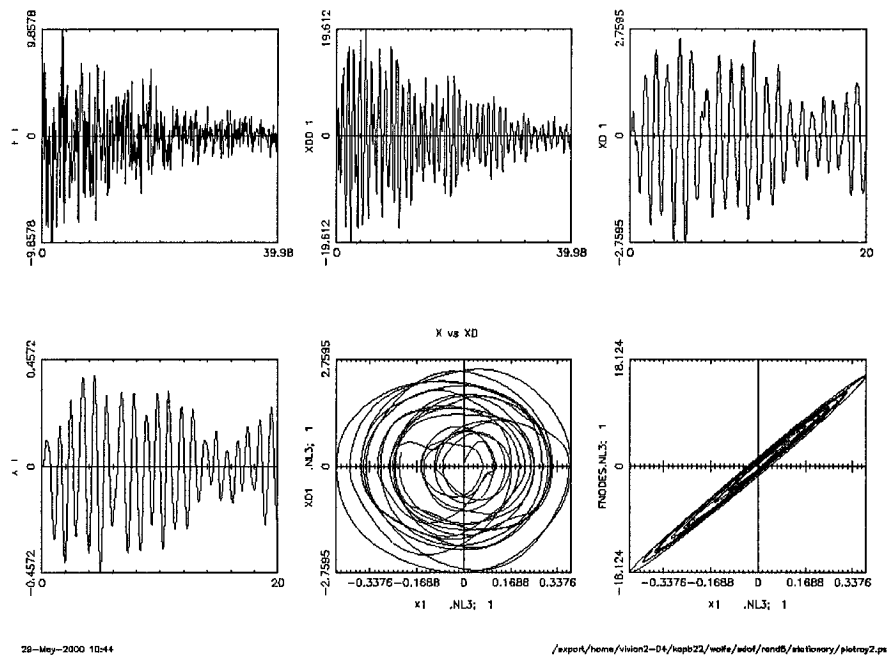
FIGURE 6.14. Noise-free stationary random ($\sigma = 5$) damper data
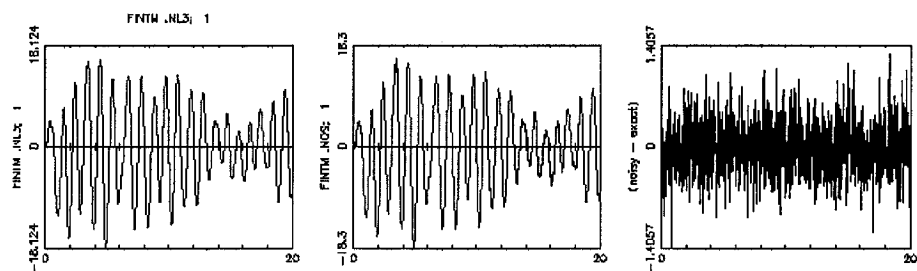
FIGURE 6.15. Noise-polluted internal element forces w/ stationary random

($\sigma = 5$) excitation

85
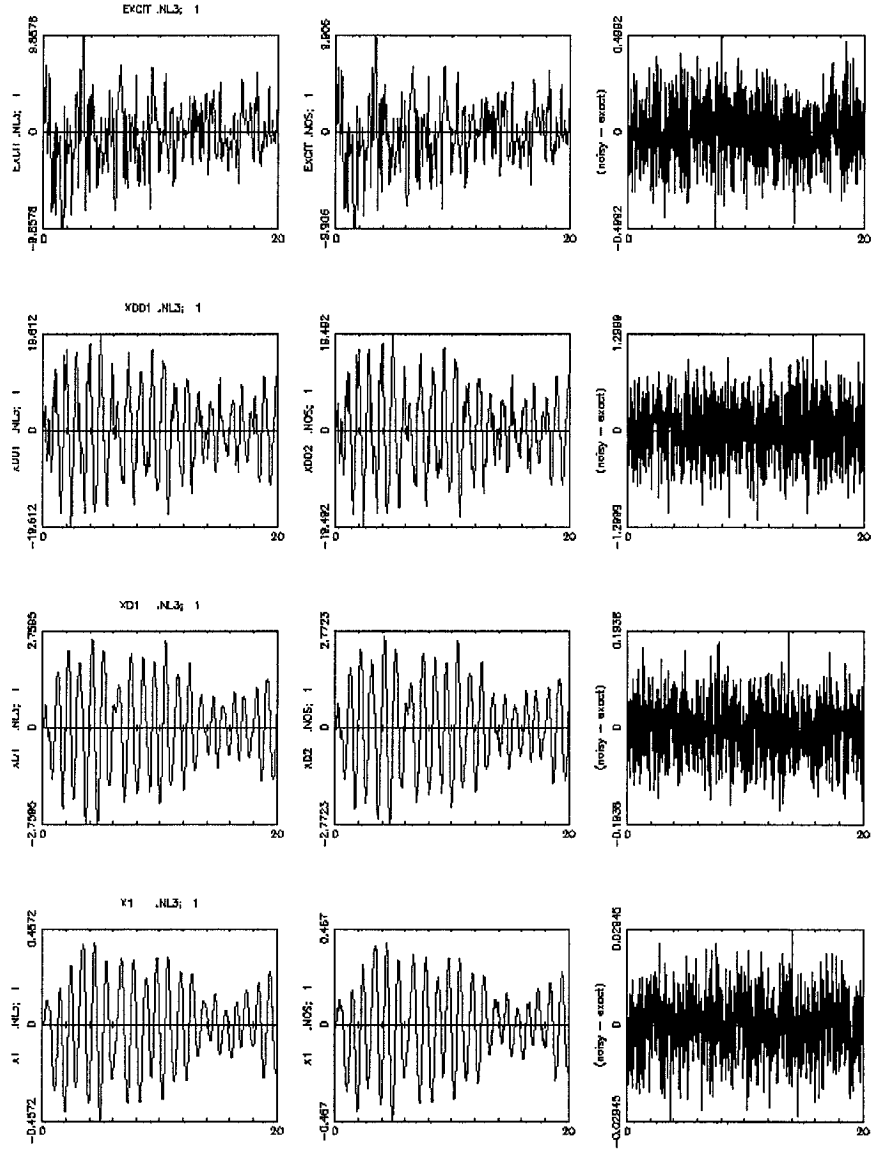
FIGURE 6.16. Noise-polluted stationary random ($\sigma = 5$) damper data

6.2.1.1.4 Nonstationary random excitation

The nonstationary random excitation function envelope was characterized by the following equation:

$$y(t) = A_1 e^{A_2 t} + A_3 e^{A_4 t} \tag{6.10}$$

where A_1 and A_2 and μ were as defined in 6.2.1.1.3, and $A_3 = -1.0$, $A_4 = -1.5$. Again, the standard deviation was as prescribed below.

6.2.1.1.4.1 Nonstationary random excitation with $\sigma = 1$

Returning to the model developed in Section 6.2.1.1.1, simulation data was developed with a nonstationary random excitation. The standard deviation was set at $\sigma = 1$ to yield a slight nonlinear system behavior. The simulated data is depicted in Figures 6.17 - 6.19.

6.2.1.1.4.2 Nonstationary random excitation with $\sigma = 5$

Additional nonstationary random excitation data was simulated with a standard deviation, of $\sigma = 5$ to yield a higher degree of system nonlinearities. This data is depicted in Figures 6.20 - 6.22 below.

87
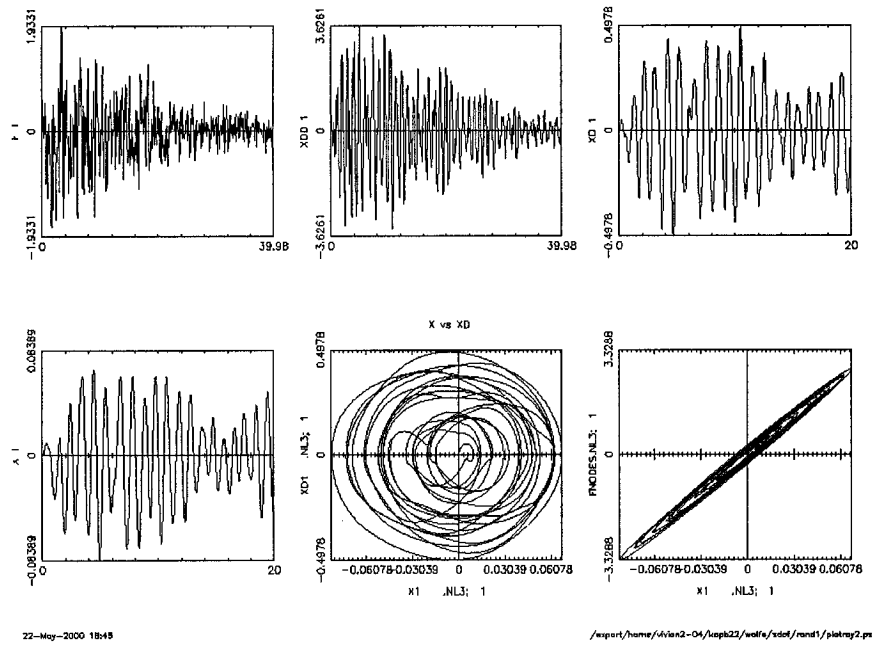
FIGURE 6.17. Noise-free nonstationary random ($\sigma = 1$) damper data
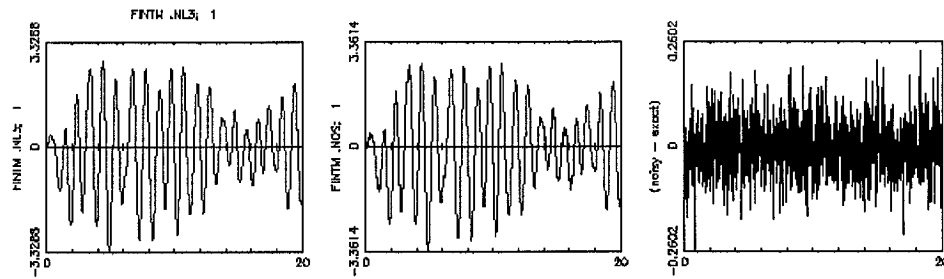
FIGURE 6.18. Noise-polluted internal element forces w/ nonstationary random

($\sigma = 1$) excitation

88
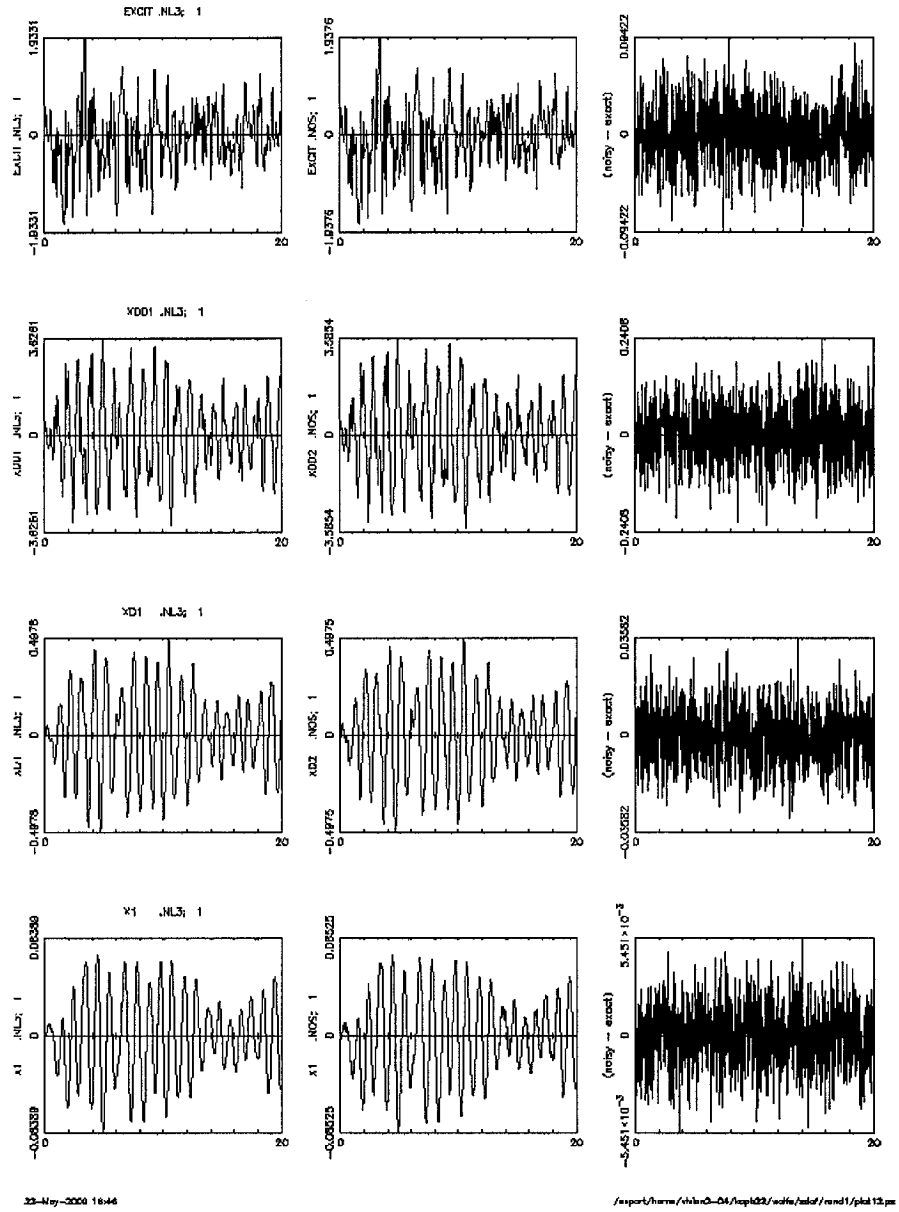
FIGURE 6.19. Noise-polluted nonstationary random ($\sigma = 1$) damper data
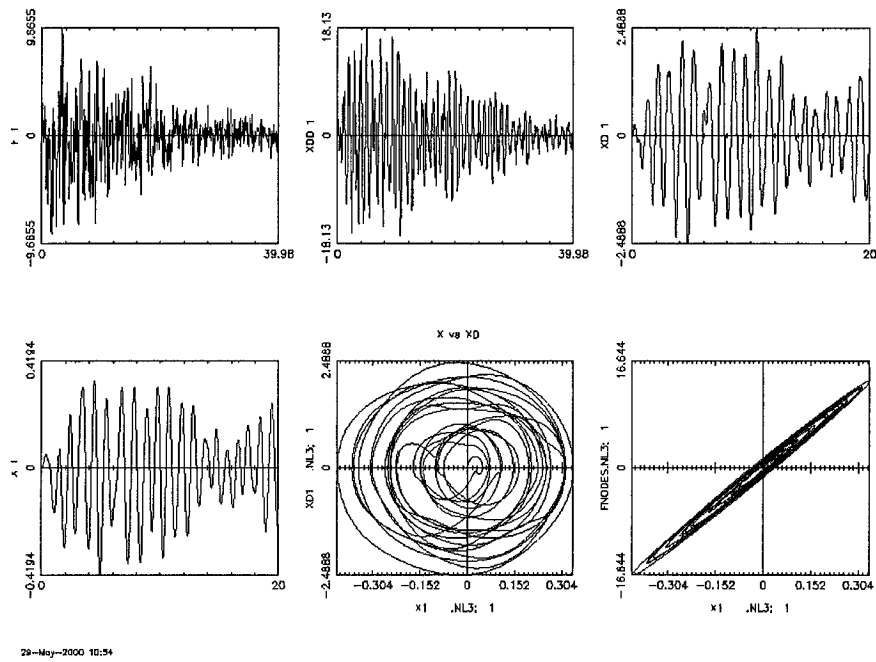
FIGURE 6.20. Noise-free nonstationary random (σ = 5) damper data
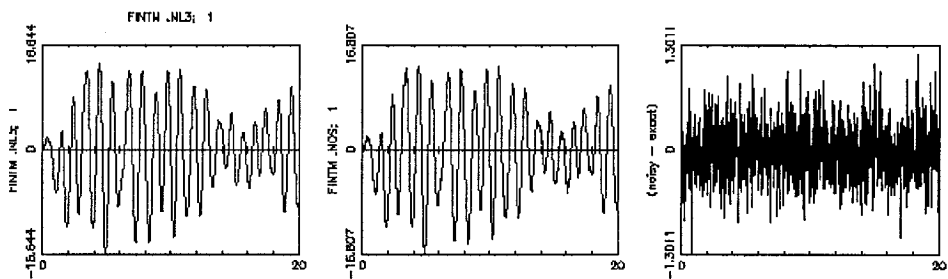
FIGURE 6.21. Noise-polluted internal element forces w/ nonstationary random

(σ = 5) excitation

FIGURE 6.22. Noise-polluted random ($\sigma = 5$) damper data

6.2.1.2 Nonlinear Systems

6.2.1.2.1 Duffing oscillator

The first nonlinear damper type considered is a Duffing oscillator. The restoring force for a Duffing oscillator can be written as

$$f(x, \dot{x}) = m[2\zeta \omega \dot{x} + \omega^2 (x + \varepsilon x^3)] \tag{6.11}$$

where the mass, system frequency, damping coefficient and epsilon are defined as m = 1, ω = 1, ζ = 0.02, ε = 0.003, respectively.

6.2.1.2.1.1 Nonstationary random excitation

Simulation data for the Duffing oscillator excited by nonstationary random excitations with σ = 1 are given below in Figures 6.23 – 6.25, as prescribed in Section 6.2.1.1.4.
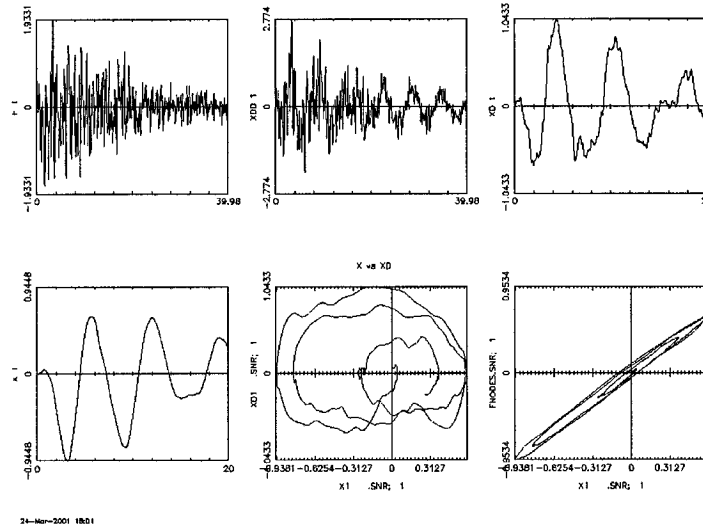
FIGURE 6.23. Noise-free nonstationary random (σ=1) damper data

92
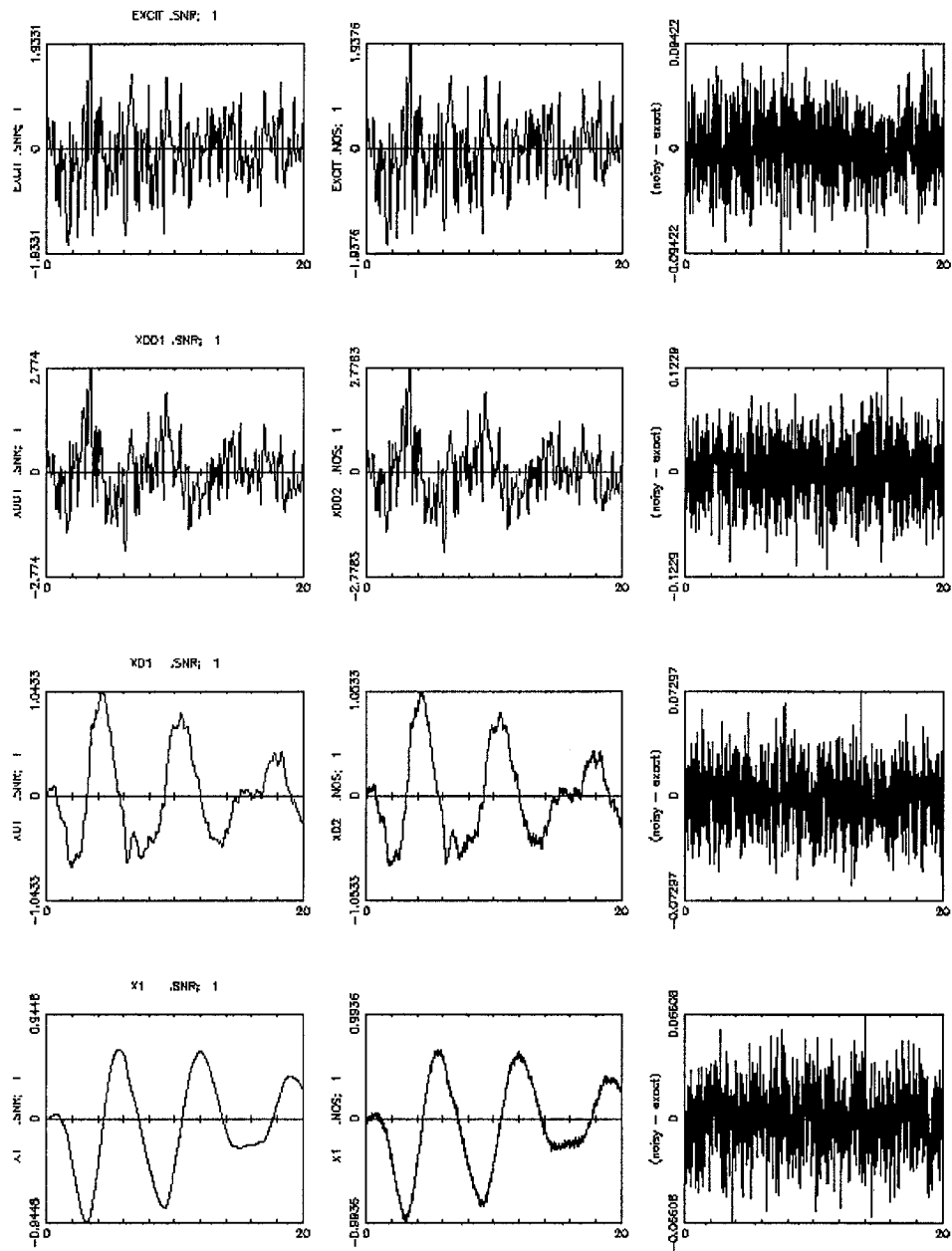
FIGURE 6.24. Noise-polluted nonstationary random (σ=1) damper data

93
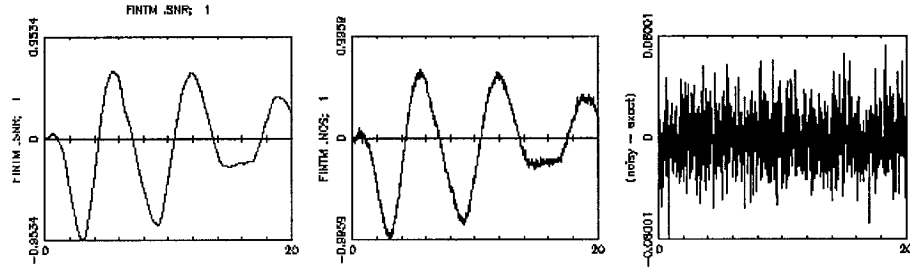
FIGURE 6.25. Noise-polluted internal element forces w/ nonstationary random

(σ=1) excitation

6.2.1.2.2 Van der Pol oscillator

A second nonlinear damper type considered is the Van der Pol oscillator. The restoring force for this oscillator can be written as

$$f(x, \dot{x}) = -\varepsilon(1 - x^2)\dot{x} + x \tag{6.12}$$

where the system mass, frequency and epsilon are defined as $m = 1$, $\omega = 1$,

$\varepsilon = 0.2$, respectively.

The Van der Pol oscillator will be discussed later.

6.3 Runge-Kutta Modeling

The Runge-Kutta computation procedure was chosen for this application largely due to the fact that it is a self-starting method with a high degree of accuracy. The

94

accuracy of the Runge-Kutta algorithm is comparable to that of a Taylor series

solution incorporating terms through h^4.

Application of the Runge-Kutta method to the damper problem can be illustrated

with a simple second order differential equation. First, the second-order differential

equation is reduced to two first-order equations. Recall that the damper problem can

be expressed in differential form as

$$m\ddot{x} + g(x,\dot{x}) = F(t) \tag{6.13}$$

Performing a change of variables such that $x_1 = x$, then setting $x_2 = \dot{x}_1$, Equation

6.14 is reduced to the following two first-order equations:

$$\dot{x}_1 = x_2$$

$$\dot{x}_2 = F(x_1, x_2, t) = \frac{1}{m}[F(t) - g(x_1, x_2)] \tag{6.14}$$

A Taylor series expansion of x_1 and x_2 in the neighborhood of x_{1i} and x_{2i},

respectively, yields the following two expressions:

$$x_1 = x_{1i} + \left(\frac{dx_1}{dt}\right)_i h + \left(\frac{d^2 x_1}{dt}\right)_i \frac{h^2}{2} + \cdots$$

$$x_2 = x_{2i} + \left(\frac{dx_2}{dt}\right)_i h + \left(\frac{d^2 x_2}{dt}\right)_i \frac{h^2}{2} + \cdots \tag{6.15}$$

Note that the time increment, Δt, was replaced by variable h for clarity of

presentation. A simpler set of equations is derived by replacing the first derivative in

the Taylor series expression depicted above with an average slope. The average

95

slope for the two state variables for the system under consideration can be expressed as

$$x_1 = x_{1i} + \left(\frac{dx_1}{dt}\right)_{i_{ave}} h$$

$$x_2 = x_{2i} + \left(\frac{dx_2}{dt}\right)_{i_{ave}} h$$

(6.16)

Applying Simpson's rule, the expanded form of the average slope in the time interval h becomes

$$\left(\frac{dx_2}{dt}\right)_{i_{ave}} = \frac{1}{6}\left[\left(\frac{dx_2}{dt}\right)_{t_i} + 4\left(\frac{dx_2}{dt}\right)_{t_i+\frac{h}{2}} + \left(\frac{dx_2}{dt}\right)_{t_i+h}\right]$$

(6.17)

The 4th-order Runge-Kutta method follows suit with the above, except that the second term is divided into two terms. Then, the four values of t, x_1, x_2, and f are computed at each point i as follows:

t	x_1	$x_2 = \dot{x}_1$	$f = \dot{x}_2 = \ddot{x}$
$T_1 = t_i$	$X_{1_1} = x_{1_i}$	$X_{2_1} = x_{2_i}$	$F_1 = f(T_1, X_{1_1}, X_{2_1})$
$T_2 = t_i + \dfrac{h}{2}$	$X_{1_2} = x_{1_i} + X_{2_1}\dfrac{h}{2}$	$X_{2_2} = x_{2_i} + F_1\dfrac{h}{2}$	$F_2 = f(T_2, X_{1_2}, X_{2_2})$
$T_3 = t_i + \dfrac{h}{2}$	$X_{1_3} = x_{1_i} + X_{2_2}\dfrac{h}{2}$	$X_{2_3} = x_{2_i} + F_2\dfrac{h}{2}$	$F_3 = f(T_3, X_{1_3}, X_{2_3})$
$T_4 = t_i + h$	$X_{1_4} = x_{1_i} + X_{2_3}h$	$X_{2_4} = x_{2_i} + F_3 h$	$F_4 = f(T_4, X_{1_4}, X_{2_4})$

Substituting the computed values into the following recurrence formulas allows the point-wise solution of x and $\dot{x}$ as

$$x_{1_{i+1}} = x_{1_i} + \frac{h}{6}\left(X_{2_1} + 2X_{2_2} + 2X_{2_3} + X_{2_4}\right)$$

$$x_{2_{i+1}} = x_{2_i} + \frac{h}{6}\left(F_1 + 2F_2 + 2F_3 + F_4\right)$$

(6.18)

Recall that the various identification algorithms are performed on the simulated excitation data from Section 6.2.1. The various identification algorithms yield the coefficients or weights of the mathematical representation of the system excitation. This data is then fed into the Runge-Kutta algorithm to compute the state variables, x_1 and x_2. Finally, once the timehistories of x_1 and x_2 for the various identification algorithms are computed using the Runge-Kutta method, they can be evaluated in a mean square sense for optimization. The various steps for this process can be easily shown in outline form as:

1. create simulated system data; $x, \dot{x}, \ddot{x}, r(x, \dot{x})$,

2. input simulated system data into identification algorithm to develop mathematical representation of system; ie., the coefficients of a polynomial or mesh fit (Chebyshev coefficients),

3. feed identified system coefficients (Chebyshev coefficients or other) into the forward differential equation to compute the state variables,

4. finally, compare computed state variables with original simulated system data using mean-squared error evaluation.

In addition, the Runge-Kutta routine can be used in lieu of the algorithms discussed in Section 6.2.1 to derive the variables x and $\dot{x}$ for a known system. The restoring

97

force can then be computed at each pair of variables in time, and then this

information can be fed into one of the identification algorithms to develop the

mathematical representation of the system. Figure 6.26 below presents the Runge-

Kutta procedure in flowchart form.
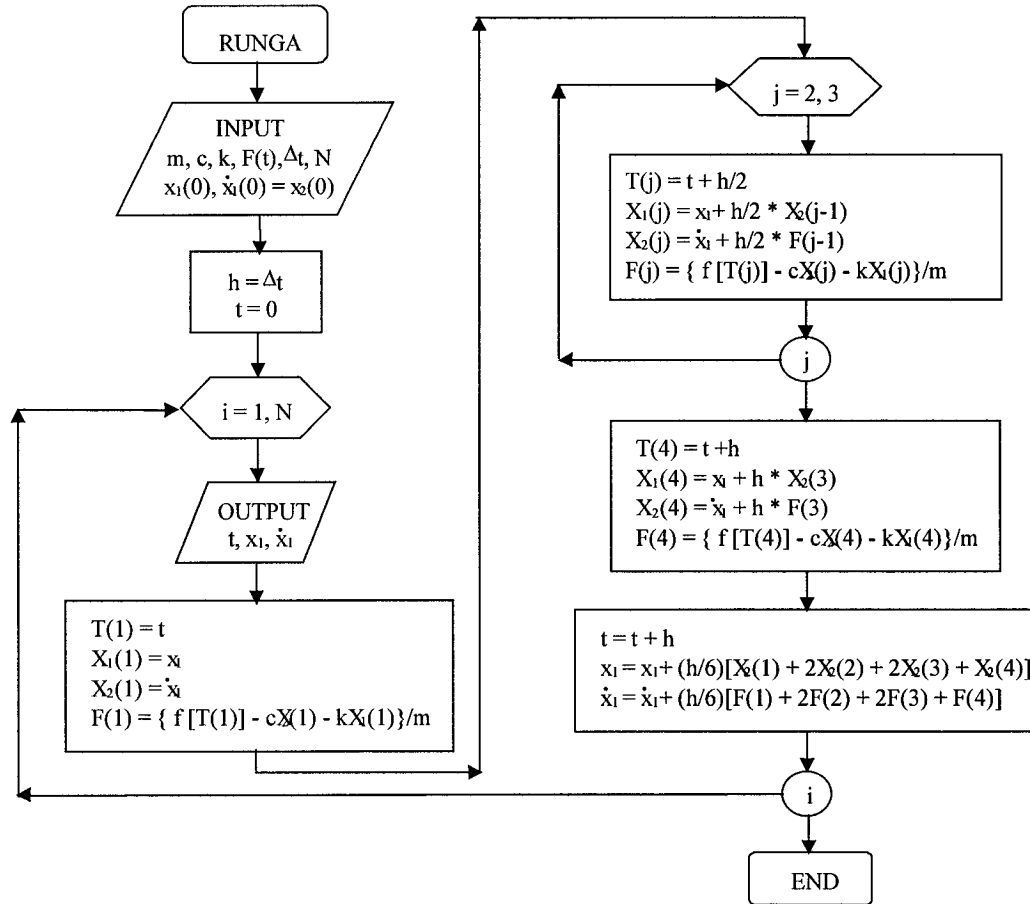
FIGURE 6.26. Runge-Kutta algorithm

The data derived from the previous simulations represents a sdof system

incorporating a damper element. The output information emulates measured data

from a physically realizable, instrumented system. As with physical online data, the simulated system data can be fed into an identification algorithm.

6.3.1 Algorithm Verification

Verification of the coded Runge-Kutta algorithm was conducted by computing the actual solution to a differential equation and comparing results against that output from the code. A linear sdof model with $m = 1$, $k = 1$, and $\zeta = 0.05$ was chosen. The excitation force was a sinusoidal input with $F_0 = 1$ and $\omega = 1$. The differential equation of motion describing the system can be written as

$$m\ddot{x} + c\dot{x} + kx = F_0 \sin(wt) \tag{6.19}$$

which reduces to

$$\ddot{x} + 0.1\dot{x} + x = \sin(t) \tag{6.20}$$

Note that this equation is similar to that reported in the linear solutions from the Fortran Runge-Kutta codes. The general homogeneous solution to equation (6.20) is

$$ms^2 + cs + k = 0 \tag{6.21}$$

$$s_{1,2} = -\frac{c}{2m} \pm \sqrt{\left(\frac{c}{2m}\right)^2 - \frac{k}{m}}$$

Since $c^2 < 4mk$, the system is underdamped; hence, the solution takes the form

$$s_1 = -\alpha + i\omega^*, \quad s_2 = -\alpha - i\omega^* \tag{6.22}$$

where

99

$$\alpha = \frac{c}{2m}, \quad \omega^* = \sqrt{\frac{k}{m} - \left(\frac{c}{2m}\right)^2} \qquad (6.23)$$

Thus,

$$x_h(t) = e^{-\alpha t}\left(A\cos(\omega^* t) + B\sin(\omega^* t)\right)$$

$$(6.24)$$

$$x_h(t) = C e^{-\alpha t}\cos(\omega^* t - \delta)$$

where $C^2 = A^2 + B^2$ and $\tan\delta = \dfrac{B}{A}$.

Substituting system parameters from above yields $f = \dfrac{\omega^*}{2\pi} \cong 0.159$, $\alpha = 0.05$, and ω^*

$= 0.99875$. Then, $s_1 = -0.05 + 0.99875i$, $s_2 = -0.05 - 0.99875i$, and the homogeneous

solution can be expressed as

$$x_h(t) = e^{-0.05t}\left[A\cos(0.99875t) + B\sin(0.99875t)\right] \qquad (6.25)$$

Next, the particular solution follows:

$$x_p(t) = a\cos(\omega t) + b\sin(\omega t)$$

$$\dot{x}_p(t) = a\omega\sin(\omega t) + b\omega\cos(\omega t) \qquad (6.26)$$

$$\ddot{x}_p(t) = -a\omega^2\cos(\omega t) - b\omega^2\sin(\omega t)$$

Substituting the above into the differential equation yields

$$\left[(k - m\omega^2)a + \omega c b\right]\cos(\omega t)$$

$$(6.27)$$

$$+ \left[-\omega c a + (k - m\omega^2)b\right]\sin(\omega t) = F_0\sin(\omega t)$$

Equating coefficients of cosine and sine terms yields

100

$$(k - m\omega^2)a + \omega c b = 0$$

(6.28)

$$-\omega c a + (k - m\omega^2)b = F_0$$

Coefficients a and b are computed by solving these equations simultaneously.

$$a = -F_0 \frac{\omega c}{(k - m\omega^2)^2 + (\omega c)^2}$$

(6.29)

$$b = F_0 \frac{(k - m\omega^2)}{(k - m\omega^2)^2 + (\omega c)^2}$$

Thus,

$$x_p(t) = F_0 \frac{1}{(k - m\omega^2)^2 (c\omega)^2} \left[-c\omega \cos(\omega t) + (k - m\omega^2)\sin(\omega t) \right]$$

(6.30)

$$x_p(t) = -10\cos t$$

Combining the homogeneous and particular solutions by superposition, the system differential equation solution can be written as

$$x(t) = e^{-\alpha t}\left(A\cos(\omega^* t) + B\sin(\omega^* t) \right)$$

(6.31)

$$+ F_0 \frac{1}{(k - m\omega^2)^2 + (\omega c)^2} \left[-(\omega c)\cos(\omega t) + (k - \omega c)\sin(\omega t) \right]$$

The final solution to the differential equation is computed by substituting the initial conditions, $x(0) = \dot{x}(0) = 0$, yielding A = -20 and B = -1.00125. Thus, the solution becomes

$$x(t) = e^{-0.05t}[10\cos(0.9975t) + 0.50125\sin(0.9975t)] - 10\cos t$$

$$\dot{x}(t) = -0.05e^{-0.05t}[10\cos(0.9975t) + 0.50125\sin(0.9975t)] \qquad (6.32)$$

$$+ e^{-0.05t}[-9.975\sin(0.9975t) + 0.5\cos(0.9975t)] + 10\sin t$$

The excellent comparison between the above differential equation solution for a system excited by a sinusoidal input and the Runge-Kutta solution of the same system are depicted below in Figures 6.27 and 6.28. Note that the displacement and velocity curves are nearly identical overlays. The computed "goodness-of-fit" (reference Section 6.4) was 0.006, clearly revealing that the coded Runge-Kutta algorithm accurately replicated the differential equation solution.
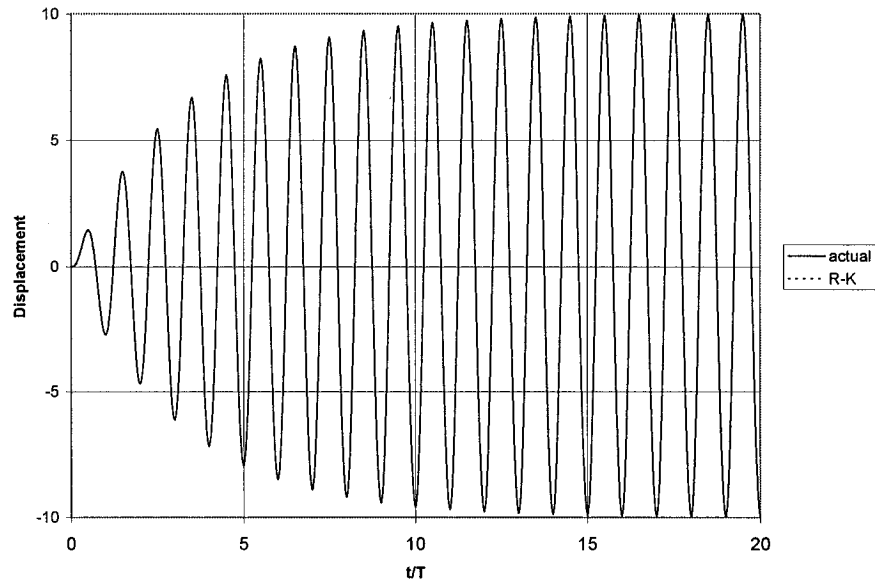
FIGURE 6.27. Displacement comparison

102
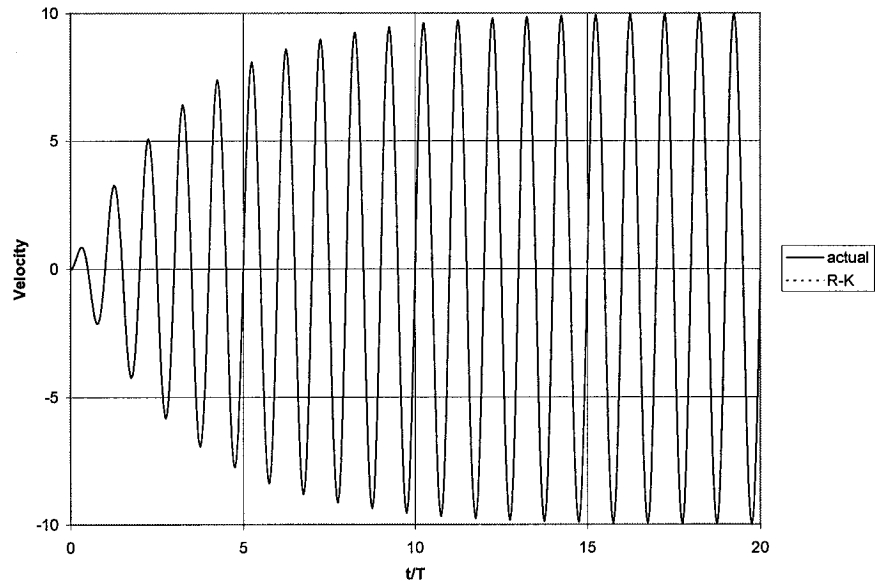
FIGURE 6.28. Velocity comparison

6.4 Goodness-of-fit

A measure of the goodness-of-fit between the actual surface f and the approximate

one $\hat{f}$ at n discrete points corresponding to the n pairs of data $(x_i, \dot{x}_i), i = 1, 2, ..., n$

is computed as the ratio of the root-mean-square (rms) values of $f(x, \dot{x})$ and the

deviation $e = \hat{f} - f$;

103

$$S_f = \left[\frac{1}{n}\sum_{i=1}^{n} f^2(x_i, \dot{x}_i)\right]^{1/2}$$

$$S_e = \left[\frac{1}{n}\sum_{i=1}^{n} e_i^2\right]^{1/2} \tag{6.33}$$

$$\varepsilon^* = S_e \Big/ S_f$$

Given the swept sine excitation, the goodness-of-fit was computed as shown in Table 6.1 below.

System type	Solution Algorithm	Runge-Kutta	Chebyshev 1-D	Chebyshev 2-D
linear	Masri et al (1979)	-------	0.0287	0.0167
linear	revised	-------	-------	0.0600
Duffing	revised	-------	-------	0.0284
Van der Pol	revised	-------	-------	0.181

TABLE 6.1 Goodness-of-fit, ε^*

104

6.5 Runge-Kutta Simulations

Several programs were written to facilitate the simulation and experimental studies of multi-degree-of-freedom linear or nonlinear systems. These included a Fortran code to generate system excitation force timehistories, a Runge-Kutta differential equation solver, and a code for computing the Chebyshev 1D and 2D polynomial coefficients. Matlab® was used for generating the data plots from these various codes.

The system excitation timehistories were computed in a Fortran code called *swept*. This program was designed to generate sinusoidal, swept sine, and stationary/nonstationary random excitations. Amplitude, frequency, time increments, beginning and maximum solution time were user-specified parameters.

The output from *swept* was fed into a separate Fortran code called *nonlin*, which solved the system differential equation for the specified excitation. The Runge-Kutta algorithm was utilized to solve the reverse differential equation, given the system parameters; mass, stiffness, and damping. Nonlinear models include the Duffing, Van der Pol, and hysteretic. This program was also designed to solve the differential equation of motion when the system parameters were not known, but rather a mathematical representation of the system was supplied. The system could be represented in terms of Chebyshev 1D or 2D polynomial coefficients, or as weights and biases defining a neural network. The state variables, displacement and velocity

105

were output for each algorithm applied in the solution of the system differential equation.

Two approaches were taken in computing the Chebyshev polynomial coefficients. First, the procedure described in the paper by Masri et al., 1979 was programmed in Matlab®. The raw data produced by the Runge-Kutta solution of the excited system was read, then processed to determine the coefficients. The state variable data, displacement and velocity, were normalized to +/-1, then a user-specified tolerance was applied along the abscissa and ordinate axes to select data for the 1D fit. Next, the selected data was interpolated to recover equally spaced data for computation with the cosine function. With the 1D coefficients, the 2D values were then computed. The procedure required translating the normalized phase plane data by $\cos \theta$, then interpolating to a specified grid. Interpolation was accomplished using two methods, a bilinear and a quardic equation. These can be expressed as:

$$f_{bilinear}(x, y) = a_0 + a_1 x + a_2 y + a_3 xy$$

$$f_{quardic}(x, y) = a_0 + a_1 x + a_2 y + a_3 xy + a_4 x^2 + a_5 y^2$$

(6.34)

The bilinear interpolation proved the most accurate in the final solution. Successful application of the interpolation strategies required searching the normalized, translated phase plane data for points in each quadrant surrounding each grid point. A search radius was prescribed to ensure relative accuracy of the interpolated data at each grid intersection. Data within this radius was searched to locate the closest

106

points to the grid intersection of interest in each quadrant. Once the grid was

populated with interpolated data, the 1D Chebyshev polynomial fit was used to fill

the remainder of the grid. This phase plane grid surface representation of the system

restoring force was then integrated to compute the Chebyshev 2D polynomial

coefficients. Accuracy as measured by the goodness-of-fit algorithm described

above proved excellent for linear and pseudo-linear systems; however,

computational difficulties were encountered with most higher order nonlinear

systems. A linear example of this algorithm is illustrated in Figures 6.31-6.39, with

Figures 6.29 and 6.30 depicting the damped system and excitation, respectively.

To address the nonlinear problems, a slightly different approach was utilized.

Instead of computing the 1D Chebyshev polynomial coefficients as described above,

the system state variable phase plane data was interpolated to a grid, then the

interpolated data was extrapolated to complete the population of the grid.

Interpolation was accomplished by locating the three closest points to the grid

intersection and fitting a plane through these points. Extrapolation was performed by

stepping through the grid along the displacement axis and fitting a curve to the

interpolated grid restoring force. The fitted curve was then used to extrapolate

missing grid data along the perimeter of the interpolated data set. The above could

be further fine-tuned by extrapolating along the velocity axis after performing the

operation along the displacement axis, then averaging the results. The excellent rms

data fit reported for the extrapolation along one axis only, however, did not warrant

107

additional computational effort and time. The extreme values of the restoring force along the displacement axis were set to the computed minimum and maximum values as there typically existed at most one interpolated value along these gridlines, making curve fitting unreasonable. Additional polynomial smoothing algorithms were added to adjust the extrapolated data set near the displacement extremes on the grid. To accomplish this, polynomial curves were fit along the velocity gridlines, covering approximately 10% of the grid space in the displacement direction. The slope of the two points preceding the limits for application of the out-of-plane smoothing polynomials was used to transition the smoothing algorithm. These curves yielded a smoother restoring force surface for integration in the areas where only limited data was available from the grid interpolation processing. Again, these smoothing techniques were simply to address the regions on the grid where limited interpolated data existed to provide accurate extrapolated information.

In addition to the algorithm modifications used in populating the restoring force grid, a slightly different integration scheme was employed. The discretized integration equation given in Masri et al., 1979, weighted all the integrated values equally, causing the end values to be dominant. The general form of this integration routine is depicted in Equation 6.35 below, with the limits of integration also shown.

$$v_{ij} = \sum_{k=1}^{MX2} \sum_{l=1}^{NY2} f_{kl} \cos[i\Delta\theta(k-1)]\cos[j\Delta\phi(l-1)]\Delta\theta\Delta\phi$$

$$0 \le i \le m2-1, \quad 0 \le j \le n2-1 \tag{6.35}$$

$$\Delta\theta = \frac{\pi}{(MX2-1)}, \quad \Delta\phi = \frac{\pi}{(NY2-1)}$$

In lieu of this procedure, integration was performed following finite element

strategies. Each grid square was considered a finite element, and the four corner

restoring force values were summed and averaged to determine their mean value.

This mean was assumed applied at the center of each element. Once all the mean

values were computed for each finite element grid square, their sum was computed

and divided by the number of elements less one.

$$v_{ij} = \frac{1}{(n-1)} \sum_{p=1}^{n} \left(\sum_{k=k_0}^{k_0+1} \sum_{l=l_0}^{l_0+1} \frac{f_{kl}}{4} \right)$$

$$\tag{6.36}$$

$$0 \le i \le m2-1, \quad 0 \le j \le n2-1$$

The combination of these changes yielded excellent rms error values in data

comparisons, as well as near overlays of the actual system response and the

approximated one from the computed Chebyshev polynomial coefficients. These

results are depicted below for a linear and several nonlinear models excited by swept

sinusoids. A linear example of this algorithm is illustrated in

Figures 6.40-6.43. Nonlinear cases included a Duffing oscillator, reference

Figures 6.44-6.52 and a Van der Pol oscillator, reference Figures 6.53-6.61. The

goodness-of-fit for each case is tabulated in Table 6.1, Section 6.4.

An important note is that while the revised algorithm yielded excellent surface fits for the various nonlinear systems investigated, the linear results were not quite as accurate as those reported from the original methodology. This can be explained by a review of the two methods. The method presented by Masri and Caughey utilizes the 1D Chebyshev polynomial fit to populate the grid where interpolated data was not available. Since the linear model can easily be replicated with 1D Chebyshev polynomials, this algorithm results in highly accurate linear system identification with very low polynomial order; ie., a 2x2 as depicted in the following example. However, utilization of the 1D Chebyshev polynomials for nonlinear system identification results in discontinuities in the restoring force surface.

These discontinuities are difficult to reconcile for the integration scheme employed in computing the Chebyshev 2D polynomial coefficients from the populated restoring force surface. Tests revealed that the higher the system nonlinearity, the more pronounced the discontinuities in the populated restoring force surface. Meanwhile, the revised algorithm does not rely on the Chebyshev 1D polynomials to populate the grid voids, but rather applies smoothing polynomials along the displacement axis to extrapolate using the interpolated data sets. This method then relies largely on the actual interpolated restoring force data, with smoothing techniques applied to rectify those areas where limited data resides, such as along the extremes along the displacement axis. The result is a smooth rectangular grid

110

surface built solely from the interpolated data. The extrapolation and smoothing techniques applied in this algorithm do not change the values of the actual data set, so the surface replicates the data set well.

6.5.1 Linear System Data

6.5.1.1 Excitation data

The prescribed excitation was swept-sine, as defined below:

$$F_1(t) = F_0 \sin \Omega(t)t$$

$$F_0 = 1, \omega_1 = 0.5, \omega_2 = 2.5$$

$$T_s/T = 49$$
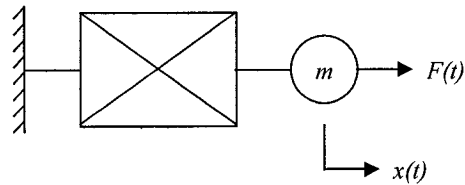
FIGURE 6.29. Model of nonlinear single-degree-of-freedom system
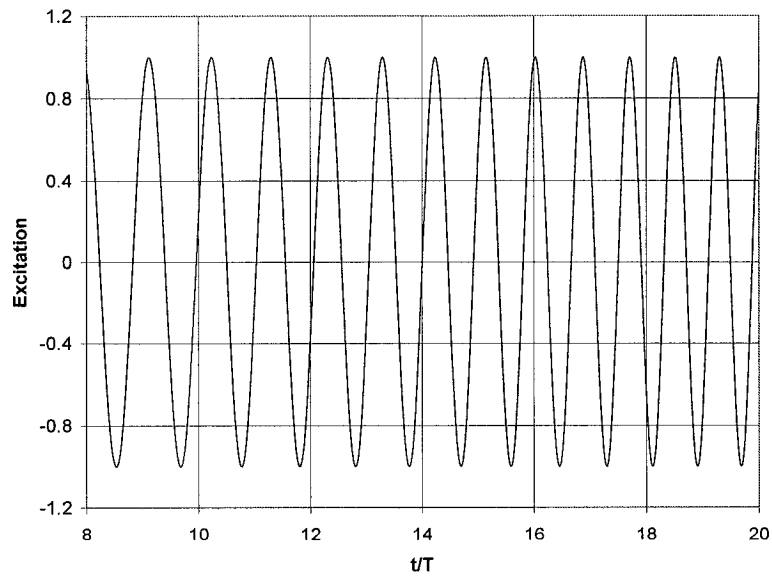
FIGURE 6.30. Excitation data

6.5.1.2 Masri et al., 1979 algorithm

The system parameters utilized for the analysis are:

$$Exact \ f(x, \dot{x}): \quad m(2\varsigma\omega\dot{x} + \omega^2 x)$$

$$m = 1, \ \omega = 1, \ \varsigma = 0.05$$

(6.37)

Typical time-history records for $f(x, \dot{x})$ corresponding to a linear SDOF system under the swept-sine excitation defined above are given in Figure 6.31.
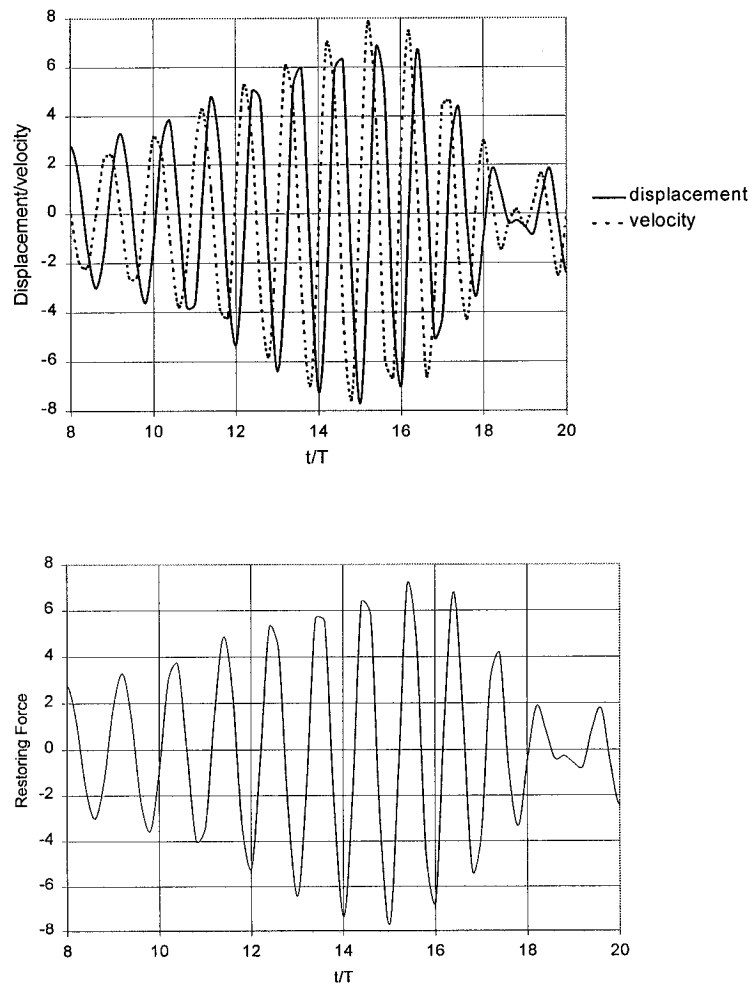
FIGURE 6.31. Identification data for a linear system

112

6.5.1.2.1 Chebyshev approximation

The Matlab® output is listed below with comparison numbers in parentheses:

```
» clear all
» restorfsub('matlabin.txt',1,0.05,1,0.05,'poly1.txt','poly2.txt','minmax.txt');
xMax =   7.6622              (7.57)
xMin =  -7.7209              (-7.72)
xdMax =   8.0080             (7.97)
xdMin =  -7.9022             (-7.89)
ans =   705                 (282)           % length of g(x)
ans =   1177                (465)           % length of h(xd)
a =  -0.0202    7.6840       (-0.09   7.63)
b =  -0.0303    0.8299       (-0.20   0.61)
r =    0.2500
xGridSize =    25
yGridSize =    25
C = -0.038530976   0.819183349      (-0.22   0.65)
     7.669988499  -0.003831229      (7.64    0.003)
eps1D =    0.0280
eps2D =    0.0167
fitCntr =    0         % counter indicating numerical instabilities encountered in
2-D
              interpolation fit
elapsed_time =  258.9200              % cpu solution time in seconds
```

Note that timehistory data is first acquired by running a Fortran code called *swept* with the prescribed frequency, time and amplitude parameters noted above. This data is then fed into the master Fortran code which computes the Runge-Kutta solution of the system (in this case an sdof system) and writes the displacement, velocity and force data to a text file called *matlabin*. This file is then read by the Matlab® code and processed according to the algorithms described in the above-noted paper. This code computes the 1D and 2D Chebyshev coefficients for the data set and plots the various fits.

113

The raw data generated from the Runge-Kutta solution of the linear system

differential equation is plotted in Figure 6.32 below.
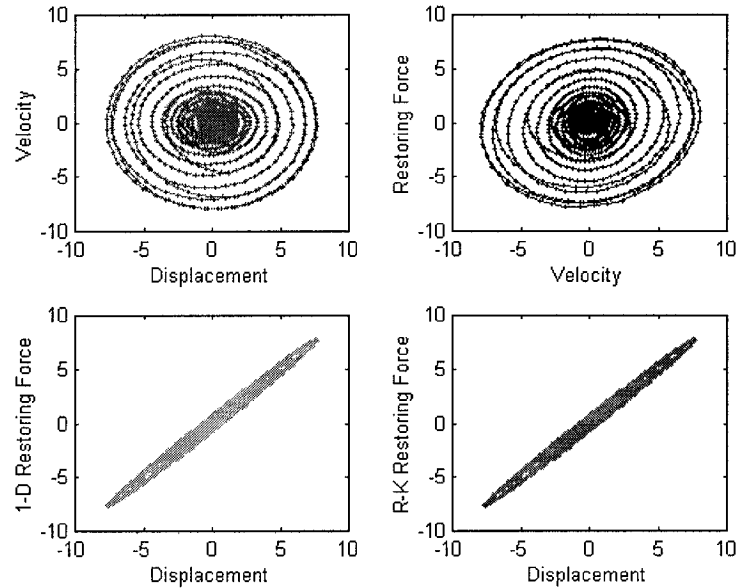
FIGURE 6.32. State variable plots for a linear system

The coordinate system of the state variable phase plane data is transformed as

depicted in Figure 6.33 to allow application of the processing algorithm.
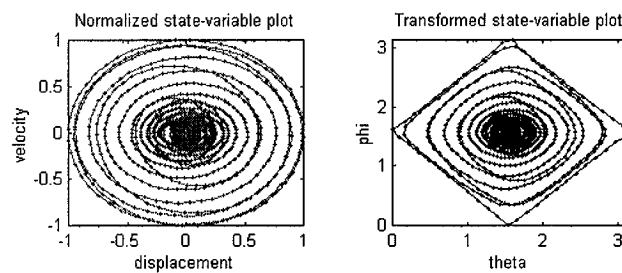
FIGURE 6.33. Transformed state variable plots for a linear system

114

Figure 6.34 displays the 3D mesh of interpolated equidistant points of the data set represented in Figure 6.33. The vertical axis represents the restoring force amplitude, while the horizontal axes represent the transformed coordinate displacement and velocity. Figure 6.34 displays the same data set after data averaging to remove any substantial discontinuities from the interpolated set prior to integration. The diamond shape outline evident in Figures 6.34 and 6.35 define the interpolated data derived from interpolating on the phase plane representation in Figure 6.33, while the remainder of the grid was populated using the 1D Chebyshev polynomial fit algorithm discussed earlier. Figure 6.36 simply displays the interpolated and averaged data as seen in Figure 6.35, without the 1D Chebyshev approximation to fill the voids in the restoring force mesh. The least-squares Chebyshev approximation of the data represented in Figure 6.35 is given in Figure 6.37. This plot was derived from the 2D Chebyshev polynomial coefficients computed after integrating the data in Figure 6.35 in accordance with the algorithm presented by Masri et al, 1979. The excellent fit between the initial displacement and velocity data utilized to derive the Chebyshev polynomial coefficients, and that computed from these coefficients, is displayed in Figure 6.39. The actual Chebyshev coefficients are tabulated in Table 6.2. Note that there are three curves displayed in the displacement and velocity plots, one representative of the initial Runge Kutta data fed into the above algorithm, and the other two representing the state variables generated from the Chebyshev 1D and 2D polynomial fits. For the linear case, excellent comparisons were realized with both the simpler Chebyshev 1D and 2D

115

approximations of the actual system displacement and velocity. The Chebyshev 1D approximation populates the grid entirely with the one dimensional polynomial, instead of applying the algorithm above. This is adequate for representing linear systems, but will not capture the subtle data shifts inherent in nonlinear systems, and thus was only shown for the linear case for completeness. It is also important to note that while a 1st order 2D Chebyshev representation of the data was adequate for the linear case, higher order polynomial representations are necessary to accurately approximate nonlinear systems.

The search radius and grid specified in the algorithm was varied to yield the highest degree of accuracy of the fit to the original data set. Multiple iterations of the algorithm were performed to minimize the approximation error. Plots of the error versus search radius for specific mesh sizes are given in Figure 6.38. It is clear that the optimum search radius was 0.25 units for a 25x25 grid mesh.

116

2-D interpolated values of f(x,xd)
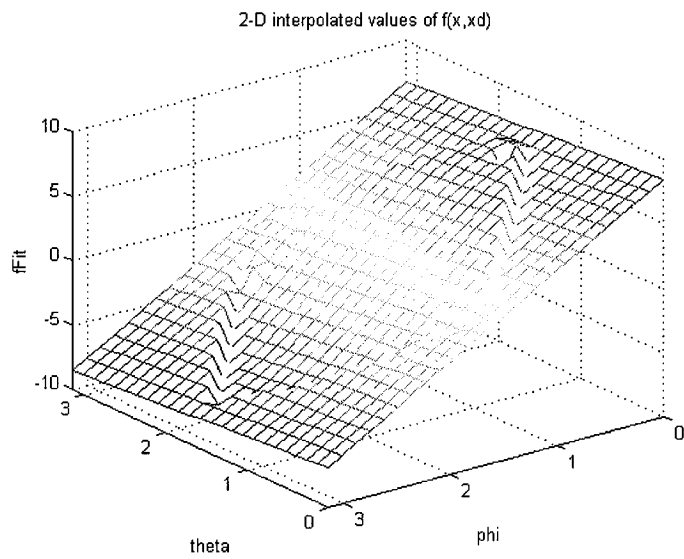
FIGURE 6.34. Interpolated values of $f(x, \dot{x})$ at equidistant points in θ and ϕ for a linear system

2-D estimated values of f(x,xd)
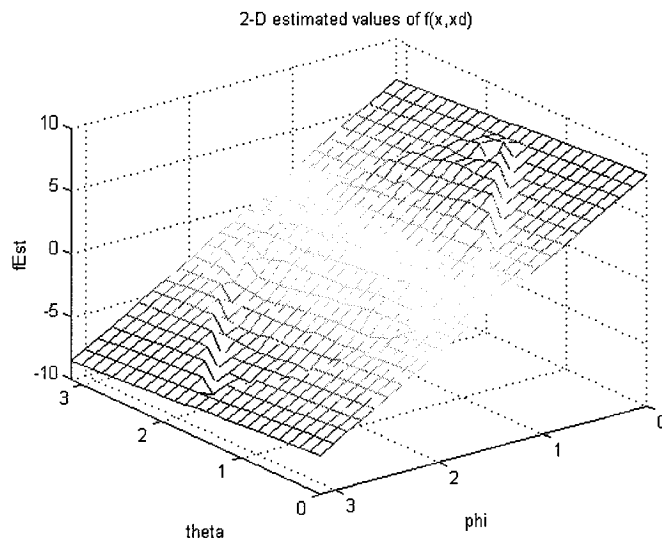
FIGURE 6.35. Averaged values of $f(x, \dot{x})$ at equidistant points in θ and ϕ for a linear system

117

2-D estimated values of f(x,xd)
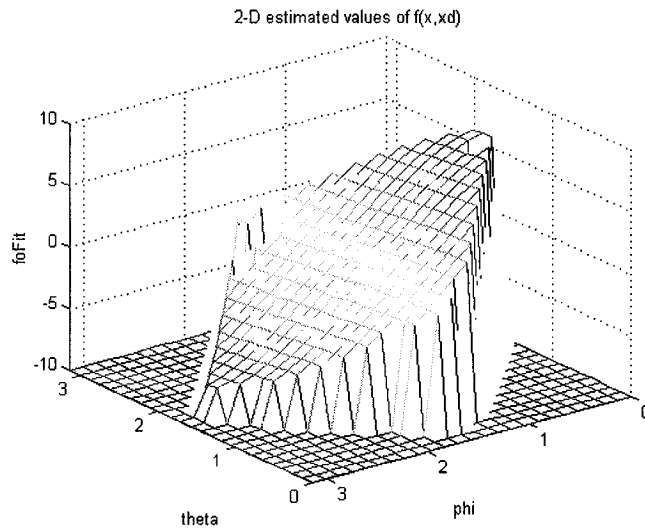
FIGURE 6.36. 2D interpolated values of $f(x,\dot{x})$ at equidistant points in θ and ϕ for a linear system without 1-D data fit along perimeter

Least-squares Chebyshev polynomial approximation f(x,xd)
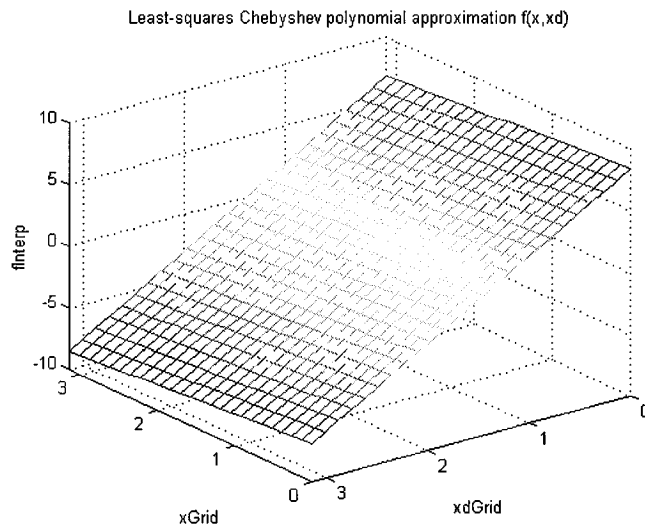
FIGURE 6.37. Least-squares Chebyshev polynomial approximation $\hat{f}(x,\dot{x})$ to $f(x,\dot{x})$ for a linear system

118
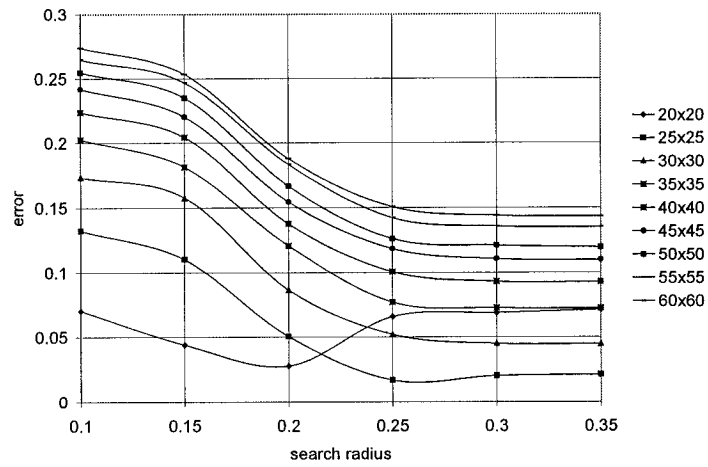
FIGURE 6.38. Chebyshev 2D data fit error for the linear oscillator

i/j	$T_0(\dot{x}')$	$T_1(\dot{x}')$
$T_0(x')$	-0.0385	0.8192
$T_1(x')$	7.6700	-0.0038

TABLE 6.2. Chebyshev coefficients for the linear oscillator

119
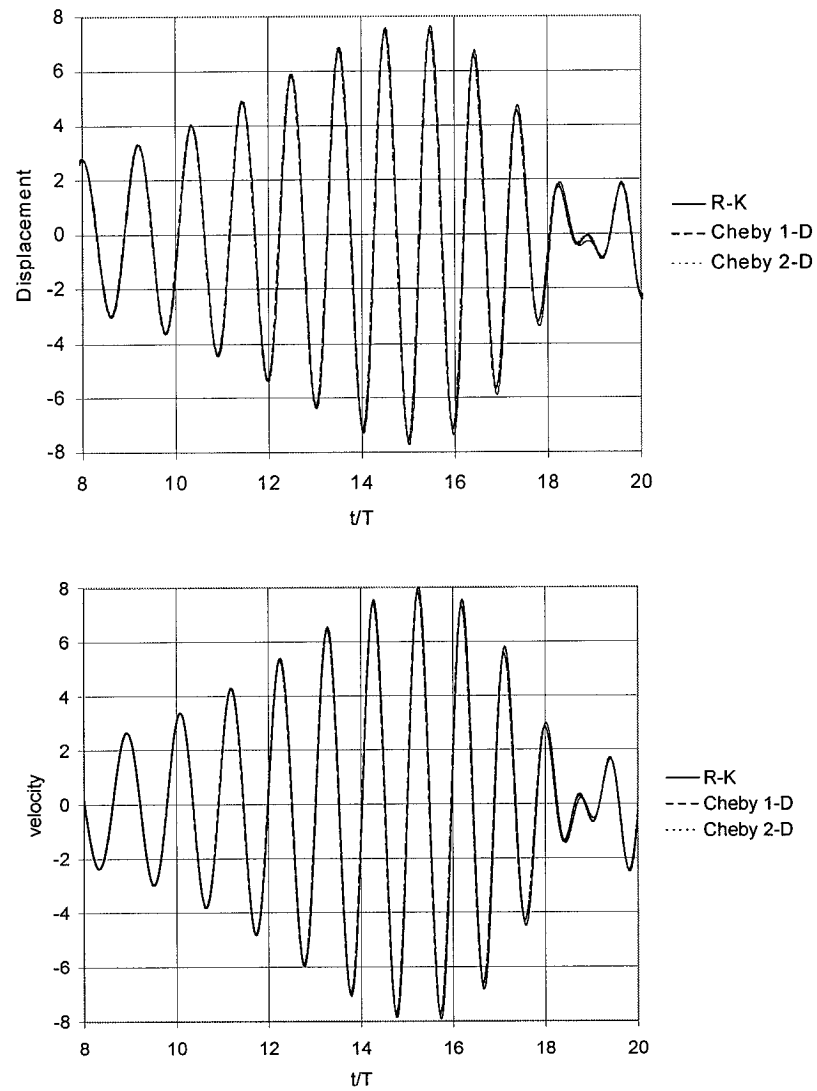
FIGURE 6.39. Comparison of exact and approximate results for the linear oscillator

120

6.5.1.3 Revised algorithm

The results contained herein were generated from the revised algorithm described above. The goodness-of-fit for this algorithm solution is given in Section 6.4, Table 6.1. As noted in the example above, typical time-history records for $f(x, \dot{x})$ corresponding to the linear SDOF system under the swept-sine excitation defined above are given in Figure 6.31. Figures 6.32 and 6.33 depict the state-variable plots and their transformed state for the linear case under consideration.
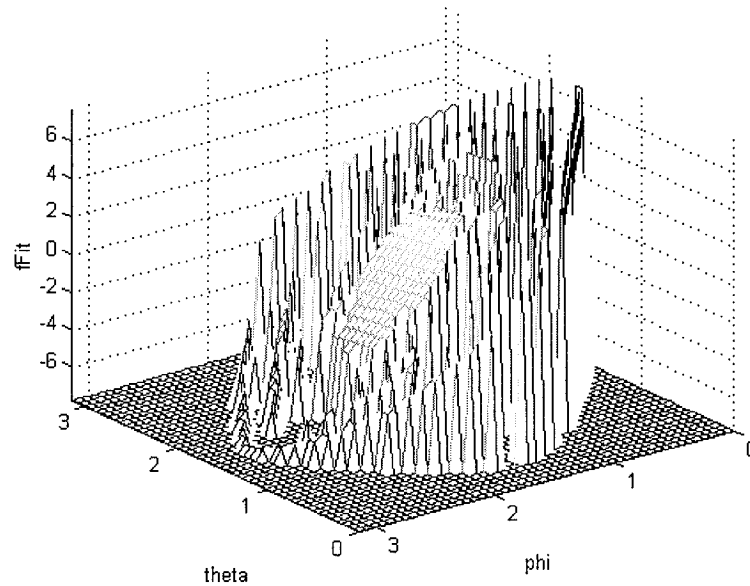
FIGURE 6.40. Interpolated values of $f(x, \dot{x})$ at equidistant points in θ and ϕ for a linear system

121
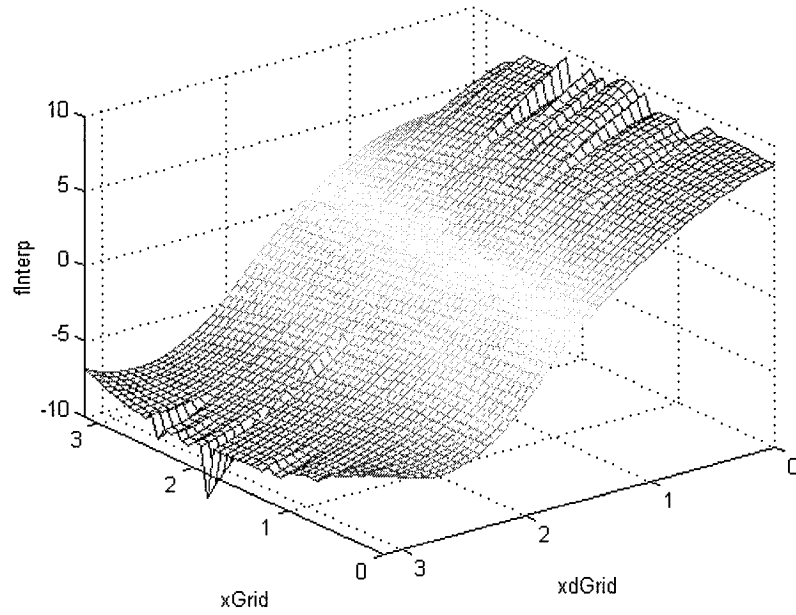
FIGURE 6.41. Interpolated and extrapolated values of $f(x, \dot{x})$ at equidistant points in θ and ϕ for a linear system
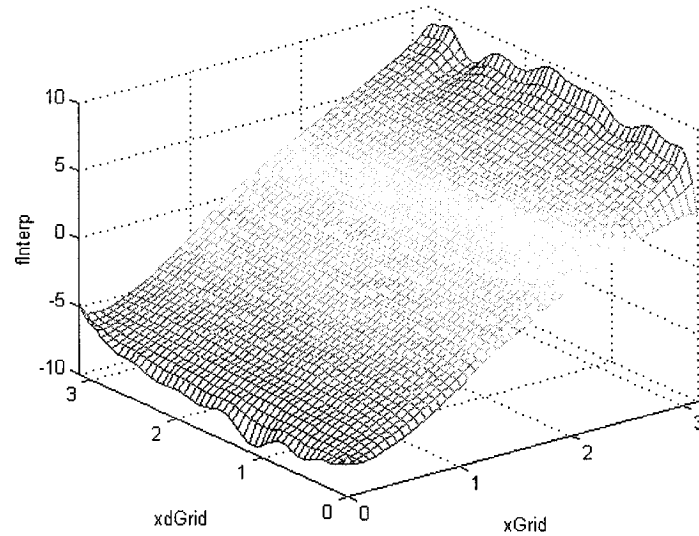
FIGURE 6.42. Least-squares Chebyshev polynomial approximation $\hat{f}(x, \dot{x})$ to $f(x, \dot{x})$ for a linear system

122
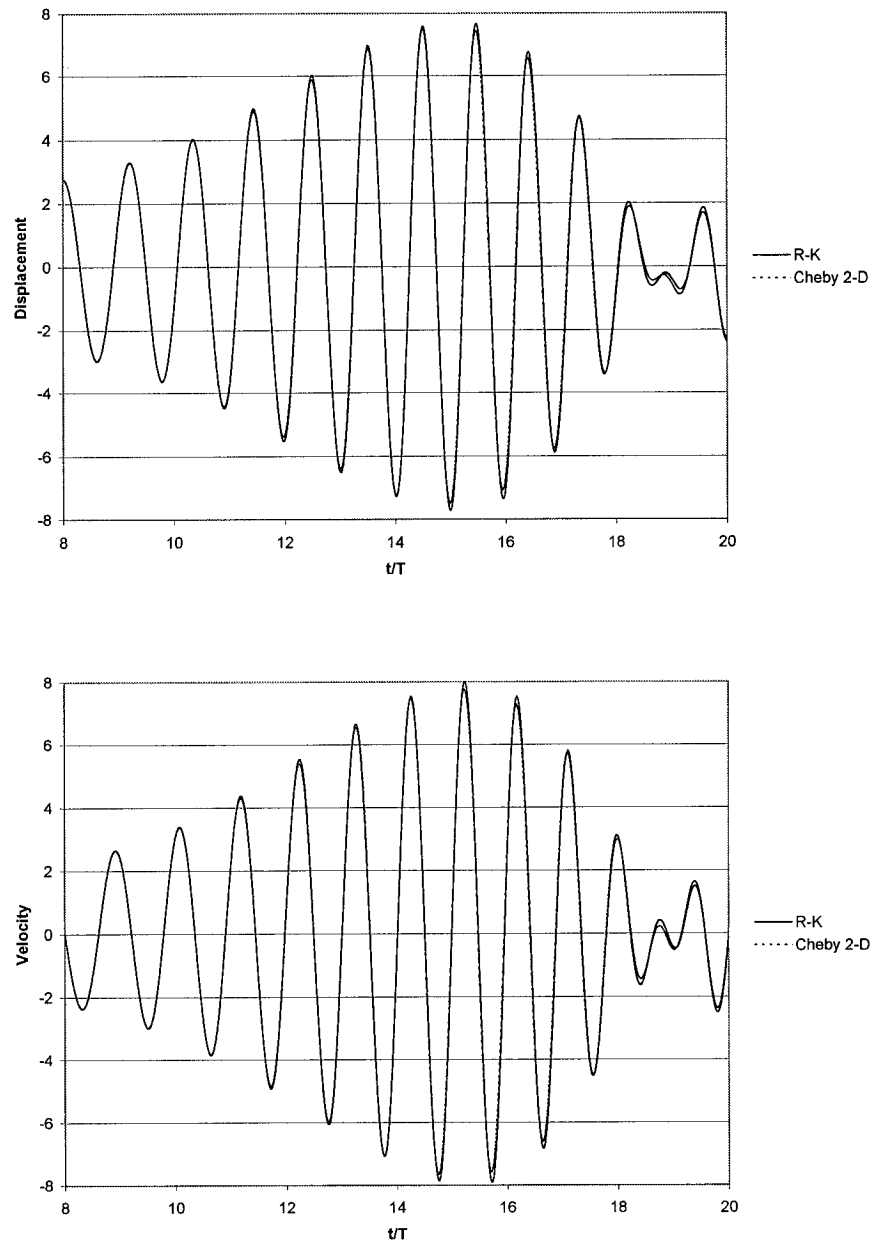
FIGURE 6.43. Comparison of exact and approximate results for the linear oscillator

123

The 2D Chebyshev polynomial coefficients generated as a mathematical

representation of the system with the revised algorithm are included in the

Appendices. A 20x20 polynomial representation was necessary with this algorithm,

even for the linear oscillator, as discussed previously.

6.5.2 Nonlinear System Data

6.5.2.1 Duffing oscillator

6.5.2.1.1 Excitation data

The prescribed excitation for the nonlinear Duffing oscillator was a swept-sine as

defined below:

$F_1(t) = F_0 \sin \Omega(t)t$

$F_0 = 4$, $\omega_1 = 0.5$, $\omega_2 = 2.5$
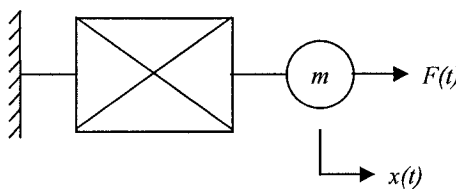
$T_s/T = 49$

FIGURE 6.44. Model of nonlinear single-degree-of-freedom system
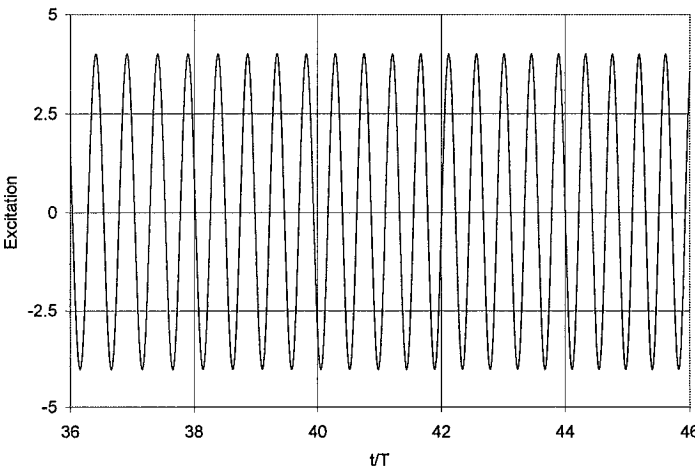
FIGURE 6.45. Excitation data

6.5.2.1.2 Chebyshev approximation

The system parameters utilized for the nonlinear Duffing analysis are:

$$Exact\ f(x, \dot{x}): \quad m\left[2\varsigma\omega\dot{x} + \omega^2(x + \varepsilon x^3)\right]$$

(6.38)

$$m = 1, \omega = 1, \varsigma = 0.02, \varepsilon = 0.003$$

Typical timehistory records for $f(x, \dot{x})$ corresponding to a nonlinear Duffing

oscillator SDOF system under the swept-sine excitation defined above are given in

Figure 6.46 below.
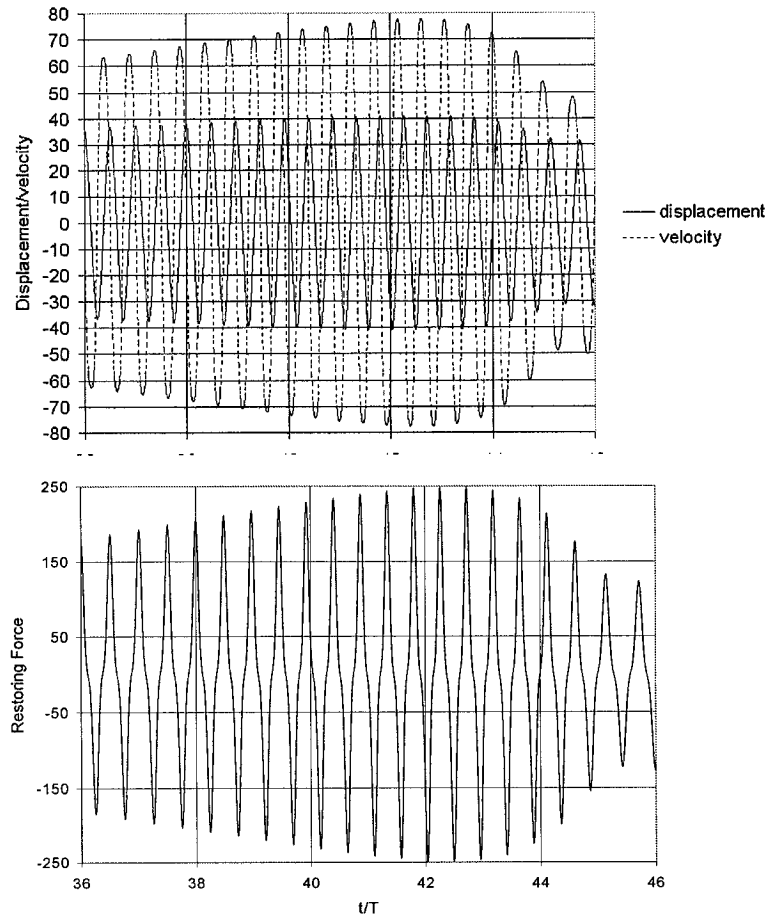
FIGURE 6.46. Identification data for a Duffing oscillator

125

Following the procedures outlined above, the raw data generated from the Runge-Kutta solution of the nonlinear Duffing oscillator system differential equation is plotted in Figure 6.47. Note that the data processing is performed utilizing the modified or revised algorithm defined in Section 6.5.1.3.
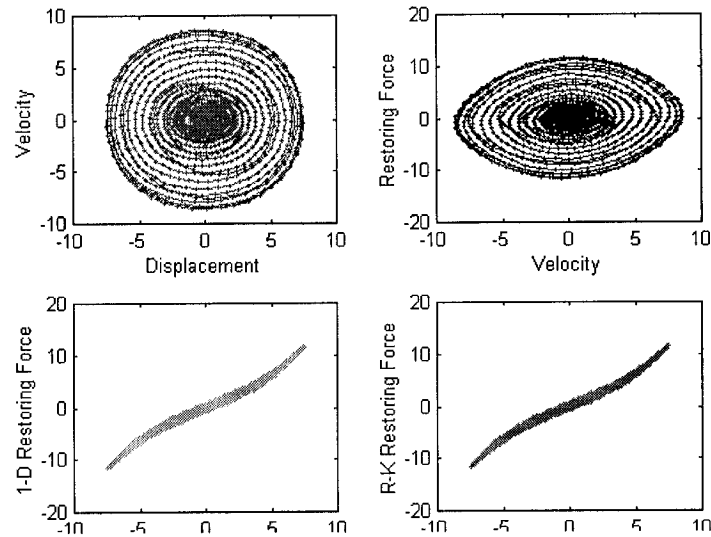
FIGURE 6.47. State-variable plots for a Duffing oscillator

The coordinate system of the state variable phase plane data is transformed as depicted in Figure 6.48 to allow application of the processing algorithm.
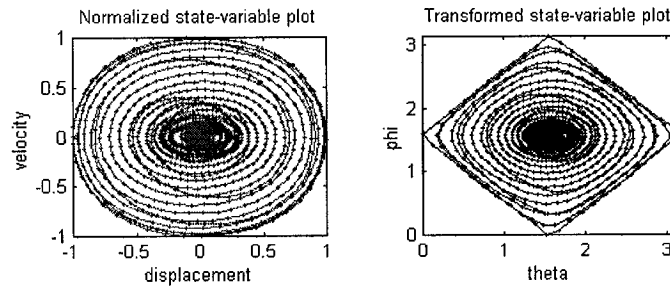
FIGURE 6.48. Transformed state-variable plots for a Duffing oscillator

126
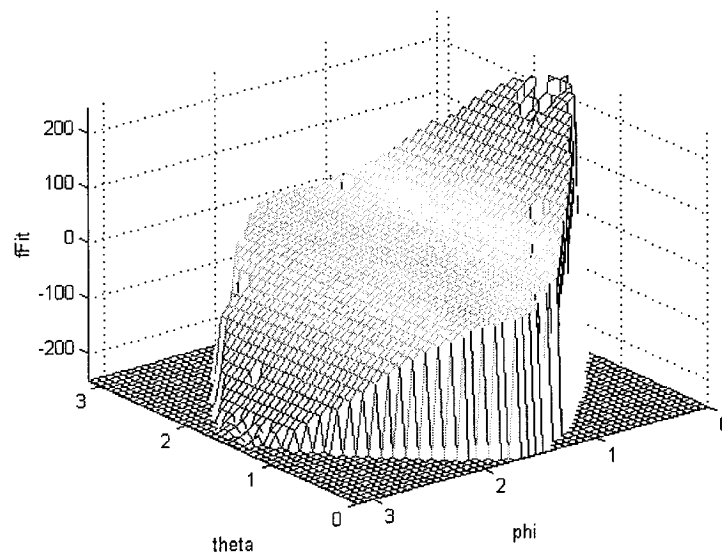
FIGURE 6.49. Interpolated values of $f(x, \dot{x})$ at equidistant points in θ and ϕ for a Duffing oscillator
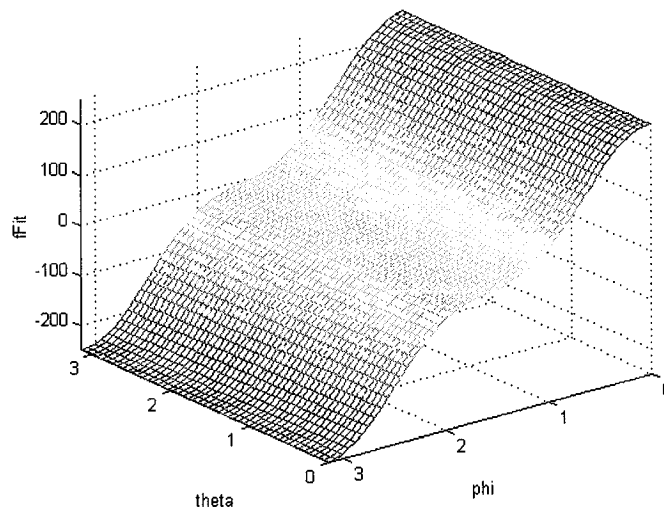
FIGURE 6.50. Interpolated and extrapolated values of $f(x, \dot{x})$ at equidistant points in θ and ϕ for a Duffing oscillator

127
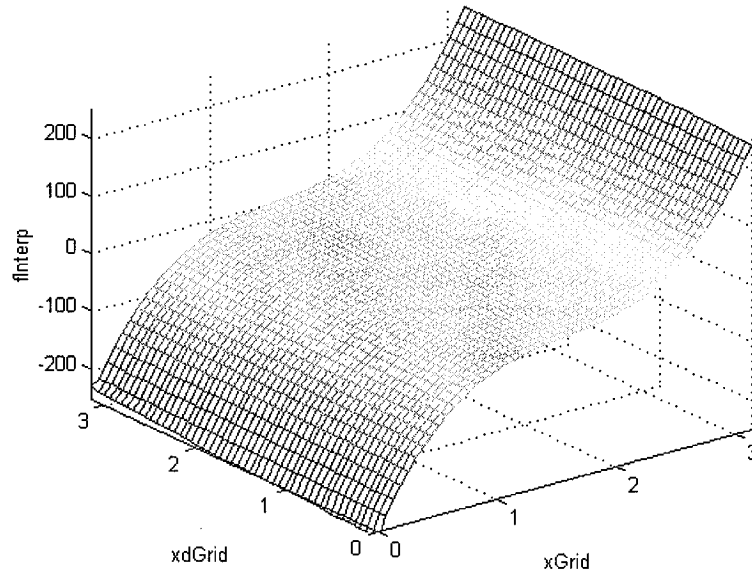
FIGURE 6.51. Least-squares Chebyshev polynomial approximation $\hat{f}(x,\dot{x})$ to $f(x,\dot{x})$ for a Duffing oscillator

The 2D Chebyshev polynomial coefficients generated as a mathematical representation of the system with the revised algorithm are included in the Appendices. A 20x20 polynomial representation was utilized.

128
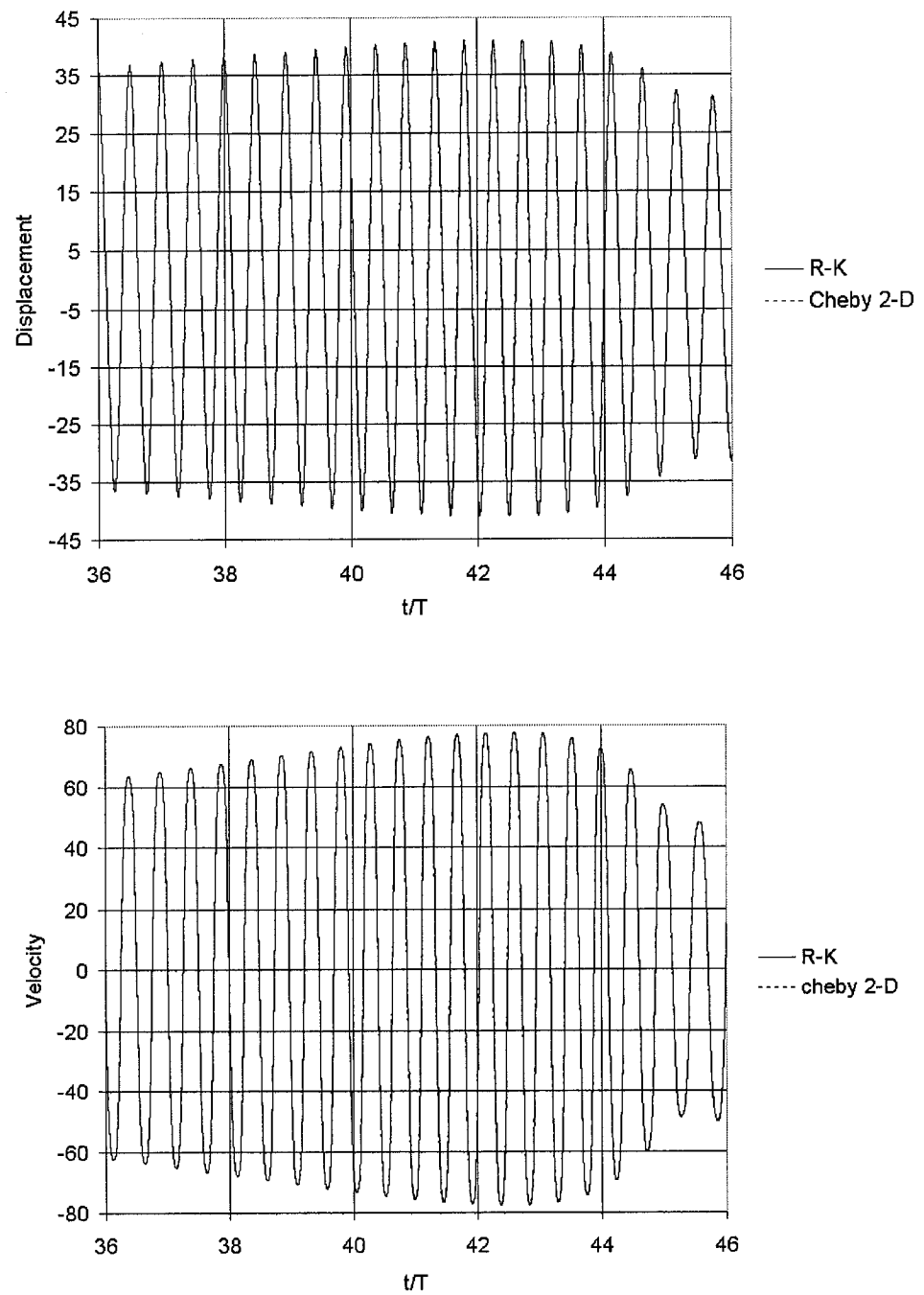
FIGURE 6.52. Comparison of exact and approximate results for a Duffing oscillator

129

6.5.2.2 Van der Pol oscillator

6.5.2.2.1 Excitation data

The prescribed excitation for the nonlinear Van der Pol oscillator was a swept-sine as defined below:

$$F_1(t) = F_0 \sin \Omega(t)t$$

$$F_0 = 10, \ \omega_1 = 0.5, \ \omega_2 = 2.5$$

$$T_s/T = 10$$
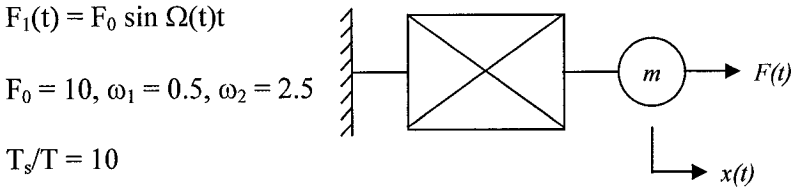
FIGURE 6.53. Model of nonlinear single-degree-of-freedom system
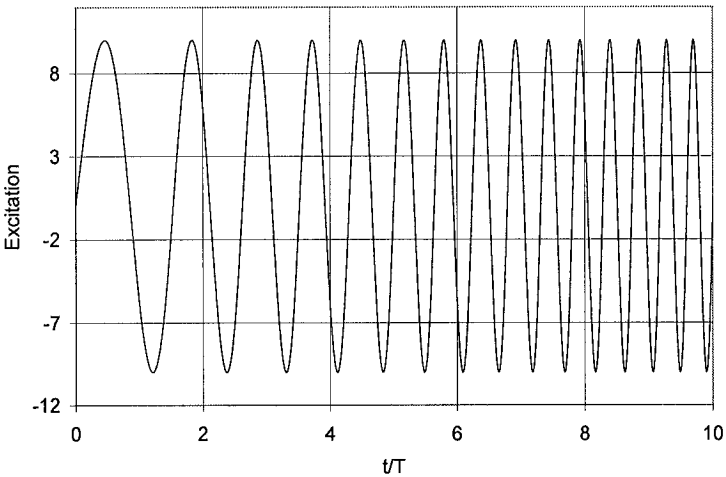
FIGURE 6.54. Excitation data

130

6.5.2.2.2 Chebyshev approximation

The system parameters utilized for the nonlinear Van der Pol analysis are:

$$Exact \; f(x, \dot{x}): \quad -\varepsilon(1 - x^2)\dot{x} + x$$

$$m = 1, \; \varepsilon = 0.2$$

(6.39)

Typical timehistory records for $f(x, \dot{x})$ corresponding to a nonlinear SDOF system under the swept-sine excitation defined above are given in Figure 6.55.
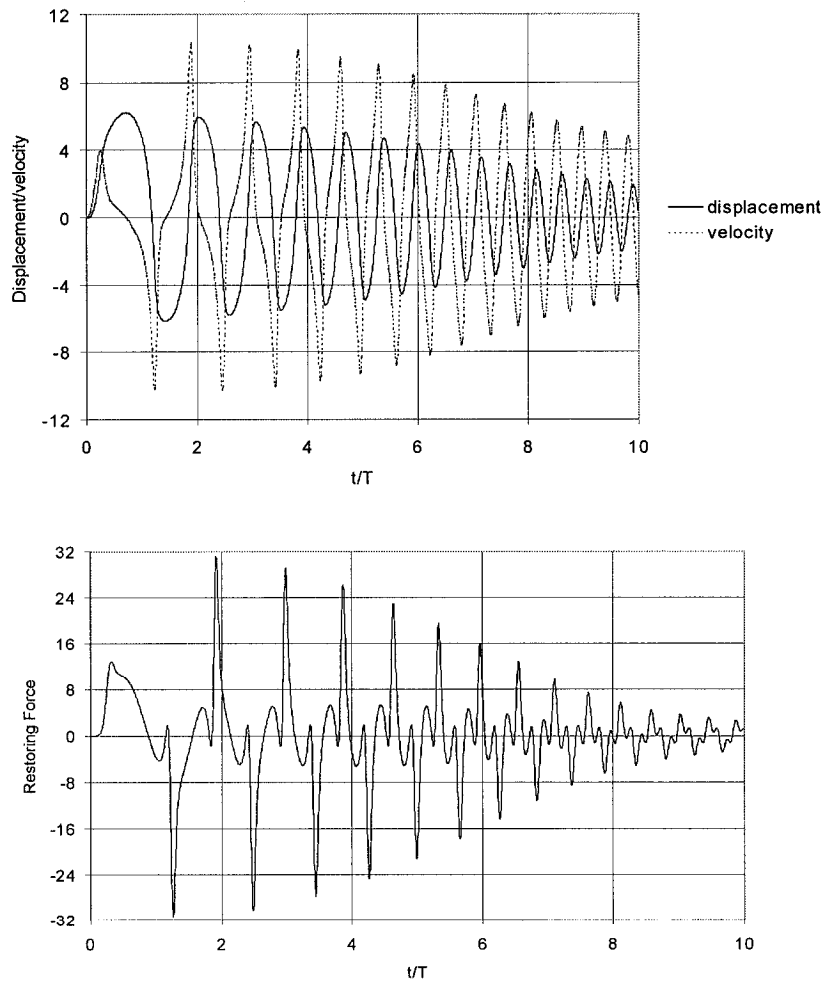
FIGURE 6.55. Identification data for a Van der Pol oscillator

131

Following the procedures outlined above, the raw data generated from the Runge-Kutta solution of the nonlinear Van der Pol oscillator system differential equation is plotted in Figure 6.56. Note that the data processing is performed utilizing the modified or revised algorithm defined in Section 6.5.1.3.
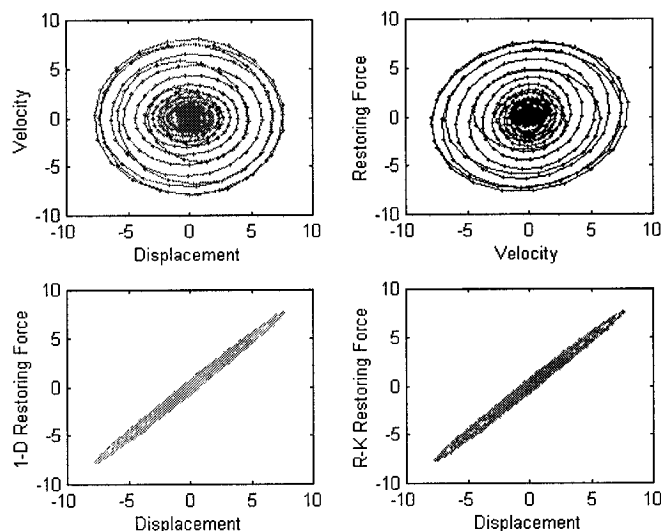
FIGURE 6.56. State-variable plots for a Van der Pol oscillator

The coordinate system of the state variable phase plane data is transformed as depicted in Figure 6.57 to allow application of the processing algorithm.
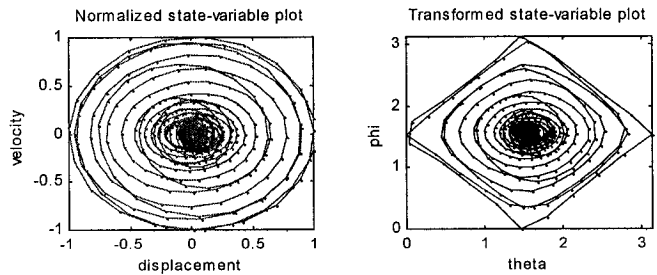
FIGURE 6.57. Transformed state-variable plots for a Van der Pol oscillator

132
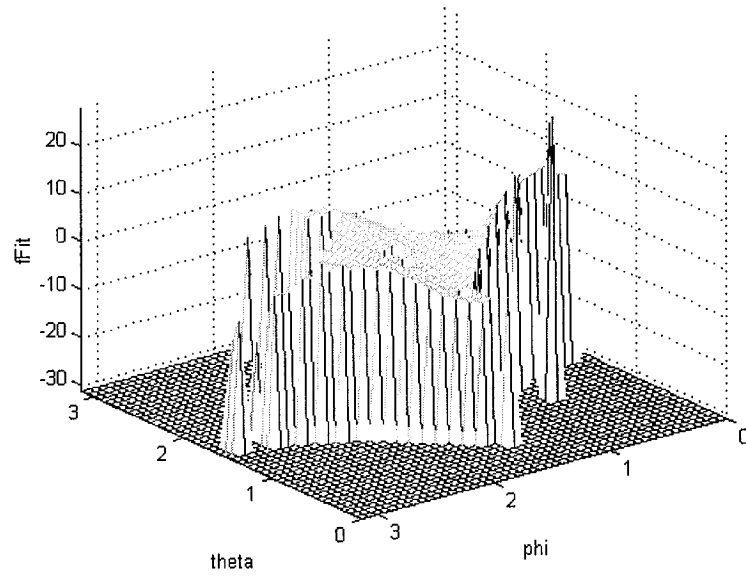
FIGURE 6.58. Interpolated values of $f(x, \dot{x})$ at equidistant points in θ and ϕ for a Van der Pol oscillator
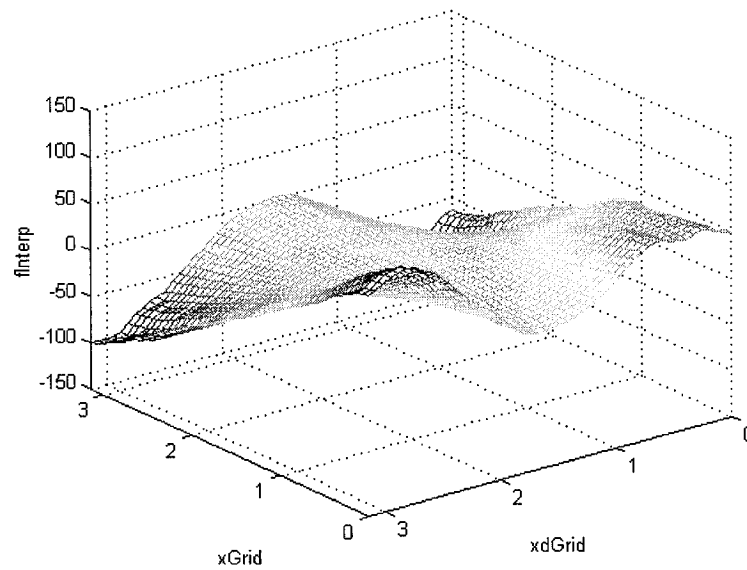
FIGURE 6.59. Interpolated and extrapolated values of $f(x, \dot{x})$ at equidistant points in θ and ϕ for a Van der Pol oscillator

133
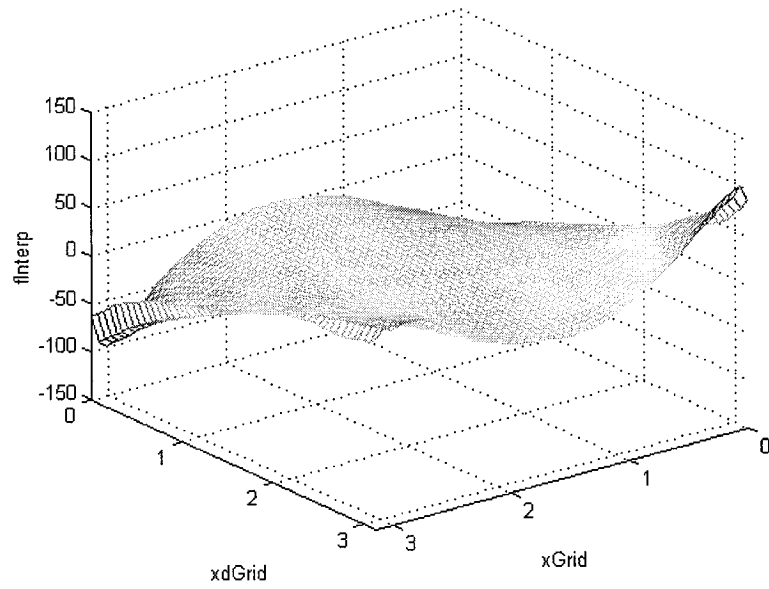
FIGURE 6.60. Least-squares Chebyshev polynomial approximation $\hat{f}(x,\dot{x})$ to $f(x,\dot{x})$ for a Van der Pol oscillator

134
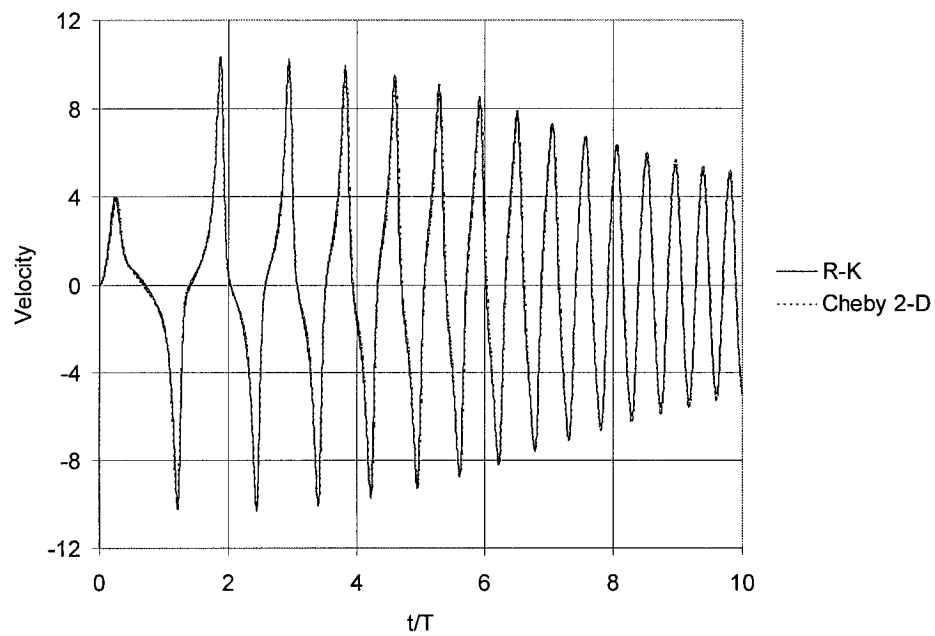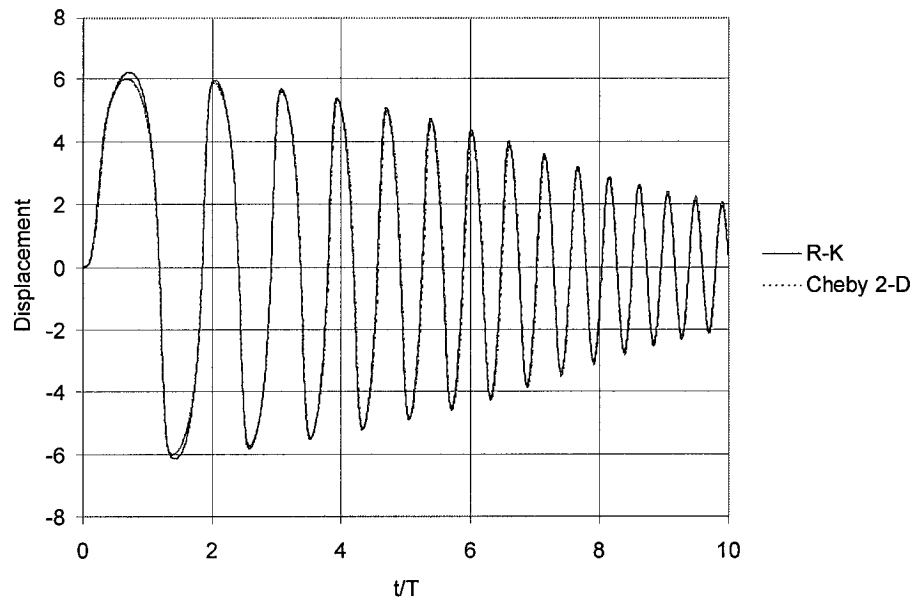
FIGURE 6.61. Comparison of exact and approximate results for a Van der Pol oscillator

6.6 Statistical Analysis

As stated previously, it is the intent of this research to determine the most effective system identification tool from the three discussed for the purpose of identifying subtle variations in system performance which could be indicators of damper system degradation. To accomplish this, simulation data was fed into each of the three system identification tools and the error between the approximated system state variables and the simulated results was computed.

Statistical analysis was introduced at this juncture in an attempt to replicate the anticipated damper system parameter variations prevalent in any mechanical system. With the failure threshold parameters known for the system mass, stiffness and coefficient of damping, random perturbations in these values were added to the original system representation. The models of the damped system used were: linear, Duffing oscillator, and the Buoc-Wen oscillator. These oscillators are discussed at length in section 6.5 of the text. The statistical sample size was initially set at 5000, then revised down to 3000 as discussed later. The results of these simulations were plotted, with the number of samples on the abscissa and the computed state variable error on the ordinate. Figure 6.62 depicts the systems excited by a stationary random input, with the three lines representing the three identification algorithms under consideration. It is important to note that these curves only represent the degree of accuracy or level of confidence associated with the analytical tool's ability to replicate the system state variables; i.e., the baseline cases.

136
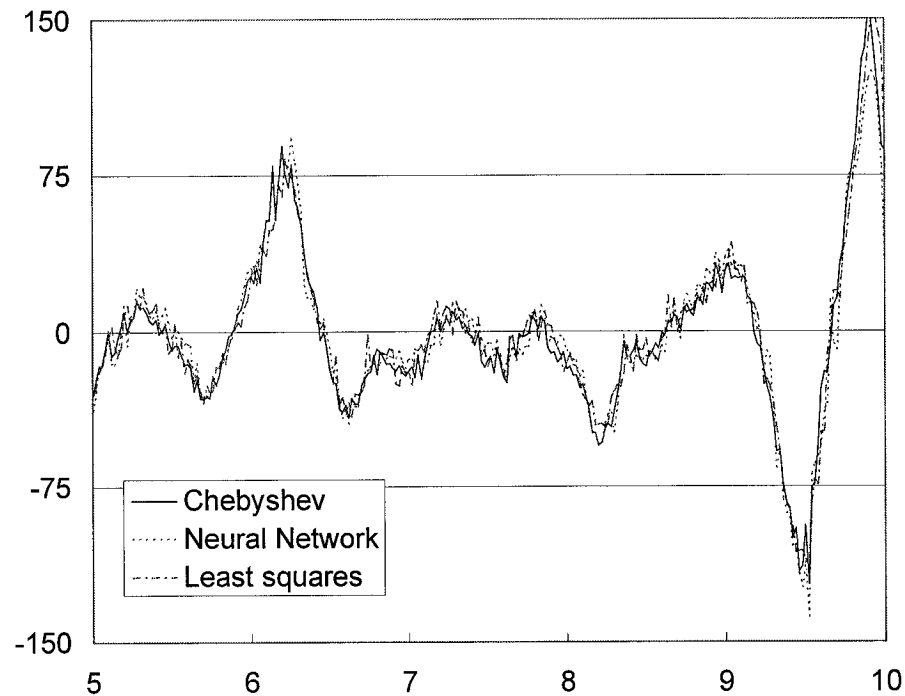
FIGURE 6.62. Identification algorithm comparison

Based on the results of these studies, the least squares recursive algorithm and restoring force method using Chebyshev polynomials provide the highest confidence levels in matching the system state variables. In-depth studies of these algorithms are presented in Sections 6.6.4.2, 6.6.4.3 and 6.6.4.4.

As the system parameters are tweaked to ascertain the sensitivity of the identification algorithms, it is possible that one algorithm may be more sensitive to certain system variations while another discriminates other system parameters more adeptly. In this event, decision level fusion techniques might yield the highest degree of confidence in identifying system degradation. Basically, this concept relies on evaluating the

137

output of multiple identification algorithms, and combining the results to determine the overall health of the system.

With the baseline cases developed for a random sample set, the parameters were varied beyond their acceptable performance ranges to determine threshold system identification sensitivity. The parameter variations in this analysis were first controlled to determine the identification algorithm sensitivities, then randomly varied about the revised degraded parameter means to further study the identification algorithms' robustness in quantifying the degradation. This process was repeated for various excitation signals and the results are plotted below.

6.6.1 Quantification and Propagation of Uncertainties in Linear/nonlinear Systems

A comprehensive Monte Carlo simulation was conducted to investigate the propagation of uncertainties in model structure, as well as parametric uncertainties, on the response of reduced-order nonparametric identification (NPI) system models. These simulations were performed on the Unix machine utilizing batch file capabilities to fully automate the studies. Known random perterbations of system parameters, individually, then collectively, yield some variability in the restoring force. These studies are crucial to the establishment of damage detection thresholds, as any physical system inherently incorporates some degree of variability. Examples

include manufactured products, where components are built within some prescribed

tolerance, and naturally occuring systems which are inherently random.

A measure of the percent error from the baseline case, defined with the system

parameters set to their mean values ($m=1$, $k=39.478$, $c=1.2566$), is quantified for

each parameter variation in Tables 6.3 and 6.4. This error in the identified system

parameter for the prescribed parameter variation is defined as

$$\varepsilon = \frac{(f^* - f^{(0)})}{f^{(0)}}$$
(6.40)

where f^* is the mean of the identified stiffness or damping from Chebyshev

polynomial coefficients for each simulation, and $f^{(0)}$ is the exact value of the system

stiffness or damping as computed from the reference case. Following similar

notation, the frequency changes resulting from perterbing the system parameters are

quantified as

$$\Delta\omega = \frac{(\omega^* - \omega^{(o)})}{\omega^{(0)}}$$
(6.41)

6.6.1.1. Linear model

For calibration purposes, initially these studies centered on linear models. A linear

sdof model was developed with 10% damping. This model was similar to that

discussed earlier; with a unit mass and period, and a natural frequency of 2π. With

these parameters, the system stiffness was 39.478, and the damping coefficient was

1.2566.

139

Parametric uncertainty analysis was studied by introducing randomness into the stiffness, mass, and damping parameters, then in combination. The parameters were randomized with a zero-mean unit variance Gaussian distribution. 5000 simulations of each model were investigated. Further uncertainties were introduced into the system by randomizing the excitation for each simulation. The seeds used to generate the random numbers were different for each parameter variation, to ensure uniqueness.

Noise pollution of 5% was added to study the NPI algorithm's ability to detect parametric variations under the constraint of measurement noise. Selected pdf curves detailing these studies are included in Figure 6.63. The dashed curves on Figure 6.63 and in the associated Appendices represent the noise polluted simulations, while the solid lines depict the perturbed system parameters in the absence of noise pollution. More encompassing data representation is included in the Appendices. Results of these studies are compiled and tabulated in Tables 6.3 through 6.5, depicting the cause and effect relationship of known parameter variation to the system restoring force. The left column of plots in Figure 6.63 depicts the distribution of NPI Chebyshev coefficients C(1,2), and the right column depicts the C(2,1) coefficients.

140

Case #	Noise Pollution level %	Changes relative to original model parameters
1	0	None (reference case)
2	0	mass normally distributed ($\mu = 1$, $\sigma = 0.05$)
3	0	stiffness normally distributed ($\mu = 1$, $\sigma = 0.05$)
4	0	damping normally distributed ($\mu = 1$, $\sigma = 0.05$)
5	0	all normally distributed ($\mu = 1$, $\sigma = 0.05$)
6	5	None (reference case)
7	5	mass normally distributed ($\mu = 1$, $\sigma = 0.05$)
8	5	stiffness normally distributed ($\mu = 1$, $\sigma = 0.05$)
9	5	damping normally distributed ($\mu = 1$, $\sigma = 0.05$)
10	5	all normally distributed ($\mu = 1$, $\sigma = 0.05$)

TABLE 6.3. Summary of linear sdof simulation cases

	Case 1	Case 2	Case 3	Case 4	Case 5
m^*	1	1.0007435	1	1	1.0007435
$k^{(0)}$	39.478	39.478	39.47845	39.478	39.47845
k^*	---	41.03719	40.86992	40.94081	41.00218
ε_k	---	0.039495	0.035246	0.037054	0.038597
ω^*	6.283152	6.403648	6.392959	6.398501	6.400916
$\Delta\omega$	---	0.019178	0.017476	0.018358	0.018743
$c^{(0)}$	1.2566	1.2566	1.2566	1.254344	1.254344
c^*	---	1.329195	1.351043	1.321912	1.331494
ε_c	---	0.057771	0.075158	0.053867	0.061506

TABLE 6.4. Linear sdof identification results w/o noise pollution

	Case 6	Case 7	Case 8	Case 9	Case 10
m^*	1	1.0007435	1	1	1.0007435
$k^{(0)}$	39.478	39.478	39.47845	39.478	39.47845
k^*	---	40.95554	40.63259	40.92315	40.89848
ε_k	---	0.037427	0.029235	0.036606	0.03597
ω^*	6.283152	6.397274	6.37437	6.39712	6.392816
$\Delta\omega$	---	0.018163	0.014518	0.018139	0.017454
$c^{(0)}$	1.2566	1.2566	1.2566	1.254344	1.254344
c^*	---	1.48166	1.470834	1.494487	1.494749
ε_c	---	0.179102	0.170487	0.191449	0.191658

TABLE 6.5. Linear sdof identification results w/noise pollution

141
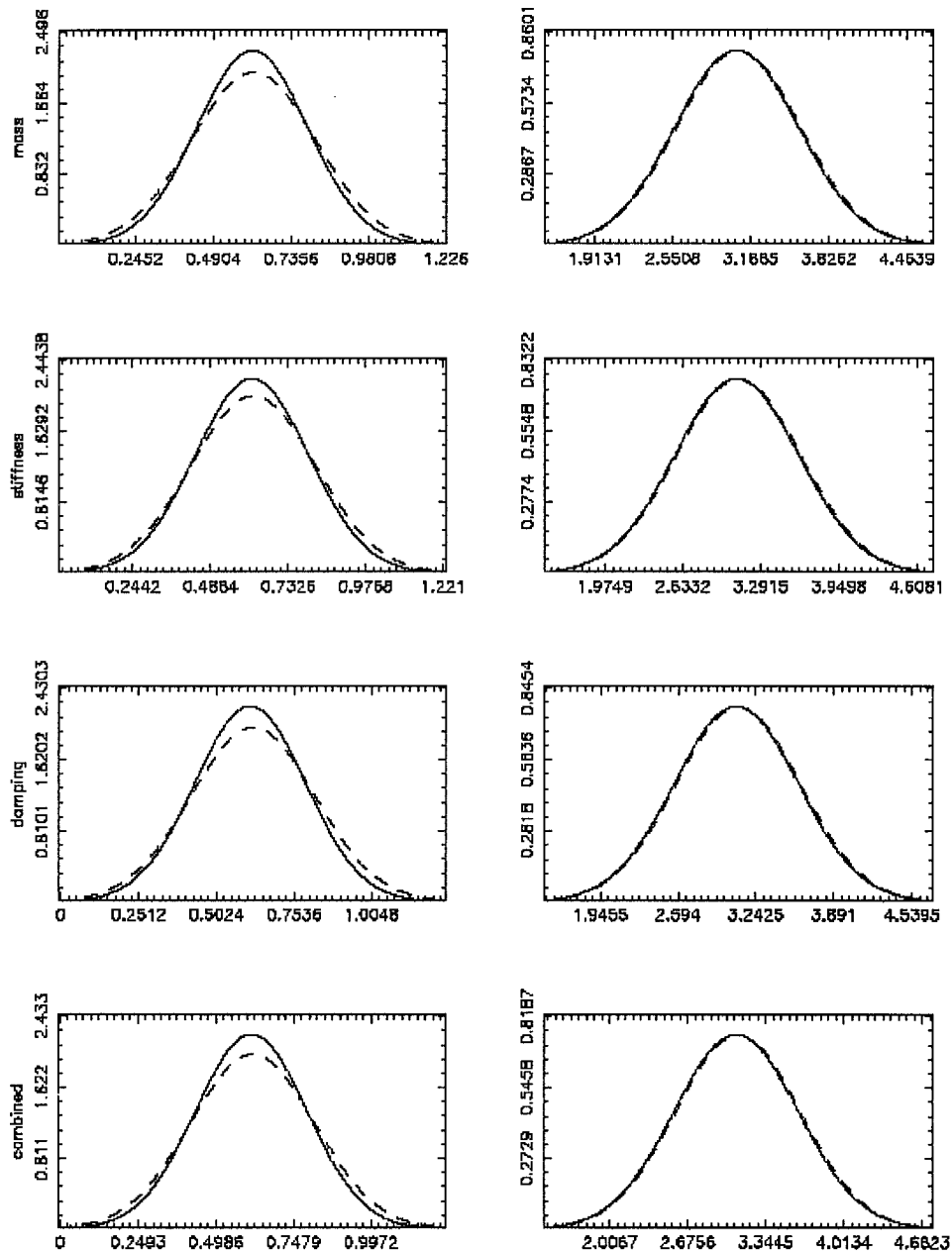
FIGURE 6.63. Linear oscillator, noise-free and noise-polluted data
(- = w/o noise, -- = 5% noise pollution)

142

It is important to note that the pdf results depicted in Figure 6.63 statistically tend towards Gaussian distributions for large sample sizes. This fact follows intuition and confirms the central tendency theorem (Kreysig, 1993). Recall that the parameter variation was normally distributed, as was the stationary random excitation. Since the system model under investigation is linear, a second order Chebyshev representation is adequate to accurately emulate its behavior. A Chebyshev model with sixteen coefficients was assumed. Thus, in many of the Appendices, the computed means of coefficients C(1,2) and C(2,1) are the only two that vary substantially from zero. A review of the transformation to a Power Series representation reveals that these two parameters are primary contributors to the system damping and stiffness parameters, respectively. This transformation is discussed in greater detail in a later section.

It can be seen from Figure 6.63 that a random perterbation of the system parameters with noise pollution assumed at 5% does not appreciably degrade the NPI Chebyshev identification results. These results establish the variance or variability of a large sample set from a sdof system with quantifiable parameter uncertainties, excited by a stationary random signal. Again, for the linear case, only two parameters are necessary to completely quantify the system behavior.

6.6.1.2. Nonlinear model

The next phase investigated nonlinear models. One such model reviewed was a Duffing oscillator. The Duffing oscillator parameters were established as $m=1$,

k=39.478, c=1.2566, and ε=11.23. To truly study the effect of the nonlinear term, ε, a measure of the level of nonlinearity was formulated as

$$\varepsilon_r = \frac{\varepsilon_0 \, x_{max}^3}{k_0 \, x_{max}} \tag{6.42}$$

such that ε_r=1 resulted in a near equal contribution of the linear system stiffness and the nonlinear term. As k and ε were previously defined for the Duffing oscillator, the level of stationary excitation was varied to affect x_{max}. An iterative approach revealed that when the stationary excitation amplitude was 33, x_{max}=1.89, yielding ε_r=1.02. The contribution of the stiffness and Duffing nonlinear terms were 74.6 and 75.8, respectively. Next, validation of the nonlinear solution was verified by halving the integration step size from 0.0025 to 0.00125. System response values were nearly identical to those previously reported, with larger integration step sizes, as expected for a stable solution. Once again, selected pdf curves detailing these studies are included in Figure 6.64, with more details included in the Appendices. The cause/effect relationship of the prescribed parameter variation to the system restoring force is depicted in Tables 6.6 through 6.8.

144
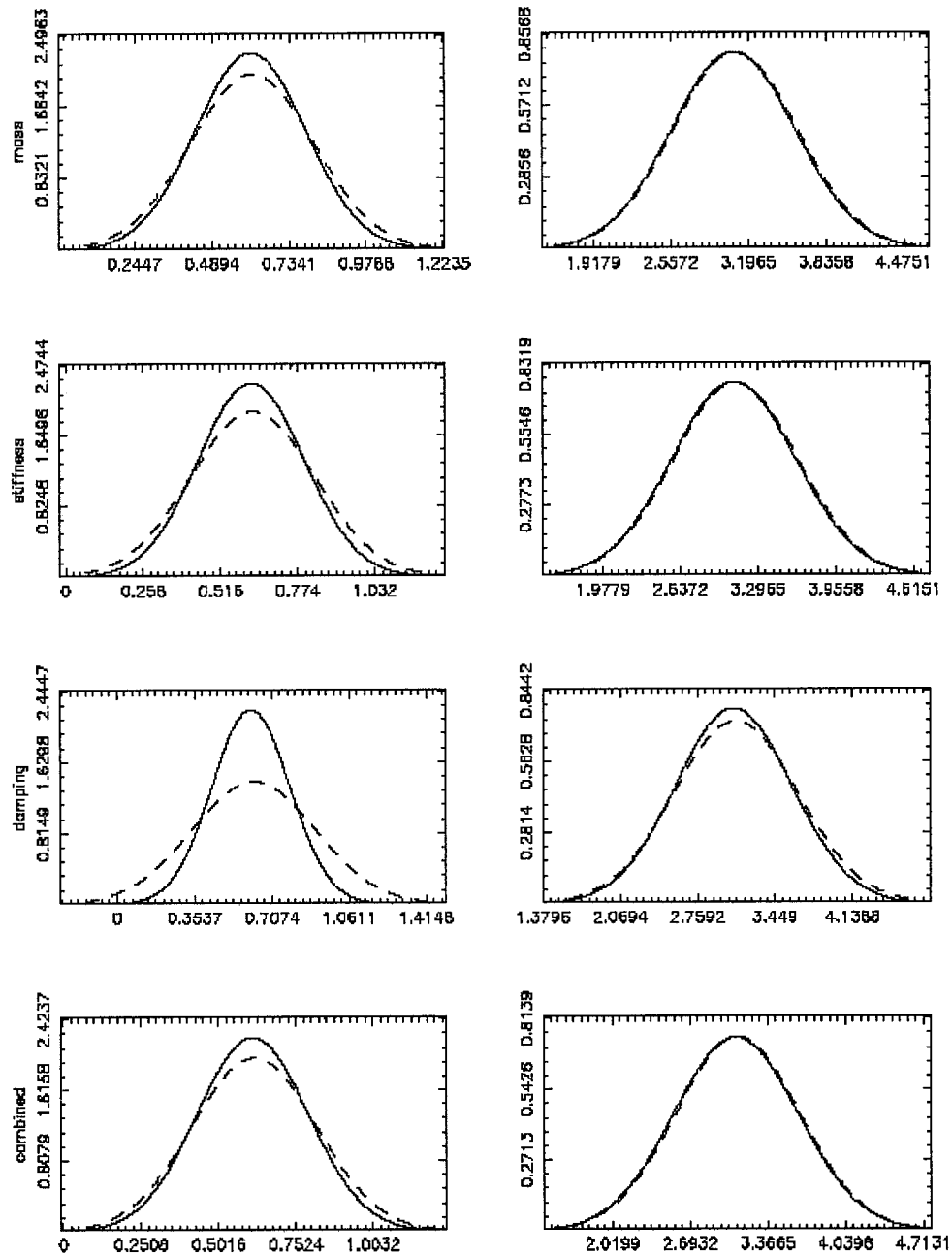
FIGURE 6.64. Duffing oscillator, noise-free and noise-polluted data
(- = w/o noise, -- = 5% noise pollution)

145

Case #	Noise Pollution level %	Changes relative to original model parameters
1	0	None (reference case)
2	0	mass normally distributed ($\mu = 1$, $\sigma = 0.05$)
3	0	stiffness normally distributed ($\mu = 1$, $\sigma = 0.05$)
4	0	damping normally distributed ($\mu = 1$, $\sigma = 0.05$)
5	0	epsilon normally distributed ($\varepsilon = 1$, $s = 0.05$)
6	0	all normally distributed ($\mu = 1$, $\sigma = 0.05$)
7	5	None (reference case)
8	5	mass normally distributed ($\mu = 1$, $\sigma = 0.05$)
9	5	stiffness normally distributed ($\mu = 1$, $\sigma = 0.05$)
10	5	damping normally distributed ($\mu = 1$, $\sigma = 0.05$)
11	5	epsilon normally distributed ($\varepsilon = 1$, $s = 0.05$)
12	5	all normally distributed ($\mu = 1$, $\sigma = 0.05$)

TABLE 6.6. Summary of Duffing oscillator sdof simulation cases

	Case 1	Case 2	Case 3	Case 4	Case 5	Case 6
m	1	1.0007435	1	1	1	1.0007435
$k^{(0)}$	39.478	39.478	39.47845	39.478	39.478	39.47845
k	---	41.02134	40.93922	40.90954	40.94738	40.98318
ε_k	---	0.039094	0.037002	0.036262	0.03722	0.038115
ω^*	6.283152	6.402411	6.398376	6.396057	6.399014	6.399432
$\Delta\omega$	---	0.018981	0.018339	0.017969	0.01844	0.018507
$c^{(0)}$	1.2566	1.2566	1.2566	1.254344	1.2566	1.254344
c	---	1.332604	1.320576	1.324866	1.353308	1.321661
ε_c	---	0.060484	0.050912	0.056222	0.07696	0.053667

TABLE 6.7. Duffing oscillator sdof identification results w/o noise pollution

Similar to the presentation of Figure 6.63, the left column of plots in Figure 6.64

depicts the distribution of NPI Chebyshev coefficients C(1,2), and the right column

depicts the C(2,1) coefficients. As seen in the linear case, the Monte-Carlo results

plotted tend to a Gaussian norm. However, in the nonlinear case, a higher order

Chebyshev representation is necessary to fully quantify the system behavior. Also,

the robustness of the NPI Chebyshev identification algorithm discriminates 5%

noise-polluted data nearly equally as well as the reference cases without noise.

146

	Case 7	Case 8	Case 9	Case 10	Case 11	Case 12
m	1	1.0007435	1	1	1	1.0007435
$k^{(0)}$	39.478	39.478	39.47845	39.478	39.478	39.47845
k	---	40.87501	40.90121	41.64627	40.86564	40.885
ε_k	---	0.035387	0.036039	0.054923	0.03515	0.035628
ω^*	6.283152	6.390981	6.395405	6.453392	6.392624	6.391762
$\Delta\omega$	---	0.017162	0.017866	0.027095	0.017423	0.017286
$c^{(0)}$	1.2566	1.2566	1.2566	1.254344	1.2566	1.254344
c	---	1.478855	1.519603	1.651211	1.493506	1.465099
ε_c	---	0.17687	0.209298	0.316394	0.188529	0.16802

TABLE 6.8. Duffing oscillator sdof identification results w/noise pollution

6.6.2. Investigation of System Parameter Uncertainty

More intensive, high-resolution simulation studies of the sdof system were performed by varying the system parameters, individually, then collectively. Noise pollution effects were also included in this analysis. A Monte Carlo approach was utilized to quantify the effects of varying the system parameters. This enabled establishment of identification results under system parameter uncertainty or variability.

Initially, 5000 simulations were performed. The resulting data sets were then plotted to ascertain the required number of simulations for ergodicity. Superposing Gaussian curves derived from pdf analysis of the varying length data sets with identical means and variances indicates that only 3000 simulations are necessary to achieve reasonably accurate statistical results. These results are plotted in Figures 6.65 and 6.66 below for the first eight Chebyshev coefficients. The solid line in each

147

of the plots in Figures 6.65 and 6.66 represents the pdf derived from 5000 simulations as a comparison baseline. The data was retrieved from the same output file, simply varying the number of simulations processed.

A review of these figures reveals that most of the Chebyshev coefficients are centered about zero. This is expected for a linear system. In fact, coefficients $C(1,2)$ and $C(2,1)$ deviate the most from zero, being the primary representations of the system damping and stiffness coefficients, respectively.

As the response of the sdof damped system is most susceptible to variations in the system stiffness, a detailed analysis was concentrated on this parameter. This is because the contribution of the stiffness term is greatest in the restoring force representation of the system. The stiffness parameter was varied normally by 1, 2, 3, 5, 7, 10, 15, 20 and 25 percent standard deviation from the prescribed mean. This uncertainty analysis attempts to quantify the variance expected in manufactured dampers and evaluate the reliability of the identification algorithms.

Measurement uncertainty was investigated by introducing known stiffness and damping parameter degradation, then applying varying levels of normally distributed random noise. As before, the noise was additive as an epsilon error to the system variables. Mean values of the applied noise were 1, 5, 10 and 20% of the system excitation.

148
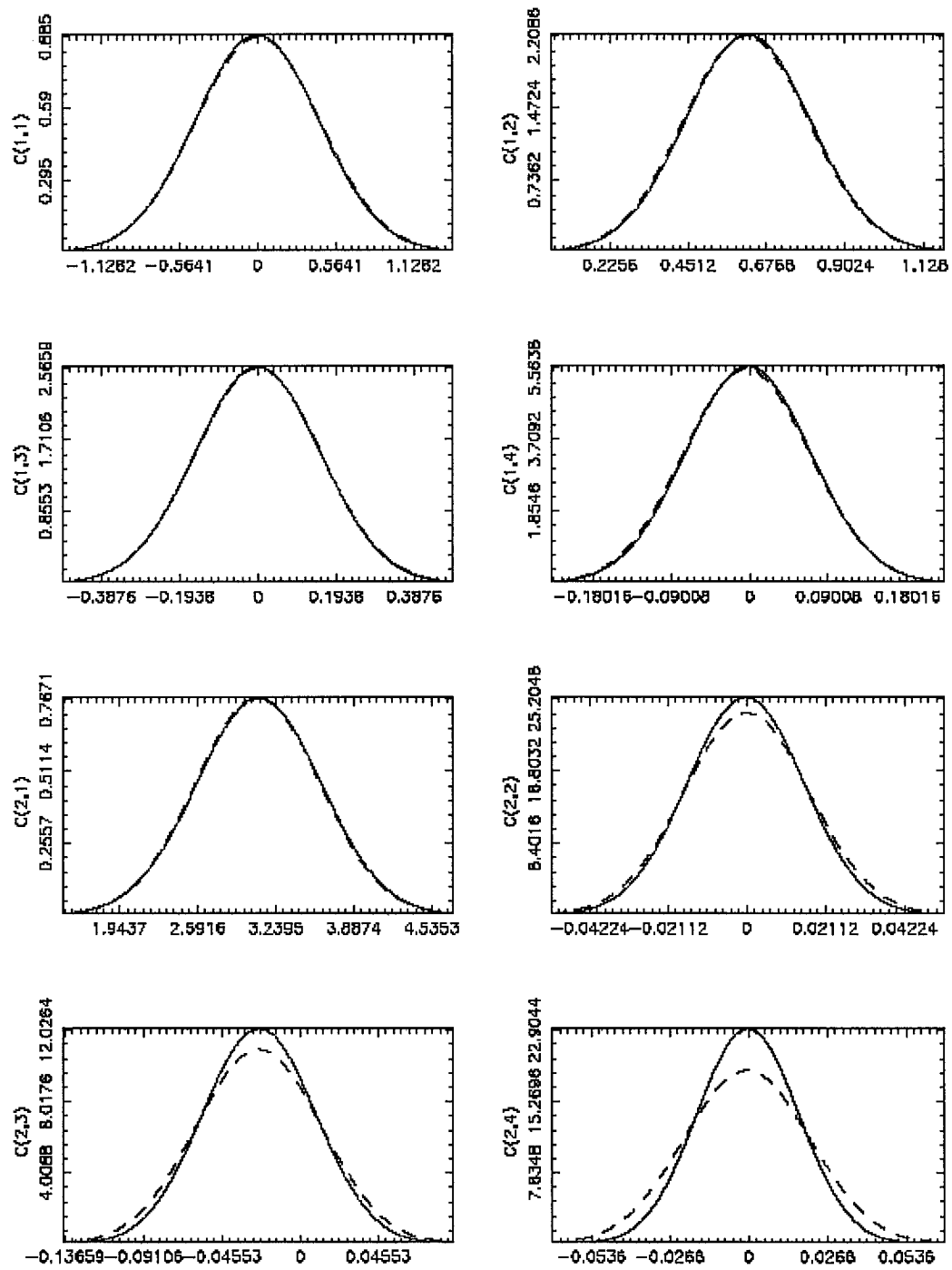
FIGURE 6.65. 1000 simulations versus 5000 simulations
(- = w/o noise, -- = 5% noise pollution)

149
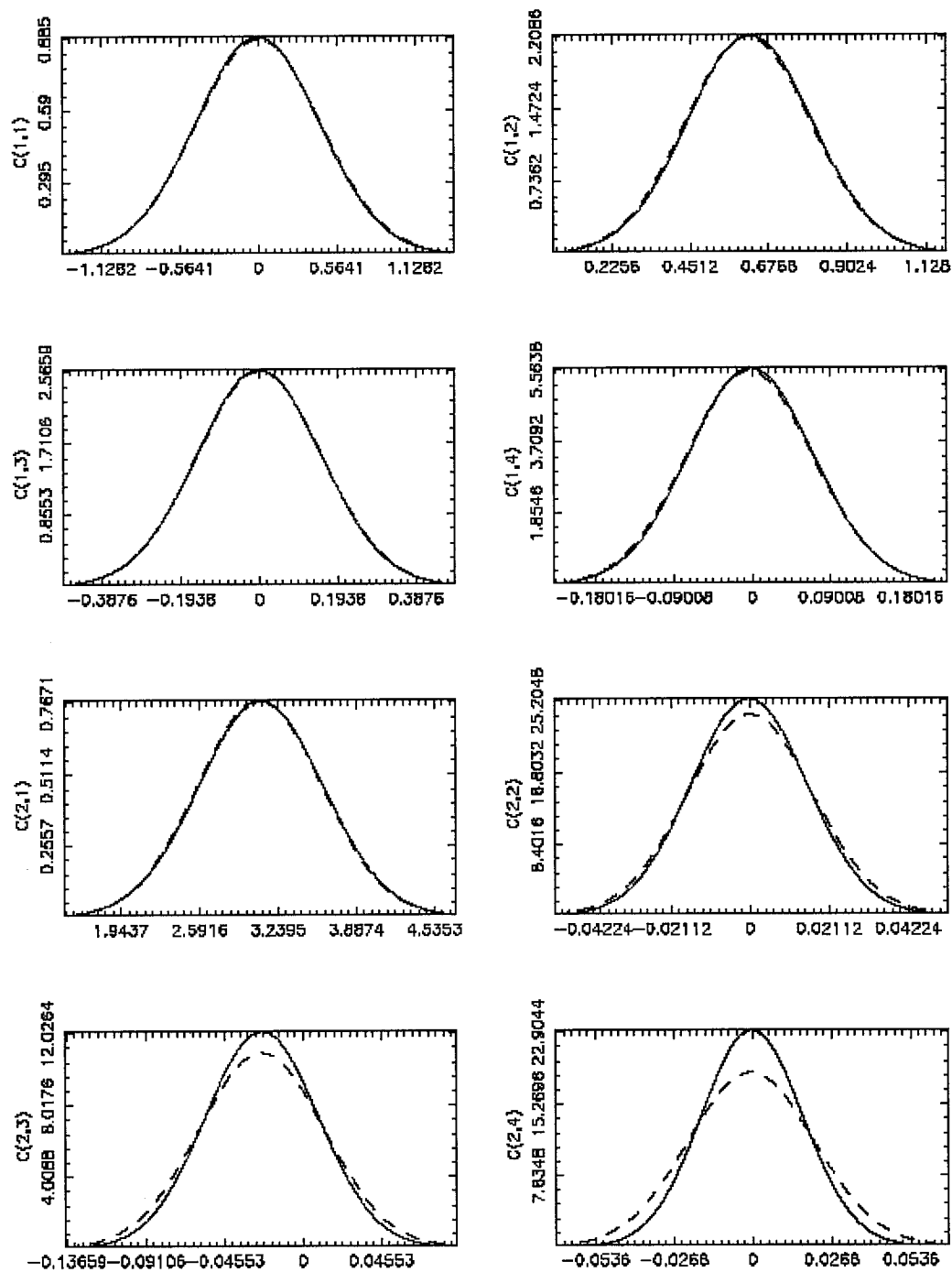
FIGURE 6.66. 3000 simulations versus 5000 simulations
(- = w/o noise, -- = 5% noise pollution)

It is important to note that in the limiting case, the linear model with constant defining parameters yields identical identification results when a normally distributed random excitation is fed to the system. This result is expected and further validates the model.

The results of this study are condensed in Figures 6.67 and 6.68. The left column of plots in both figures depict the distribution of NPI Chebyshev coefficient C(1,2), and the right column displays the distribution of Chebyshev coefficient C(2,1). These Chebyshev coefficients are primary contributors to the system stiffness and damping parameters in the conversion from the Chebyshev restoring force representation to the Power Series representation, which is discussed in detail later. Variations in the stiffness parameter of 1, 2, 3, 5 and 7% are included in Figure 6.67. Figure 6.68 includes plots with the stiffness parameter varied normally by 1, 5, 10, 15 and 20%. Each plot includes varying levels of noise pollution. There are four curves in each plot; the solid line depicting 1% noise pollution, the dashed line representing 5% noise pollution, the dot-dashed line displaying the system with 10% noise pollution, and the dotted line depicting 20% noise pollution.

As depicted in Figures 6.67 and 6.68, the mean of the system stiffness and damping parameters identified with the restoring force method varies only slightly with increasing input system stiffness parameter variance. However, the distribution of the identified stiffness and damping parameters does increase with increased input

151

system stiffness variance. Additionally, it is clear from the plots that increasing system noise reduces the ability of the identification algorithm to correctly identify the stiffness and damping parameters. In general, the stiffness parameter can be reasonably identified even at 20% stiffness parameter variation. Even so, the damping parameter identification degrades substantially with only 5% measurement noise and at greater than 10% variation of the stiffness parameter. With measurement noise at 10% or greater, identification of the system damping parameter with the restoring force method degrades rapidly. This result follows intuition, as the damping component of the restoring force is much less than that of the stiffness for a linear sdof system. Hence, the damping parameter is much more susceptible to the effects of system noise than the stiffness parameter.

152
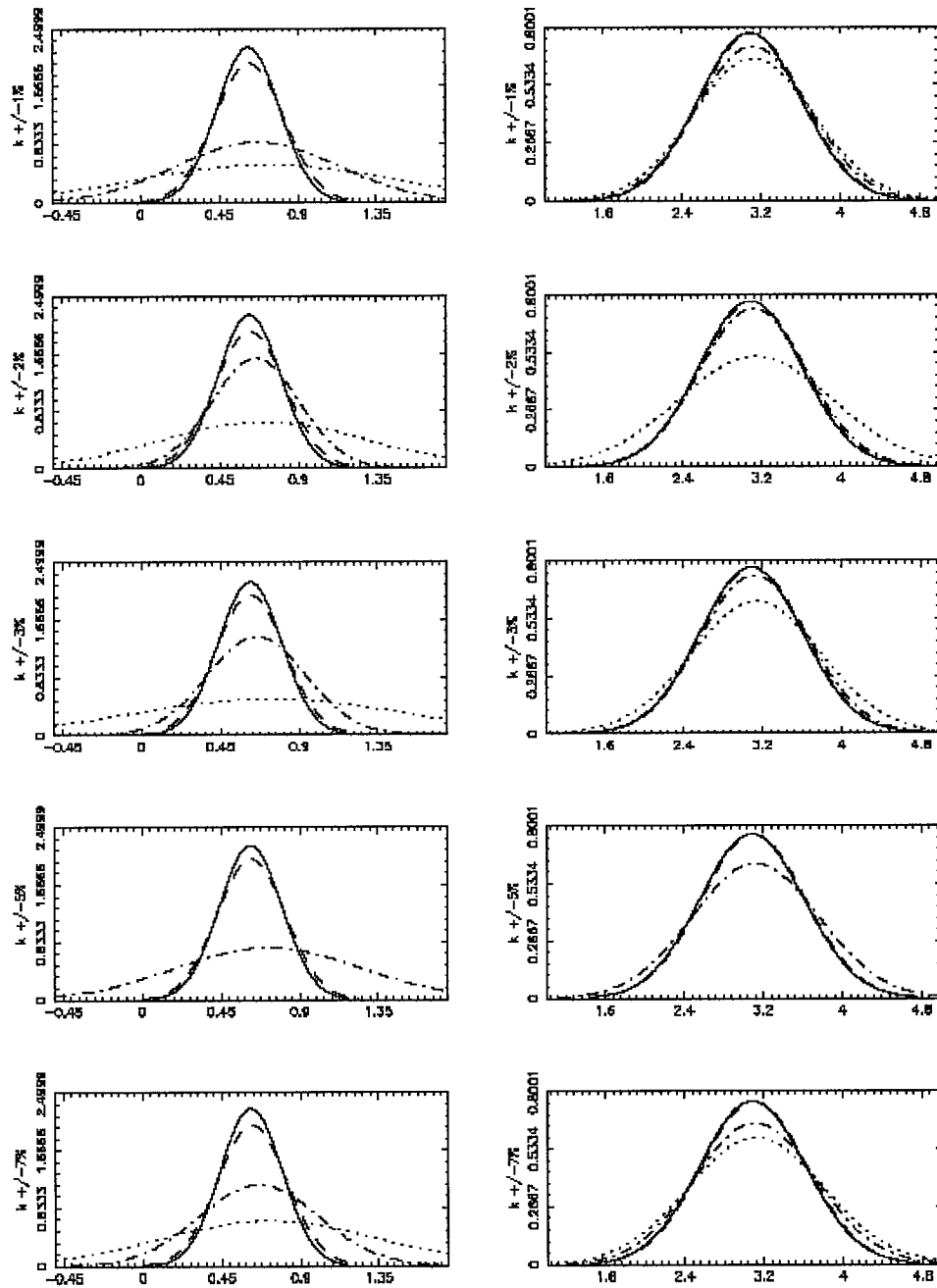
FIGURE 6.67. Measurement uncertainty, stiffness degraded with noise pollution
(- = w/o noise, -- = 5% noise pollution)

153
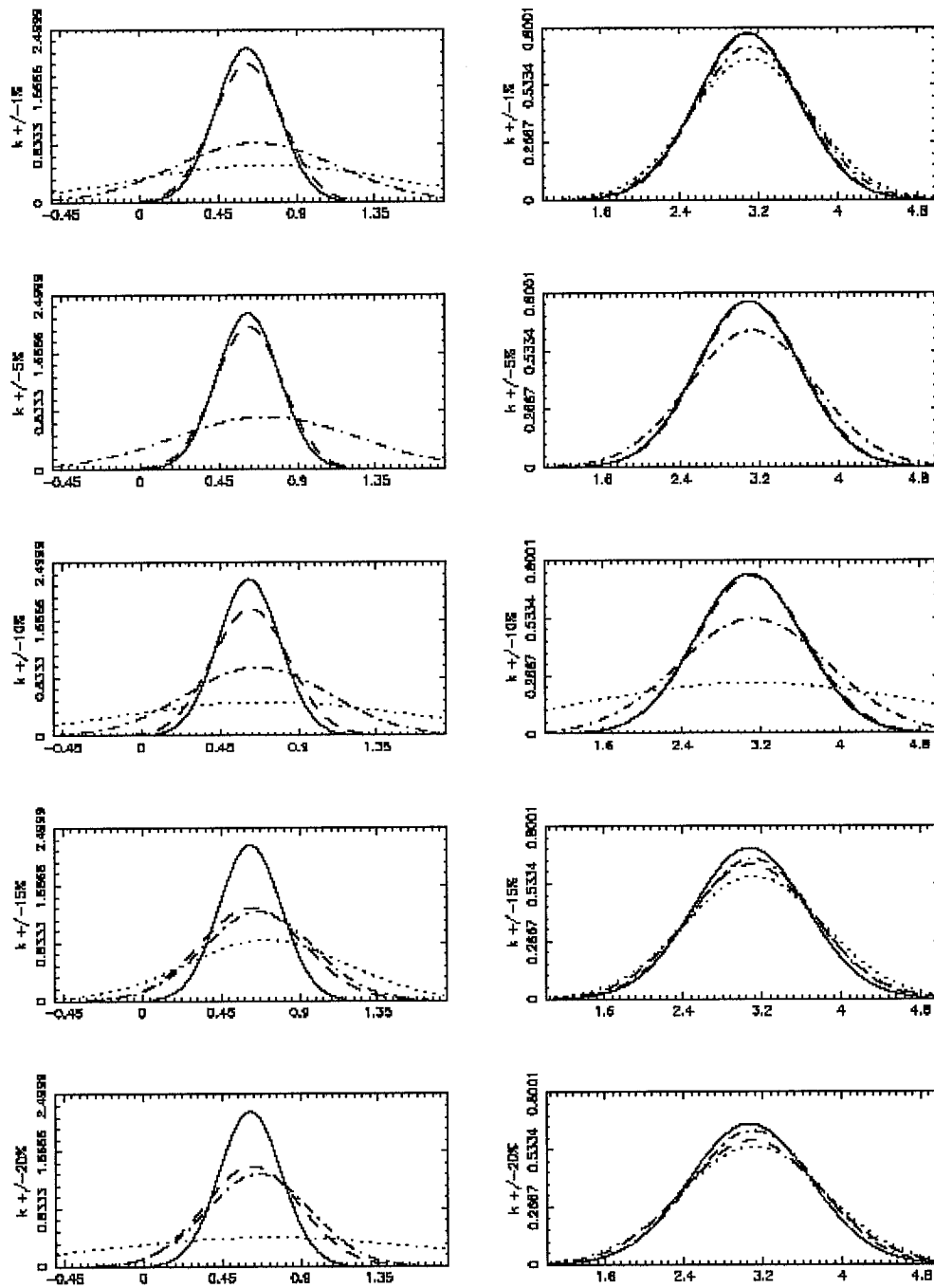
FIGURE 6.68. Measurement uncertainty, stiffness degraded with noise pollution
(- = w/o noise, -- = 5% noise pollution)

154

6.6.3. NPI Chebyshev to Power Series Restoring Force Equation

Representation

The NPI Chebyshev coefficients must be transformed to an equivalent Power Series representation to allow direct correlation of computed coefficients to the assumed physical system. While cumbersome, this transformation is fairly straightforward. Following the presentation in Masri and Caughey [1], the estimated restoring force is expressed in terms of two-dimensional orthogonal polynomials as

$$\hat{f}(x,\dot{x}) = \sum_{i=1}^{m}\sum_{j=1}^{n} C_{ij} T_{i-1}(x') T_{j-1}(\dot{x}') \tag{6.43}$$

where the T's are chosen as Chebyshev polynomials for their equal-error approximation within the interval of interest. The Chebyshev polynomials are defined as

$$T_n(\xi) = \cos(n\cos^{-1}\xi) \qquad -1 \le \xi \le 1 \tag{6.44}$$

satisfying the weighted orthogonality property

$$\int_{-1}^{1} \frac{T_n(\xi)T_m(\xi)d\xi}{\sqrt{1-\xi^2}} = \begin{cases} 0 & n \ne m \\ \pi/2 & n = m \ne 0 \\ \pi & n = m = 0 \end{cases} \tag{6.45}$$

The normalized displacement and velocity values are defined as

$$\begin{aligned} x' &= [x - (x_{max} + x_{min})/2]/[(x_{max} - x_{min})/2] \\ \dot{x}' &= [\dot{x} - (\dot{x}_{max} + \dot{x}_{min})/2]/[(\dot{x}_{max} - \dot{x}_{min})/2] \end{aligned} \tag{6.46}$$

The identification simulations yield the normalized Chebyshev coefficients. In order to evaluate the accuracy of the identified coefficients, a power series expansion of

155

the estimated restoring force surface described in equation (6.43) must be performed. This expansion yields

$$
\begin{aligned}
\hat{f}(x,\dot{x}) = {} & (C_{11} - C_{13} - C_{31} + C_{33}) + (C_{21} - C_{23} - 3C_{41} + 3C_{43})x' \\
& + (C_{12} - 3C_{14} - C_{32} + 3C_{34})\dot{x}' + (2C_{31} - 2C_{33})x'^2 \\
& + (2C_{13} - 2C_{33})\dot{x}'^2 + (C_{22} - 3C_{24} - 3C_{42} + 9C_{44})x'\dot{x}' \\
& + (4C_{14} - 4C_{34})\dot{x}'^3 + (4C_{41} - 4C_{43})x'^3 + (2C_{32} - 6C_{34})x'^2\dot{x}' \\
& + (2C_{23} - 6C_{43})x'\dot{x}'^2 + (4C_{24} - 12C_{44})x'\dot{x}'^3 \\
& + (4C_{42} - 12C_{44})x'^3\dot{x}' + (4C_{33})x'^2\dot{x}'^2 + (8C_{34})x'^2\dot{x}'^3 \\
& + (8C_{43})x'^3\dot{x}'^2 + (16C_{44})x'^3\dot{x}'^3
\end{aligned}
\qquad (6.47)
$$

Finally, replacing all occurrences of x' *and* $\dot{x}'$ with the definition in equation (6.46) denormalizes equation (6.47). Completing this and combining like terms yields the denormalized power series expansion of the estimated restoring force. It can be seen from equation (6.47) that several coefficients contribute to the stiffness and damping terms. A detailed conversion was performed using Mathematica®, and is included in the Appendices.

6.6.4. Investigation of System Damage Detection Methodology

Next, the damage detection methodology was investigated. The purpose was to identify and analyze the impact of stiffness and damping parameters. Various levels of degradation or enhancement of each were tested. Additionally, noise pollution effects were assessed. The results for both linear and nonlinear tests are presented in the following pages.

156

6.6.4.1 Linear model

First, the nominal stiffness parameter of 39.478 was reduced by fixed percentages of 1, 5, 10 and 25%. Solutions for each case were computed; and, the identification results for the stiffness and damping parameters were verified. Then, various levels of damping degradation and enhancement were analyzed. Finally, combinations of stiffness and damping parameter variations were investigated. Noise pollution levels were added to further evaluate the identification algorithm. Plots of the Chebyshev coefficient degraded states for stiffness only, damping only and their various combinations are given in Figures 6.69 through 6.73, respectively.

In each of Figures 6.69 through 6.73, the first column of plots represents the Chebyshev coefficient C(1,2); the second column represents C(2,1). Each plot also presents four curves, depicting the 1, 5, 10 and 20% noise pollution simulations introduced earlier in Figure 6.67.

Figure 6.69 incorporates five rows of plots, labeled *a* through *e*. The two plots in row *a* depict the Monte Carlo results of the undamaged system state. Those in rows *b* through *e* represent Monte Carlo system simulations with 1, 5, 10 and 25% stiffness degradation.

Figures 6.70 and 6.71 present only four rows of plots, as the undamaged system is already displayed in the first row of Figure 6.69. Rows *a* through *d* in Figure 6.70

157

depict Monte Carlo system simulations with 1, 5, 10 and 25% damping parameter degradation. Figure 6.71 follows the description for Figure 6.70, <u>except</u> that the damping parameter is enhanced rather than degraded by 1, 5, 10 and 25%; the attendant plots are shown in rows *a* through *d*, respectively.

Only three rows of plots are included in Figures 6.72 and 6.73. Rows *a* through *c* in Figure 6.72 display the combined stiffness and damping parameter reductions of 1, 5 and 10%. Alternatively, in Figure 6.73, the first row depicts a 1% degradation in the stiffness parameter degradation and a 1% enhancement of the damping parameter enhancement. The second row represents a stiffness parameter degradation of 5% and a damping parameter enhancement of 5%. The last row includes degradation of the stiffness parameter by 10%, coupled with a 10% damping parameter enhancement.

158
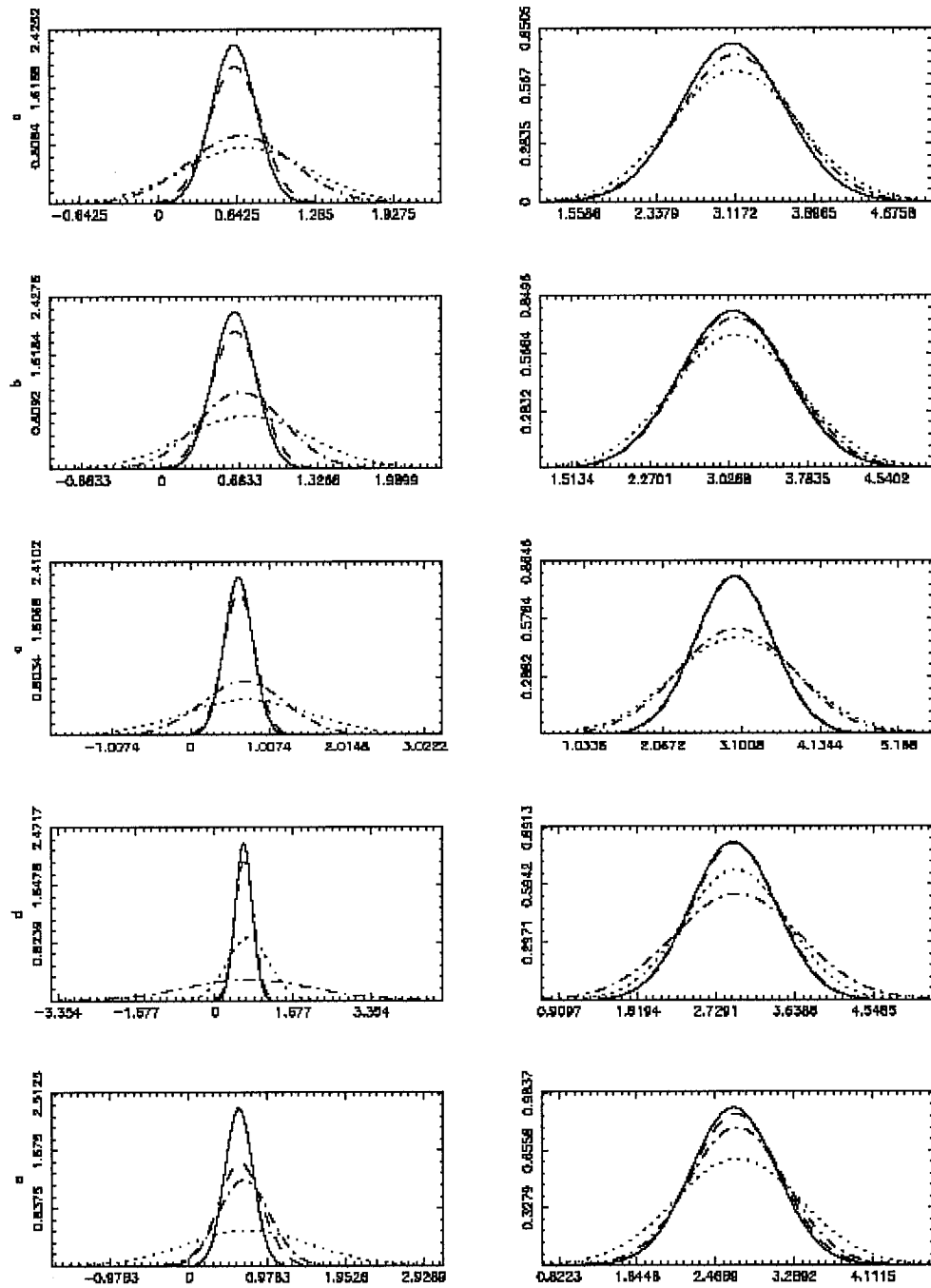
FIGURE 6.69. Chebyshev coefficients, C(1,2) and C(2,1), stiffness parameter reduction (- = 1%, -- = 5%, .- = 10%, . = 20% noise pollution)

159
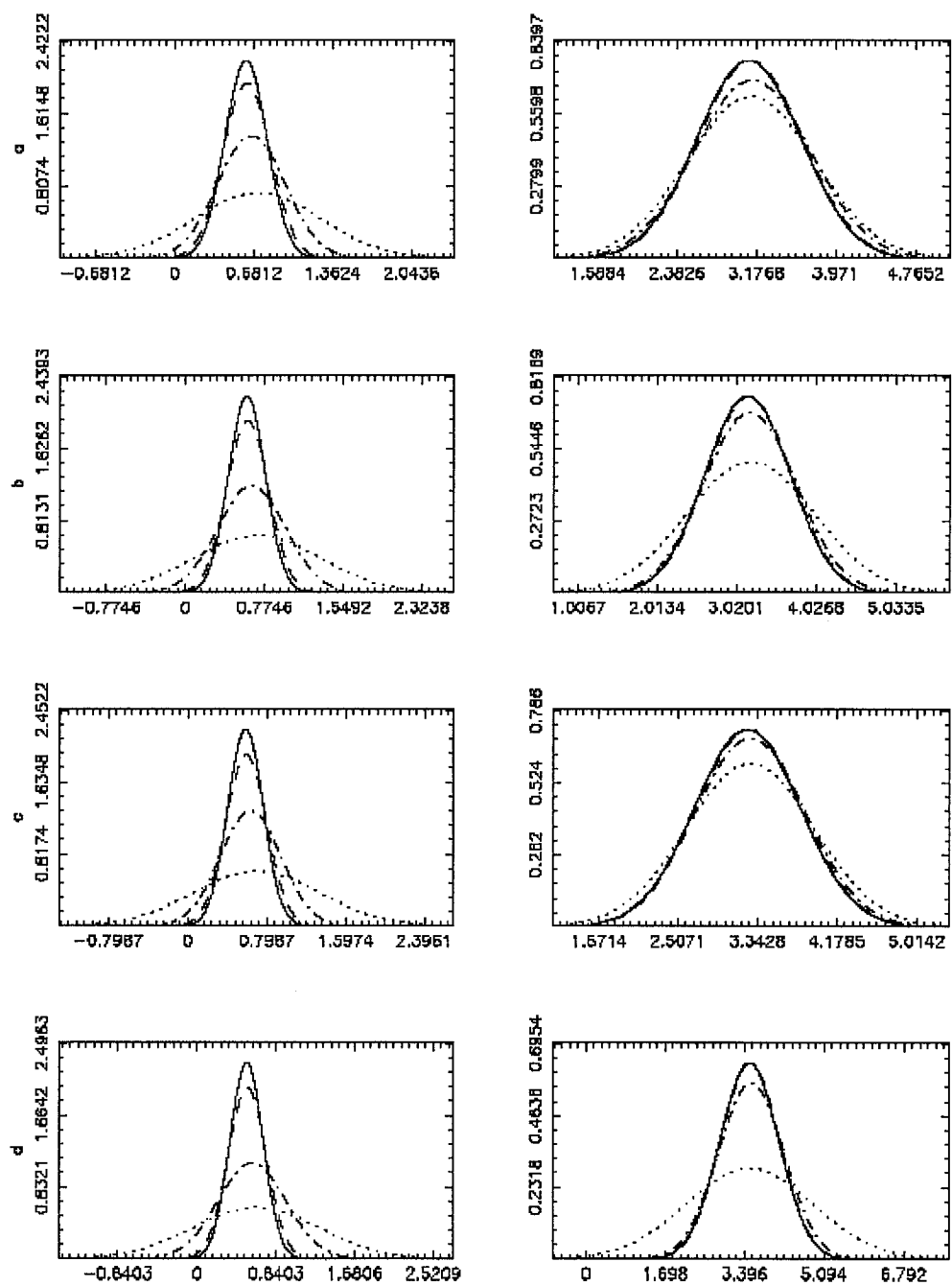
FIGURE 6.70. Chebyshev coefficients, C(1,2) and C(2,1), damping parameter reduction (- = 1%, -- = 5%, .- = 10%, . = 20% noise pollution)

160
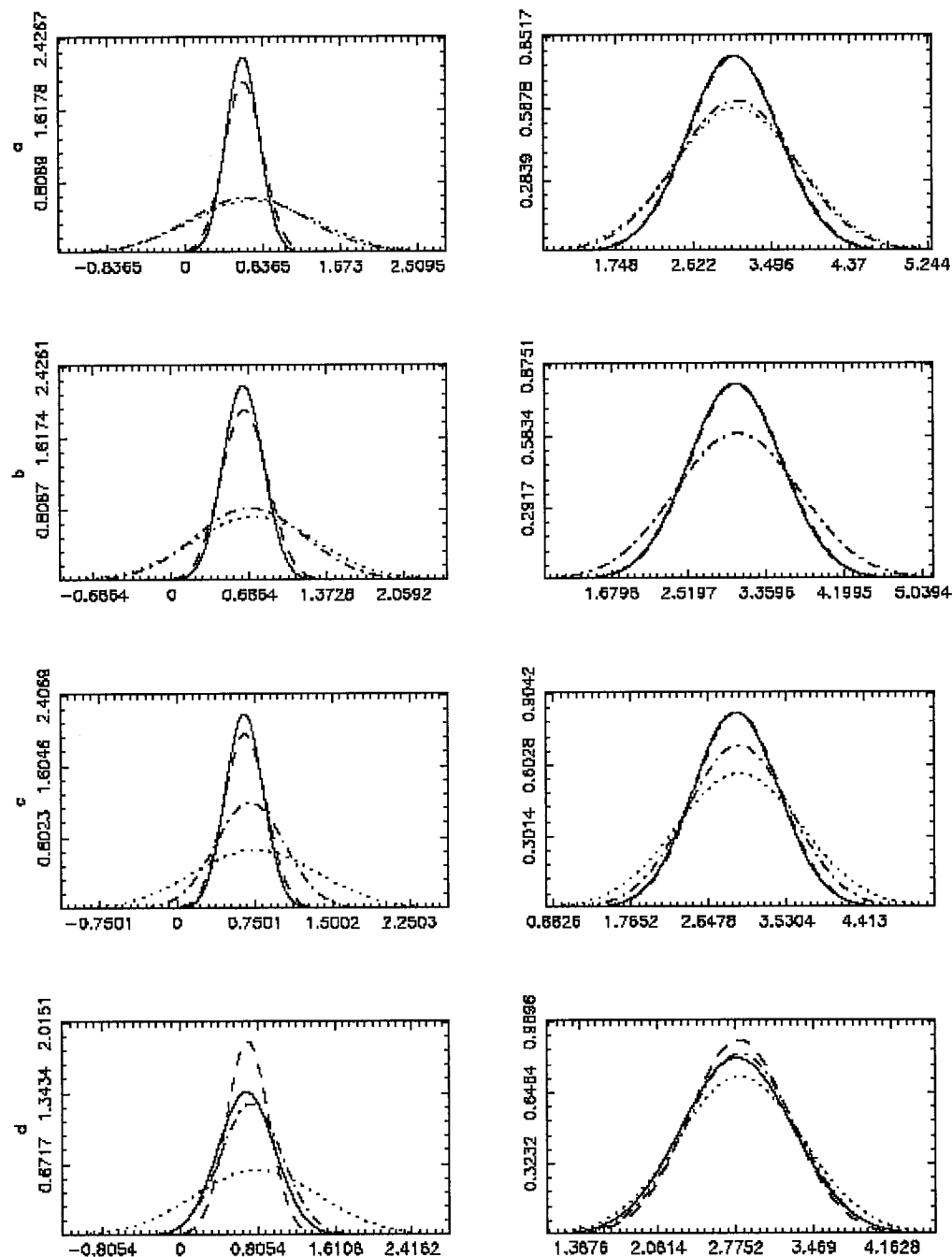
FIGURE 6.71. Chebyshev coefficients, C(1,2) and C(2,1), damping parameter enhancement (- = 1%, -- = 5%, .- = 10%, . = 20% noise pollution)

161
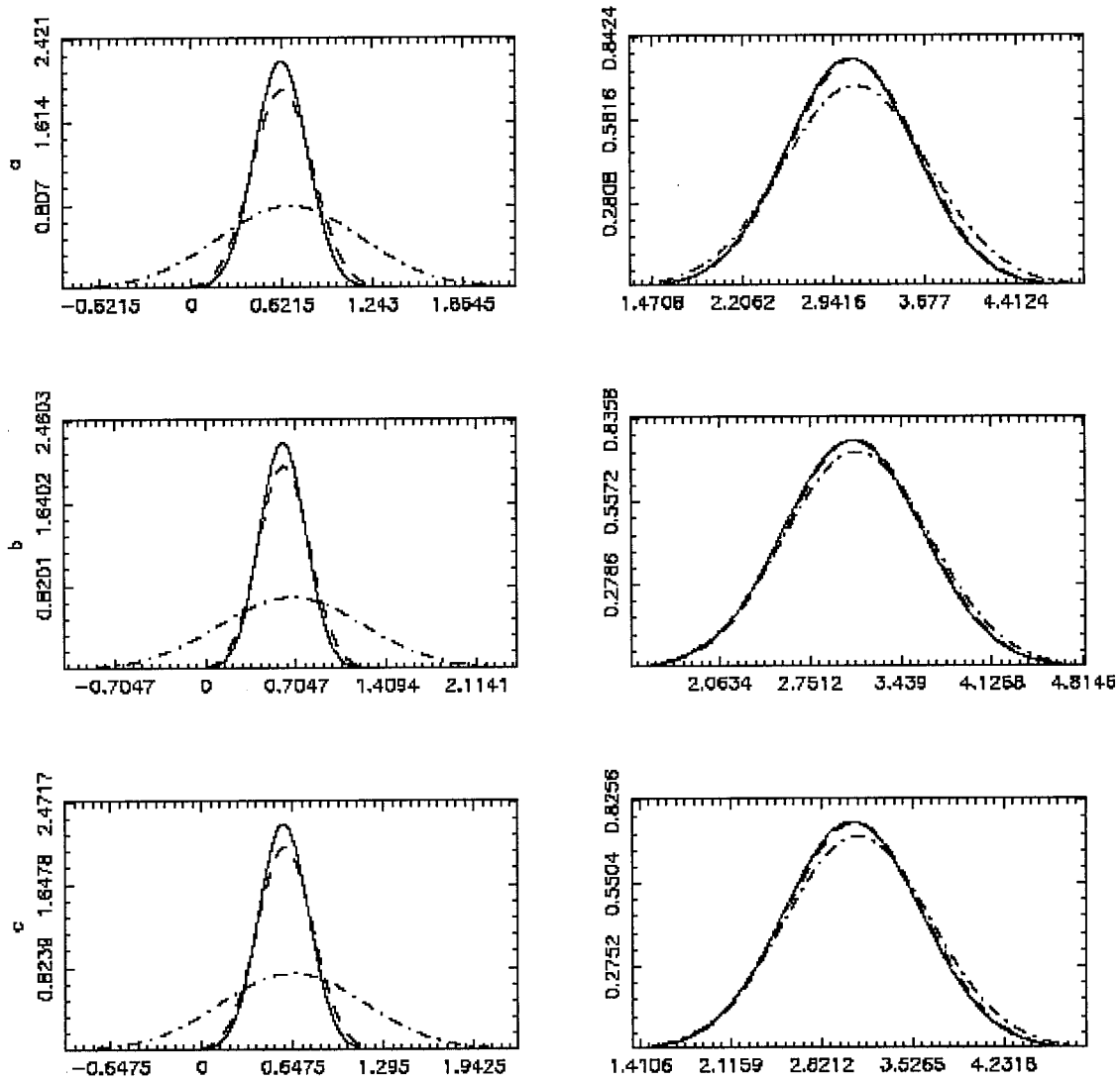
FIGURE 6.72. Chebyshev coefficients, C(1,2) and C(2,1), combined stiffness and damping parameter reduction (- = 1%, -- = 5%, .- = 10%, . = 20% noise pollution)

162

Clearly, the data represented in Figures 6.69 through 6.73 reveal that increasing

noise pollution levels to 20% reduces the identification algorithm's ability to

successfully detect the system state variables consistently over a large sample set.
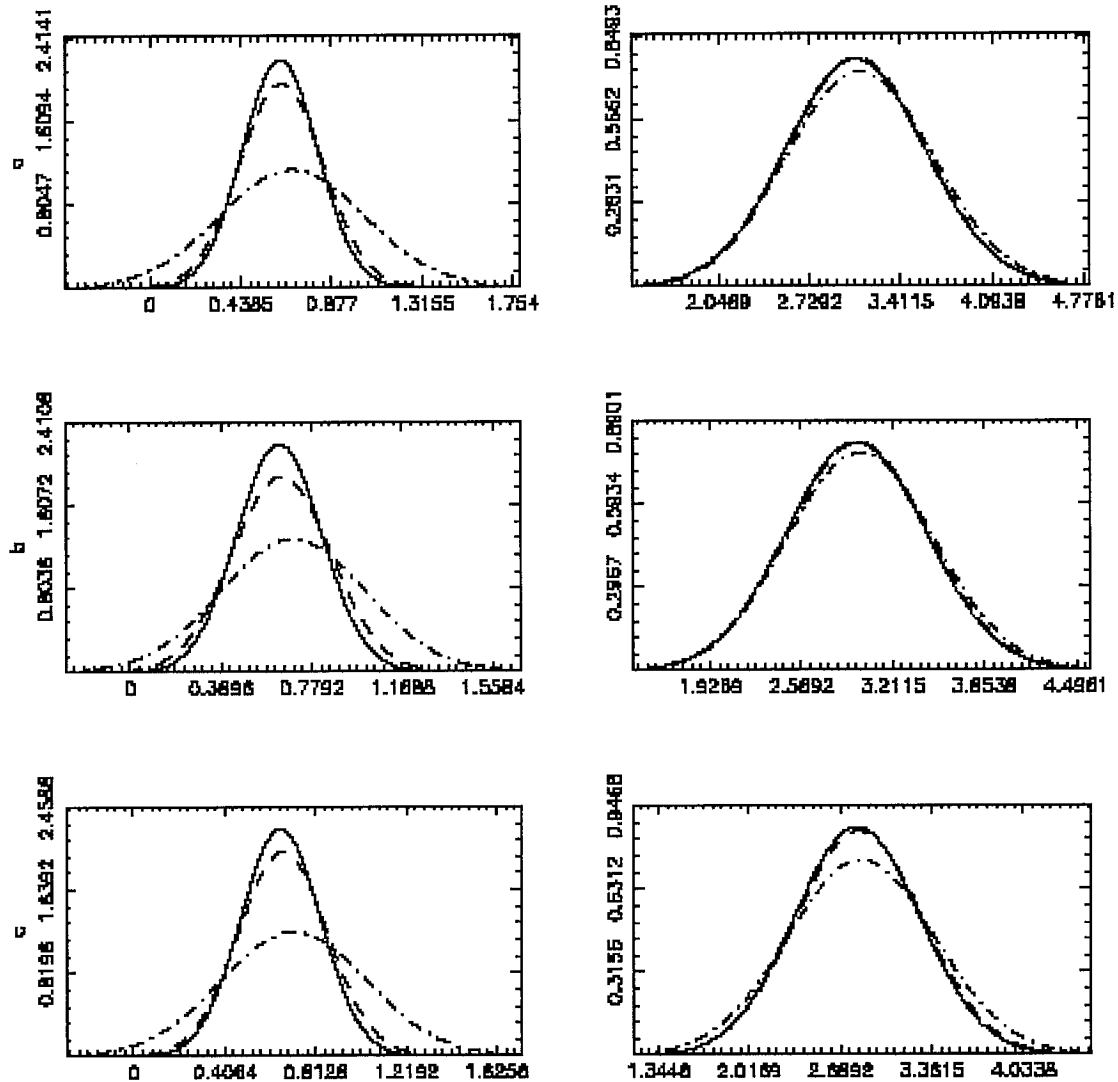
FIGURE 6.73. Chebyshev coefficients, C(1,2) and C(2,1), combined stiffness parameter reduction and damping parameter enhancement (- = 1%, -- = 5%, .- = 10% noise pollution)

163

Interestingly, though, the mean of the identified parameters does not exhibit a large shift for higher levels of noise pollution. The effect of increasing noise pollution for all cases is evidenced in the variance of the distribution.

The effect of increasing the linear system stiffness parameter degradation does result in a shift in the identified damping parameter, as illustrated in Figure 6.69. Additionally, damping parameter degradation does have an affect on the identified mean of the stiffness parameter. This result is highlighted in Figure 6.70. The identitifed mean of the identified Chebyshev parameter C(2,1) when the system was only subjected to noise pollution was reported as approximately 0.64. Under a 5% damping parameter reduction, this value increased to approximately 0.75. A value of 0.80 was approached when the stiffness parameter was further degraded to 20%. Similar results are reported in Figure 6.71 for damping parameter enhancement. Recall that Chebyshev parameter C(2,1) is a primary contributor to the Power Series linear term, which is associated with a system's stiffness.

Figure 6.72 highlights the effect of combined stiffness and damping parameter reduction of various levels. Figure 6.73 reveals the effect of damping parameter enhancement and stiffness degradation. As noted earlier, the identified mean values, while not greatly influenced by noise, do change under system parameter variances. The effects of system parameter changes are more clearly illustrated in a review of the statistics of the identified parameters. These effects are discussed in detail in the following section.

164

6.6.4.1.1 Identification of linear system parameters with noise pollution

A total of 77 cases were evaluated. The statistical data in each case were derived from at least 3000 system simulations, as previously discussed. The first 20 cases (reference Table 6.9) represent various levels of reduction in the stiffness parameter. Cases 21 through 56 model damping enhancement and reduction (reference Table 6.10). Finally, combinations of stiffness parameter reduction and damping variations are included in cases 57 through 77 (reference Table 6.11). All cases incorporate several levels of noise pollution.

Case #	Noise Pollution level %	Changes relative to original model parameters
1	1	None (reference case)
2	1	Reduce k by 1% from 39.478 to 39.0832
3	1	Reduce k by 5% from 39.478 to 37.5041
4	1	Reduce k by 10% from 39.478 to 35.5304
5	1	Reduce k by 25% from 39.478 to 29.6085
6	5	None (reference case)
7	5	Reduce k by 1% from 39.478 to 39.0832
8	5	Reduce k by 5% from 39.478 to 37.5041
9	5	Reduce k by 10% from 39.478 to 35.5304
10	5	Reduce k by 25% from 39.478 to 29.6085
11	10	None (reference case)
12	10	Reduce k by 1% from 39.478 to 39.0832
13	10	Reduce k by 5% from 39.478 to 37.5041
14	10	Reduce k by 10% from 39.478 to 35.5304
15	10	Reduce k by 25% from 39.478 to 29.6085
16	20	None (reference case)
17	20	Reduce k by 1% from 39.478 to 39.0832
18	20	Reduce k by 5% from 39.478 to 37.5041
19	20	Reduce k by 10% from 39.478 to 35.5304
20	20	Reduce k by 25% from 39.478 to 29.6085

TABLE 6.9. Investigated test cases with stiffness degradation

165

Case #	Noise Pollution level %	Changes relative to original model parameters
21	1	None (reference case)
22	1	Reduce c by 1% from 1.2566 to 1.2440
23	1	Reduce c by 5% from 1.2566 to 1.1938
24	1	Reduce c by 10% from 1.2566 to 1.1309
25	1	Reduce c by 25% from 1.2566 to 0.9425
26	1	Increase c by 1% from 1.2566 to 1.2692
27	1	Increase c by 5% from 1.2566 to 1.3194
28	1	Increase c by 10% from 1.2566 to 1.3823
29	1	Increase c by 25% from 1.2566 to 1.5708
30	5	None (reference case)
31	5	Reduce c by 1% from 1.2566 to 1.2440
32	5	Reduce c by 5% from 1.2566 to 1.1938
33	5	Reduce c by 10% from 1.2566 to 1.1309
34	5	Reduce c by 25% from 1.2566 to 0.9425
35	5	Increase c by 1% from 1.2566 to 1.2692
36	5	Increase c by 5% from 1.2566 to 1.3194
37	5	Increase c by 10% from 1.2566 to 1.3823
38	5	Increase c by 25% from 1.2566 to 1.5708
39	10	None (reference case)
40	10	Reduce c by 1% from 1.2566 to 1.2440
41	10	Reduce c by 5% from 1.2566 to 1.1938
42	10	Reduce c by 10% from 1.2566 to 1.1309
43	10	Reduce c by 25% from 1.2566 to 0.9425
44	10	Increase c by 1% from 1.2566 to 1.2692
45	10	Increase c by 5% from 1.2566 to 1.3194
46	10	Increase c by 10% from 1.2566 to 1.3823
47	10	Increase c by 25% from 1.2566 to 1.5708
48	20	None (reference case)
49	20	Reduce c by 1% from 1.2566 to 1.2440
50	20	Reduce c by 5% from 1.2566 to 1.1938
51	20	Reduce c by 10% from 1.2566 to 1.1309
52	20	Reduce c by 25% from 1.2566 to 0.9425
53	20	Increase c by 1% from 1.2566 to 1.2692
54	20	Increase c by 5% from 1.2566 to 1.3194
55	20	Increase c by 10% from 1.2566 to 1.3823
56	20	Increase c by 25% from 1.2566 to 1.5708

TABLE 6.10. Investigated test cases with damping parameter variation

166

Case #	Noise Pollution level %	Changes relative to original model parameters
57	1	None (reference case)
58	1	Reduce k by 1% and c by 1%
59	1	Reduce k by 1% and increase c by 1%
60	1	Reduce k by 5% and c by 5%
61	1	Reduce k by 5% and increase c by 5%
62	1	Reduce k by 10% and c by 10%
63	1	Reduce k by 10% and increase c by 10%
64	5	None (reference case)
65	5	Reduce k by 1% and c by 1%
66	5	Reduce k by 1% and increase c by 1%
67	5	Reduce k by 5% and c by 5%
68	5	Reduce k by 5% and increase c by 5%
69	5	Reduce k by 10% and c by 10%
70	5	Reduce k by 10% and increase c by 10%
71	10	None (reference case)
72	10	Reduce k by 1% and c by 1%
73	10	Reduce k by 1% and increase c by 1%
74	10	Reduce k by 5% and c by 5%
75	10	Reduce k by 5% and increase c by 5%
76	10	Reduce k by 10% and c by 10%
77	10	Reduce k by 10% and increase c by 10%

TABLE 6.11. Investigated test cases with combined parameter variation

Four distinct "damage" levels are identified in Table 6.9; stiffness reductions of 1, 5, 10 and 25%. Each level of induced damage is also simulated with various degrees of noise pollution. Cases 1, 6, 11 and 16 are reference cases (shaded in Tables 6.9 through 6.11); i.e., they incorporate noise pollution but no "damage" to the stiffness parameter. These cases are used as baselines to quantify the statistics of the identified changes to the system parameters at the corresponding levels of noise pollution.

167

Error analysis is facilitated through the introduction of non-dimensional terms in Tables 6.12 through 6.19. k^* is defined as the exact stiffness value of the known system. $k^{(0)}$ is the exact value of the stiffness parameter for the reference case. Δk is then a dimensionless change in k^* defined as

$$\Delta k = \frac{\left(k^* - k^{(0)} \right)}{k^{(0)}} \tag{6.48}$$

$\bar{k}$ (= kbar in the tables) represents the mean value of the identified system stiffness, and S is the corresponding standard deviation. The dimensionless error in the identified mean relative to the exact stiffness is defined as

$$e = \frac{\left(\bar{k} - k^* \right)}{k^*} \tag{6.49}$$

The dimensionless change in the mean value of the identified stiffness with respect to the corresponding mean value associated with the "undamaged" reference case (i.e., case 1) is defined as

$$r = \frac{\left(\bar{k} - \bar{k}^{(0)} \right)}{\bar{k}^{(0)}} \tag{6.50}$$

The dimensionless change in $\bar{k}^{(0)}$ with respect to the identified $\bar{k}$ corresponding to the reference case and expressed as a multiple of the corresponding standard deviation is written as

$$d = \frac{\left(\bar{k} - \bar{k}^{(0)} \right)}{s} \tag{6.51}$$

Finally, a dimensionless ratio of natural frequencies, ω, to the frequencies corresponding to the "undamaged" reference case is computed as

$$\Delta\omega = \frac{\left(\omega - \omega^{(0)}\right)}{\omega^{(0)}} \qquad (6.52)$$

Tables 6.12 through 6.22 include measures E, R, and D derived from the stiffness parameter as well as the damping parameter. The first seven rows in each table are dedicated to the dimensionless variations computed from the stiffness parameter. The last seven rows consider the same ratios, only computed from the damping parameter. The system frequency and associated dimensionless ratio to the undamaged case $\Delta\omega$ divides each table (shaded rows in Tables 6.12 through 6.22).

6.6.4.1.1.1 Identification of baseline and degraded stiffness states at 1% noise pollution

The identified results and computed statistics for cases 1 through 5 are listed in Table 6.12. Case 1 does not include any "damage" to the system, simply noise pollution at 1%. This level of noise yields a 4% error in the mean value of the identified stiffness and 6% in the identified damping parameter. The identified natural frequency is 6.4 Hz, which is 1.8% greater than the exact value.

Clearly, the errors detected in the stiffness and damping parameters are much greater than that from the identified natural frequency. Thus, either one of these identified parameters is a potential candidate for detecting system change from the reference or baseline case. Noise pollution effects will dictate which parameter is best suited for this application, as discussed below.

169

Reviewing Case 2, a reduction of 1% in the stiffness parameter yields a 4% error in the identified mean value of the stiffness parameter and 5% in the mean value of the identified damping parameter. The corresponding standard deviations are 3 and 0.5.

Given the above, the stiffness parameter is a more logical choice for use in detecting system changes when system damping is low. This point is further highlighted upon review of cases 3, 4 and 5, where the mean and standard deviation of the identified damping parameter does prescribe to an intuitive trend when considering the associated induced damage.

Concentrating then on the stiffness parameter statistics only for cases 2 through 5, the percentage change in the mean values of identified system stiffness $\bar{k}$ closely replicate the actual stiffness parameter reduction k^*. Recall from earlier definitions that R_k is the identified version of Δk (reference equation 6.50).

A measure of the confidence level in the identified changes to the system is represented in D_k, which reveals the quantitative change in $\bar{k}$ relative to the reference $\bar{k}^{(0)}$ expressed as a fraction of the standard deviation. For these cases, the measure of confidence ranges from 12 to 200 %.

170

	Case 1	Case 2	Case 3	Case 4	Case 5
k*	39.48	39.08	37.50	35.53	29.61
Δk	---	-0.01	-0.05	-0.10	-0.25
kbar	40.97	40.60	38.97	36.93	30.84
S_k	2.85	3.06	4.88	3.67	5.13
E_k	0.04	0.04	0.04	0.04	0.04
R_k	---	-0.01	-0.05	-0.10	-0.25
D_k	---	-0.12	-0.41	-1.10	-1.98
ω	6.40	6.37	6.24	6.08	5.55
$\Delta\omega$	---	0.00	-0.02	-0.05	-0.13
c*	1.26	1.26	1.26	1.26	1.26
Δc	---	0.00	0.00	0.00	0.00
cbar	1.33	1.32	1.34	1.34	1.35
S_c	0.38	0.48	0.82	0.51	0.98
E_c	0.06	0.05	0.07	0.07	0.07
R_c	---	0.00	0.01	0.01	0.02
D_c	---	-0.01	0.02	0.02	0.02

TABLE 6.12. Summary of identification results, stiffness degraded, 1% noise

The damage levels represented in these cases resulted in very small changes detected in the natural frequencies, with percentages ranging from less than 1% in Case 2, to 13% in Case 5. Hence, higher levels of damage can be detected in the natural frequency shifts, but low levels of damage are not easily discernable.

6.6.4.1.1.2 Identification of baseline and degraded stiffness states at 5% noise pollution

Table 6.13 highlights the identified results for cases 6 through 10. The stiffness is again degraded by 1, 5, 10 and 25 percent as in cases 2 through 5, but the noise pollution is set at 5% for these cases.

171

	Case 6	Case 7	Case 8	Case 9	Case 10
k^*	39.48	39.08	37.50	35.53	29.61
Δk	---	-0.01	-0.05	-0.10	-0.25
kbar	40.84	40.62	38.85	36.89	30.76
S_k	4.95	7.01	8.34	8.65	9.40
E_k	0.03	0.04	0.04	0.04	0.04
R_k	---	-0.01	-0.05	-0.10	-0.25
D_k	---	-0.03	-0.24	-0.46	-1.07
ω	6.39	6.37	6.23	6.07	5.55
$\Delta\omega$	---	0.00	-0.02	-0.05	-0.13
c^*	1.26	1.26	1.26	1.26	1.26
Δc	---	0.00	0.00	0.00	0.00
cbar	1.48	1.53	1.52	1.53	1.60
S_c	1.01	1.46	1.30	1.26	3.16
E_c	0.18	0.22	0.21	0.22	0.27
R_c	---	0.04	0.03	0.03	0.08
D_c	---	0.04	0.03	0.04	0.04

TABLE 6.13. Summary of identification results, stiffness degraded, 5% noise

Case 6 is the reference case for the simulations with 5% noise pollution. The computed error E_k in the mean value of the identified stiffness is 3%, and the identified natural frequency is 6.4 Hz, both similar to the values reported in Case 1.

In cases 7 through 10, the percent change R_k in the mean values of the identified stiffness $\bar{k}$ closely matches the artificially imposed stiffness parameter reduction k^* for each respective case. Again, this follows that reported in cases 2 through 5.

The confidence in detecting the degraded system in these cases ranges from 3% to 107%, as represented in D_k.

172

6.6.4.1.1.3 Identification of baseline and degraded stiffness states at 10% noise pollution

Cases 11 through 15 illustrate the effects of 10% noise pollution on degrading stiffness states (reference Tables 6.9 and 6.14).

The baseline case for the computed statistics in these simulations is Case 11, which does not incorporate any stiffness parameter degradation. The computed error E_k in the mean value of the identified stiffness is 2%, and the identified natural frequency is 6.3 Hz, both approximately similar to the values reported in the earlier reference cases. However, the standard deviation of the data is substantially higher at 21. This apparent dramatic increase in the dispersion of the data is readily evident upon review of the plotted curves in Figure 6.69a. As the noise level increases, the identification algorithm's ability to discriminate data is reduced. Still, the mean values of stiffness parameter from the respective data sets remain close to the actual values, as reported in the error measure E_k. Figures 6.74 through 6.76 depict this effect in bar chart form, which helps clearly illustrate the data reported in tabular form. Again, as reported above for cases 2 through 5 and 7 through 10, the percent change R_k in the mean values of the identified stiffness $\bar{k}$ closely matches the artificially imposed stiffness parameter reduction k^*.

The confidence in detecting the degraded system in these cases ranges from 2% to 44%, as represented in D_k. This reveals a substantial reduction in the identification

173

algorithm's ability to replicate the system response from the measured state variables.

Figure 6.77 details the shift in the identified Power Series representation of the stiffness parameter mean from Cases 11, 13 and a 5% variation in the nonlinear term. This plot illustrates the excellent ability of the Chebyshev algorithm to discriminate subtle changes in system parameters, even under credible levels of noise pollution.

	Case 11	Case 12	Case 13	Case 14	Case 15
k^*	39.48	39.08	37.50	35.53	29.61
Δk	---	-0.01	-0.05	-0.10	-0.25
kbar	40.16	39.83	38.60	36.17	29.88
S_k	20.99	14.81	37.35	24.55	23.32
E_k	0.02	0.02	0.03	0.02	0.01
R_k	---	-0.01	-0.04	-0.10	-0.26
D_k	---	-0.02	-0.04	-0.16	-0.44
ω	6.34	6.31	6.21	6.01	5.47
$\Delta\omega$	---	0.00	-0.02	-0.05	-0.14
c^*	1.26	1.26	1.26	1.26	1.26
Δc	---	0.00	0.00	0.00	0.00
cbar	2.05	2.03	1.97	2.12	1.91
S_c	4.47	5.98	5.57	5.95	3.30
E_c	0.63	0.61	0.57	0.69	0.52
R_c	---	-0.01	-0.04	0.03	-0.07
D_c	---	0.00	-0.01	0.01	-0.04

TABLE 6.14. Summary of identification results, stiffness degraded, 10% noise

174
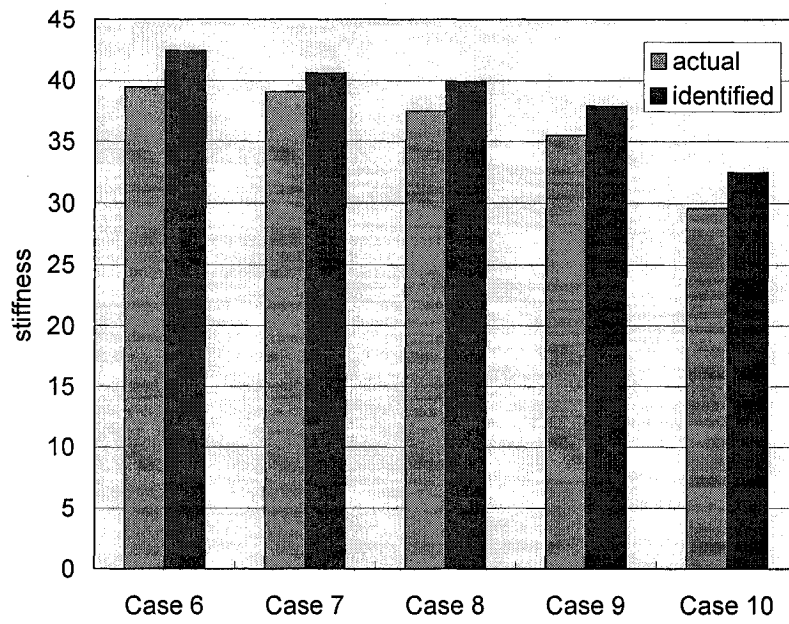
FIGURE 6.74. Stiffness discrimination

$$R = \frac{(\bar{k} - \bar{k}^{(0)})}{\bar{k}^{(0)}}$$
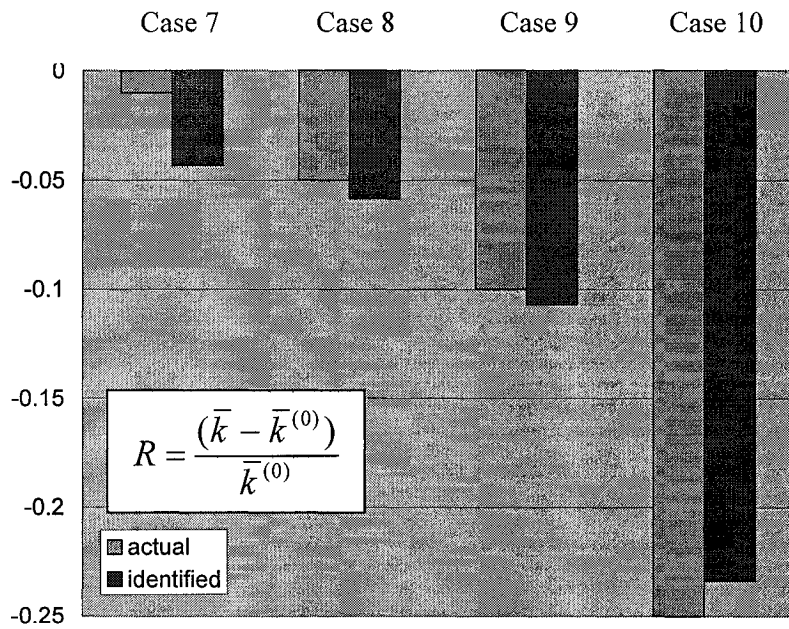
FIGURE 6.75. Detection capability, R_k

175
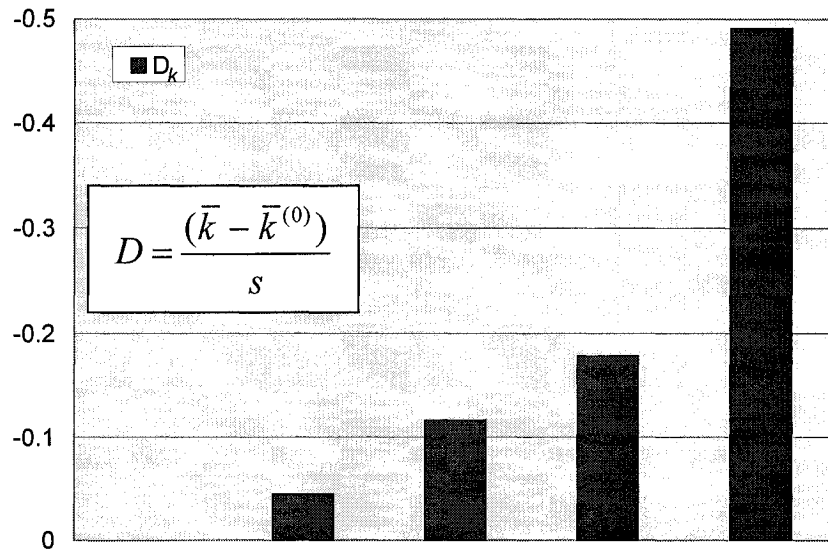
FIGURE 6.76. Detection capability, D_k

$$D = \frac{(\bar{k} - \bar{k}^{(0)})}{s}$$
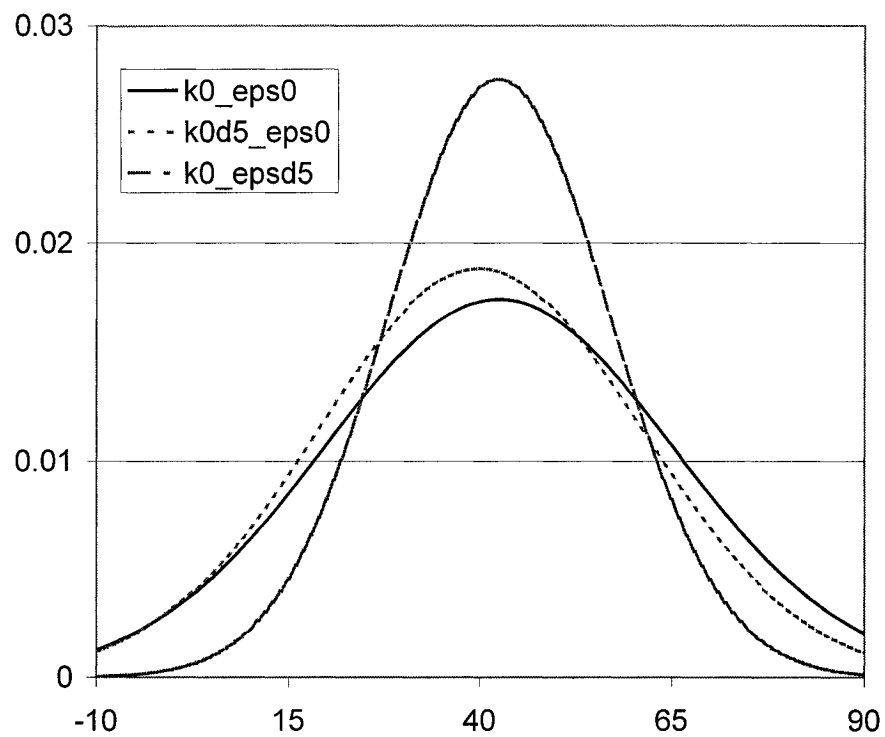
FIGURE 6.77. Mean shift comparison

176

6.6.4.1.1.4 Identification of baseline and degraded stiffness states at 20% noise pollution

Table 6.15 includes the linear system models polluted by 20% noise, cases 16 through 20 (reference Table 6.9).

As noted from Table 6.9, Case 16 reveals the noise polluted system response in the absence of parameter degradation. An inspection of the error E_k and the standard deviation S_k of the identified mean stiffness value clearly supports the conclusion from the system polluted with 10% noise; that is, while the mean of the identified stiffness parameter is well within acceptable tolerance levels compared to the actual value, the dispersion of the data is dramatic. Thus, for a large enough data set, the identification algorithm successfully discrimates the system stiffness from the noise, but the level of confidence on an individual sample will be vastly reduced from cases with noise pollution levels set orders of magnitude lower.

This hypothesis is supported in the computed measure of the system detection confidence for the degraded states (cases 17 through 20), which ranges from 2% to 42%. Recall that the level of confidence was reported at 3% to 107% in cases 7 through 10.

177

	Case 16	Case 17	Case 18	Case 19	Case 20
k*	39.48	39.08	37.50	35.53	29.61
Δk	---	-0.01	-0.05	-0.10	-0.25
kbar	38.93	38.43	36.60	35.04	29.87
S_k	29.70	22.59	39.52	34.19	21.76
E_k	-0.01	-0.02	-0.02	-0.01	0.01
R_k	---	-0.01	-0.06	-0.10	-0.23
D_k	---	-0.02	-0.06	-0.11	-0.42
ω	6.24	6.20	6.05	5.92	5.47
$\Delta\omega$	---	-0.01	-0.03	-0.05	-0.12
c*	1.26	1.26	1.26	1.26	1.26
Δc	---	0.00	0.00	0.00	0.00
cbar	2.14	2.07	1.91	1.90	2.01
S_c	5.50	6.38	6.92	5.53	6.39
E_c	0.70	0.65	0.52	0.51	0.60
R_c	---	-0.03	-0.11	-0.11	-0.06
D_c	---	-0.01	-0.03	-0.04	-0.02

TABLE 6.15. Summary of identification results, stiffness degraded, 20% noise

6.6.4.1.1.5 Identification of baseline and degraded/enhanced damping states at 1% noise pollution

Table 6.16 presents results from the next subset of cases, 21 through 29. These depict the system "damaged" by inducing various levels of damping parameter degradation and enhancement with 1% noise pollution (reference Table 6.10). Based on this definition, the baseline for these simulations, Case 21, is identical to Case 1, and is included here for clarity in presentation only.

Since the damping parameter is being varied in these cases, this discussion will include effects on the identified damping parameter to the extent deemed appropriate. Recall that the damping parameter is highly susceptible to noise effects

178

as it represents a minor component in the restoring force equation for the linear system under investigation herein. Thus, the focus of the identification algorithm's ability to successfully discriminate system changes should remain on the stiffness parameter, which is not as sucseptible to the effects of noise.

Cases 22 through 25 represent simulations with the damping parameter reduced by 1, 5, 10 and 25%. The errors computed in the mean of the identified stiffness parameter for these cases hover around 3.5%. The standard deviations of the identified stiffness mean range from 1.8 to 4.6. Note that there was no initial reduction in the stiffness parameter. This variation in identified stiffness values results from system noise polluting the degraded damping parameter. The percentage change in the mean values of the identified stiffness parameter indicate only slight variations from the reference case. The percentage change in the mean values of the identified damping parameter for these cases follows the actual damping parameter reduction fairly well. Recall that there is only a slight perturbation to the system from noise for these simulations.

The computed statistics for cases 26 through 29, where the damping parameter is increased by 1, 5, 10 and 25%, reveal similar tendencies to those reported for cases 22 through 25.

6.6.4.1.1.6 Identification of baseline and degraded/enhanced damping states at 5% noise pollution

Table 6.17 reveals the effect of 5% noise pollution on the system with degraded and enhanced damping parameter variations of 1, 5, 10 and 25%. Case 30 is identical to Case 6 in Table 6.13, both representing undamaged system simulations inhibited by 5% noise.

Cases 31 through 34 represent damping parameter degradation of 1, 5, 10 and 25% respectively. Cases 35 through 38 correspond to enhancing the damping parameter by similar percentages. The errors in the identified stiffness parameter for these cases do not follow a trend as before. This fact is expected for increasing system noise due to the susceptibility of the damping parameter to noise influences, and is seen in subsequent data sets derived from damping parameter variations under 10% and 20% noise pollution (reference Tables 6.18 and 6.19). The measure of the percentage change in the mean values of the identifed damping parameter R_c holds the best hope for identifying system change in these cases.

6.6.4.1.1.7 Identification of baseline and degraded/enhanced damping states at 10% and 20% noise pollution

The effects of higher noise pollution levels on the system with damping reduction and enhancement are detailed in Tables 6.18 and 6.19. A total of 18 cases are tabulated in these two tables (reference Table 6.10). Cases 39 and 48 are identical to

cases 11 and 16, respectively (reference Tables 6.9 and 6.10); these are included only for clarity.

The identified stiffness parameters are relatively close to the actual values, but the dispersion of the data in each case is dramatic, revealing the effects of noise pollution on the damping parameter. Additionally, large errors are noted in the identified damping parameter mean values. The only conclusion that can be drawn from these cases is that the sign of the confidence level measure follows the change in the damping parameter; negative when the damping parameter is reduced and positive when enhanced.

181

	Case 21	Case 22	Case 23	Case 24	Case 25	Case 26	Case 27	Case 28	Case 29
k^*	39.48	39.48	39.48	39.48	39.48	39.48	39.48	39.48	39.48
Δk	---	0.00	0.00	0.00	0.00	0.00	0.00	0.00	0.00
kbar	40.97	40.98	40.88	40.84	40.74	40.97	41.00	41.09	41.27
S_k	2.85	4.56	1.86	1.84	3.08	2.29	2.57	3.12	4.60
E_k	0.04	0.04	0.04	0.03	0.03	0.04	0.04	0.04	0.05
R_k	---	0.00	0.00	0.00	-0.01	0.00	0.00	0.00	0.01
D_k	---	0.00	-0.05	-0.07	-0.07	0.00	0.01	0.04	0.06
ω	6.40	6.40	6.39	6.39	6.38	6.40	6.40	6.41	6.42
$\Delta\omega$	---	0.00	0.00	0.00	0.00	0.00	0.00	0.00	0.00
c^*	1.26	1.24	1.19	1.13	0.94	1.27	1.32	1.38	1.57
Δc	---	-0.01	-0.05	-0.10	-0.25	0.01	0.05	0.10	0.25
cbar	1.33	1.32	1.25	1.18	1.01	1.34	1.39	1.48	1.69
S_c	0.38	0.57	0.23	0.24	0.90	0.37	0.33	0.57	1.36
E_c	0.06	0.06	0.05	0.05	0.07	0.06	0.06	0.07	0.08
R_c	---	-0.01	-0.06	-0.11	-0.24	0.01	0.05	0.11	0.27
D_c	---	-0.02	-0.34	-0.60	-0.36	0.04	0.19	0.26	0.27

TABLE 6.16. Summary of identification results, damping variation, 1% noise pollution

182

	Case 30	Case 31	Case 32	Case 33	Case 34	Case 35	Case 36	Case 37	Case 38
k^*	39.48	39.48	39.48	39.48	39.48	39.48	39.48	39.48	39.48
Δk	---	0.00	0.00	0.00	0.00	0.00	0.00	0.00	0.00
kbar	40.84	41.01	40.80	40.84	40.67	40.98	40.93	41.10	41.01
S_k	4.95	5.74	7.24	6.50	5.52	8.41	6.88	5.79	10.21
E_k	0.03	0.04	0.03	0.03	0.03	0.04	0.04	0.04	0.04
R_k	---	0.00	0.00	0.00	0.00	0.00	0.00	0.01	0.00
D_k	---	0.03	-0.01	0.00	-0.03	0.02	0.01	0.04	0.02
ω	6.39	6.40	6.39	6.39	6.38	6.40	6.40	6.41	6.40
$\Delta\omega$	---	0.00	0.00	0.00	0.00	0.00	0.00	0.00	0.00
c^*	1.26	1.24	1.19	1.13	0.94	1.27	1.32	1.38	1.57
Δc	---	-0.01	-0.05	-0.10	-0.25	0.01	0.05	0.10	0.25
cbar	1.48	1.47	1.45	1.37	1.15	1.50	1.58	1.63	1.85
S_c	1.01	1.03	1.34	1.68	0.91	1.25	1.69	0.87	1.37
E_c	0.18	0.18	0.22	0.22	0.22	0.18	0.19	0.18	0.18
R_c	---	-0.01	-0.02	-0.07	-0.22	0.02	0.07	0.10	0.26
D_c	---	-0.01	-0.02	-0.06	-0.36	0.02	0.06	0.17	0.28

TABLE 6.17. Summary of identification results, damping variation, 5% noise pollution

183

	Case 39	Case 40	Case 41	Case 42	Case 43	Case 44	Case 45	Case 46	Case 47
k^*	39.48	39.48	39.48	39.48	39.48	39.48	39.48	39.48	39.48
Δk	---	0.00	0.00	0.00	0.00	0.00	0.00	0.00	0.00
$kbar$	40.16	39.94	39.42	40.37	39.93	39.99	39.68	40.67	39.95
S_k	20.99	23.54	30.29	16.56	30.65	24.69	49.06	31.12	22.21
E_k	0.02	0.01	0.00	0.02	0.01	0.01	0.01	0.03	0.01
R_k	---	-0.01	-0.02	0.01	-0.01	0.00	-0.01	0.01	-0.01
D_k	---	-0.01	-0.02	0.01	-0.01	-0.01	-0.01	0.02	-0.01
ω	6.34	6.32	6.28	6.35	6.32	6.32	6.30	6.38	6.32
$\Delta\omega$	---	0.00	-0.01	0.00	0.00	0.00	-0.01	0.01	0.00
c^*	1.26	1.24	1.19	1.13	0.94	1.27	1.32	1.38	1.57
Δc	---	-0.01	-0.05	-0.10	-0.25	0.01	0.05	0.10	0.25
$cbar$	2.05	1.93	1.81	1.75	1.63	2.08	2.12	2.19	2.33
S_c	4.47	3.02	5.37	2.35	5.52	7.59	4.75	6.31	4.82
E_c	0.63	0.55	0.52	0.55	0.73	0.64	0.61	0.58	0.48
R_c	---	-0.06	-0.12	-0.15	-0.21	0.01	0.03	0.07	0.14
D_c	---	-0.04	-0.04	-0.13	-0.08	0.00	0.01	0.02	0.06

TABLE 6.18. Summary of identification results, damping variation, 10% noise pollution

184

	Case 48	Case 49	Case 50	Case 51	Case 52	Case 53	Case 54	Case 55	Case 56
k^*	39.48	39.48	39.48	39.48	39.48	39.48	39.48	39.48	39.48
Δk	---	0.00	0.00	0.00	0.00	0.00	0.00	0.00	0.00
kbar	38.93	39.07	38.91	37.61	38.79	39.88	38.60	39.95	39.39
S_k	29.70	31.10	34.58	37.92	39.00	34.01	36.65	74.37	25.21
E_k	-0.01	-0.01	-0.01	-0.05	-0.02	0.01	-0.02	0.01	0.00
R_k	---	0.00	0.00	-0.03	0.00	0.02	-0.01	0.03	0.01
D_k	---	0.00	0.00	-0.03	0.00	0.03	-0.01	0.01	0.02
ω	6.24	6.25	6.24	6.13	6.23	6.32	6.21	6.32	6.28
$\Delta\omega$	---	0.00	0.00	-0.02	0.00	0.01	0.00	0.01	0.01
c^*	1.26	1.24	1.19	1.13	0.94	1.27	1.32	1.38	1.57
Δc	---	-0.01	-0.05	-0.10	-0.25	0.01	0.05	0.10	0.25
cbar	2.14	1.95	2.02	1.98	1.91	2.27	2.22	2.20	2.44
S_c	5.50	5.28	7.38	7.07	10.51	8.78	7.14	7.66	6.72
E_c	0.70	0.57	0.69	0.75	1.03	0.79	0.68	0.59	0.55
R_c	---	-0.09	-0.05	-0.08	-0.11	0.06	0.04	0.03	0.14
D_c	---	-0.04	-0.02	-0.02	-0.02	0.01	0.01	0.01	0.04

TABLE 6.19. Summary of identification results, damping variation, 20% noise pollution

185

6.6.4.1.1.8 Identification of baseline and combined variations in stiffness and damping states at 1, 5 and 10% noise pollution

The last linear cases considered incorporate combined stiffness and damping parameter changes to the system. The results of these cases are presented in Tables 6.20 through 6.22. The effects of noise pollution at levels of 1, 5 and 10% differentiate the data in each of these three tables. Parameter variations are outlined in Table 6.11.

A review of the percent change R_k in the mean values of the identified stiffness again closely matches the induced stiffness parameter reduction in these results, with the exception when the damping parameter is enhanced by 1% under 1% noise pollution. In all cases, the value of R_k is several percent higher, indicating susceptibility to system noise, as noted earlier.

The dispersion of the data indicated by the standard deviation of the identified stiffness parameter S_k also follows trends discussed previously. Increasing noise pollution results in lower expected accuracy of the identified results for an individual simulation, while the identified mean value closely replicates the actual parameter degraded state.

The confidence measure D_k ranges from 15% to 180% for the tabulated results in Table 6.20. This measure degrades when the noise pollution levels increase, as

186

indicated in Tables 6.21 and 6.22. D_k varies from 3% to 69 % in Table 6.21, and 3% to 16% in Table 6.22.

Changes in the system natural frequencies for these cases track levels of change in the stiffness parameter, but do not discriminate changes in the damping parameter well. This is particularly true at higher values of stiffness parameter degradation.

The only definitive conclusion to be drawn from a review of the statistics computed with the identified damping parameters is that noise pollution clearly dominates the result. The measure of confidence in detecting changes to the system state utilizing the damping parameter range from 4% to 35% in Table 6.20 with 1% noise pollution, and quickly deteriorate under higher levels of noise pollution. At 10% noise pollution, the maximum confidence level is only 4%, as detailed in Table 6.22.

	Case 57	Case 58	Case 59	Case 60	Case 61	Case 62	Case 63
k^*	39.48	39.08	39.08	37.50	37.50	35.53	35.53
Δk	---	-0.01	-0.01	-0.05	-0.05	-0.10	-0.10
kbar	40.97	40.51	39.38	38.97	39.03	36.88	36.98
S_k	2.85	3.12	22.74	4.76	2.97	3.03	2.21
E_k	0.04	0.04	0.01	0.04	0.04	0.04	0.04
R_k	---	-0.01	-0.04	-0.05	-0.05	-0.10	-0.10
D_k	---	-0.15	-0.07	-0.42	-0.65	-1.35	-1.80
ω	6.40	6.36	6.28	6.24	6.25	6.07	6.08
$\Delta\omega$	---	-0.01	-0.02	-0.02	-0.02	-0.05	-0.05
c^*	1.26	1.24	1.19	1.13	0.94	1.27	1.32
Δc	---	-0.01	-0.05	-0.10	-0.25	0.01	0.05
cbar	1.33	1.31	1.90	1.28	1.40	1.20	1.47
S_c	0.38	0.39	4.32	0.67	0.38	0.38	0.41
E_c	0.06	0.05	0.59	0.13	0.48	-0.06	0.12
R_c	---	-0.01	0.43	-0.04	0.05	-0.10	0.11
D_c	---	-0.04	0.13	-0.08	0.18	-0.34	0.35

TABLE 6.20. Summary of identification results, combined variation, 1% noise pollution

188

	Case 64	Case 65	Case 66	Case 67	Case 68	Case 69	Case 70
k^*	39.48	39.08	39.08	37.50	37.50	35.53	35.53
Δk	---	-0.01	-0.01	-0.05	-0.05	-0.10	-0.10
kbar	40.84	40.65	39.38	38.97	38.82	36.79	36.94
S_k	4.95	6.38	22.74	4.53	8.94	5.46	5.64
E_k	0.03	0.04	0.01	0.04	0.04	0.04	0.04
R_k	---	0.00	-0.04	-0.05	-0.05	-0.10	-0.10
D_k	---	-0.03	-0.06	-0.41	-0.23	-0.74	-0.69
ω	6.39	6.38	6.28	6.24	6.23	6.07	6.08
$\Delta\omega$	---	0.00	-0.02	-0.02	-0.03	-0.05	-0.05
c^*	1.26	1.24	1.19	1.13	0.94	1.27	1.32
Δc	---	-0.01	-0.05	-0.10	-0.25	0.01	0.05
cbar	1.48	1.49	1.90	1.43	1.59	1.35	1.64
S_c	1.01	1.42	4.32	0.89	1.28	0.77	0.93
E_c	0.18	0.20	0.59	0.26	0.68	0.07	0.24
R_c	---	0.01	0.29	-0.03	0.07	-0.08	0.11
D_c	---	0.01	0.10	-0.05	0.09	-0.16	0.18

TABLE 6.21. Summary of identification results, combined variation, 5% noise pollution

189

	Case 71	Case 72	Case 73	Case 74	Case 75	Case 76	Case 77
k*	39.48	39.08	39.08	37.50	37.50	35.53	35.53
Δk	---	-0.01	-0.01	-0.05	-0.05	-0.10	-0.10
kbar	40.16	39.38	39.38	38.13	38.38	36.11	36.12
S_k	20.99	22.74	22.74	13.69	15.45	17.92	24.74
E_k	0.02	0.01	0.01	0.02	0.02	0.02	0.02
R_k	---	-0.02	-0.02	-0.05	-0.04	-0.10	-0.10
D_k	---	-0.03	-0.03	-0.15	-0.12	-0.23	-0.16
ω	6.34	6.28	6.28	6.17	6.20	6.01	6.01
$\Delta\omega$	---	-0.01	-0.01	-0.03	-0.02	-0.05	-0.05
c*	1.26	1.24	1.19	1.13	0.94	1.27	1.32
Δc	---	-0.01	-0.05	-0.10	-0.25	0.01	0.05
cbar	2.05	1.90	1.90	1.86	2.01	1.86	2.13
S_c	4.47	4.32	4.32	5.20	2.87	5.08	4.34
E_c	0.63	0.53	0.59	0.65	1.14	0.47	0.61
R_c	---	-0.08	-0.08	-0.09	-0.02	-0.09	0.04
D_c	---	-0.04	-0.04	-0.04	-0.01	-0.04	0.02

TABLE 6.22. Summary of identification results, combined variation, 10% noise pollution

190

6.6.4.2 Nonlinear model

Nonlinear systems were also investigated. As an example, results from simulations of a Duffing oscillator with the stiffness degraded by 1, 5, 10 and 25%, and noise pollution levels of 0, 1 and 10% are included. The data is represented in tabulated form similar to that discussed in Section 6.6.4.1 above. As before, the Duffing oscillator parameters were established as $m=1$, $k=39.478$, $c=1.2566$ and $\varepsilon=11.23$.

6.6.4.2.1 Identification of nonlinear system parameters with noise pollution

A total of 30 cases of the nonlinear Duffing oscillator were evaluated. As in the linear case, the statistical data in each case were derived from at least 3000 system simulations. The first ten cases (reference Table 6.23) represent various levels of reduction in the stiffness parameter. The next ten cases simulate variations in the nonlinear term, ε. Finally, combinations of stiffness parameter reduction and nonlinear term variations are included in the last ten cases, 21 through 30. All cases incorporate two levels of noise pollution, 1% and 10%.

Following the format utilized in the linear simulations, four distinct "damage" levels are identified in Table 6.23; reductions or enhancements of 1, 5, 10 and 25 percent. Each level of induced damage is also simulated with various degrees of noise pollution. Cases 1, 6, 11, 16, 21 and 26 are reference cases; ie., they incorporate noise pollution but no "damage" to the stiffness parameter. These cases are used as

191

baselines to quantify the statistics of the identified changes to the system parameters

at the corresponding levels of noise pollution.

Case #	Noise Pollution level %	Changes relative to original model parameters
1	1	None (reference case)
2	1	Reduce k by 1% from 39.478 to 39.0832
3	1	Reduce k by 5% from 39.478 to 37.5041
4	1	Reduce k by 10% from 39.478 to 35.5304
5	1	Reduce k by 25% from 39.478 to 29.6085
6	10	None (reference case)
7	10	Reduce k by 1% from 39.478 to 39.0832
8	10	Reduce k by 5% from 39.478 to 37.5041
9	10	Reduce k by 10% from 39.478 to 35.5304
10	10	Reduce k by 25% from 39.478 to 29.6085
11	1	None (reference case)
12	1	Reduce ε by 5% from 11.23 to 10.6685
13	1	Increase ε by 5% from 11.23 to 11.7915
14	1	Reduce ε by 10% from 11.23 to 10.1070
15	1	Increase ε by 10% from 11.23 to 12.3530
16	10	None (reference case)
17	10	Reduce ε by 5% from 11.23 to 10.6685
18	10	Increase ε by 5% from 11.23 to 11.7915
19	10	Reduce ε by 10% from 11.23 to 10.1070
20	10	Increase ε by 10% from 11.23 to 12.3530
21	1	None (reference case)
22	1	Reduce k by 5% and ε by 5%
23	1	Reduce k by 5% and increase ε by 5%
24	1	Reduce k by 10% and ε by 10%
25	1	Reduce k by 10% and increase ε by 10%
26	10	None (reference case)
27	10	Reduce k by 5% and ε by 5%
28	10	Reduce k by 5% and increase ε by 5%
29	10	Reduce k by 10% and ε by 10%
30	10	Reduce k by 10% and increase ε by 10%

TABLE 6.23. Investigated Test Cases

192

6.6.4.2.1.1 Identification of baseline and degraded stiffness states at 1% noise pollution

Table 6.24 displays statistical results for the stiffness and nonlinear terms, as do the remaining tables in this section. The data in Table 6.24 represents statistical results from Monte Carlo simulations with the stiffness parameter reduced by 1, 5, 10 and 25%, as noted in Table 6.23. Clearly, the errors in identifying the stiffness and nonlinear terms are reasonable at less than 4%, except in Case 5. The variance in the identified parameters is also very small, meaning that the identified variables are close to their respective baseline values. Both R_k and R_e closely follow the actual parameter perterbations, with R_e being zero for all cases. Since the nonlinear term was not varied for these simulation cases, this was expected.

	Case 1	Case 2	Case 3	Case 4	Case 5
k^*	39.48	39.08	37.50	35.53	29.61
Δk	---	-0.01	-0.05	-0.10	-0.25
kbar	40.88	40.40	38.81	36.88	31.25
S_k	3.89	4.81	2.36	2.02	8.39
E_k	0.04	0.03	0.03	0.04	0.06
R_k	---	-0.01	-0.05	-0.10	-0.24
D_k	---	-0.10	-0.87	-1.98	-1.15
ω	6.39	6.36	6.23	6.07	5.59
$\Delta\omega$	---	-0.01	-0.03	-0.05	-0.13
ε^*	11.23	11.23	11.23	11.23	11.23
$\Delta\varepsilon$	---	0.00	0.00	0.00	0.00
εbar	10.78	10.81	10.83	10.82	10.77
S_ε	1.38	1.41	0.81	0.70	2.03
E_ε	-0.04	-0.04	-0.04	-0.04	-0.04
R_ε	---	0.00	0.00	0.00	0.00
D_ε	---	0.02	0.07	0.06	0.00

TABLE 6.24. Summary of identification results, stiffness degradation, 1% noise

193

6.6.4.2.1.2 Identification of baseline and degraded stiffness states at 10% noise pollution

Increasing the level of noise pollution to 10% does reduce the identification algorithm's ability to discern system change, but not dramatically. Cases 6 through 10 in Table 6.25 highlight the detection capability for the same degraded stiffness values used in Table 6.24, with the noise pollution level increased from 1% to 10%. The error in identified parameters increases slightly, but the dispersion of the sample set increases dramatically to almost three times that reported in Table 6.24.

	Case 6	Case 7	Case 8	Case 9	Case 10
k^*	39.48	39.08	37.50	35.53	29.61
Δk	---	-0.01	-0.05	-0.10	-0.25
kbar	42.43	40.60	39.96	37.89	32.52
S_k	22.91	40.86	21.19	25.42	20.18
E_k	0.07	0.04	0.07	0.07	0.10
R_k	---	-0.04	-0.06	-0.11	-0.23
D_k	---	-0.04	-0.12	-0.18	-0.49
ω	6.51	6.37	6.32	6.16	5.70
$\Delta\omega$	---	-0.02	-0.03	-0.05	-0.12
ε^*	11.23	11.23	11.23	11.23	11.23
$\Delta\varepsilon$	---	0.00	0.00	0.00	0.00
εbar	9.33	9.65	9.48	9.55	9.50
S_ε	5.93	11.73	6.13	6.60	5.18
E_ε	-0.17	-0.14	-0.16	-0.15	-0.15
R_ε	---	0.03	0.02	0.02	0.02
D_ε	---	0.03	0.02	0.03	0.03

TABLE 6.25. Summary of identification results, stiffness degradation, 10% noise

194

6.6.4.2.1.3 Identification of baseline and degraded epsilon states at 1% noise pollution

	Case 11	Case 12	Case 13	Case 14	Case 15
k^*	39.48	39.48	39.48	39.48	39.48
Δk	---	0.00	0.00	0.00	0.00
kbar	40.88	40.94	41.24	40.83	40.85 ·
S_k	3.89	3.90	21.75	2.67	6.38
E_k	0.04	0.04	0.04	0.03	0.03
R_k	---	0.00	0.01	0.00	0.00
D_k	---	0.02	0.02	-0.02	0.00
ω	6.39	6.40	6.42	6.39	6.39
$\Delta\omega$	---	0.00	0.00	0.00	0.00
ε^*	11.23	10.67	11.79	10.11	12.35
$\Delta\varepsilon$	---	-0.05	0.05	-0.10	0.10
εbar	10.78	10.20	11.17	9.69	11.89
S_ε	1.38	1.41	9.13	0.86	2.36
E_ε	-0.04	-0.04	-0.05	-0.04	-0.04
R_ε	---	-0.05	0.04	-0.10	0.10
D_ε	---	-0.41	0.04	-1.27	0.47

TABLE 6.26. Summary of identification results, epsilon degradation, 1% noise

Cases 11 through 15 depict the effect of reducing the Duffing system nonlinear term on the identified results. These cases include 1% noise pollution. Variations in the nonlinear term ε are tabulated in the row beginning with character string $\Delta\varepsilon$. The error in the identified nonlinear term for each of these cases is relatively low for all cases. It is important to note that the error in the identified stiffness parameters for these cases is 4% or less, illustrating the identification algorithm's ability to discriminate damage well.

6.6.4.2.1.4 Identification of baseline and degraded epsilon states at 10% noise pollution

Repeating the above cases from Table 6.26 with 10% noise pollution increases the error in the identified nonlinear term as depicted in Cases 16 through 20, Table 6.27. Again, the error reported in the identified stiffness parameter remains minor, at or below 8%.

	Case 16	Case 17	Case 18	Case 19	Case 20
k^*	39.48	39.48	39.48	39.48	39.48
Δk	0.00	0.00	0.00	0.00	0.00
kbar	42.43	42.47	41.55	41.53	41.73
S_k	22.91	14.48	34.70	26.88	24.27
E_k	0.07	0.08	0.05	0.05	0.06
R_k	0.04	0.04	0.02	0.02	0.02
D_k	0.07	0.11	0.02	0.02	0.04
ω	6.51	6.52	6.45	6.44	6.46
$\Delta\omega$	0.02	0.02	0.01	0.01	0.01
ε^*	11.23	10.67	11.79	10.11	12.35
$\Delta\varepsilon$	---	-0.05	0.05	-0.10	0.10
εbar	9.33	8.83	10.16	8.62	10.52
S_ε	5.93	4.65	11.01	7.74	7.22
E_ε	-0.17	-0.17	-0.14	-0.15	-0.15
R_ε	-0.13	-0.18	-0.06	-0.20	-0.02
D_ε	-0.24	-0.42	-0.06	-0.28	-0.04

TABLE 6.27. Summary of identification results, epsilon degradation, 10% noise

196

6.6.4.2.1.5 Identification of baseline and combined stiffness and epsilon degraded states at 1% noise pollution

Cases 21 through 25 highlight the identification statistics for the nonlinear Duffing oscillator with combined variations of stiffness degradation and epsilon degradation and enhancement. Noise pollution is defined as 1% for these cases. R_k and R_e closely match the parameter perturbations in all cases. The reported error remains 4% or less for all identified parameters. The standard deviations for the identified data are also relatively small, indicating that the data dispersion is minor for the 3000 simulations performed.

	Case 21	Case 22	Case 23	Case 24	Case 25
k*	39.48	37.50	37.50	35.53	35.53
Δk	---	-0.05	-0.05	-0.10	-0.10
kbar	40.88	38.76	38.82	37.04	36.94
S_k	3.89	4.25	2.01	4.64	3.93
E_k	0.04	0.03	0.04	0.04	0.04
R_k	---	-0.05	-0.05	-0.09	-0.10
D_k	---	-0.50	-1.02	-0.83	-1.00
ω	6.39	6.23	6.23	6.09	6.08
$\Delta\omega$	---	-0.03	-0.03	-0.05	-0.05
ϵ*	11.23	10.67	11.79	10.11	12.35
$\Delta\epsilon$	---	-0.05	0.05	-0.10	0.10
ϵbar	10.78	10.28	11.37	9.66	11.92
S_ϵ	1.38	1.22	0.74	1.35	1.09
E_ϵ	-0.04	-0.04	-0.04	-0.04	-0.04
R_ϵ	---	-0.05	0.06	-0.10	0.11
D_ϵ	---	-0.41	0.80	-0.83	1.04

TABLE 6.28. Summary of identification results, combined variation, 1% noise

197

6.6.4.2.1.6 Identification of baseline and combined stiffness and epsilon degraded states at 10% noise pollution

Cases 26 through 30 illustrate the effect of combinations of the nonlinear term degradation and enhancement with stiffness parameter degradation as in Cases 21 through 25. Noise pollution is increased to 10% for these cases. As noted in the above cases, the identified errors in the parameters is relatively low, especially given the higher noise pollution level.

	Case 26	Case 27	Case 28	Case 29	Case 30
k^*	39.48	37.50	37.50	35.53	35.53
Δk	---	-0.05	-0.05	-0.10	-0.10
kbar	42.43	39.03	40.90	38.28	38.47
S_k	22.91	65.19	21.47	33.40	27.00
E_k	0.07	0.04	0.09	0.08	0.08
R_k	---	-0.08	-0.04	-0.10	-0.09
D_k	---	-0.05	-0.07	-0.12	-0.15
ω	6.51	6.25	6.40	6.19	6.20
$\Delta\omega$	---	-0.04	-0.02	-0.05	-0.05
ε^*	11.23	10.67	11.79	10.11	12.35
$\Delta\varepsilon$	---	-0.05	0.05	-0.10	0.10
εbar	9.33	9.21	9.69	8.45	10.43
S_ε	5.93	17.09	7.04	9.72	7.75
E_ε	-0.17	-0.14	-0.18	-0.16	-0.16
R_ε	---	-0.01	0.04	-0.09	0.12
D_ε	---	-0.01	0.05	-0.09	0.14

TABLE 6.29. Summary of identification results, combined variation, 10% noise

6.6.4.3 Identification verification using Neural Networks

A number of test cases drawn from the nonlinear models identified in Table 6.23 above were processed through a neural network algorithm. The cases selected incorporated 10% noise pollution with variations in the stiffness and nonlinear terms. The cases chosen for this study included 8, 17, 18, 27 and 28 with Case 6 as the baseline. The neural network architecture followed that described in detail in Chapter 5, Section 5.3.2.2, having two inputs $(x, \dot{x})$ and one output $\hat{r}(x(t), \dot{x}(t))$. The topology of the training network incorporated 15 nodes in the first hidden layer and 10 nodes in the second hidden layer as a typical three-layer feedforward net.

The identification procedure consisted of two phases; network training utilizing the baseline case (Case 6), and identification with the degraded sets (Cases 8, 17, 18, 27 and 28). Initial estimates of the network weights and biases used in replicating the system output through iterative error comparisons were randomly assigned. The training phase was performed with Adaptive Random Search (ARS) algorithm (Masri et al, 1999) incorporating a hyperbolic tangent function defining the node nonlinearity. The ARS algorithm performs a specified number of iterations searching for a global maximum. A total of 25 global searches were specified for this effort, with 20 local searches at each step. The rms error of the fit is optimized, and leads to the selection of the weights and biases (reference Figure 6.78).
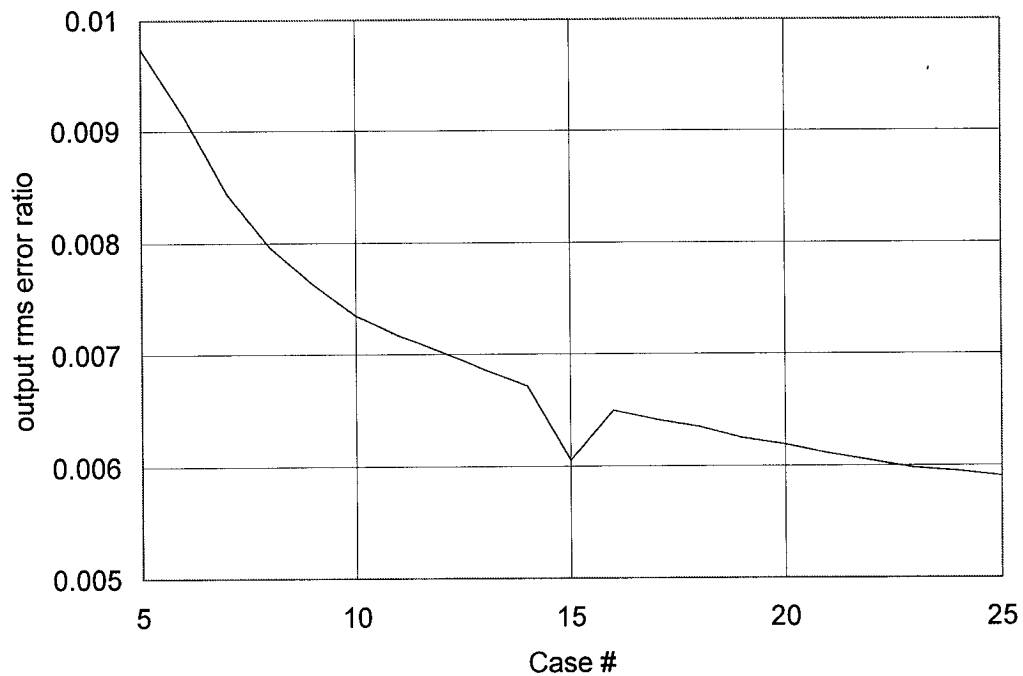
FIGURE 6.78. Neural network output rms error for nonlinear model

A comparison of the measured and identified restoring force for the baseline case, Case 6, is depicted in Figure 6.79. As noted in the studies performed with the Chebyshev restoring force algorithm, the error in identifying the system response is reasonable.

With the neural network weights and biases determined for the baseline case, the damaged states were then processed through the trained network. Comparisons of the network identified restoring force and the associated error for each damaged state reveals the trained algorithm's ability to detect system changes while under fairly substantial noise pollution. Due to the nonuniqueness of weights and biases within the neural network architecture and the fact that the algorithm is nonparametric by

200

definition (that is, the network weights and biases have no direct correspondence to the physical system's properties) changes in the structural system are best detected through statistical means. The mean-square error of the identified output from a "damaged" state, represented by cases 8, 17, 18, 27 and 28, are compared to that of the baseline case (case 6). Case 6 represents the reference or baseline state of the system with 10% noise pollution. Changes to the physical system from this state are easily noted as the reference network no longer replicates the measured output. The greater the deviation in the physical system from its baseline state (e.g., 5% stiffness degradation as in Case 8) the greater the error between the measured (physical system) and that identified through the predefined reference neural network.
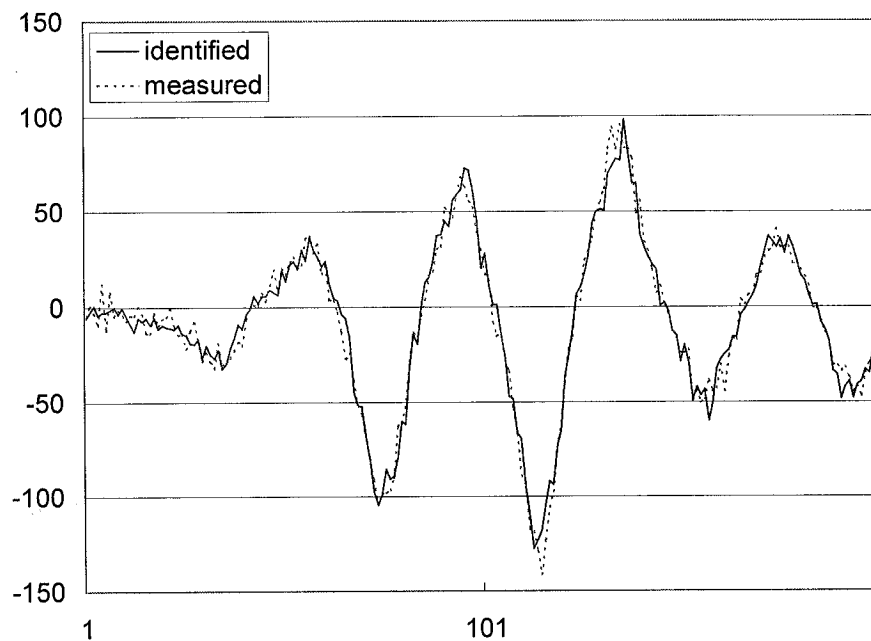
FIGURE 6.79. Measured versus identified restoring force for nonlinear model baseline case, Case 6, neural network algorithm

201

Table 6.30 highlights the mean-squared error and computed statistics for these cases. The data presented in Table 6.30 is also graphically portrayed in Figure 6.85. The second column of Table 6.30 contains the normalized mean error values of the identified system response to the measured response. The mean normalized error for the baseline case (Case 6) is 23.6%, based on the ANN weights and biases determined through training the network with a separate data set representative of the amplitude and frequency response defining Case 6. This result is relatively high due to excursions of the identified response from that measured at a few peak amplitude values as evidenced by a close inspection of Figure 6.79. A more complex network topology would reduce this reported error. However, the key is to look at the network's ability to discern changes to the baseline system.

Processing the remaining cases through the same trained network topology yields the mean and standard deviations of the computed error as given in columns 2 and 3 of Table 6.30. The estimated standard deviations center around 0.1. The variation in the mean for the various "damaged" states represented by the investigated cases is relatively small, but it is clear from inspection of the fourth column that the system has experienced changes from it's reference state (Case 6).

Recall that Case 8 represents the system with a 5% reduction in stiffness. The computed dimensionless error tabulated in column 4 for this case reveals a 1.2% increase for this case.

202

The dimensionless error ratio "R" presented in column 5 highlights the significance of the deviations in the ANN-estimated system response. Column 6 quantitatively reveals the relative significance of changes in the ANN deviation error as compared to the dispersion in the distribution of the error statistics around the sample mean.

As an example, $R = 4.3\%$ for Case 27, signifying that the mean of the deviation error has changed by 4.3% of the standard deviation of the corresponding tracking errors. This is construed as possible evidence of change in the system, although the reported variation is quite small. Further investigation of these sensitivity issues is warranted.

Case	Mean of error	Standard deviation of error	$\dfrac{\mu}{\mu_{ref}}$	$\dfrac{(\mu - \mu_{ref})}{\mu_{ref}}$	$\dfrac{(\mu - \mu_{ref})}{\sigma}$	$\dfrac{\sigma}{\sigma_{ref}}$
6	0.236	0.098	1.000	0.000	0.000	1.000
8	0.239	0.095	1.012	0.012	0.029	0.969
17	0.235	0.097	0.996	-0.004	-0.011	0.986
18	0.237	0.099	1.007	0.007	0.016	1.005
27	0.240	0.093	1.017	0.017	0.043	0.944
28	0.238	0.097	1.011	0.011	0.027	0.987

TABLE 6.30. Mean-squared error for identified damage states

Note that the data presented in the following figures (Figures 6.80 through 6.84) reveals the excellent fit of the ANN identified system response to that measured in the simulations. Each case was simulated forty times with the stationary random excitation seed varied similarly by a prescribed random number. The simulations of

203

the "damaged" cases were all polluted by 10% noise, which masked some of the

"damage" introduced in each system, such as 5% stiffness degradation.

A cursory glance at these plots might lead the reader to consider them to be identical,

but overlays of the response data suggest otherwise. There are subtle changes in the

system response amplitude and frequency content between each "damaged" case.

Figure 6.85 highlights the effect of the various cases of system degradation utilizing

a bar chart. The error statistics produced for the baseline case did not incorporate the

network training data.
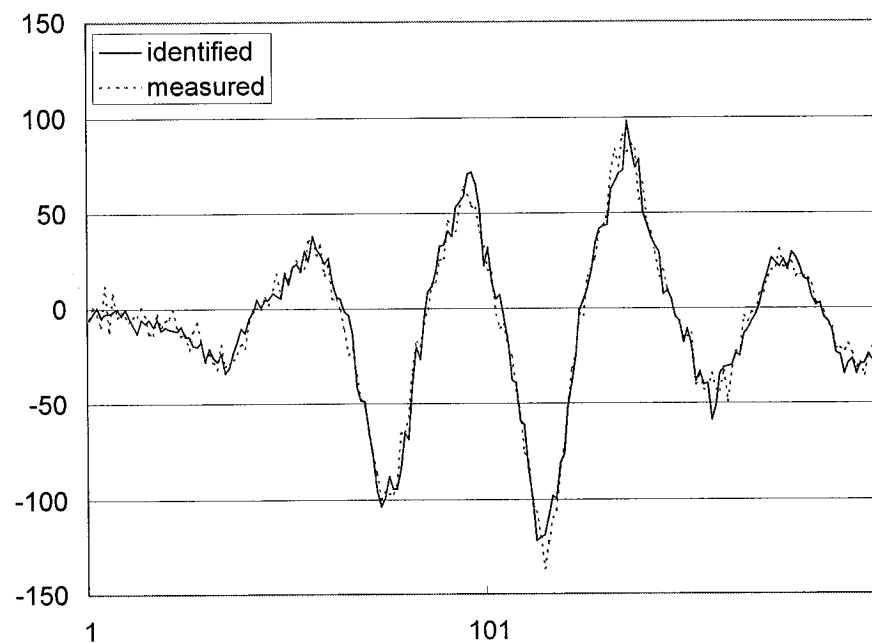
FIGURE 6.80. Trained network output comparison, Case 8
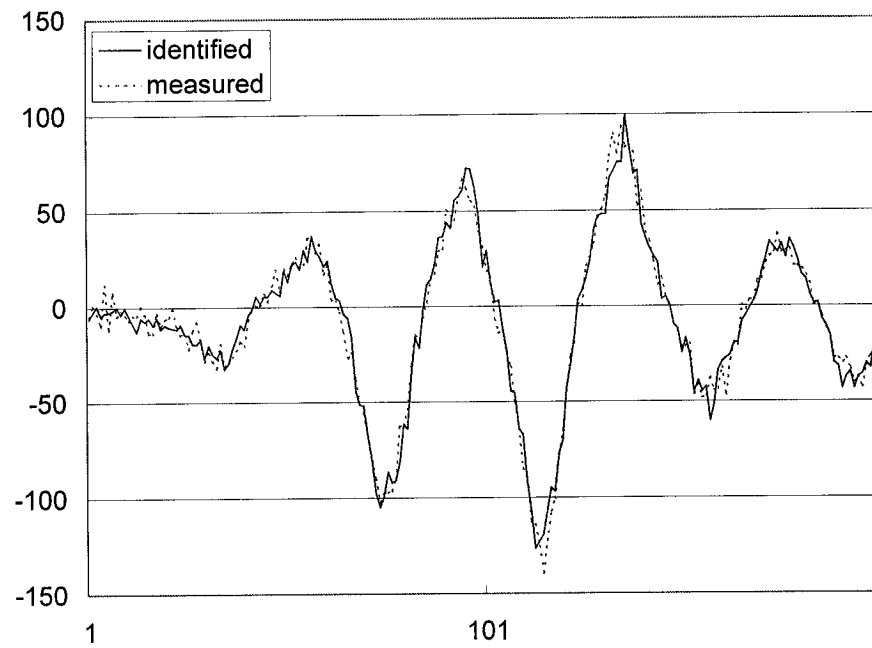
FIGURE 6.81. Trained network output comparison, Case 17
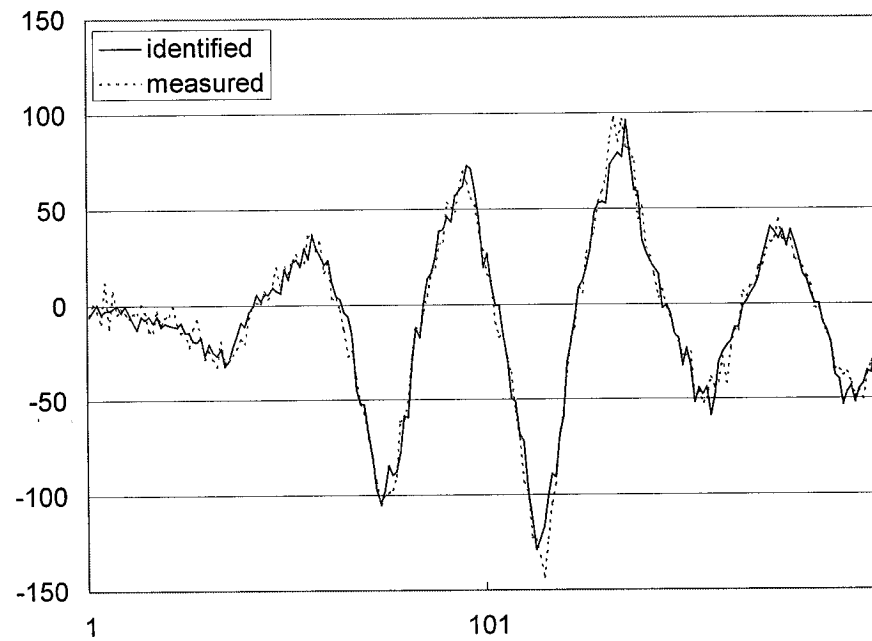
FIGURE 6.82. Trained network output comparison, Case 18

205
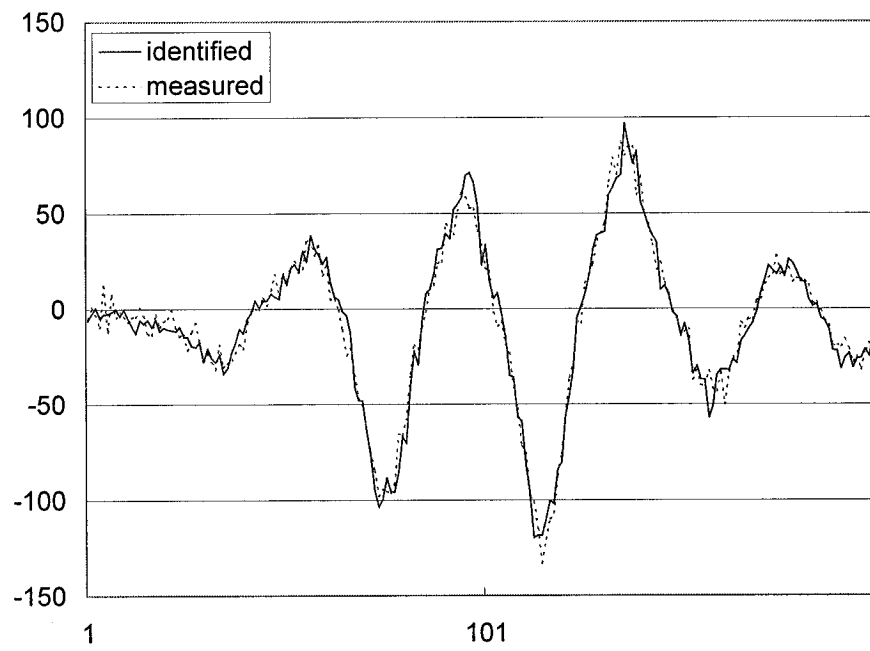
FIGURE 6.83. Trained network output comparison, Case 27
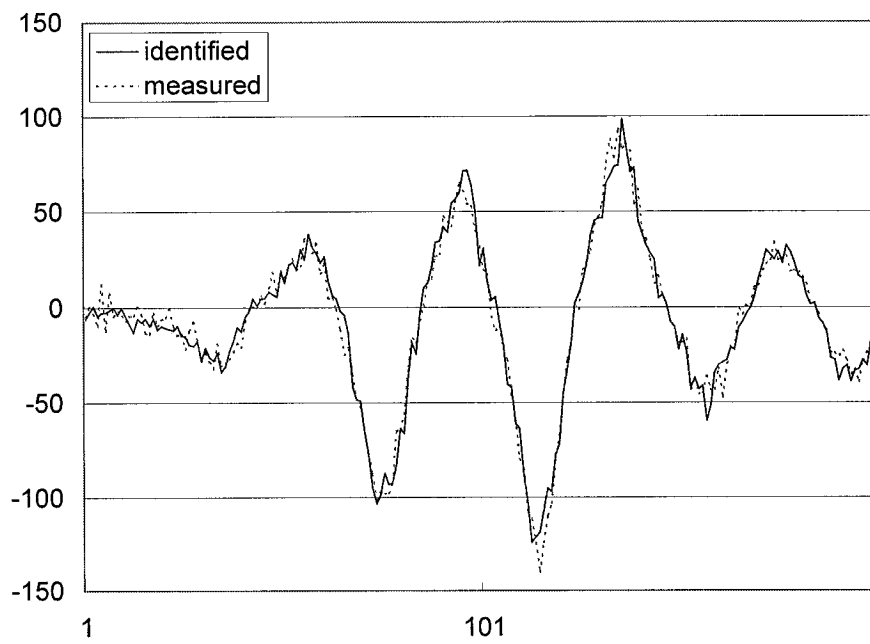
FIGURE 6.84. Trained network output comparison, Case 28

206
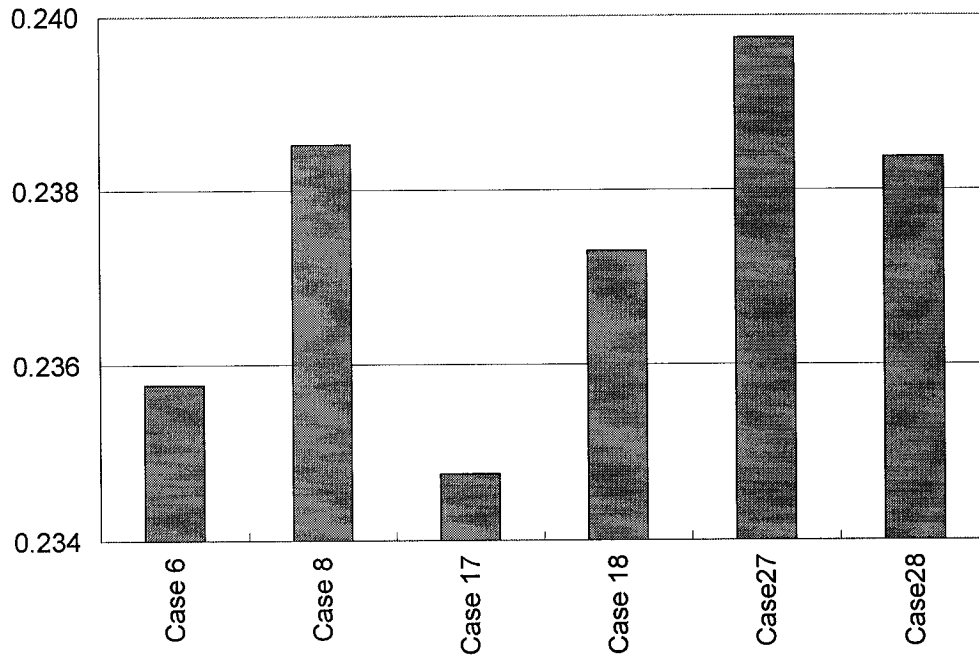
FIGURE 6.85. Comparison of error in identifying cases 8, 17, 18, 27, 28

6.6.4.4 Identification verification using the Least Squares Recursive Method

The recursive least-squares parametric identification algorithm was next utilized to evaluate the same cases selected for identification with the neural network algorithm described in Section 6.6.4.4. A detailed discussion of this algorithm is presented in Chapter 5, Section 5.3.1.

As in Section 6.6.4.3, Case 6 was considered the baseline. The damaged states were identified as cases 8, 17, 18, 27 and 28. These cases incorporated 10% noise pollution with variations in the stiffness and nonlinear terms.

Figure 6.86 highlights the excellent fit between the simulated restoring and that

identified by the recursive least-squares identification algorithm. A comparison of

the identified thetas to the baseline for each case as presented in Figures 6.87 through

6.91 reveals damage detection. Note that there is a discernable difference in the

theta values for each damaged case when referenced to the undamaged baseline case.

Each of the figures below details a particular theta parameter used in the

identification algorithm. The abscissa scaling for the plots varies to highlight the

parameter fluctuations until they reach steady state values. Note that there are

discernable variations in some of the parameters for the different cases, particularly

Case 17.
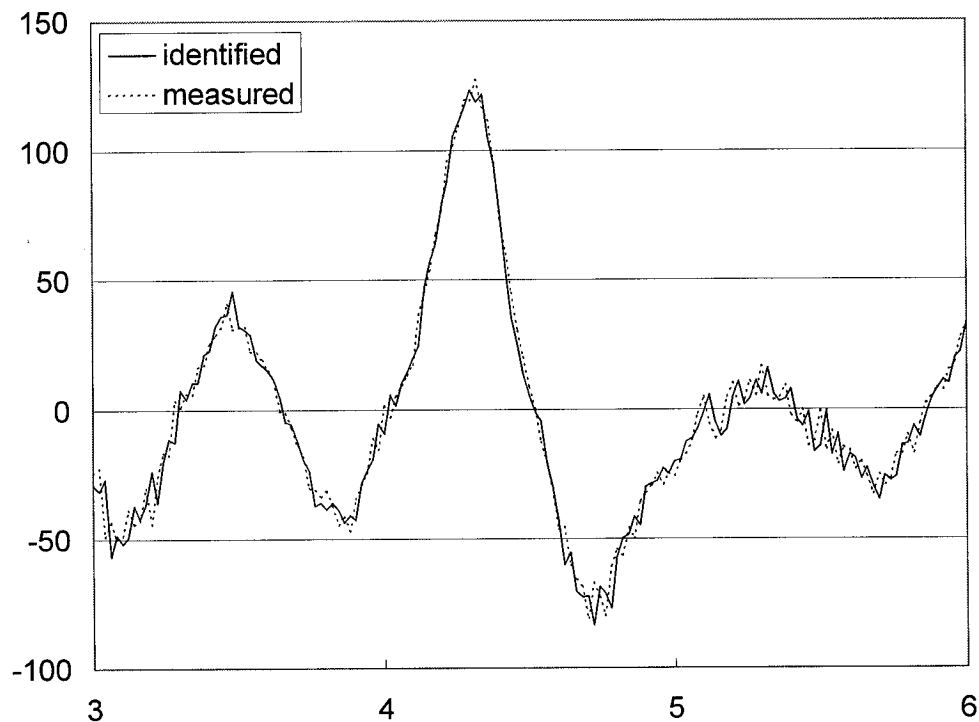
FIGURE 6.86. Measured versus identified restoring force for nonlinear model
baseline case, Case 6, recursive least-squares algorithm

208
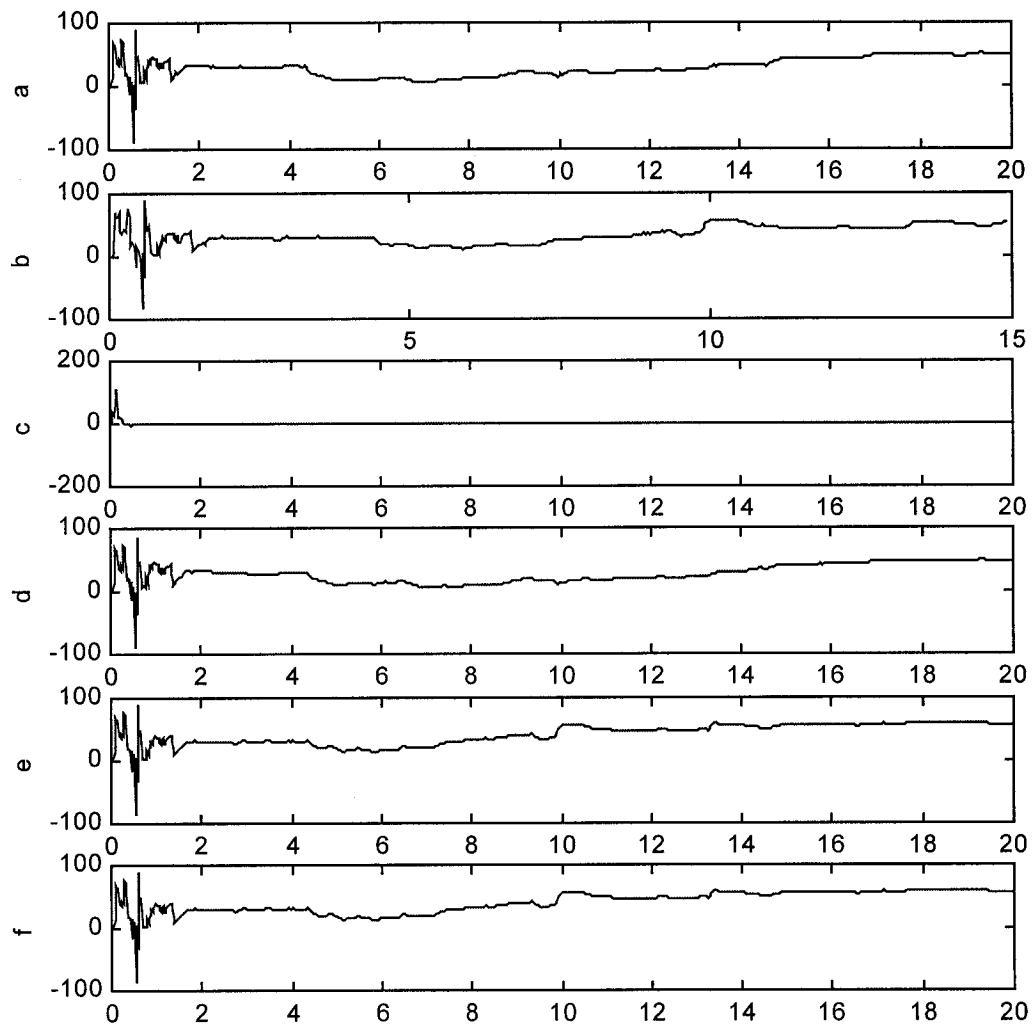
FIGURE 6.87. Theta 1. (a) Reference case. (b) Case 8. (c) Case 17. (d) Case18.
(e) Case27. (f) Case 28.
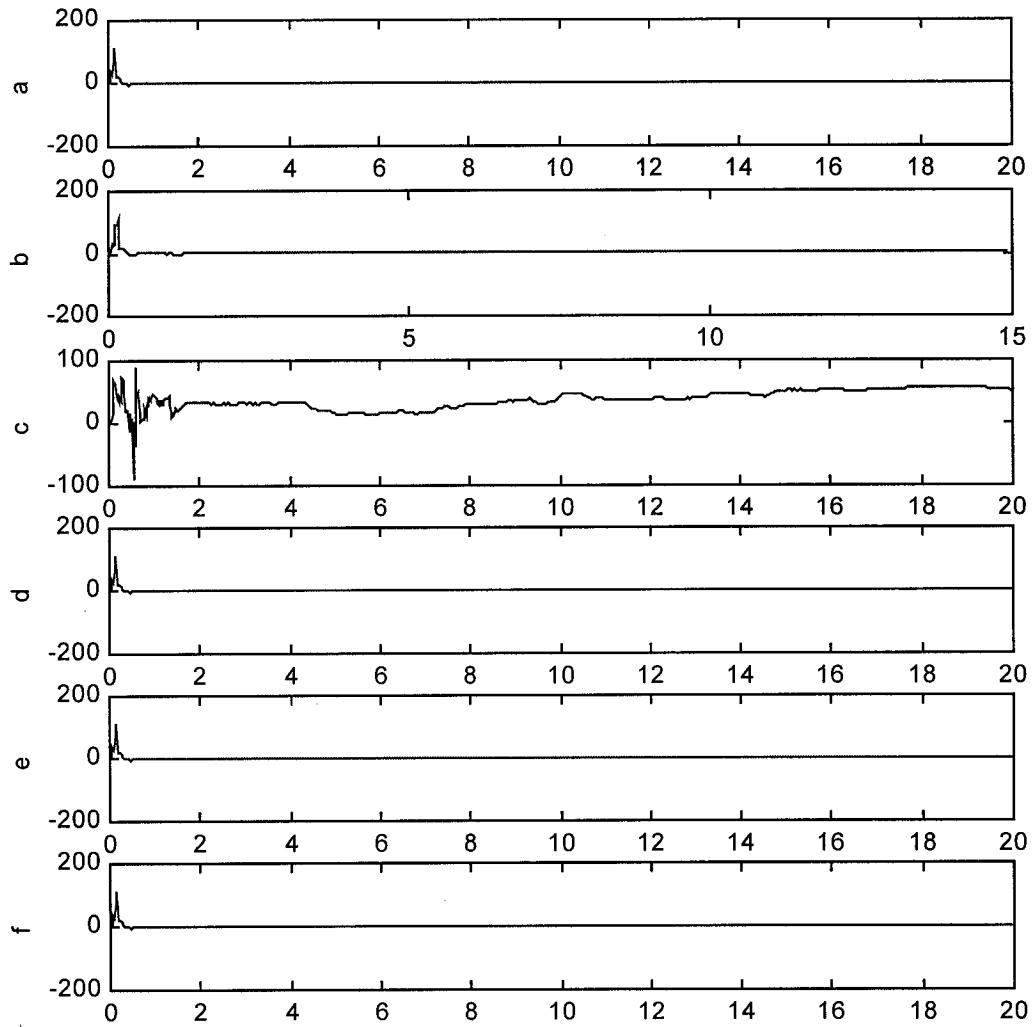
FIGURE 6.88. Theta 2. (a) Reference case. (b) Case 8. (c) Case 17. (d) Case18. (e) Case27. (f) Case 28.

210
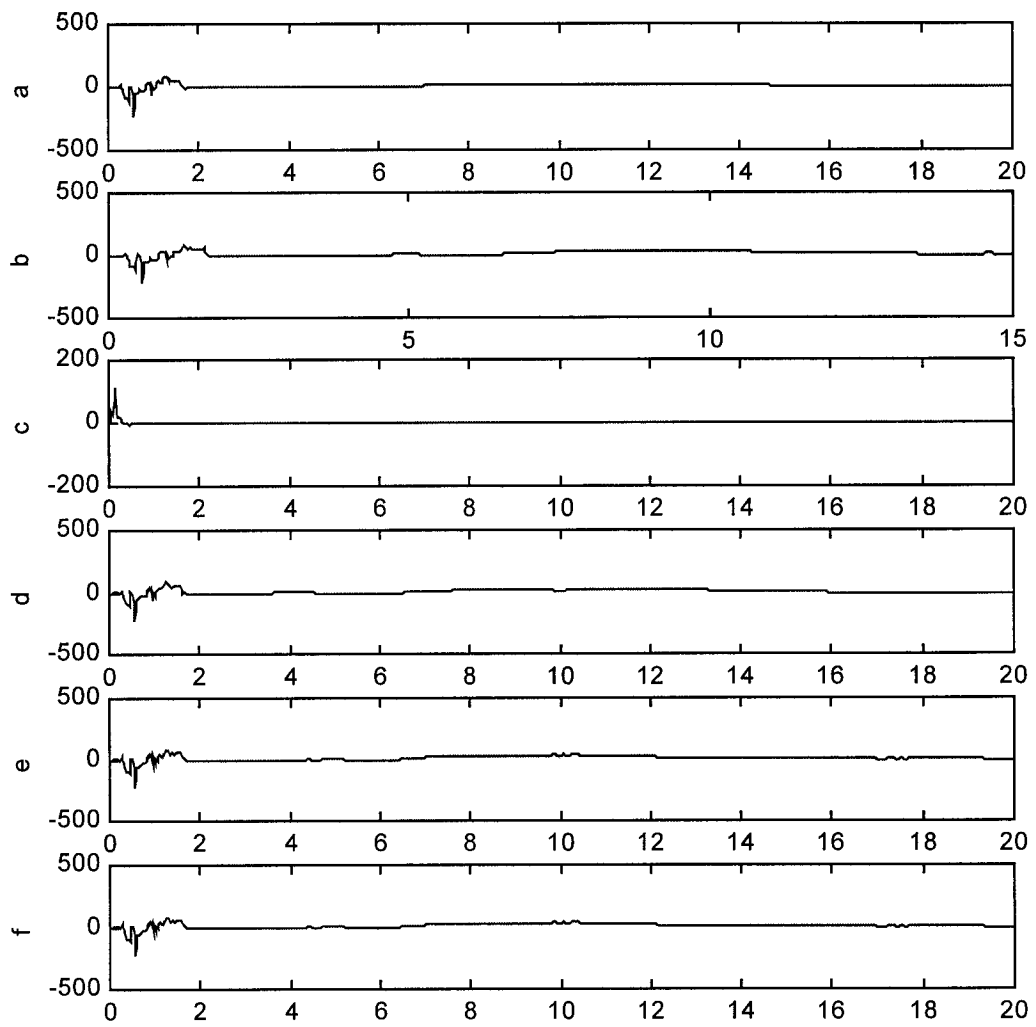
FIGURE 6.89. Theta 3. (a) Reference case. (b) Case 8. (c) Case 17. (d) Case18. (e) Case27. (f) Case 28.

211
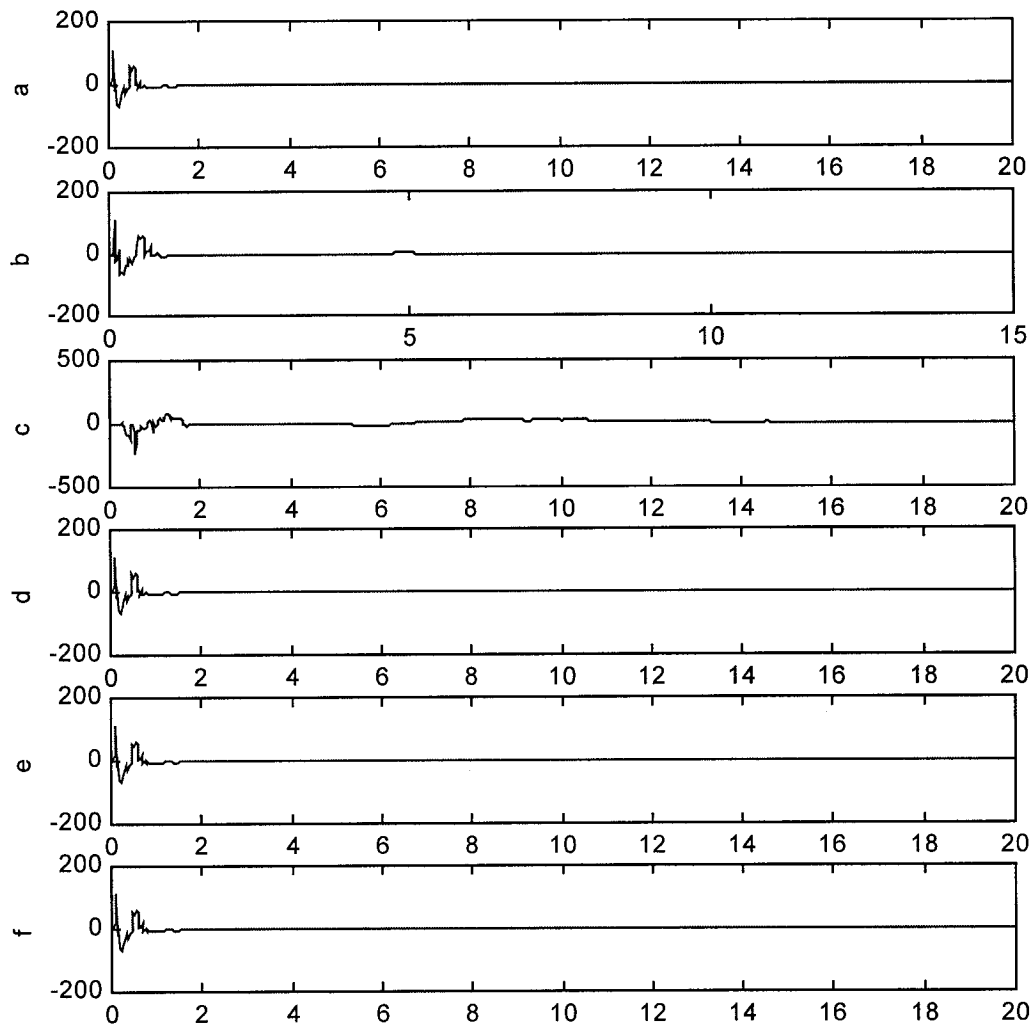
FIGURE 6.90. Theta 4. (a) Reference case. (b) Case 8. (c) Case 17. (d) Case18. (e) Case27. (f) Case 28.

212
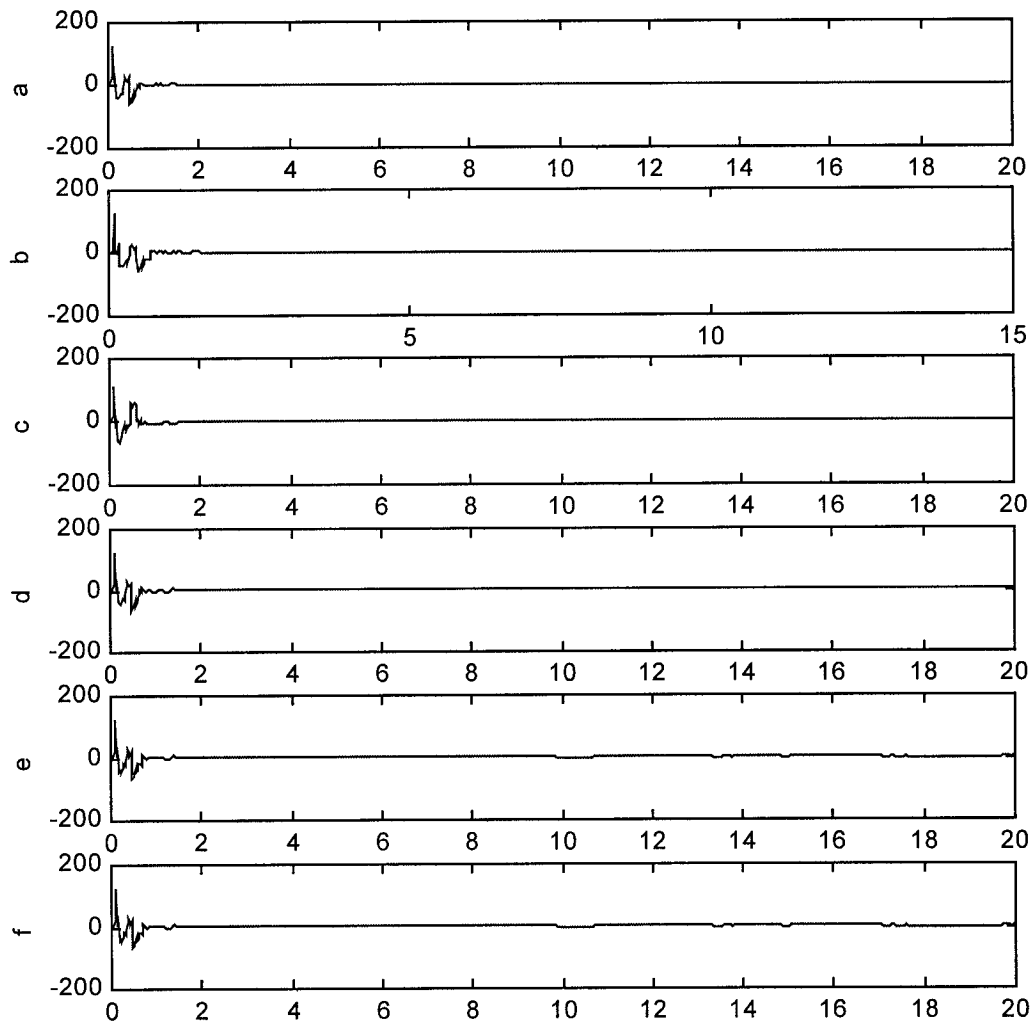
FIGURE 6. 91. Theta 5. (a) Reference case. (b) Case 8. (c) Case 17. (d) Case18. (e) Case27. (f) Case 28.

213
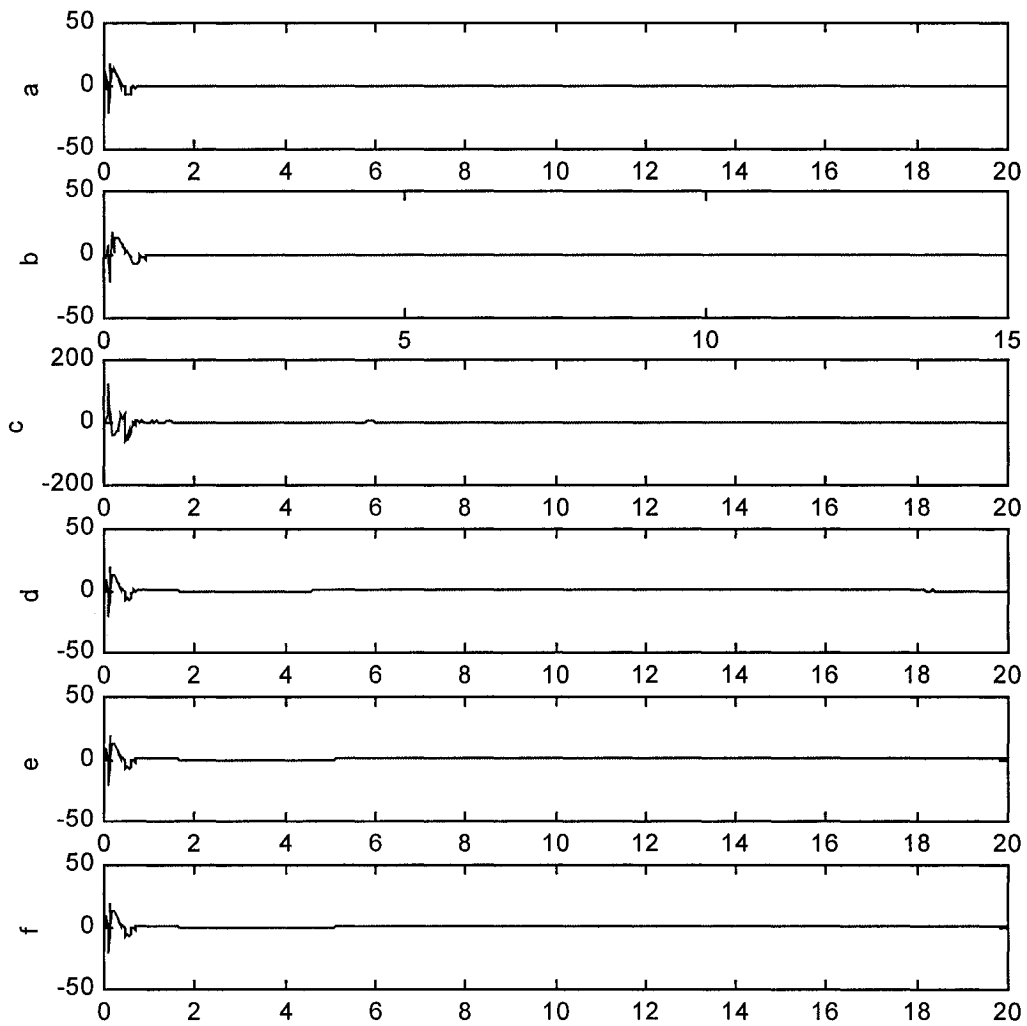
FIGURE 6. 92. Theta 6. (a) Reference case. (b) Case 8. (c) Case 17. (d) Case18. (e) Case27. (f) Case 28.

214

The variation in theta values for a particular "damaged" state can be investigated to reveal system changes due to possible degradation. As an example, Case 8 represents the system stiffness degraded by 5% with 10% noise pollution. Comparing the identified theta parameters for this case to that of the reference (Case 6), highlights the effectiveness of the Least Squares Recursive Algorithm in detecting system changes even under the influence of noise pollution. The algorithm parameters (theta values) can be correlated to specific system parameters to the extent of ascertaining change to a parameter as defined in Section 5.3.1. The mean and standard deviation of the rms error computed between the reference case and Case 8 varies for each of the seven identified theta values as illustrated in Table 6.31. The tabulated mean m* represents the rms mean of the specific case to the reference, normalized by the square of the sum of the reference values. This is similar to the presentation in Table 30. These variations from the established baseline case clearly reveal system deviations. Thus, the algorithm successfully identified the forced degradation.

Theta	Case 8		Case 17		Case 28	
	$\mu^*_{rms\ error}$	$\sigma_{rms\ error}$	$\mu^*_{rms\ error}$	$\sigma_{rms\ error}$	$\mu^*_{rms\ error}$	$\sigma_{rms\ error}$
1	0.015	268.464	0.035	902.939	0.018	302.812
2	0.005	0.039	1.170	1024.655	0.005	0.166
3	0.033	75.536	0.103	2047.326	0.028	54.521
4	0.040	15.023	0.903	3069.259	0.040	14.739
5	0.035	13.415	0.238	834.182	0.036	13.268
6	0.060	0.212	3.889	740.022	-0.060	0.208
7	0.151	0.205	2.765	55.711	0.154	0.202

TABLE 6.31. Mean-squared error for identified damage states

215

Figures 6.94 through 6.98 illustrate the identified system restoring force for each of the five investigated "damaged" cases plotted against the baseline case. Variations in peak amplitude values are readily noted in each of these plots. Larger excursions in peak amplitudes are evident in Figures 6.94, 6.97 and 6.98. These figures represent the "damaged" states wherein the stiffness parameter was degraded. The effect of changing the nonlinear term epsilon in the Duffing model is less pronounced, though evident as well.
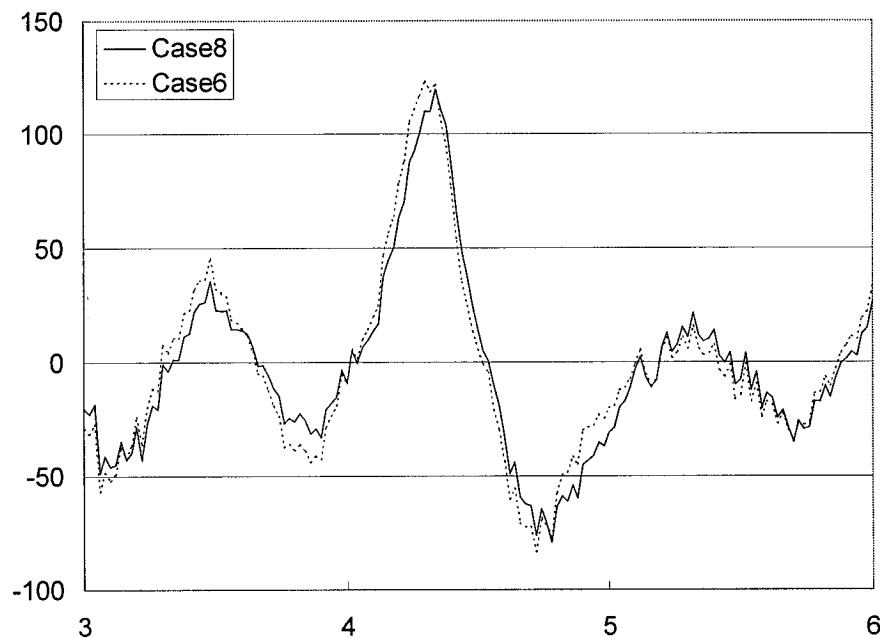
FIGURE 6. 94. Identified system response (Case 8) versus baseline case

216
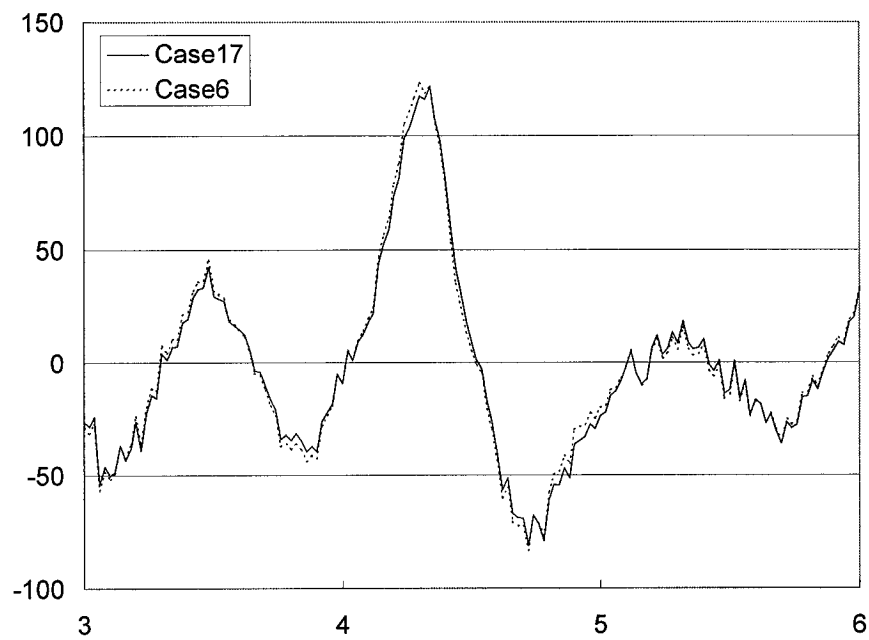
FIGURE 6. 95. Identified system response (Case 17) versus baseline case
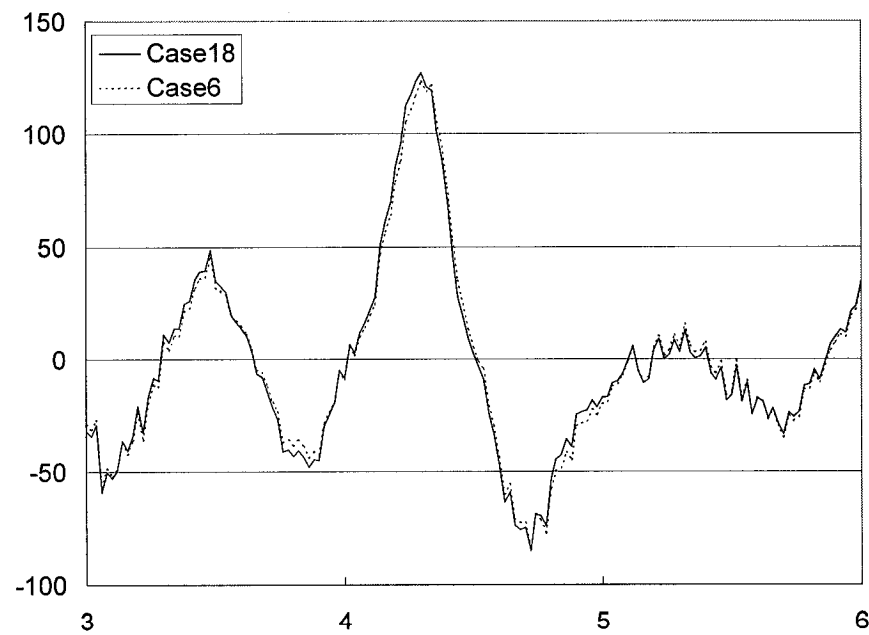
FIGURE 6. 96. Identified system response (Case 18) versus baseline case

217
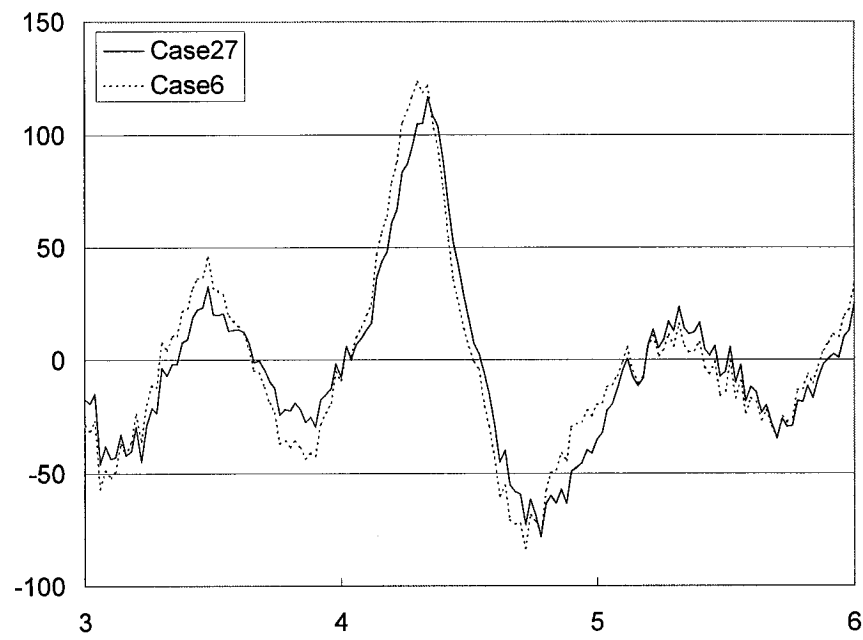
FIGURE 6. 97. Identified system response (Case 27) versus baseline case
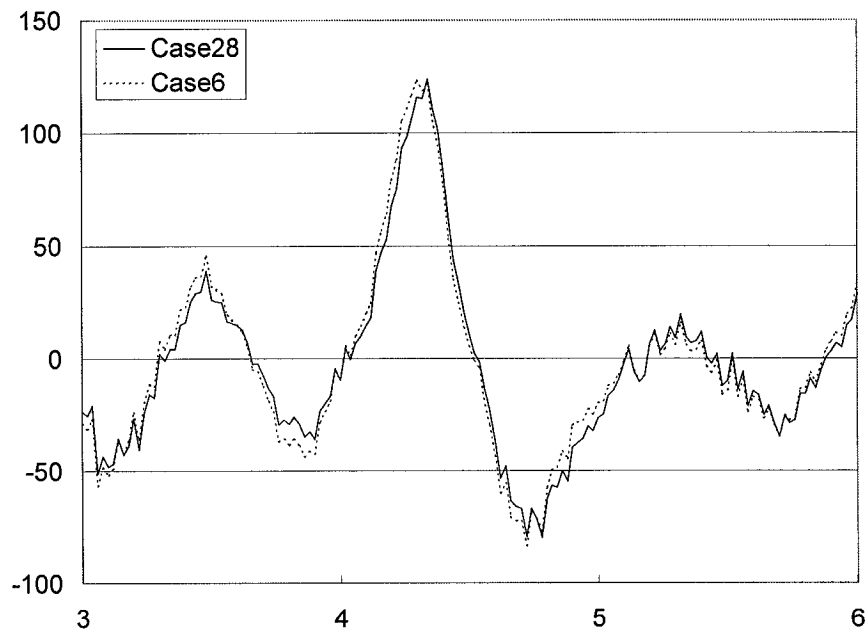
FIGURE 6. 98. Identified system response (Case 28) versus baseline case

218

6.6.4.5 Summary

Simulation data was processed through the three identified algorithms to determine their ability to detect subtle changes in the system. Various levels of noise pollution were incorporated into the simulations to realistically evaluate the algorithms' sensitivity to slight parameter changes, as real applications will always include the effects of measurement and ambient noise. The primary focus of the analysis centered on the restoring force algorithm based on orthogonal Chebyshev polynomials. The restoring force algorithm using Chebyshev polynomials was selected for the majority of the simulation studies for its ability to replicate the response of highly nonlinear systems under virtually any excitation with low-level polynomial approximations. This fact is important in any attempt to provide real-time data processing as proposed herein. Section 6.6.4.2 presented the resulting data in a variety of forms to extract the true essence of the algorithm's sensitivity to predefined system "damage". The neural network approach was discussed with selected results highlighted in Section 6.6.4.3 using a subset of the data presented earlier. Finally, the least squares recursive algorithm was evaluated for specific cases.

These three algorithms were selected because they do not require any *a priori* information of the physical system structure. The restoring force method provides the advantage that the resulting identified parameters are easily translated into power series form, thereby allowing direct correlation to the parameters of an assumed

219

system model. A disadvantage of course is reliance on an assumed model of the physical system must be carefully evaluated through substantial parametric analysis to ascertain the accuracy of the model.

6.6.4.5.1 Restoring force algorithm

The dimensionless measures of system change with respect to the reference system stiffness, R and D, as tabulated above, clearly indicate parametric variations for known system degradation. For example, the sensitivity of these measures is evident for the linear case with a prescribed stiffness reduction of only 1%. Increasing noise pollution levels are clearly discriminated in measure D, as evidenced in Tables 6.12 through 6.15.

Damping parameter reductions are more difficult to discriminate than the stiffness parameter degradation discussed previously. As noted earlier, this is to be expected because the stiffness term dominates the restoring force representation of typical physical systems. In the undamped system, recall that the stiffness parameter was set to 39.478, while the damping parameter was 1.2566, assuming 10% system damping. Thus, the ratio of the stiffness parameter to the damping parameter is approximately 31.42. Equalization of parametric contributions in the restoring force equation of the linear system

$$f(x, \dot{x}) = kx + c\dot{x} \qquad (6.53)$$

220

requires similar velocity to displacement ratios. Actual displacement and velocity values depend strongly on the excitation and system dynamics; but for a 10% damped system, the ratio of velocity to displacement will not approach that of the stiffness to damping parameters.

However, using the revised measures of change, R and D, computed from the damping parameters instead of the stiffness parameters as defined in equations 6.48 through 6.52, allows more sensitive detection of system damping changes. For clarification purposes, it is important to understand that the dimensionless ratios depicted at the bottom of these tables, computed from the damping parameter values, follows the definitions of the ratios given in equations 6.48 through 6.52. The stiffness values defined in the measures are simply replaced by the corresponding damping values.

The tabulated results of combined parameter reduction/enhancement are given in Tables 6.20 through 6.22. Once again, system changes are easily noted in the dimensionless measures.

Clearly, from the above discussion, any health monitoring system utilizing these measures must evaluate them for both the identified stiffness and damping parameters to enhance overall sensitivity to damaged states. Another approach is to rely on detected frequency shifts in the identified system referenced to a baseline

221

model. While the tabulated simulation results in Tables 6.12 through 6.22 reveal substantial increases in frequency shifts for increasing noise pollution, this measure does not discriminate well between changing system parameter values.

6.6.4.5.2 Neural network algorithm

The statistics presented in Table 6.30 indicate the presence of detected change in the identified system response from the baseline case. Figure 6.85 clearly displays the change in the identified system statistics for the "damaged" states. Development of an assumed model to replicate an actual physical system would allow damage thresholds to be established. System variations beyond the prescribed thresholds would trigger an investigation of the physical system for potential damage.

6.6.4.5.3 Least squares recursive algorithm

The least squares recursive algorithm uses a modified Buoc-Wen algorithm to define the physical or simulated system investigated. This algorithm was developed to capture a broad class of physical systems, from linear to hysteretic. The algorithm employs parameters, which are varied in a step-wise solution to converge to the exact measured system output, the restoring force in this application. Investigation of the changes in these parameters from the baseline, as presented in Figures 6.86 through 6.92, reveals system changes. Further analysis utilizing statistics to compute the rms error for each identified algorithm parameter, theta, highlights the detected system change.

222

6.6.4.5.4 Concluding remarks

The identification algorithms have been shown effective in discriminating system change at noise pollution levels of up to 10% with relatively high degrees of accuracy. The measures of R and D in the restoring force algorithm analysis, the rms error determined from the neural network results, and the rms error of the identified theta values from the least squares recursive method proves that damage detection thresholds can be safely established to facilitate detection of system degradation as a precursor to major damage.

223

7.0 Experimental Studies

7.1 Impetus

The simulation tools discussed earlier provide an excellent means of calibrating the identification algorithms under investigation. They also allow in-depth statistical analysis of various system scenarios. The relationships between degrading parameter states and the system response are easily quantified. Parameter variability studies and noise pollution effects are also readily obtained at a fraction of the cost of experimental testing.

However, there are a number of system influences not necessarily apparent from simulation efforts, regardless of the detail. While issues of parameter variability, noise pollution effects and the sensitivity of identification algorithms can be well documented from simulation work, modeling errors inherent with any attempt at simulating real-world physics are not easily defined. Dynamic systems generally cannot be categorized or modeled accurately due to subtle nonlinearities. Thus, the purpose of experimental testing is to define the underlying physics of the problem.

This chapter introduces the experimental design, data and results. Systemic dependencies across key variables – amplitude, frequency, temperature – are explored. Comparisons are drawn between these experimental results and those predicted by simulation models. Discussions on the implications of this testing and

224

analysis on the prospects for structural health monitoring tools are interspersed throughout this chapter.

7.2 Anticipated Results

A key result to be obtained in the experimental testing of a viscous damper lies in the identification of the damper properties. Dampers are specified according to the simple equation

$$F_d = c\dot{x}^n \tag{7.1}$$

where F_d represents the damped system force, c is the coefficient of system damping, $\dot{x}$ is the measured velocity, and the exponent n defines the degree of nonlinearity inherent in the damper. The design specifications typically cite maximum force, stroke, velocity and operating temperature requirements, with the exponent n determined to resolve these quantities and provide the necessary system damping. The size and number of fluid orifices, the damper fluid chamber volume, and the viscous fluid all contribute to meeting the design specifications.

The damper utilized in these tests was designed with a force rating of 10 kips, a velocity capacity of 70 ips, and a 12 inch total stroke. The damping coefficient c and the exponent n were set to meet the specified parameters. Experimental data was then fed into the identification algorithms to determine the damping coefficient, following the procedures discussed in the simulation studies earlier.

Quantifying the modeling errors from the simulated mathematical representations of the system is another key result of experimental testing. Simulation models of the system for study inherently incorporate modeling errors, as the exact dynamical behavior of the system cannot easily be replicated through mathematical representations without some *a priori* information. The real system will not likely fit the models assumed in the simulation work. The Duffing, Van der Pol, and Buoc-Wen simulation models may exhibit similar system characteristics to that measured during experimental testing, but will not likely reveal the subtle underlying physics of the damped system. The importance of this discussion is that while much work can be accomplished through simulation efforts, including in-depth variability analysis as reported in Chapter 6, the assumption of model types used in simulation studies does introduce some level of error. Experimental testing is the only true means of quantifying the behavior of a system in the absence of validated modeling knowledge.

Another distinction to be made is that while errors exist in simulation studies from assumed mathematical descriptions of the system, the identification procedures utilized to process system response data are largely immune to these effects. The identification algorithms simply fit a mathematical representation of the system from measured or simulated system state variable data.

226

7.3 Test Plan

The test plan developed to gather data for this study addressed amplitude, frequency, and temperature effects. For nonlinear systems, which this viscous damper is assumed to be, the effects of amplitude, frequency and temperature variations are expected to be substantial. The silicone fluid in the damper was rated to yield fairly linear output in the range of –40°F to 130°F. Tables 7.1 and 7.2 reveal the test plan for studying the effects of amplitude, frequency and temperature influences on the damper.

Initially, sinusoidal excitations were utilized; then, stationary random signals were applied. The sinusoidal excitation was programmed in an MTS Microconsole. Amplitude gain was controlled via a dial gauge on the MTS Controller front panel.

Temp. Range = 70F-80F		Temp. Range = 90F-100F		Temp. Range = 100F-110F	
Ampl. pk-pk, in	Frequency	Ampl. pk-pk, in	Frequency	Ampl. pk-pk, in	Frequency
1	0.5	1	0.5	1	0.5
2	0.5	2	0.5	2	0.5
4	0.5	4	0.5	4	0.5
6	0.5	6	0.5	6	0.5
1	1	1	1	1	1
2	1	2	1	2	1
4	1	4	1	4	1
1	5	1	5	1	5
2	5	2	5	2	5

TABLE 7.1. Test plan, sinusoidal excitation

227

The random excitation was derived through the following procedure:

1.) creating a vector of normally distributed random numbers,

2.) performing the Fast Fourier Transform (FFT) of this data set,

3.) truncating the frequency content with a Boxcar or rectangular window,

4.) applying a cosine taper at both ends, and

5.) performing the inverse Fast Fourier Transform (IFFT).

The signal frequency content was designed to contain frequencies from DC to 25 Hz through the above technique. The purpose of the cosine taper at the upper and lower bounds of the truncated signal frequencies was to preclude large amplitude scaling effects resulting from the inverse FFT. The taper was applied to the first and last 0.1 Hz frequencies of the windowed signal. Figure 7.1 depicts the psuedo-broadband random signal generation. The amplitude gain was again controlled via a dial gauge on the MTS controller, as it was for the sinusoidal excitation. Figure 7.1a displays the random signal generated as described in

step 1 above. Note that the mean and variance of the random generator were set to one. The power spectral density (PSD) of this signal is given in Figure 7.1b after steps 2 through 4 were completed. Finally, Figure 7.1c reveals the processed data set after step 5, the IFFT was performed.

228
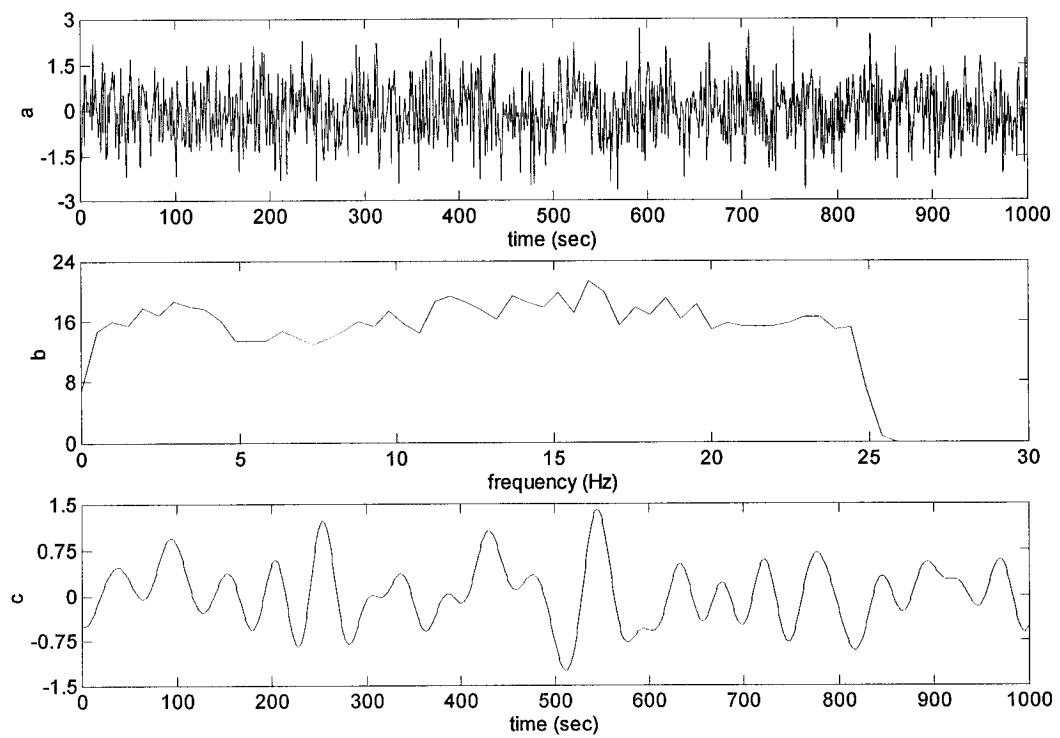
FIGURE 7.1. Psuedo-broadband random excitation generation

Ampl. pk., in	Temp., degrees F
1.6	82
4	92

TABLE 7.2. Test plan, stationary random excitation

7.4 Instrumentation

The system response was captured with various instruments as discussed generally in Chapter 3. These instruments and the procedure employed are discussed below.

An MTS 661.2 force transducer with a factory-calibrated range of ±11000 pounds was coupled to the interface between the actuator and damper. Calibration was verified in the lab by applying a known tensile load to the actuator utilizing a threaded rod assembly. The tapered preload rings on the force transducer were then set and the load removed.

The displacement transducer is also an MTS component coupled to the actuator. It was calibrated to yield 0.5 in/volt output. In addition, a velocity transducer (Alnico-V 7L9-VTZ, S/N 6531) was attached to the system at the damper/actuator interface, and connected to the rigid table. The velocity calibration factor was 7.143 ips/volts.

Acceleration measurements were achieved using an Endevco variable capacitance transducer (S/N 15771) with a calibration factor of 5.032 g's/volt. Temperature was measured with an externally attached transducer calibrated to yield a linear output over the range of 0 to 212°F in an ice bath. The transducer calibration factor was 100°F/volt.

7.5 Calibration

A series of tests were performed to validate the system setup. Physical measurements provided assurances that the displacements and accelerations matched those called for in the system excitation. A Mitoyo® dial gauge with reported accuracy of 0.001 inches was mounted on the reaction mass experimental table to provide direct displacement readings. The system was excited at 0.25 Hz to facilitate visual confirmation of the system displacement. The maximum recorded error between the system displacement input and that directly measured with the gauge was 1.3% at 0.5 in-pk.

The accelerometer was verified by simply placing it on the test table orientated to read positive and then negative vertical acceleration. Measurements of 0.78 g's in the positive direction and 1.23 g's in the negative orientation were recorded. Next, a zero offset of 0.22 g's was measured by setting the accelerometer on edge. Demeaning the acceleration data with this offset yielded −0.99 g's in the negative direction and 1.01 g's in the positive direction. Acquired data for 30 seconds proved that the accelerometer output was stable. The effects of digitization were analyzed and are presented in section 5.2.1.

7.6 Damper Identification

The measured response of the system to various excitations was processed through the restoring force identification algorithm to determine the damper stiffness and

231

damping parameters. Acquired data was first stored in ASCII format in the Unix database discussed in section 5.2.2, then processed through the identification software.

7.6.1 Sinusoidal Excitation

In order to quantify the variability of the system, various representations of the acquired data are presented. Statistical analysis of the data can be derived from amplitude, frequency and temperature variations, utilizing any one of these as the sample set. Additional statistics can be gathered from the same data, only varying multiple parameters. A measure of data scatter, the coefficient of variation ($\frac{\sigma}{rms}$) is used to quantify parameter variation effects. Experimental tests were performed to sufficiently produce statistical confidence in the system behavior.

The test plan utilizing a sinusoidal input to the damper as defined in Table 7.1 was repeated ten times. Data was acquired from each test for 60 seconds. Then, this data was divided in half for processing. Thus, a statistical sampling comprised of 20, 30-second segments was available for analysis. While substantially less rigorous than the sample sets processed during the simulation studies, valuable variability information was gathered nonetheless. Note that only a few tests were performed at 5 Hz, due to the severity of the test on the damper.

The processed data from these tests is presented herein in a variety of plots and tables. Recall from Table 7.1 that the primary variables in the excitation to the damper were amplitude, frequency and temperature. Thus, the presentation of the data attempts to quantify these effects.

Figures 7.2 through 7.15 illustrate the system response output for a constant temperature range between 90° F and 100° F. Figures 7.2, 7.4, 7.6, 7.8, 7.10, 7.12 and 7.14 depict the excitation timehistory and the phase plane plots of the system. Detailed plots of the displacement, velocity and force timehistories are presented in Figures 7.3, 7.5, 7.7, 7.9, 7.11, 7.13 and 7.15. The excitation amplitude is varied with the frequency of excitation held constant at 0.5 Hz for Figures 7.2 through 7.9. The system response plotted in Figures 7.2 and 7.3 was derived from 0.5 in-pk excitation amplitude, and that in Figures 7.4 through 7.9 depict the system response with excitation amplitudes of 1, 2, and 3 in-pk.
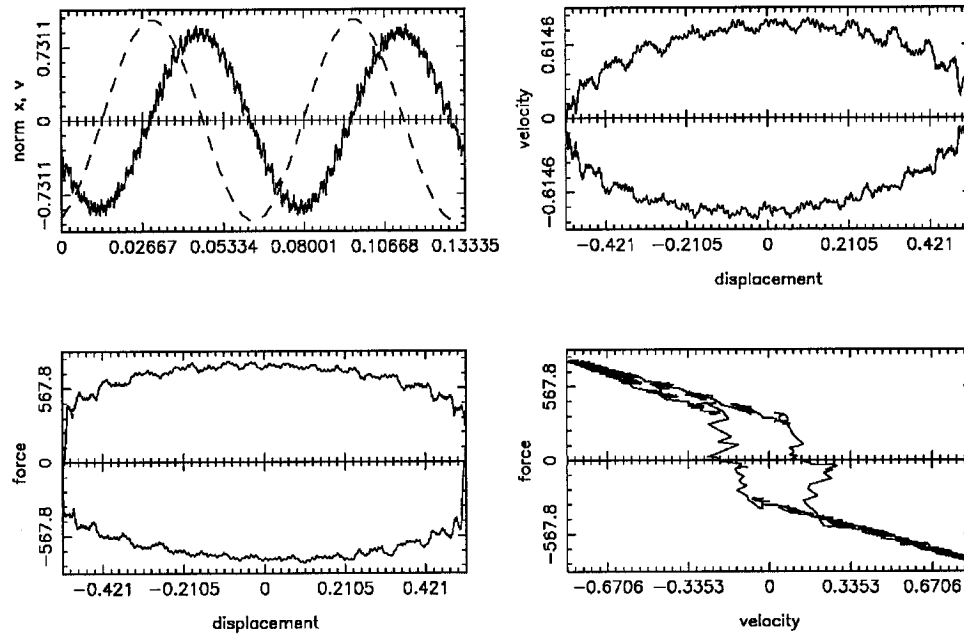
FIGURE 7.2. Damper response with excitation amplitude = 0.5 in-pk, ω=0.5 Hz
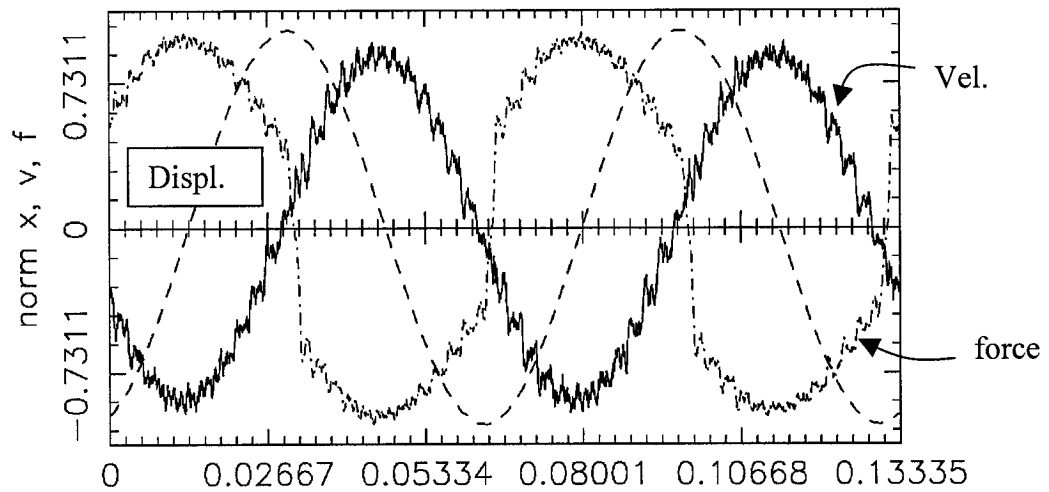
FIGURE 7.3. Normalized system variables with excitation amplitude = 0.5 in-pk, ω=0.5 Hz

234
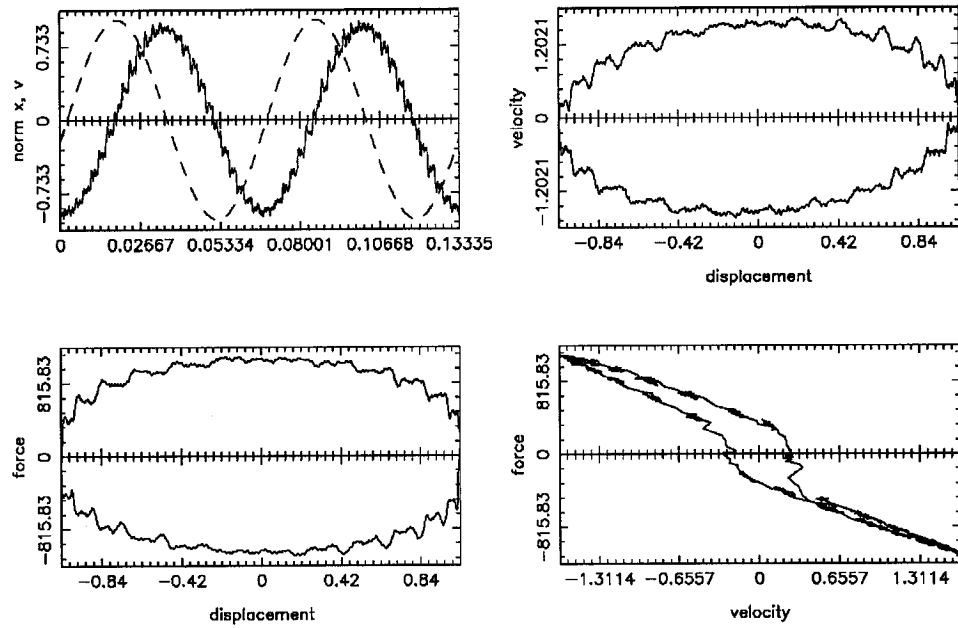
FIGURE 7.4. Damper response with excitation amplitude = 1 in-pk, ω=0.5 Hz
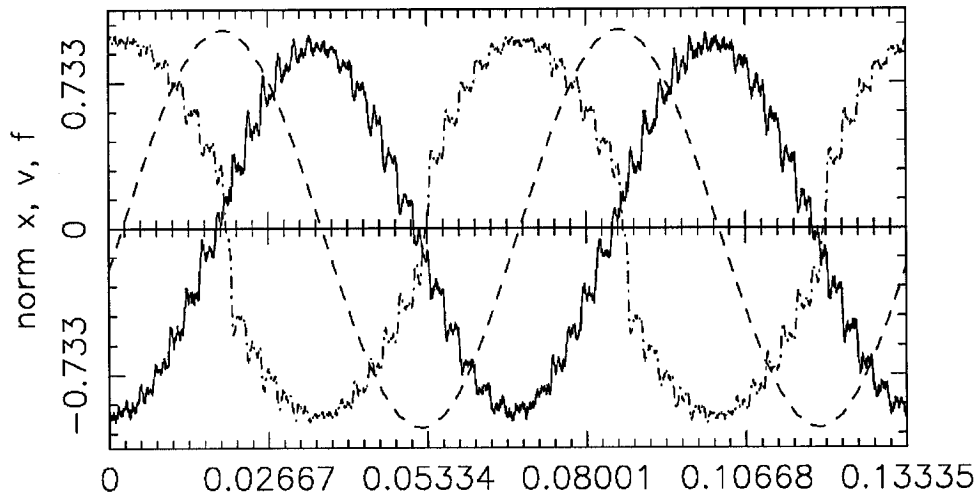
FIGURE 7.5. Normalized system variables with excitation amplitude = 1 in-pk, ω=0.5 Hz

235
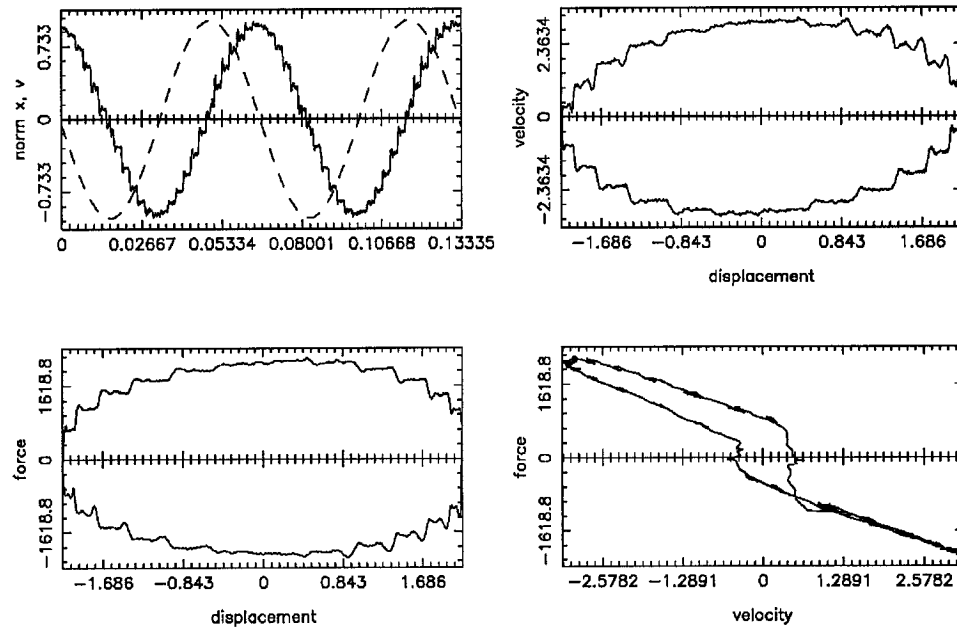
FIGURE 7.6. Damper response with excitation amplitude = 2 in-pk, ω=0.5 Hz
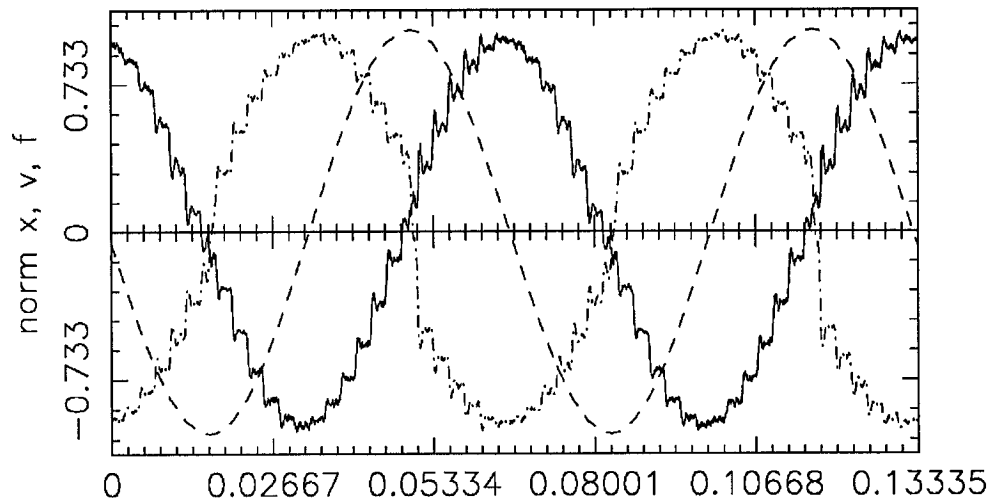
FIGURE 7.7. Normalized system variables with excitation amplitude = 2 in-pk, ω=0.5 Hz

236
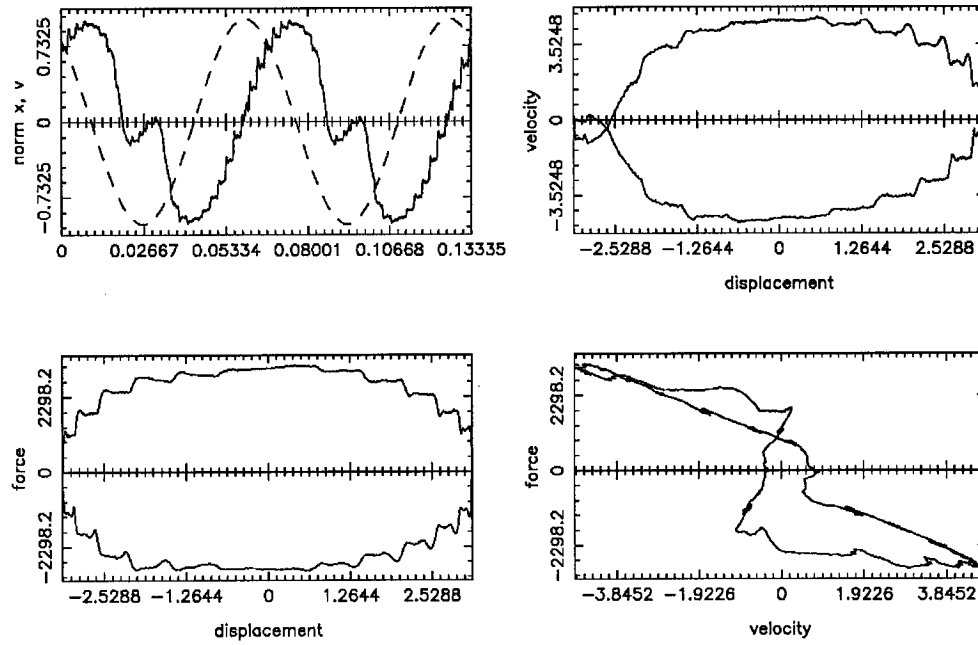
FIGURE 7.8. Damper response with excitation amplitude = 3 in-pk, ω=0.5 Hz
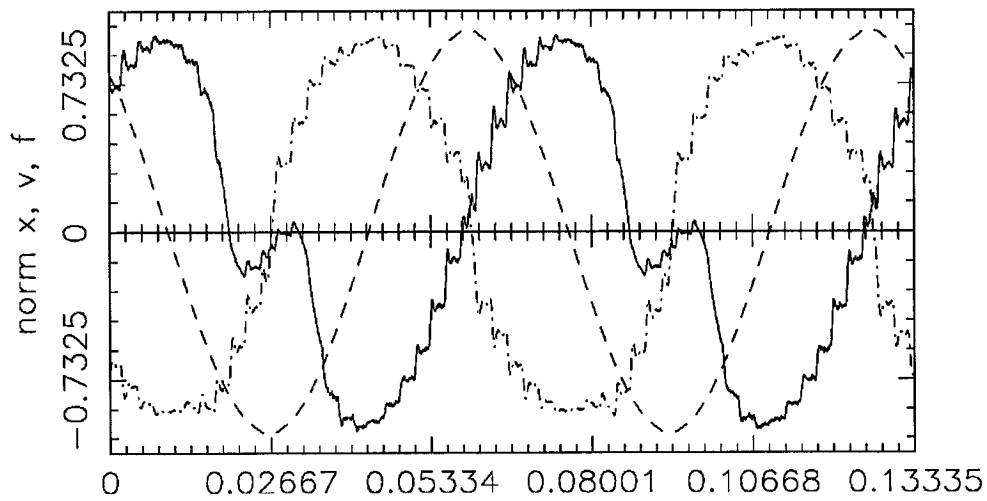
FIGURE 7.9. Normalized system variables with excitation amplitude = 3 in-pk, ω=0.5 Hz

237

Following a similar format, Figures 7.10 through 7.15 detail the system response at

0.5, 1, and 2 in-pk amplitude excitations, respectively, with the excitation frequency

at 1 Hz. These plots were included to detail the highly nonlinear damper response,

which is particularly evident in the phase plane representation of the velocity and

force. As discussed previously and displayed in Figures 7.2 through 7.9, increasing

excitation amplitude does correlate to amplified system nonlinear response.

Interestingly, though, the effect of increasing excitation frequency tends to mask the

nonlinear behavior so readily apparent in the phase plane representation of the

system response excited by a 0.5 Hz signal. The system response appears to have

been smoothed from that illustrated in Figures 7.2 through 7.9. Close investigation

of the velocity/force phase plane plots for the system excited by a 1 Hz siganl still

reveal similar nonlinearities, just not to the degree evidenced in the response to a 0.5

Hz excitation.

238
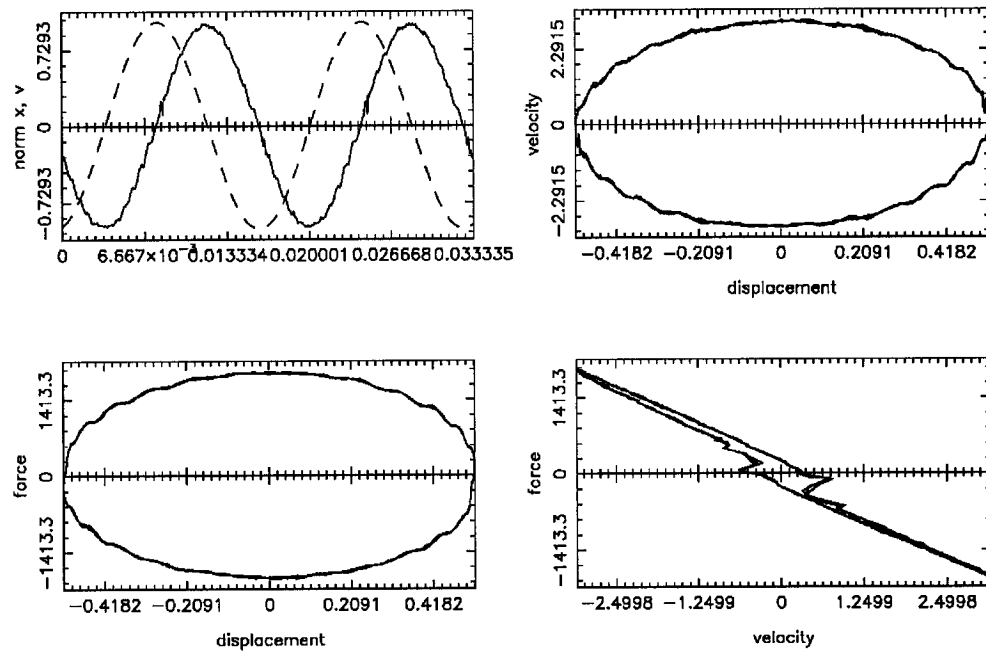
FIGURE 7.10. Damper response with excitation amplitude = 0.5 in-pk, ω=1 Hz
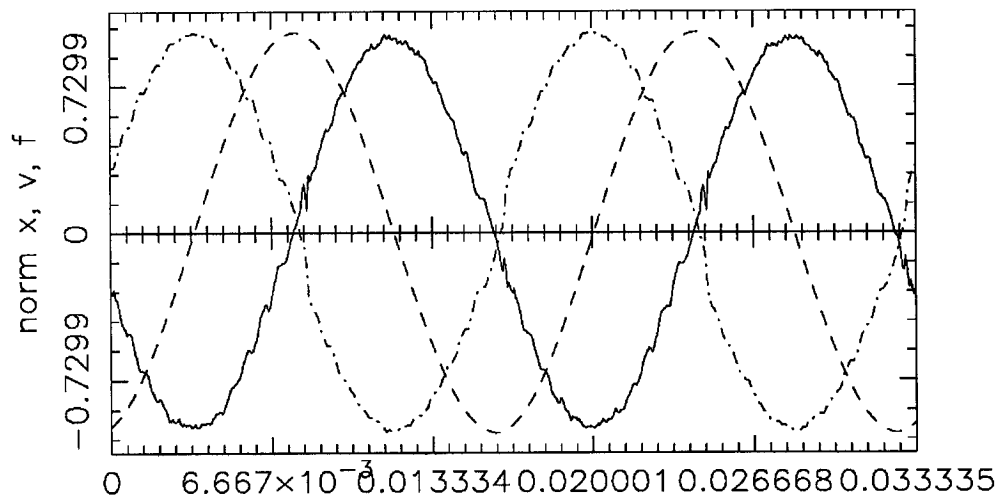
FIGURE 7.11. Normalized system variables with excitation amplitude = 0.5 in-pk, ω=1 Hz

239
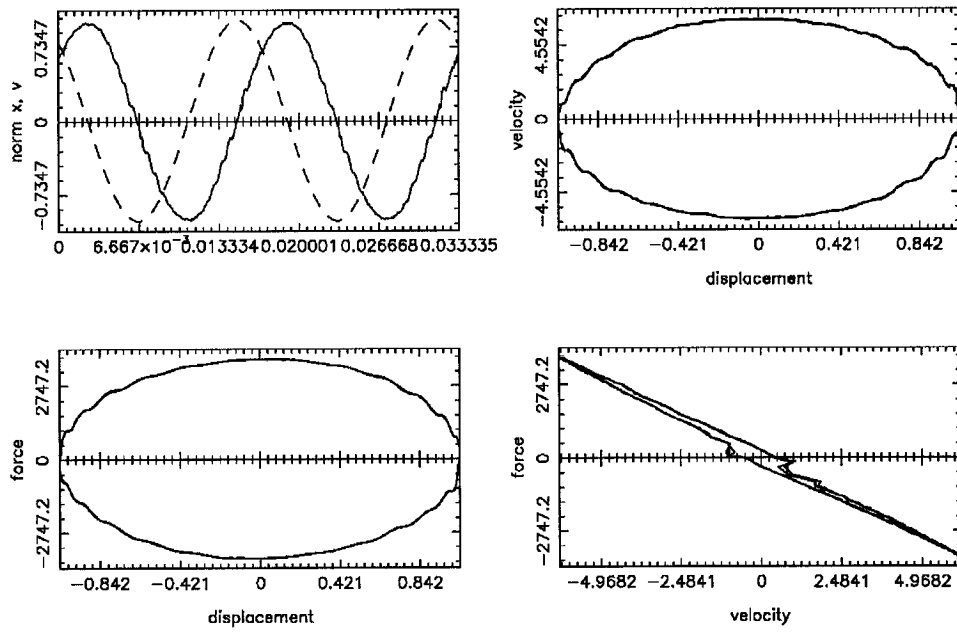
FIGURE 7.12. Damper response with excitation amplitude = 1 in-pk, ω=1 Hz
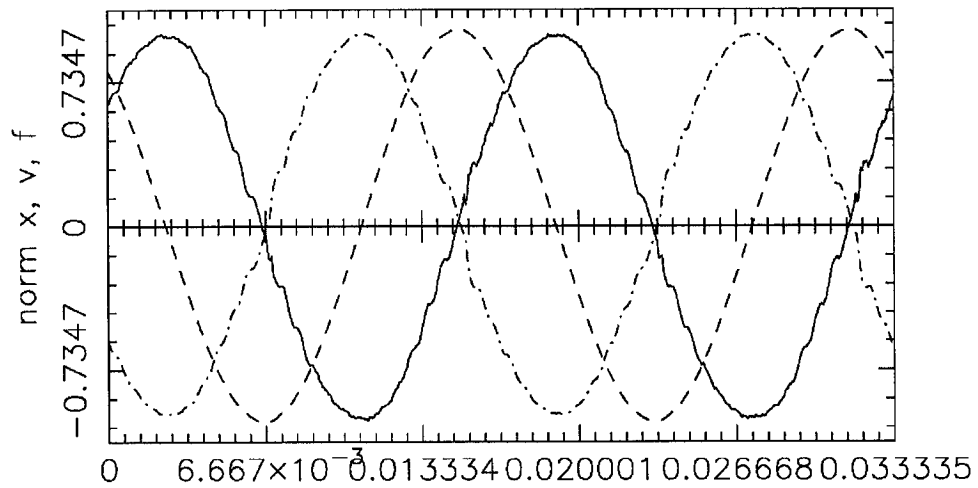
FIGURE 7.13. Normalized system variables with excitation amplitude = 1 in-pk, ω=1 Hz

240
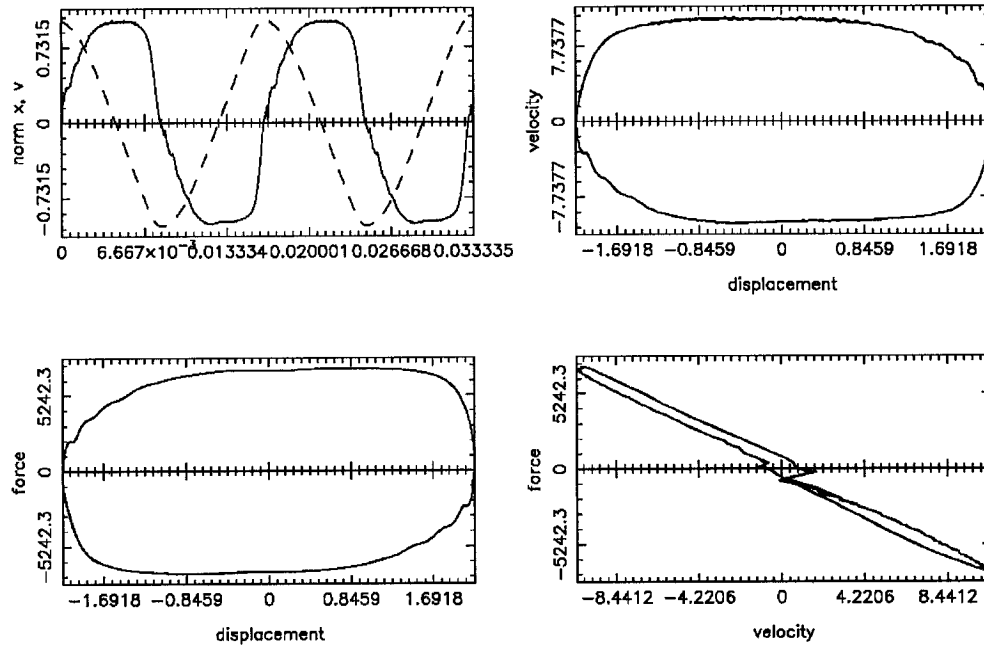
FIGURE 7.14. Damper response with excitation amplitude = 2 in-pk, ω=1 Hz
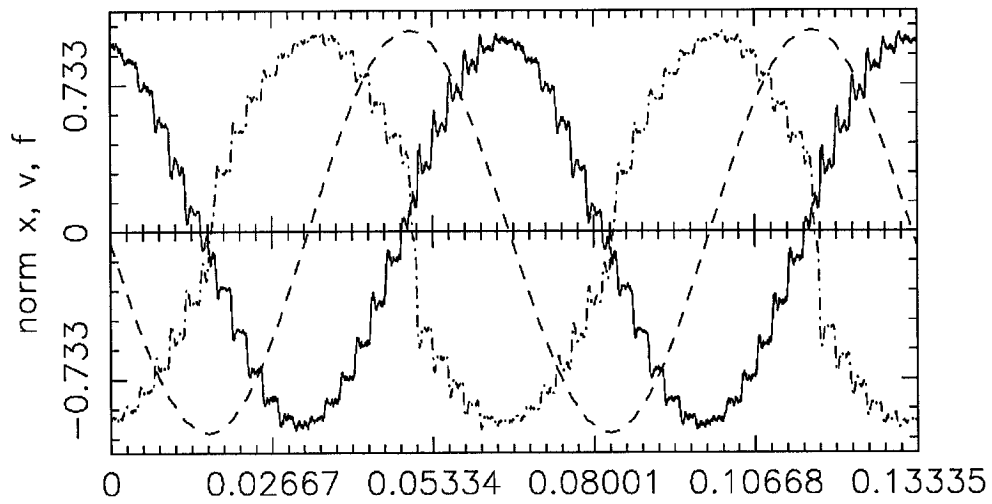
FIGURE 7.15. Normalized system variables with excitation amplitude = 2 in-pk, ω=1 Hz

241

To further detail the effects of excitation amplitude and frequency variations on the damper, phase plots with these parameters varied are depicted in Figures 7.16 and 7.17. First, various excitation amplitudes are overlaid in Figure 7.16 with the excitation frequency held constant at 0.5 Hz. Figure 7.17 is similar to Figure 7.16, except the excitation frequency is changed to 1 Hz.

Note that the larger parameter excursions result from increased excitation amplitude; thus, these plots reveal that increasing the excitation amplitude yields higher damping forces at the maximum relative velocity. This result follows intuition. A comparison of the two figures reveals that increasing the system excitation frequency also increases the output force at the maximum velocity point.
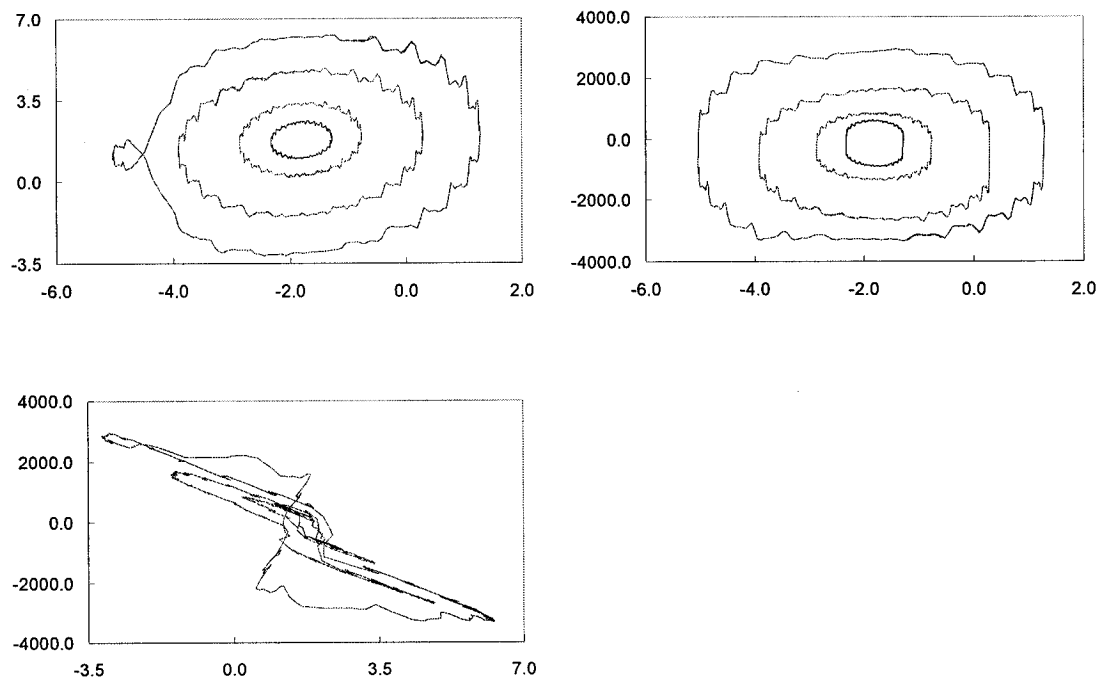
FIGURE 7.16. Damper response with various excitation amplitudes, ω=0.5 Hz

242
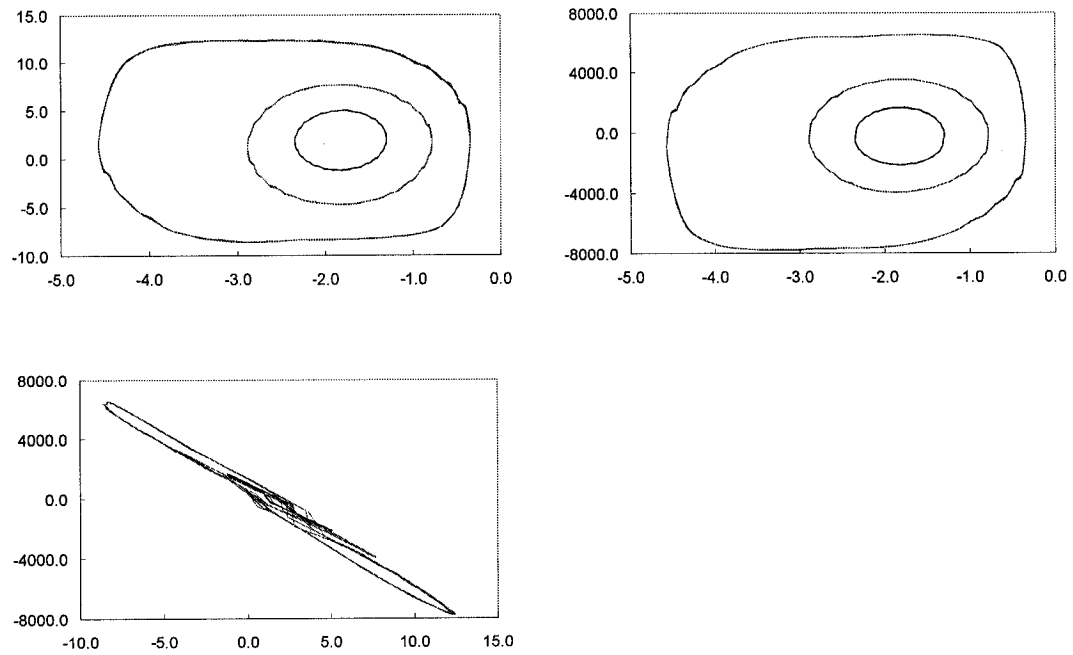
FIGURE 7.17. Damper response with various excitation amplitudes, ω=1 Hz

The identified Chebyshev and Power Series coefficients for the above test cases are depicted in Tables 7.3 through 7.9. The damper temperature remained constant within a 90-100° F range for all of these results.

Chebyshev coefficients				
i/j	1	2	3	4
1	6.46	-823.41	21.94	52.68
2	281.35	-5.87	57.06	1.01
3	-9.41	-10.93	12.91	62.80
4	11.50	9.01	55.17	10.35
Power Series coefficients				
i/j	1	2	3	4
1	11.11	-932.34	27.11	-68.20
2	673.68	137.91	-578.77	-390.34
3	-149.39	-1710.88	207.78	3055.83
4	-1189.35	-761.52	4251.41	1914.41

TABLE 7.3. Identified damper coefficients, A=0.5 in-pk, ω=0.5 Hz

243

Chebyshev coefficients				
i/j	1	2	3	4
1	28.02	-1195.79	4.77	40.60
2	292.16	-17.15	58.63	19.06
3	-0.49	-30.99	35.46	51.91
4	-1.34	5.32	55.53	12.95
Power Series coefficients				
i/j	1	2	3	4
1	70.65	-689.59	-22.38	-10.30
2	384.37	17.63	-75.71	-17.08
3	-61.88	-208.09	43.77	85.62
4	-194.95	-75.24	140.73	40.63

TABLE 7.4. Identified damper coefficients, A=1 in-pk, ω=0.5 Hz

Chebyshev coefficients				
i/j	1	2	3	4
1	72.81	-2308.08	-7.40	81.15
2	633.61	-61.71	124.37	53.58
3	-9.18	-60.85	59.72	121.64
4	-4.31	29.72	140.46	47.26
Power Series coefficients				
i/j	1	2	3	4
1	139.11	-659.55	-13.15	-4.83
2	447.82	15.81	-27.32	-4.98
3	-32.03	-59.28	5.49	6.53
4	-62.05	-14.48	11.65	2.41

TABLE 7.5. Identified damper coefficients, A=2 in-pk, ω=0.5 Hz

Chebyshev coefficients				
i/j	1	2	3	4
1	317.30	-3288.15	361.61	39.15
2	-18.51	-56.49	-191.72	150.07
3	1296.98	1.81	-37.83	9.95
4	-759.46	-112.83	68.37	160.23
Power Series coefficients				
i/j	1	2	3	4
1	-1403.25	-701.32	34.84	1.04
2	846.59	83.13	-11.40	-3.80
3	265.31	-1.48	-0.64	0.08
4	-105.42	-15.61	0.84	0.74

TABLE 7.6. Identified damper coefficients, A=3 in-pk, ω=0.5 Hz

244

Chebyshev coefficients			
i/j	1	2	3	4
1	-4.99	-1947.53	4.42	17.60
2	273.30	-1.19	47.00	0.17
3	-4.36	-10.07	-4.64	11.39
4	5.35	2.60	47.61	-0.96
Power Series coefficients			
i/j	1	2	3	4
1	-7.38	-618.88	1.86	0.79
2	674.26	-10.25	-36.62	0.70
3	7.84	-102.19	-8.13	10.53
4	-1177.27	45.38	265.51	-3.37

TABLE 7.7. Identified damper coefficients, A=0.5 in-pk, ω=1 Hz

Chebyshev coefficients			
i/j	1	2	3	4
1	42.86	-3831.84	7.15	15.06
2	442.94	-5.95	90.06	6.40
3	-6.48	-21.06	21.35	-4.66
4	-1.40	4.05	87.96	5.82
Power Series coefficients			
i/j	1	2	3	4
1	34.27	-620.71	-0.68	0.33
2	589.96	1.50	-8.52	-0.17
3	-49.69	-1.86	1.93	-0.14
4	-306.59	-5.92	15.55	0.33

TABLE 7.8. Identified damper coefficients, A=1 in-pk, ω=1 Hz

Chebyshev coefficients			
i/j	1	2	3	4
1	-659.11	-7229.47	101.26	41.47
2	98.24	-120.65	-47.04	-6.20
3	27.93	-47.89	-453.20	62.60
4	6.31	25.67	-146.26	139.61
Power Series coefficients			
i/j	1	2	3	4
1	-1208.04	-675.74	9.95	-0.07
2	-152.09	48.04	3.46	-0.68
3	214.67	-9.41	-3.64	0.09
4	65.27	-15.64	-1.14	0.20

TABLE 7.9. Identified damper coefficients, A=2 in-pk, ω=1 Hz

245

Selecting two terms from the Power Series expansion for plotting, the coefficient of the linear quantity and that of the quadratic term, otherwise known as the system damping and stiffness, reveals the effect of excitation variation. In Figure 7.18, indices i and j define the related test case, with index i describing the test cases wherein $\omega = 0.5$ Hz and index j for $\omega = 1$ Hz. The data tabulated in Table 7.3 for $A = 0.5$ in-pk and $\omega = 0.5$ Hz is then indexed as $i = 1$, and that from Table 7.6 is indexed as $i = 4$. Similarly, index j relates the data contained in Table 7.7 through 7.9, with $j = 1$ describing data from Table 7.7. It is evident that excitation amplitude and frequency variations dramatically alter the system response. Hence, any attempt to quantify system parameter variations utilizing system identification techniques will require a fairly in-depth understanding of the physics of the test specimen. Substantial testing to develop envelopes of expected parameter performance over the range of anticipated excitations is then indispensable. Further analysis may be necessary to define the system variability between dampers before damage detection thresholds can be established.
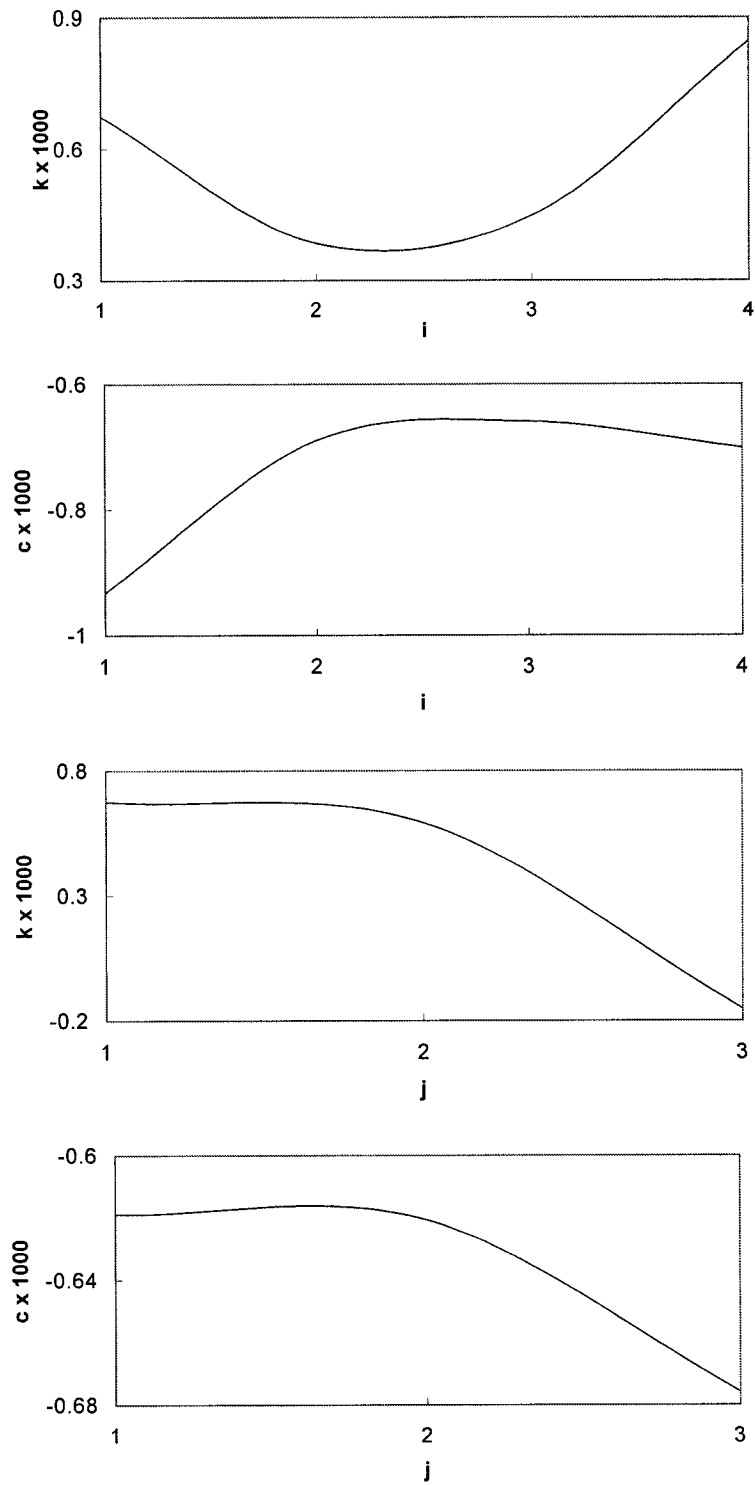
FIGURE 7.18. Variance of *k* and *c*

Finally, comparative time domain plots of the measured and identified damper force

for parametric identification algorithms of the above seven test cases reveal the

excellent fit of the identified system response to the measured response (reference

Figures 7.19 through 7.27). The dashed line in these figures represents the measured

damping force and the unbroken line traces the identified force utilizing the

Chebyshev restoring force algorithm. Note that the identification results detailed in

these figures were derived from a 4th-order Chebyshev polynomial approximation.

Identification results are repeated for the case depicted in Figure 7.23 utilizing a 24th-

order Chebyshev polynomial, and are included as Figure 7.24 for comparative

purposes.

Due to system noise; that is, mechanical noise generated through the actuator and

linear bearings at the actuator/damper interface (reference Figures 4.6 and 4.7), as

well as instrumentation and cabling noise, the system response is nonlinear. As the

excitation amplitude is increased, these effects are amplified (reference Figures 7.19

through 7.21).

The effects of increasing excitation frequency tend to override some of the noise

contributors so evident in the plots for the system excited at 0.5 Hz (reference

Figures 7.19 through 7.23). As the system response is smoother under 1 Hz

excitation at all tested amplitude levels, 0,5, 1 and 2 in-pk, the 4th-order Chebyshev

algorithm replicates the measured restoring force to a higher degree of fidelity than

248

apparent for the 0.5 Hz test cases, particularly with increasing amplitude levels.

Increasing the polynomial degree in the approximation results in more accurate

correlation between the fit and measured data sets. This is demonstrated in Figure

7.23 for the 3 in-pk amplitude 0.5 Hz excitation.

In general, it is important to note that the system response can be replicated with a

high degree of accuracy using low order Chebyshev polynomials. This fact

highlights the robustness of the Chebyshev restoring force algorithm and allows on-

line system identification with minimal computer resources.
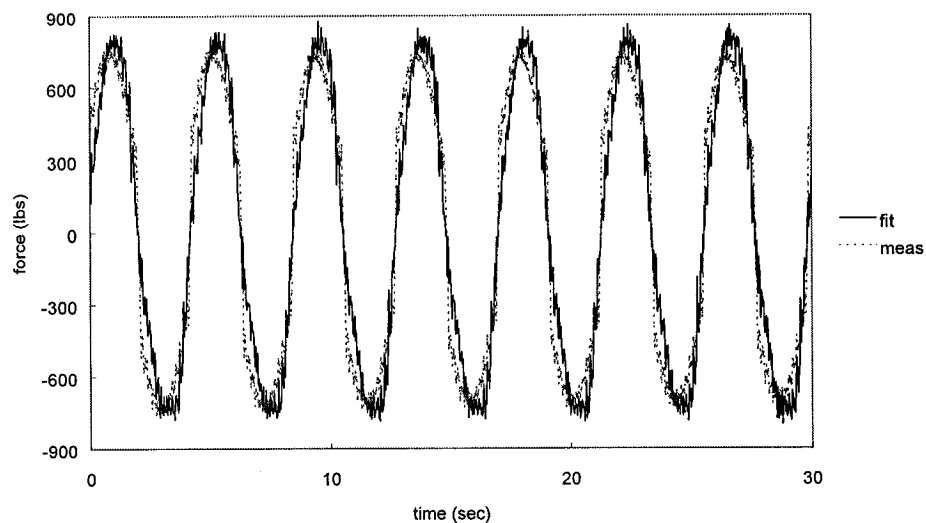
FIGURE 7.19. Measured versus identified damper force, A=0.5 in-pk, ω=0.5 Hz
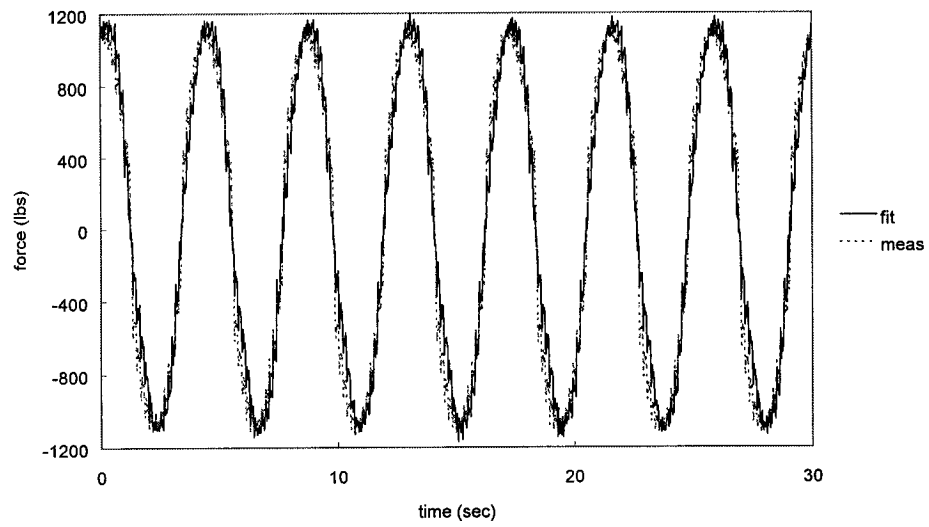
FIGURE 7.20. Measured versus identified damper force, A=1 in-pk, ω=0.5 Hz
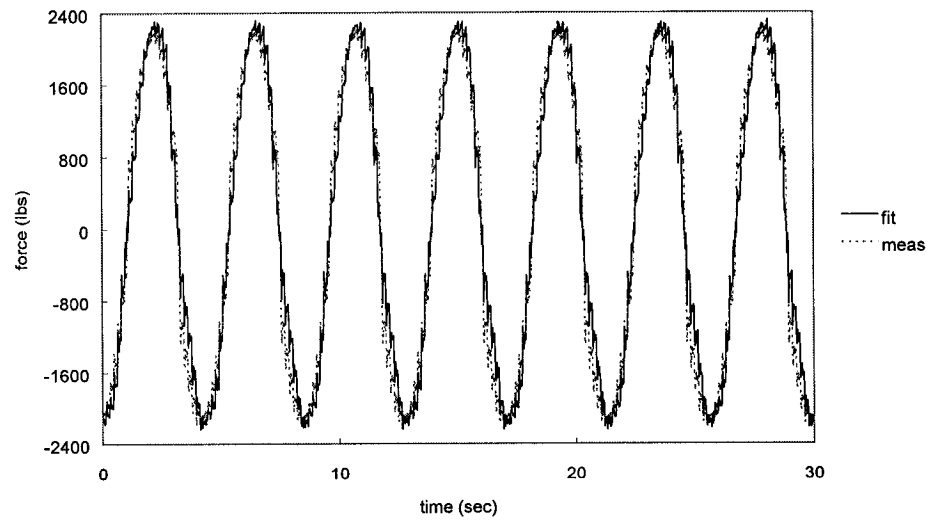
FIGURE 7.21. Measured versus identified damper force, A=2 in-pk, ω=0.5 Hz

250

The system response captured in Figure 7.22 provides a great example of this commentary. This data was derived for 3 in-pk 0.5 Hz system excitation. As noted above, Figure 7.23 illustrates that increasing the polynomial degree in the identification algorithm results in improved data replication. Figure 7.24 displays a close-up of two cylces of the measured force data from the test case depicted in Figures 7.22 and 7.23. This plot highlights the nonlinear response of the system near the point of minimum velocity, where the system response reverses polarity in a highly irregular, nonlinear transition. Clearly, as commented earlier, on the discussions in Figures 7.2 through 7.15, increasing the excitation frequency reduces the nonlinearities evident in the system response.
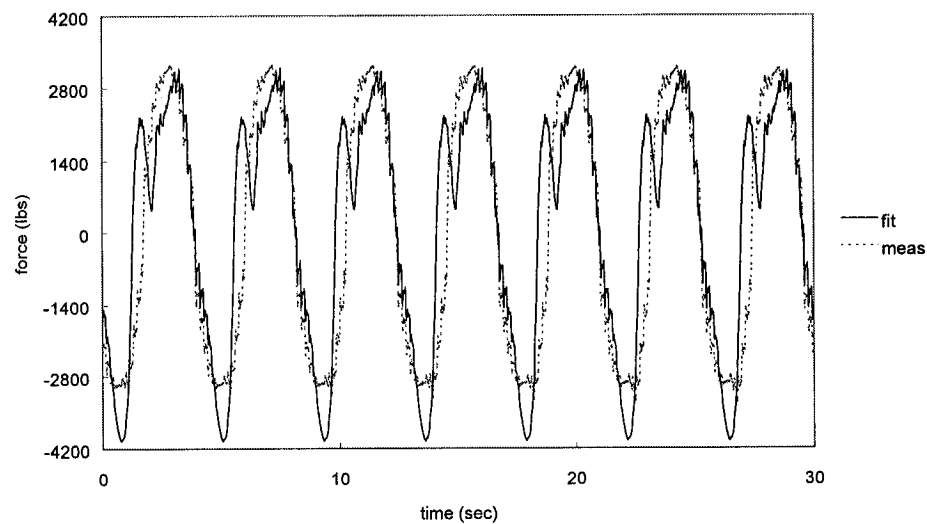
FIGURE 7.22. Measured versus identified damper force, A=3 in-pk, ω=0.5 Hz

251
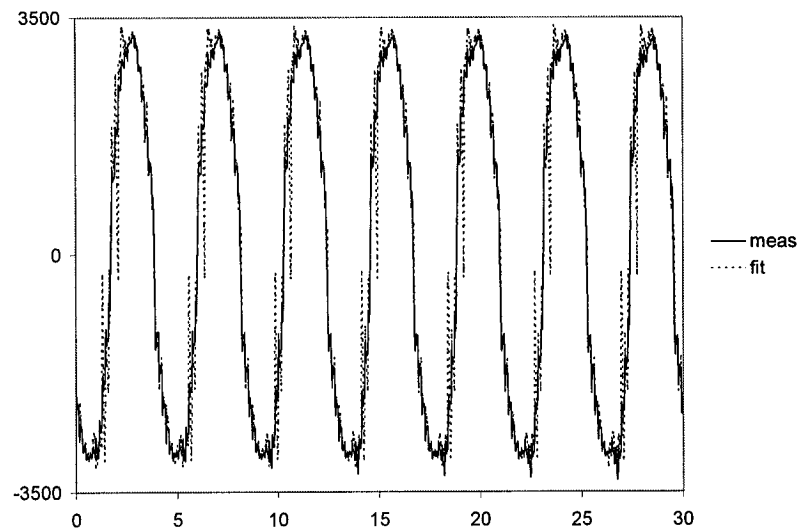
FIGURE 7.23. Measured versus identified damper force, A=3 in-pk, ω=0.5 Hz, 24th order fit
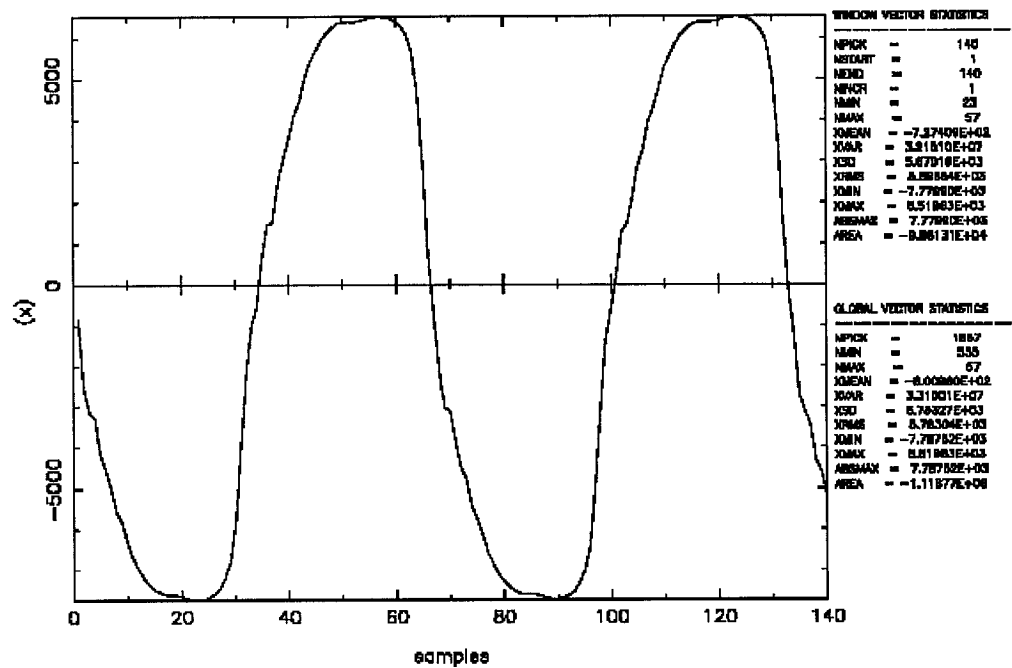
FIGURE 7.24. Close-up of measured damper force, A=3 in-pk, ω=0.5 Hz
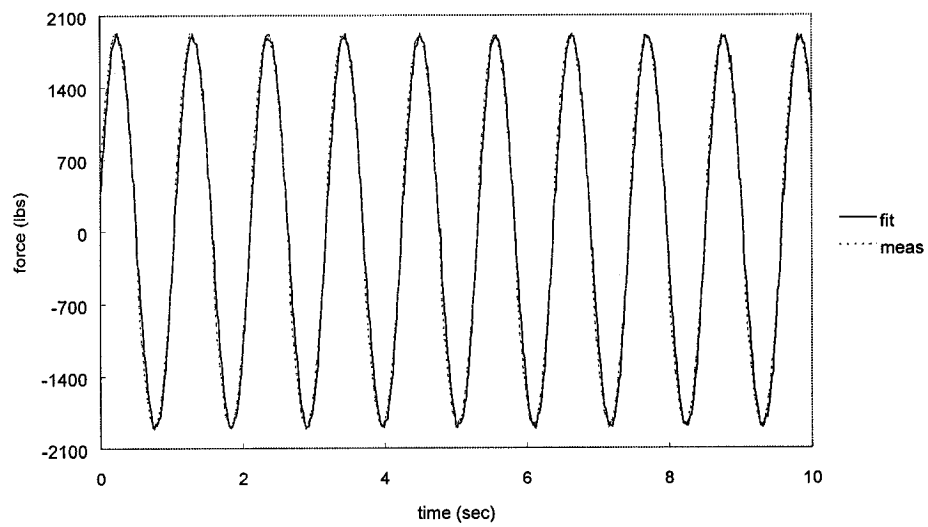
FIGURE 7.25. Measured versus identified damper force, A=0.5 in-pk, ω=1 Hz
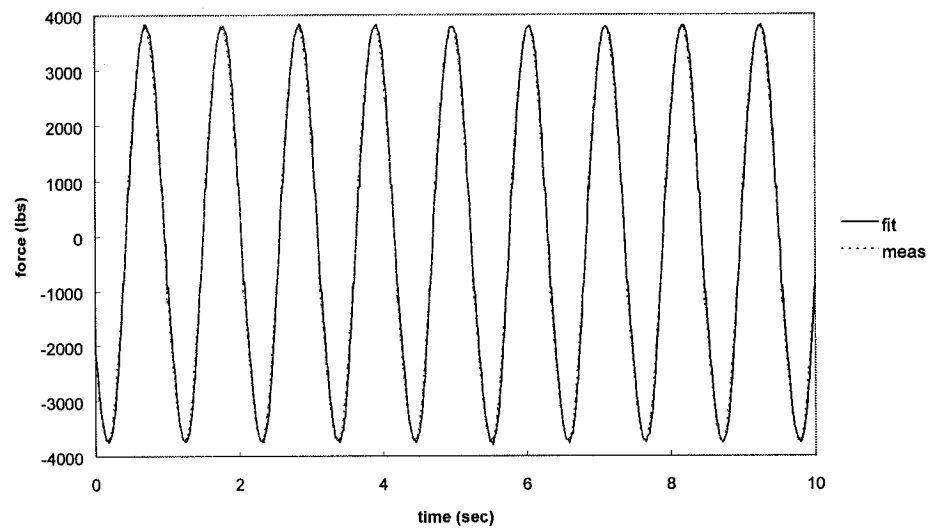
FIGURE 7.26. Measured versus identified damper force, A=1 in-pk, ω=1 Hz

253
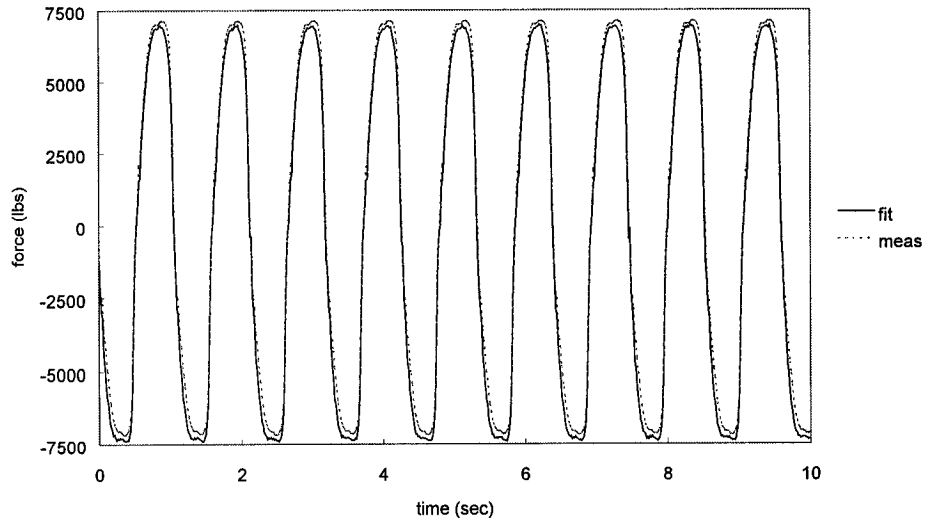
FIGURE 7.27. Measured versus identified damper force, A=2 in-pk, ω=1 Hz

7.6.1.2 Statistical analysis

The statistics of varying the amplitude, frequency and temperature ranges were also studied. As stated above, the pdf statistics were computed from a total of 20 samples of each test case outlined in Table 7.1. Figures 7.28 through 7.33 depict the distribution of the damper response with curves of constant amplitude contained in each plot. Figures 7.34 through 7.42 contain curves of constant excitation frequency. Finally, Figures 7.43 through 7.49 reveal the dependence of the system to temperature effects by displaying constant temperature curves for given amplitude and excitation frequency. For clarity of presentation, the temperature ranges are defined as T1 = 70-80° F, T2 = 90-100° F, and T3 = 110-120° F in Figures 7.28 through 7.49.

254
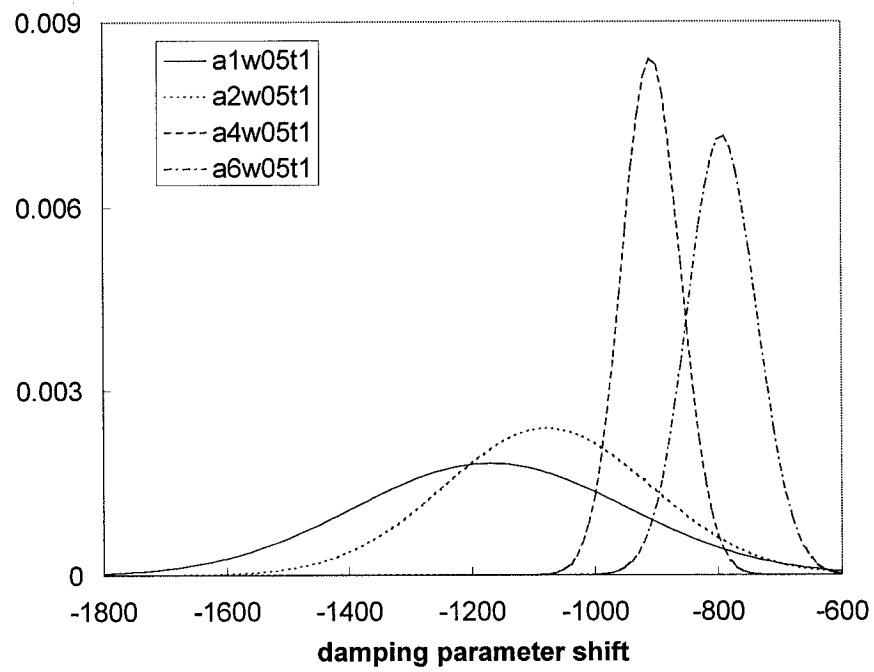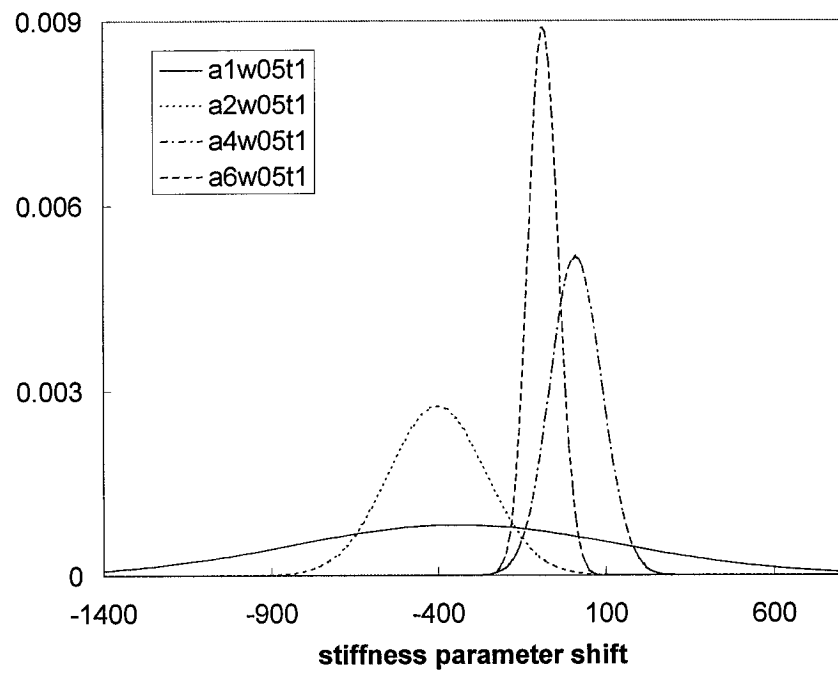
FIGURE 7.28. Amplitude effects, ω=0.5 Hz, T1

255
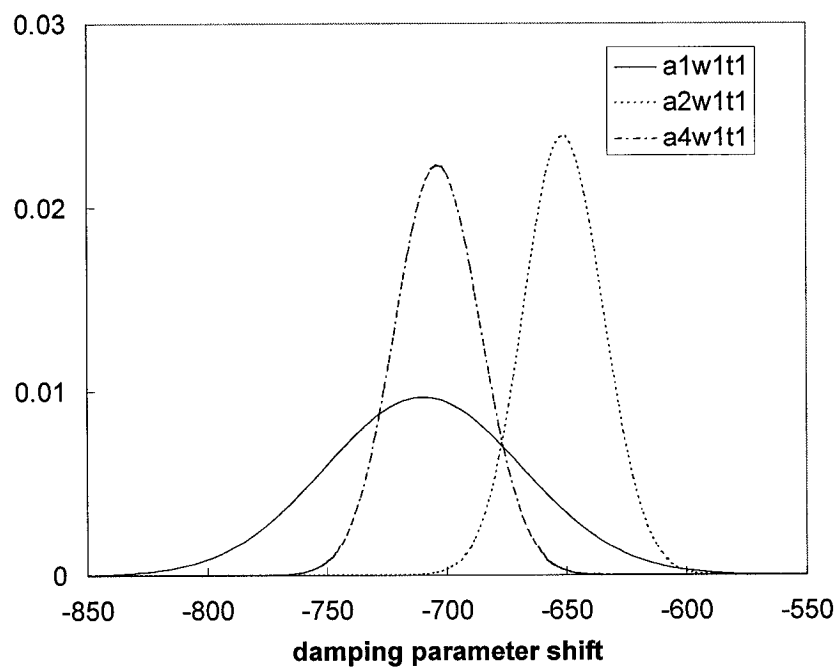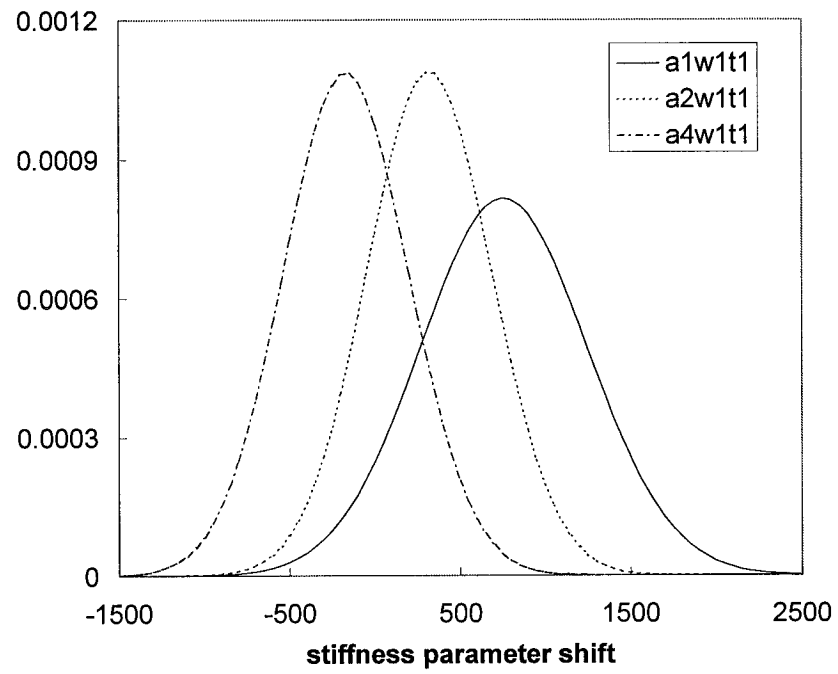
FIGURE 7.29. Amplitude effects, ω=1 Hz, T1
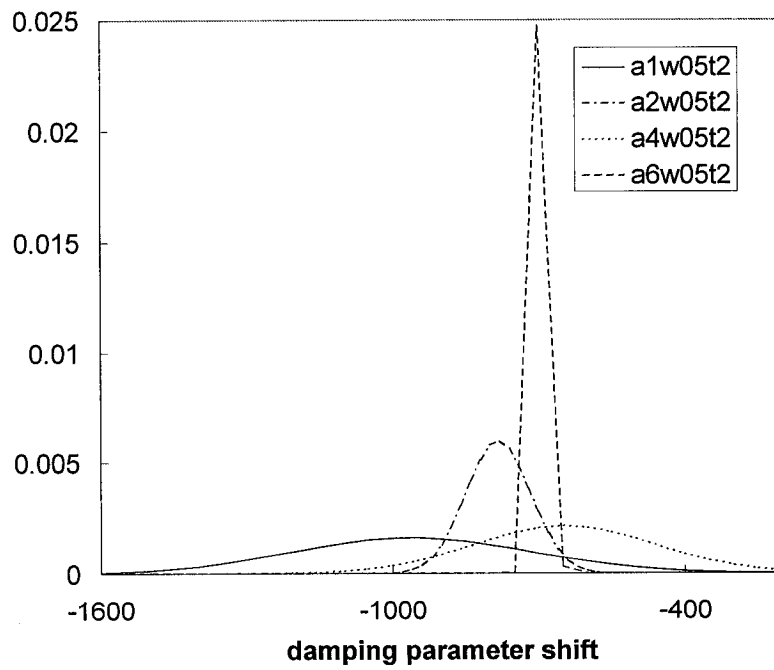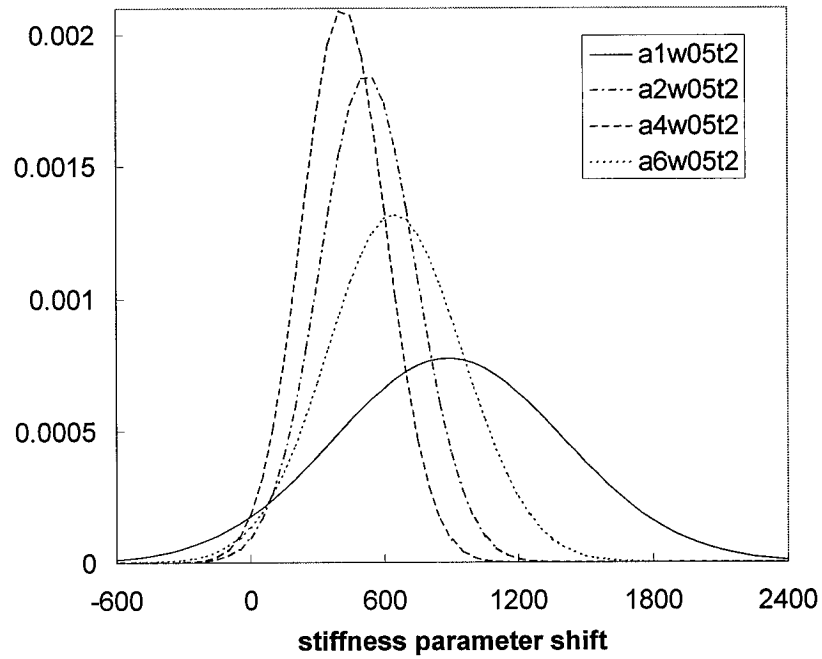
FIGURE 7.30. Amplitude effects, ω=0.5 Hz, T2

257
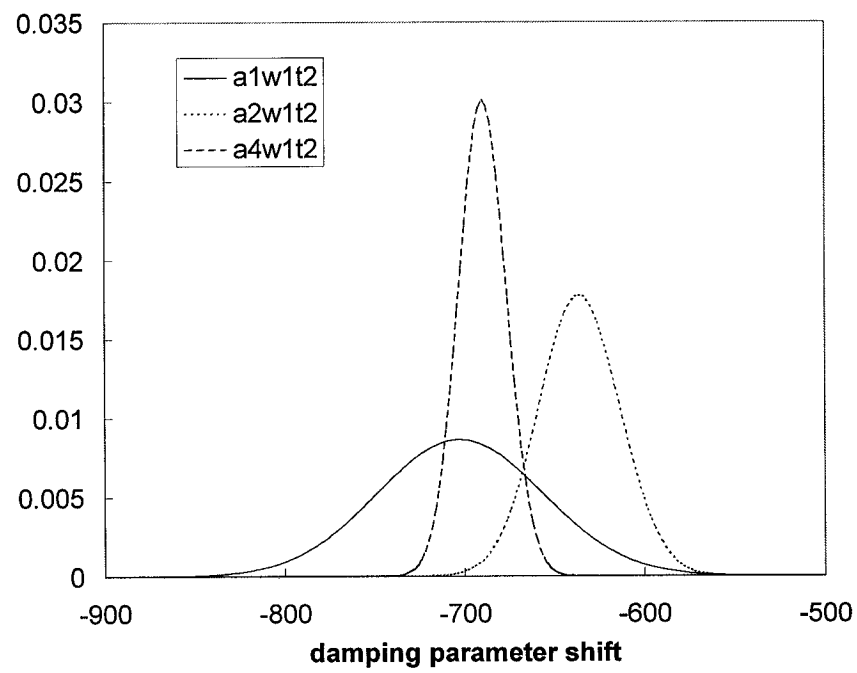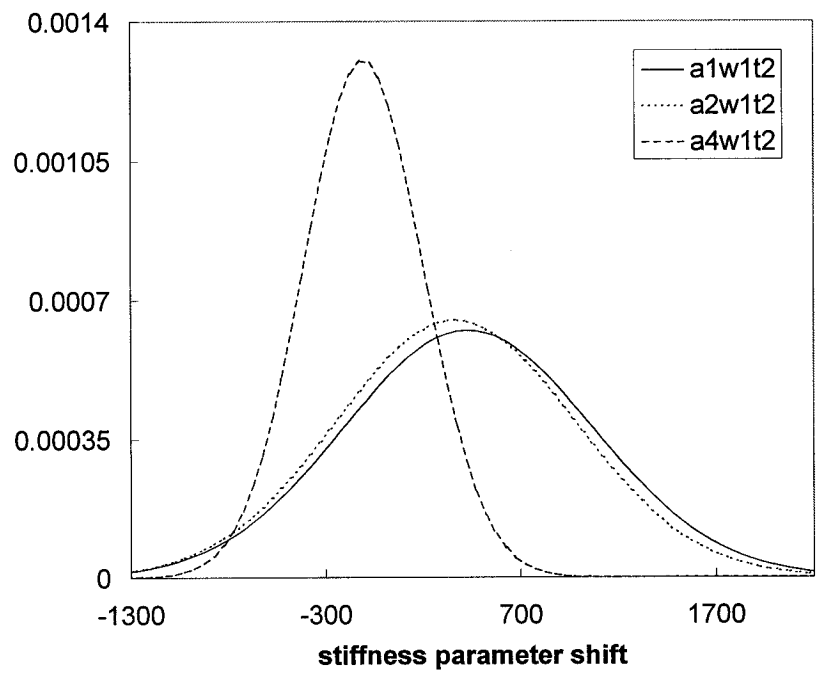
FIGURE 7.31. Amplitude effects, ω=1 Hz, T2

258
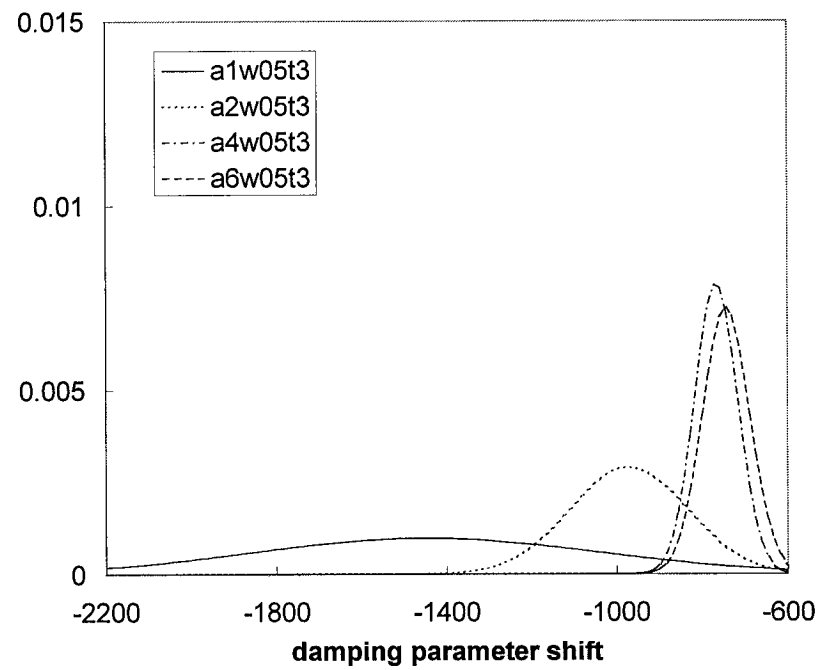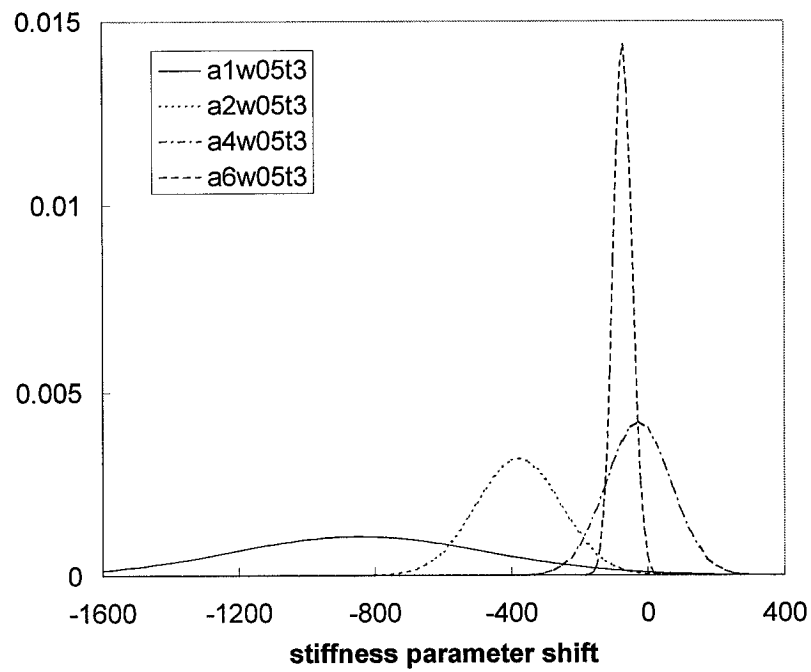
FIGURE 7.32. Amplitude effects, ω=0.5 Hz, T3

259
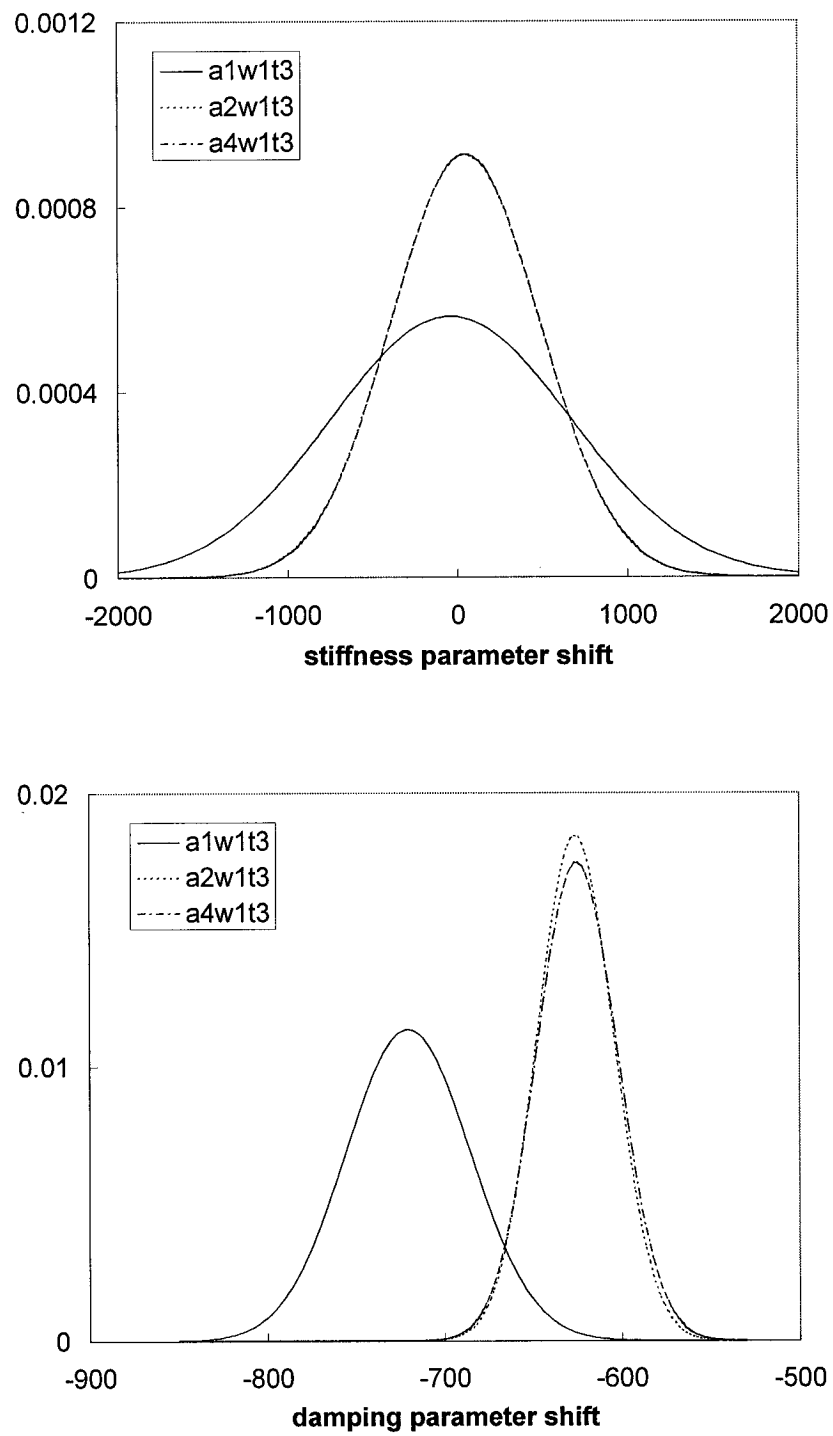
FIGURE 7.33. Amplitude effects, ω=1 Hz, T3

260
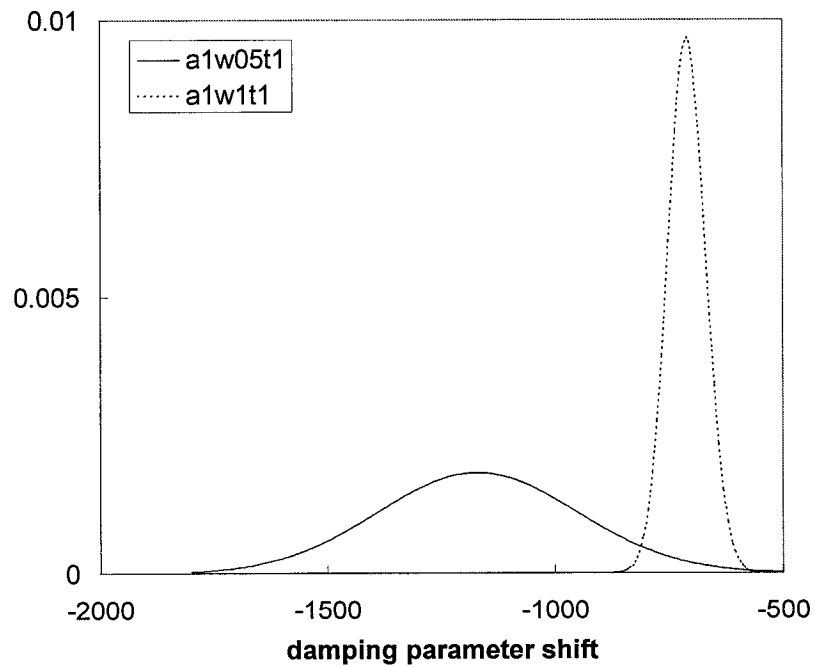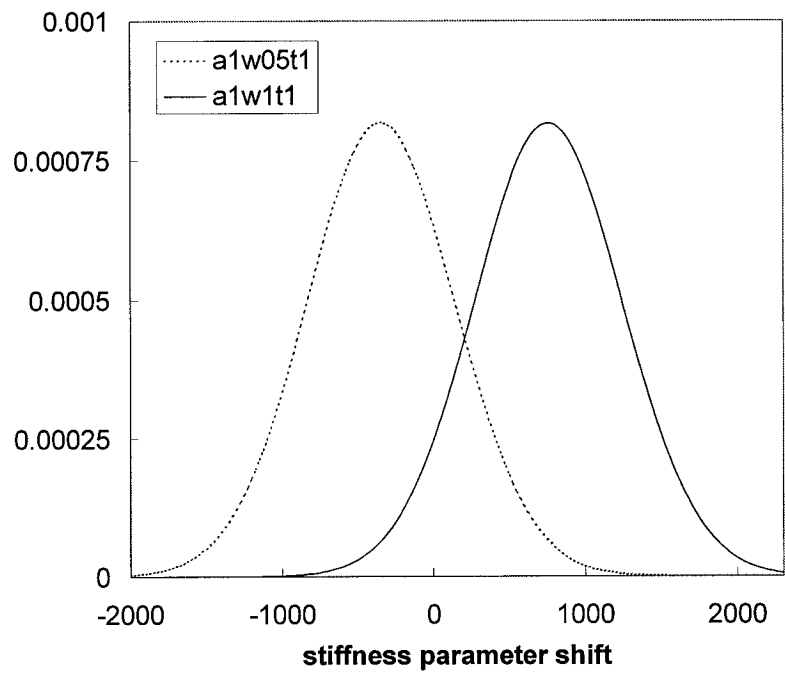
FIGURE 7.34. Frequency effects, A=0.5 in-pk, T1

261
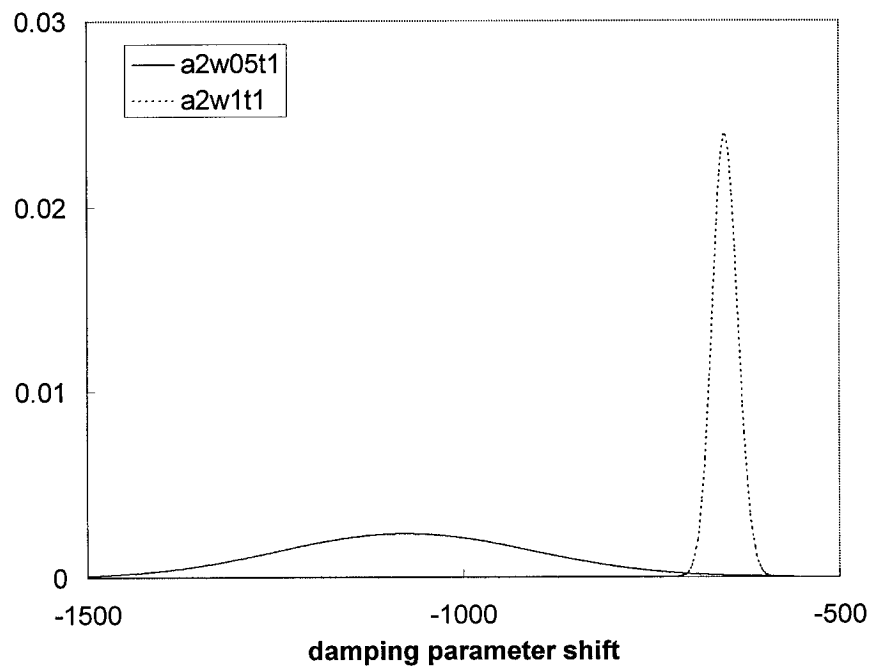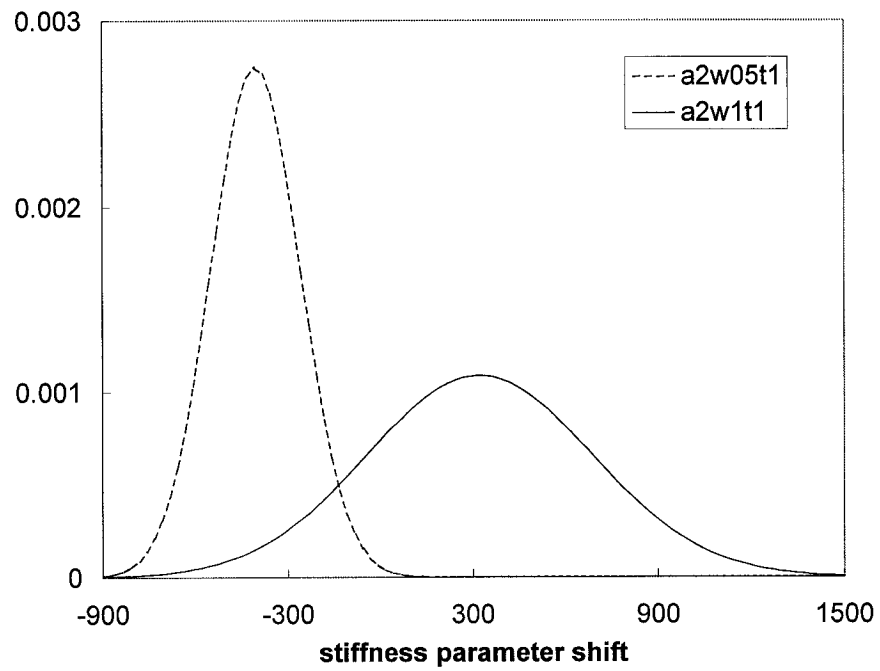
FIGURE 7.35. Frequency effects, A=1 in-pk, T1

262
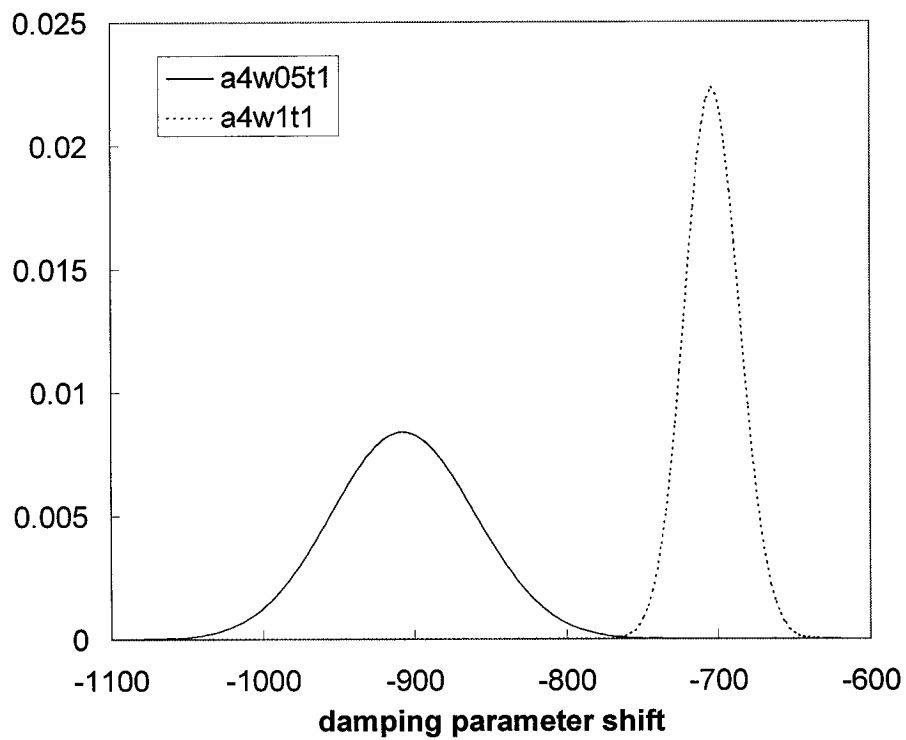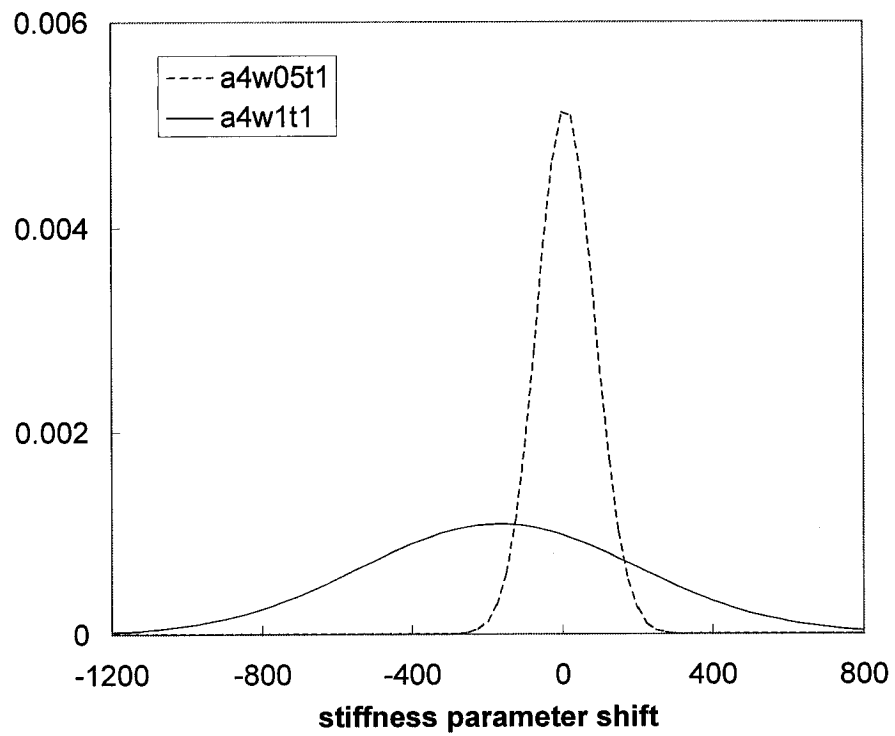
FIGURE 7.36. Frequency effects, A=2 in-pk, T1

263
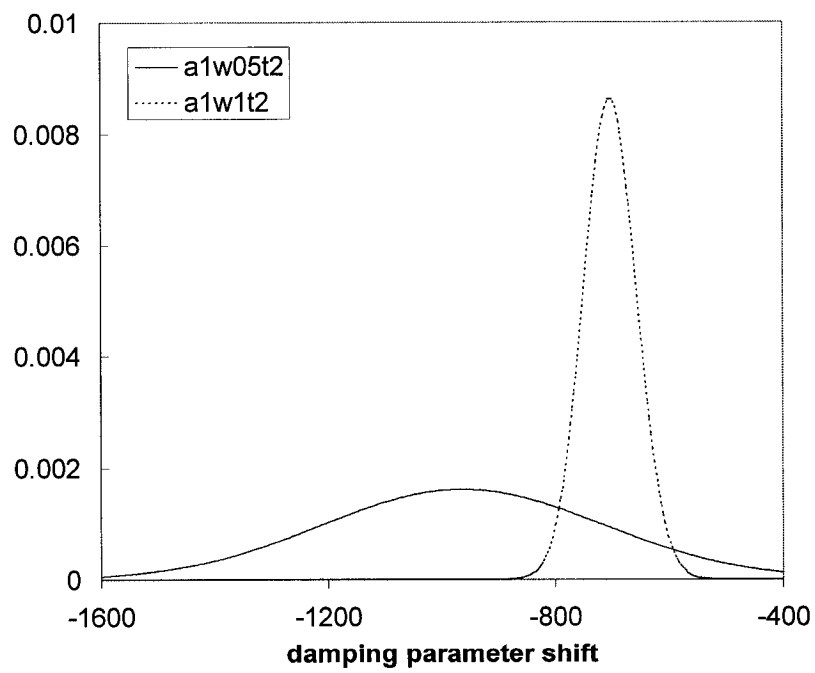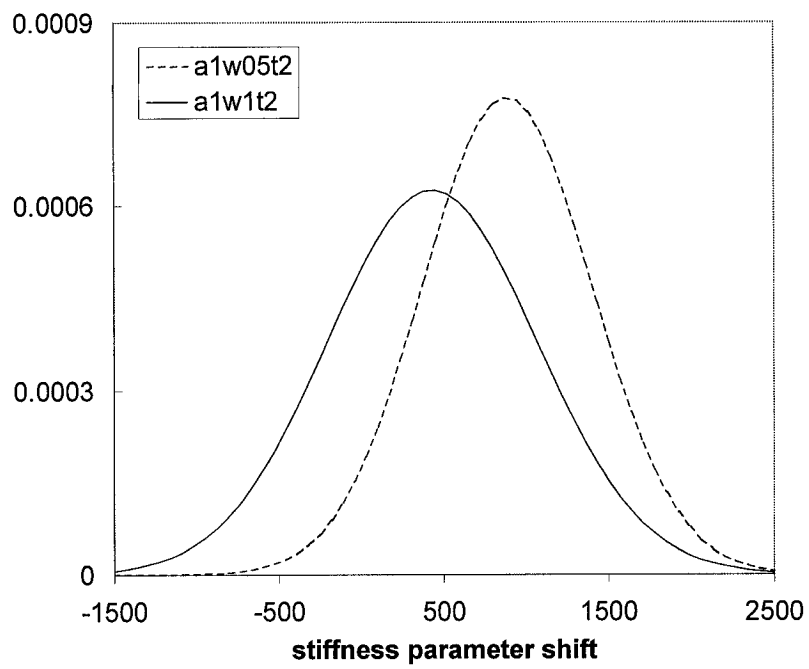
FIGURE 7.37. Frequency effects, A=0.5 in-pk, T2

264
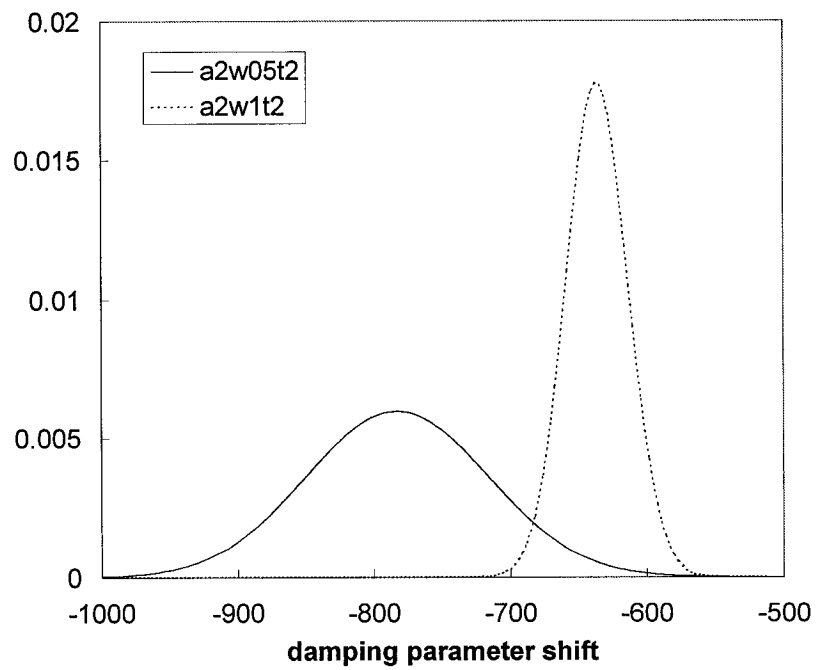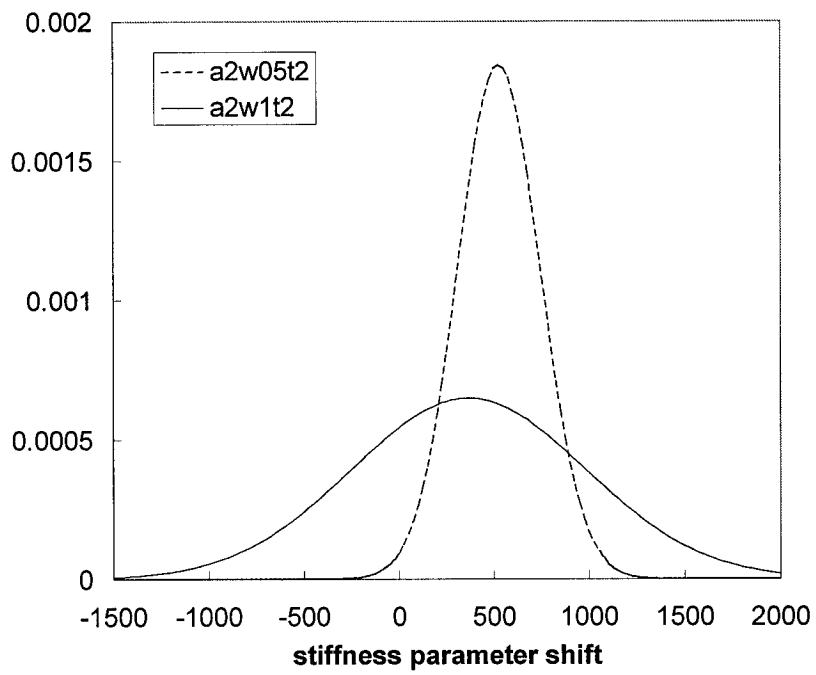
FIGURE 7.38. Frequency effects, A=1 in-pk, T2
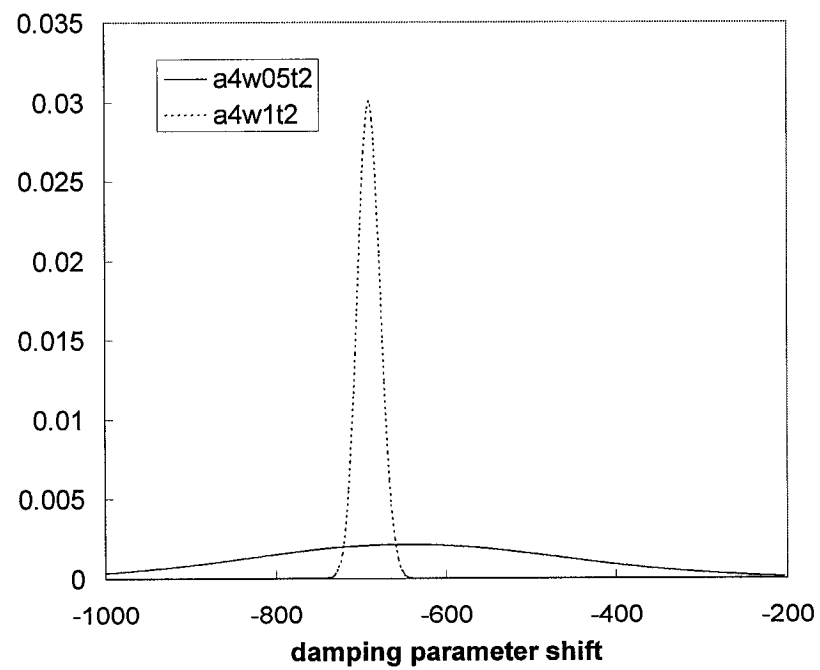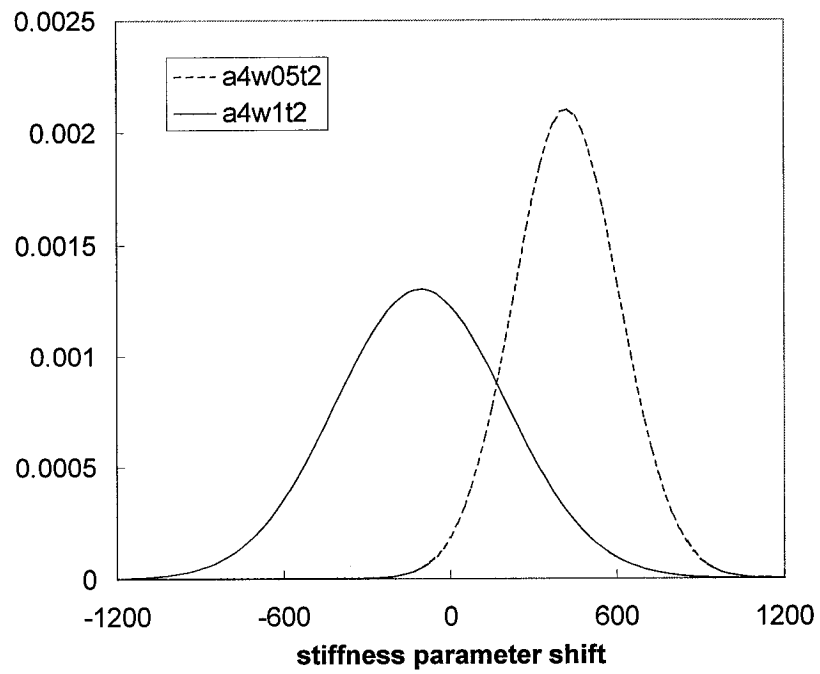
FIGURE 7.39. Frequency effects, A=2 in-pk, T2

266
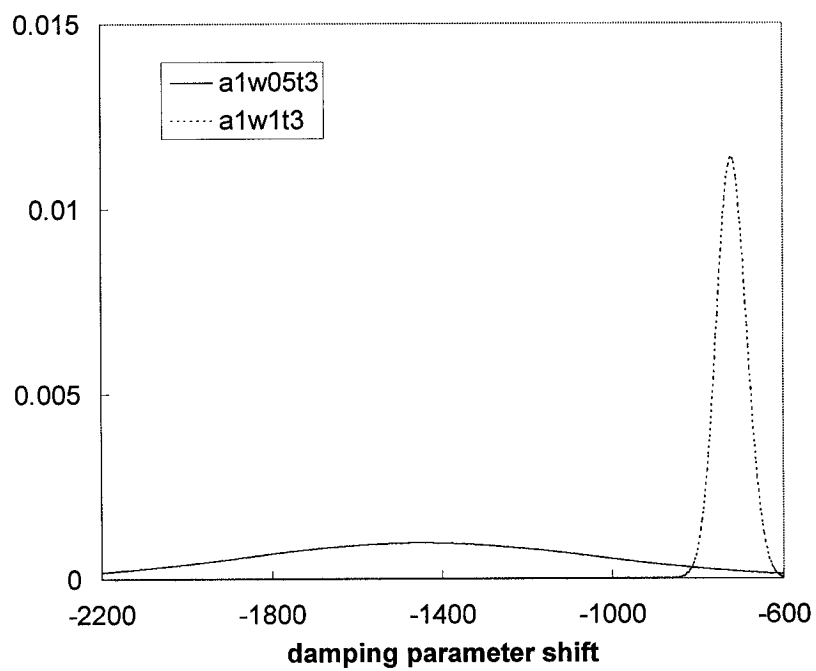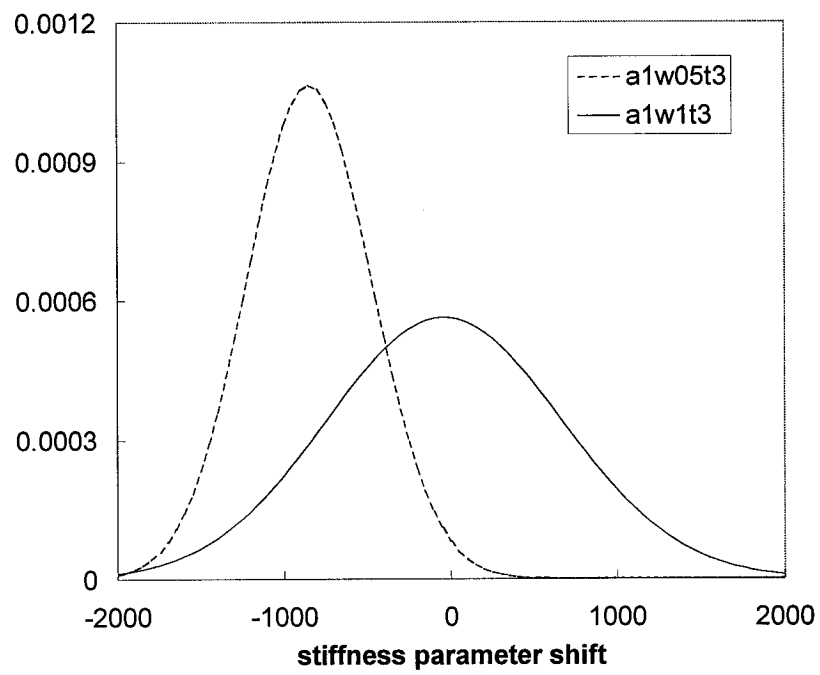
FIGURE 7.40. Frequency effects, A=0.5 in-pk, T3

267
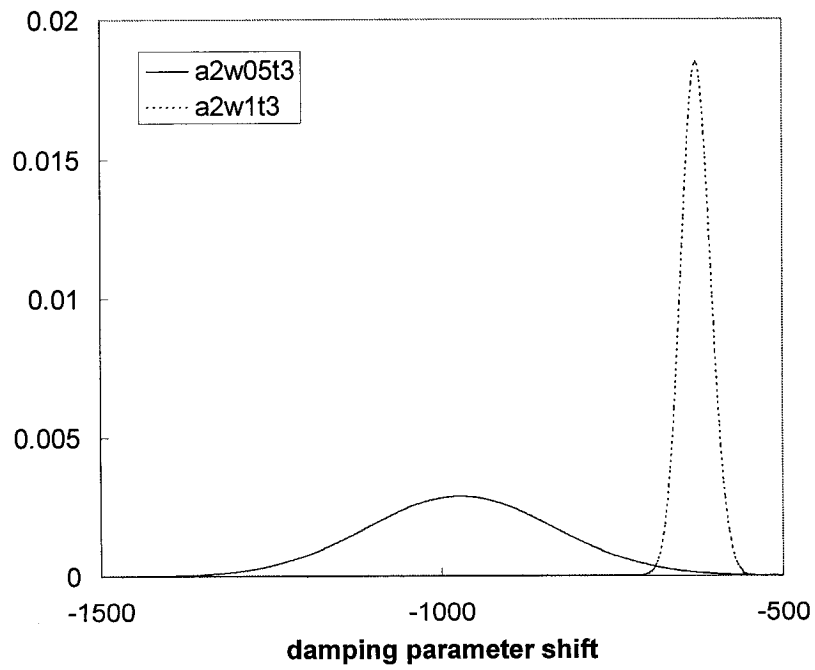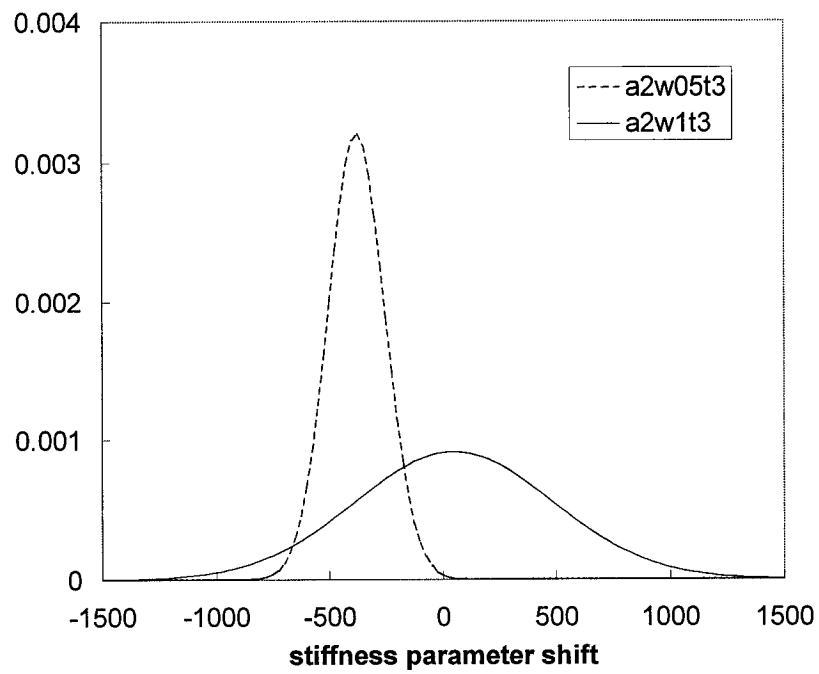
FIGURE 7.41. Frequency effects, A=1 in-pk, T3

268
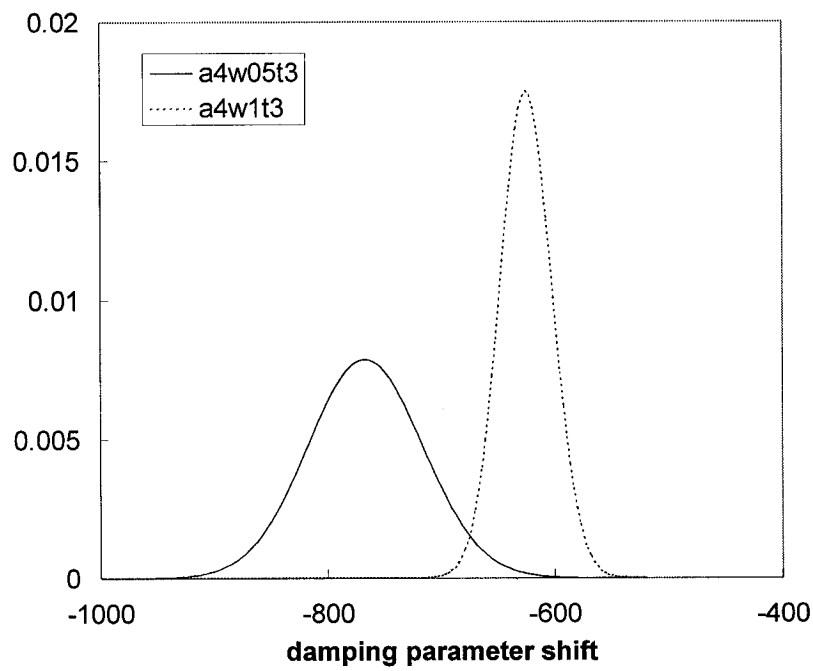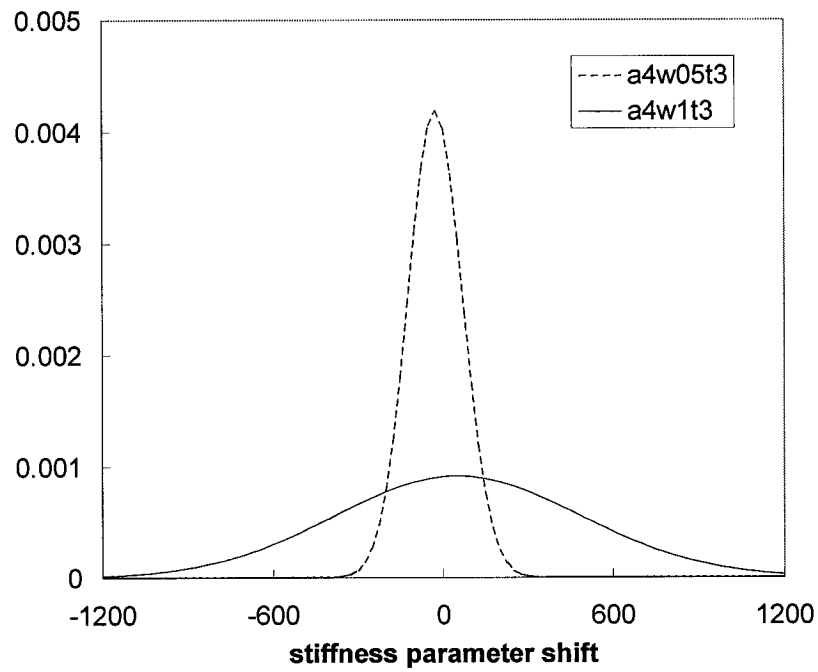
FIGURE 7.42. Frequency effects, A=2 in-pk, T3

269
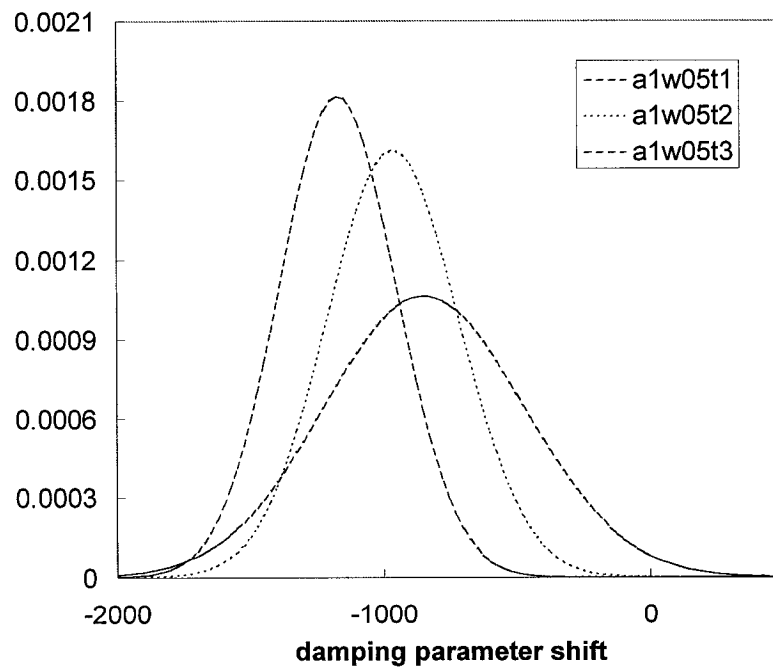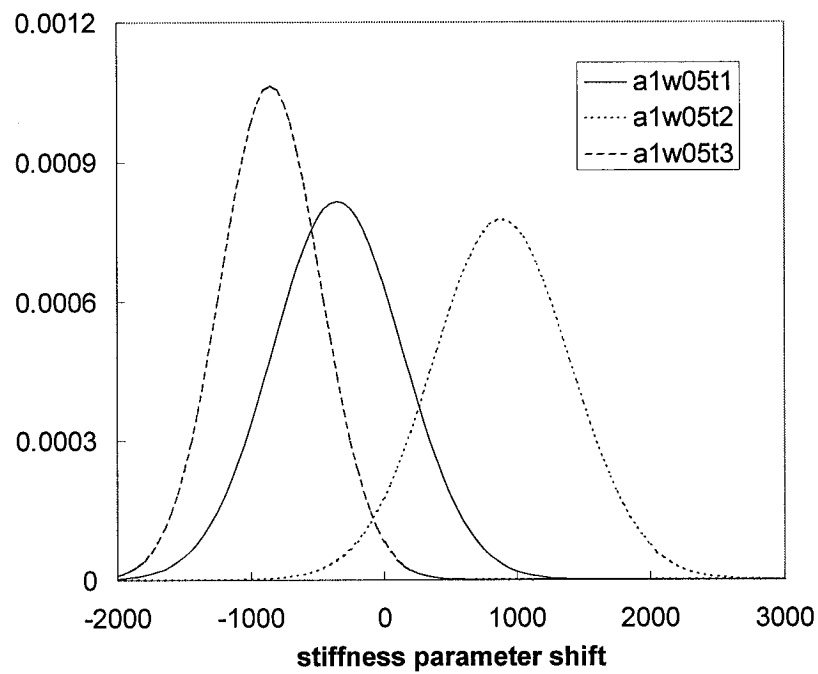
FIGURE 7.43. Temperature effects, A=0.5 in-pk, ω=0.5 Hz

270
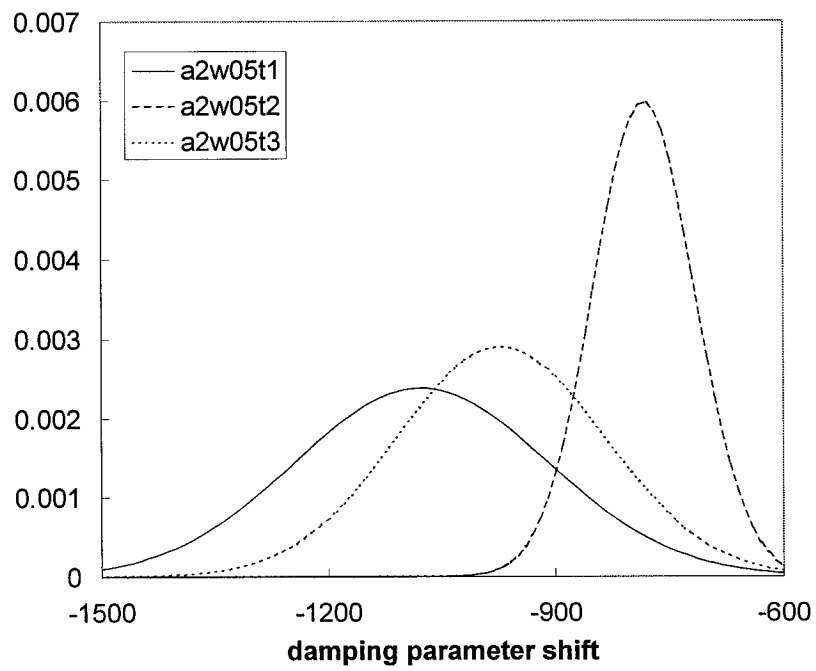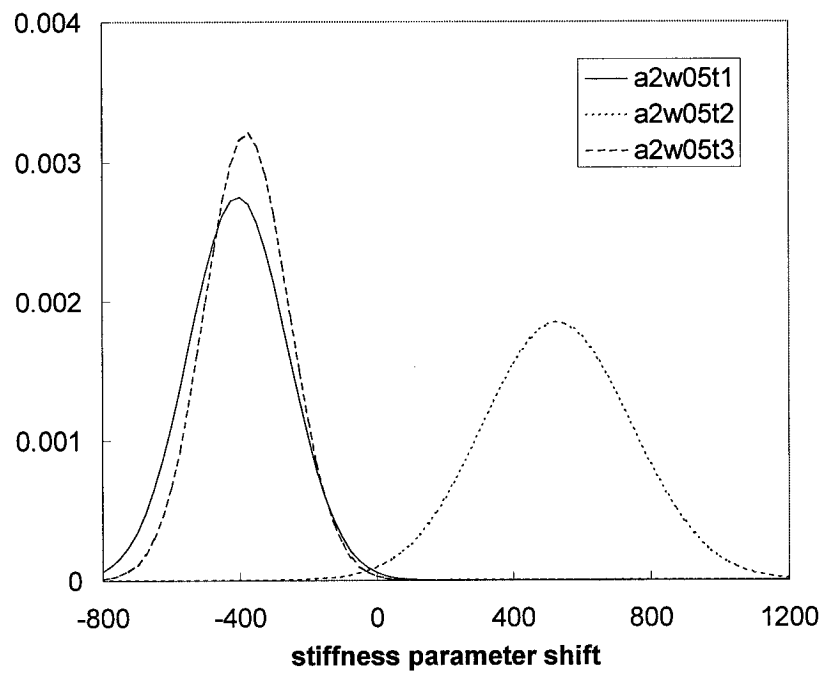
FIGURE 7.44. Temperature effects, A=1 in-pk, ω=0.5 Hz

271
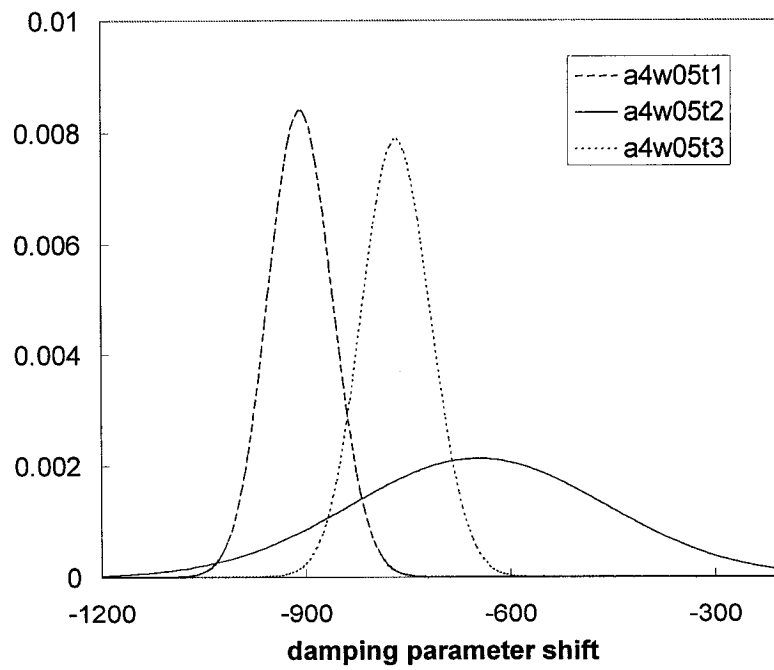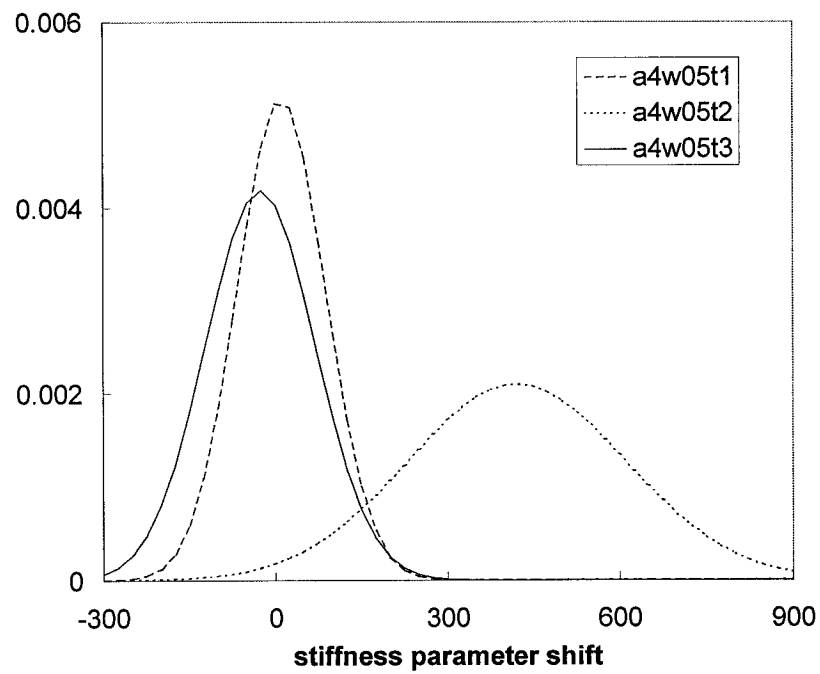
FIGURE 7.45. Temperature effects, A=2 in-pk, ω=0.5 Hz

272
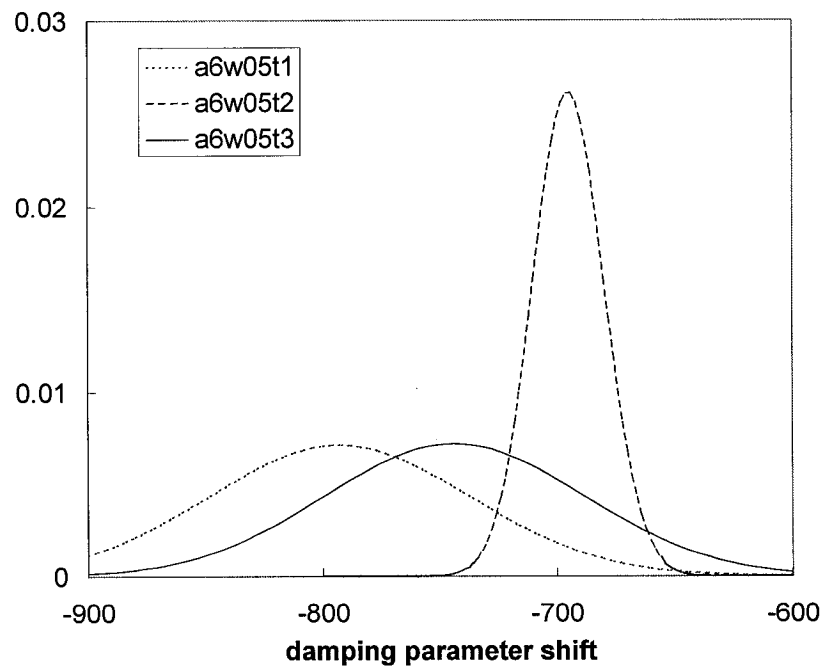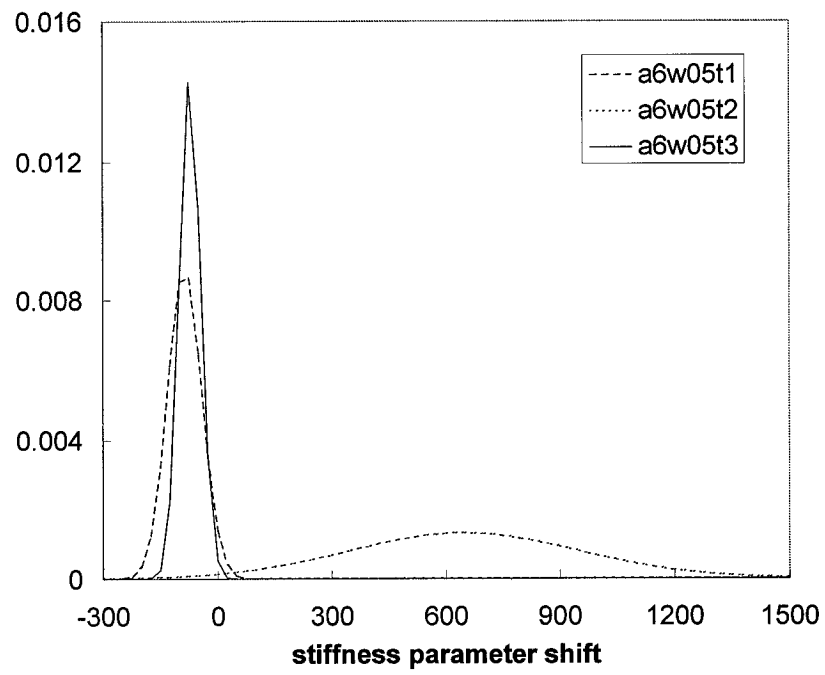
FIGURE 7.46. Temperature effects, A=3 in-pk, ω=0.5 Hz

273
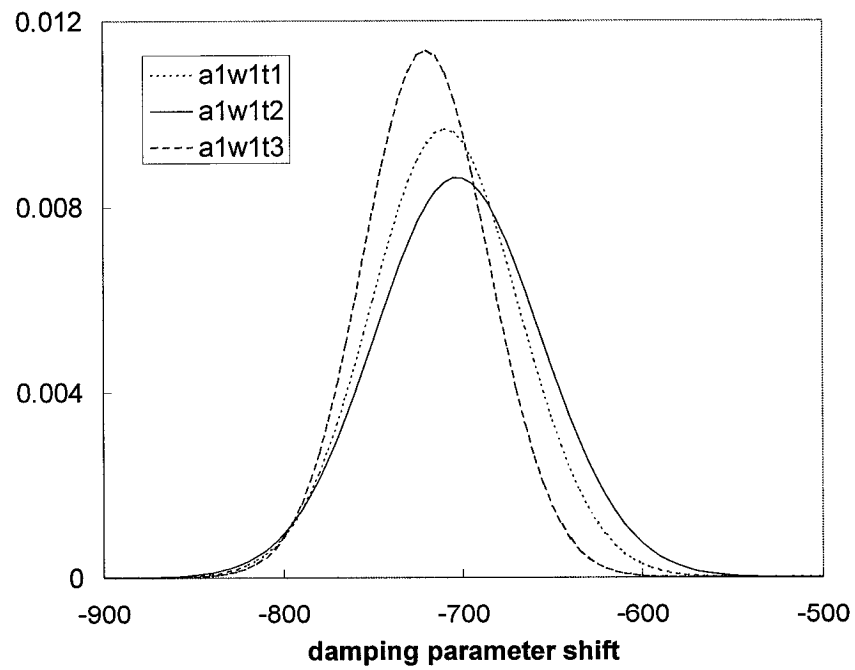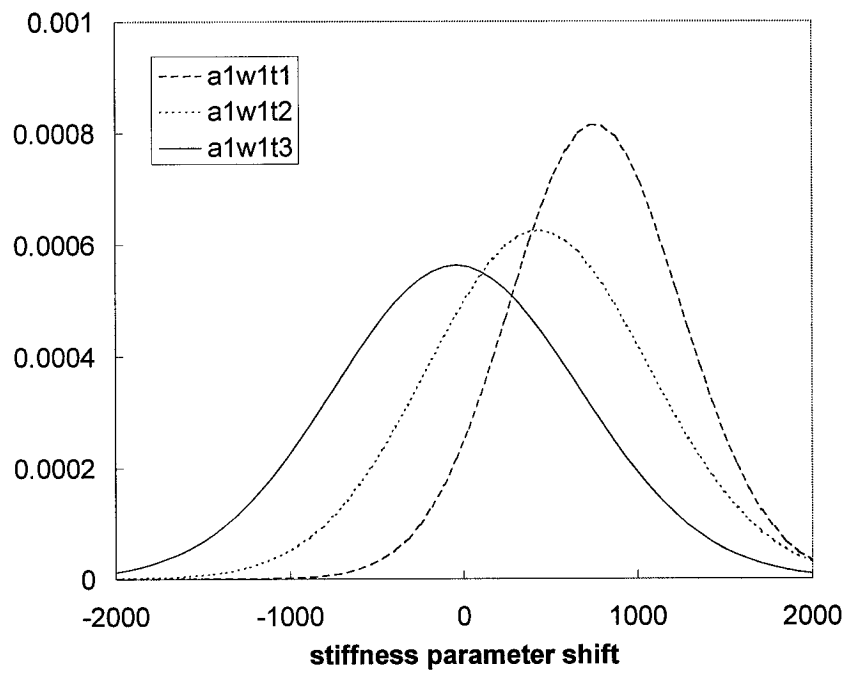
FIGURE 7.47. Temperature effects, A=0.5 in-pk, ω=1 Hz
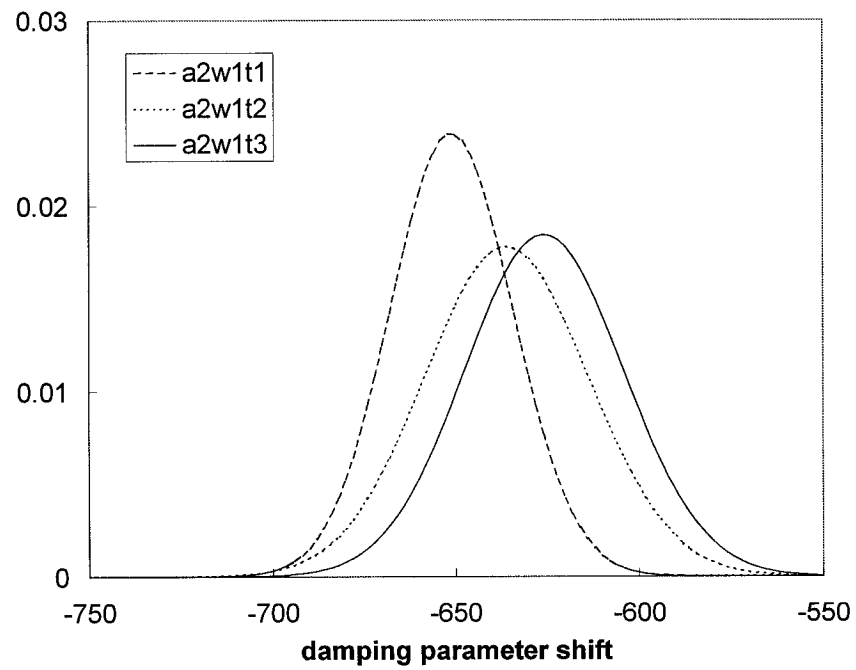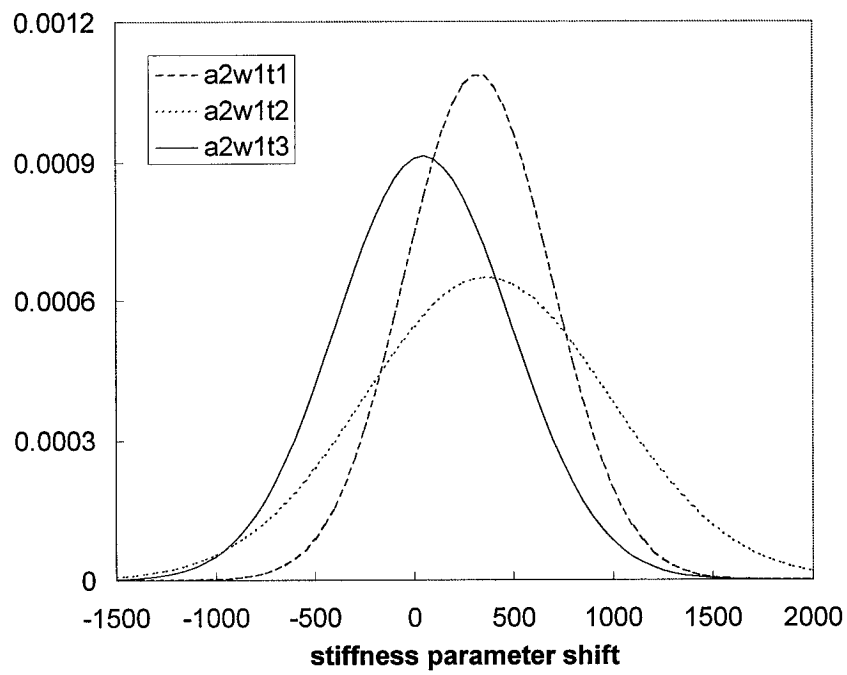
FIGURE 7.48. Temperature effects, A=1 in-pk, ω=1 Hz

275
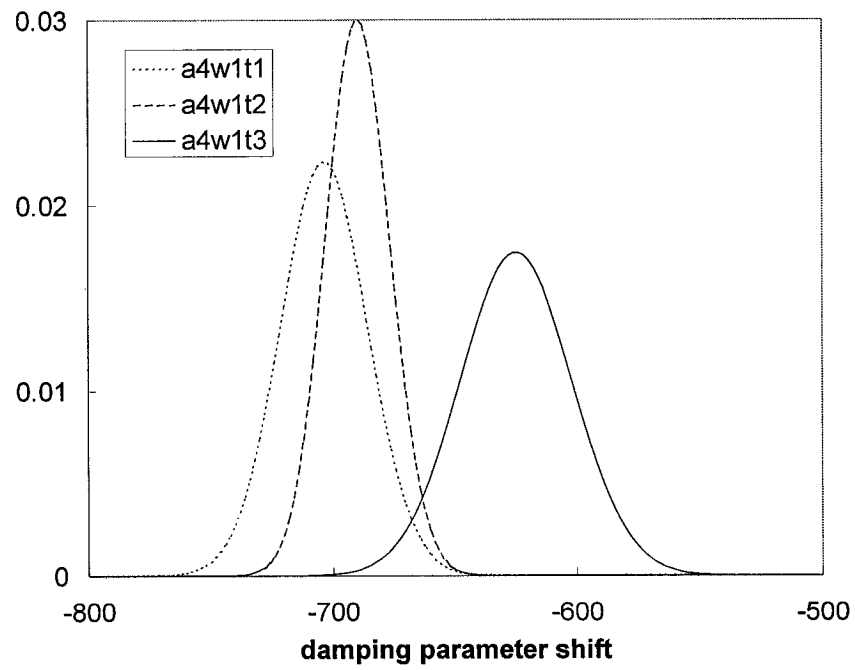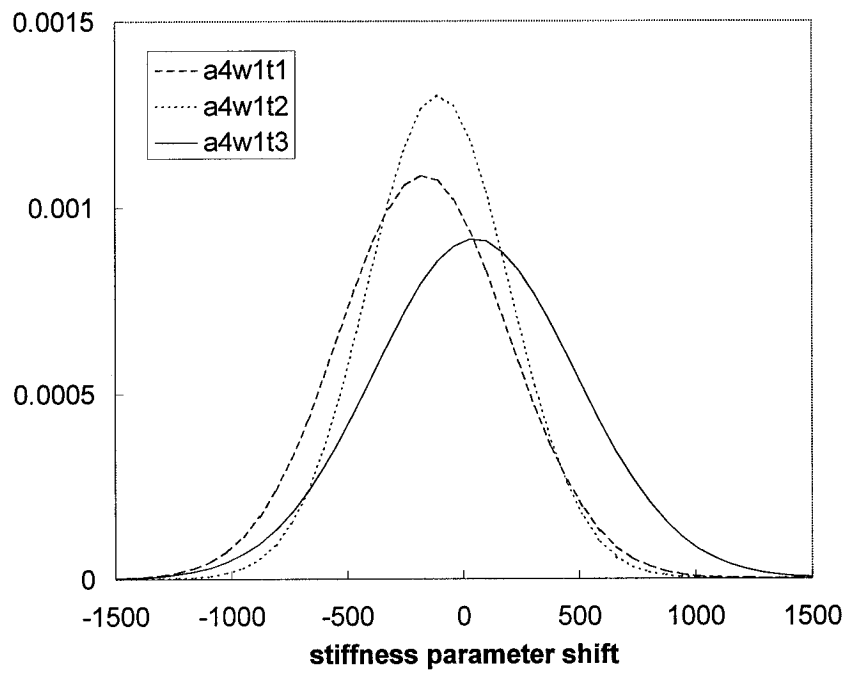
FIGURE 7.49. Temperature effects, A=2 in-pk, ω=1 Hz

These figures clearly display shifts in the mean identified stiffness and damping parameters when amplitude, frequency and temperature are varied according to Table 7.1. Interestingly, thermal effects appear to dominate the system response, masking other effects to a degree. This is particularly evident for higher amplitude tests where the temperature rise during the 60-second test was recorded as 30-40°F.

A simplified explanation of this phenomenon lies with the thermal characteristics of viscous fluids such as used in the tested damper. Higher velocities dramatically increase the friction within the fluid, resulting in large temperature rises. This result follows basic fluid dynamics theory and must be addressed in future studies to facilitate decoupling of the respective parameter influences.

The results of Figures 7.28 through 7.49, when ignoring higher velocity tests, illustrate gradual shifts in the system stiffness and damping parameters. The tendency is for the parameter mean values to either increase or decrease given prescribed changes to the excitation. Clearly, amplitude and frequency changes in the excitation impose identifiable system trends, but these effects are not easily uncoupled from each other or from temperature effects. Thus, attributing respective contributions to amplitude, frequency and temperature effects is difficult in the absence of more refined test protocols. A first step involves tighter controls over temperature test parameters to draw definitive results beyond stating that the effect

277

of varying any of the three test parameters is noted in the identified system response parameters.

Clearly the three dimensional nonlinear fluid/orifice dynamic effects are complicating factors not adequately addressed in these tests. The questionable higher amplitude results illustrate the pitfalls of too simplified an approach to a highly nonlinear problem. Recall that the temperature was controlled within 10°F increments, with T1 defined between 70-80°F, T2 ranging from 90-100°F, and T3 defined as 110-120°F. Rapid thermal increases introduce unanticipated excursions beyond these temperature ranges which skews the results with undefined system thermal characteristics. Future studies should incorporate more indepth modeling and test plan controls to identify and quantify these and all other effects inherent in such a highly nonlinear system. Some of these efforts are currently underway.

In short, these results clearly reveal that a more rigorous control of the temperature range throughout the test period must be investigated and formalized. The damper is a time varying system, and is thus subject to the dynamic thermal effects resulting from increasing velocities. Further evaluation and testing should approach the system as a nonstationary problem and address the time varying effects in test planning and execution. Test protocols designed to fully characterize the time-varying nonlinear behavior of a similar damper are necessary to draw useful conclusions beyond that stated above.

278

7.6.2 Broadband Random Excitation

Two experiments were conducted with broadband excitations having different amplitudes as described in Table 7.2. Preliminary testing of the damper with low-level broadband excitations revealed that the system was severely driven in the higher frequencies of the response spectra defined in Figure 7.1. This fact was further substantiated through tests being conducted concurrently at the University of California, Berkeley, on physically damaged dampers using the same excitation developed herein. In both cases, it was determined that the frequency content should be reduced from 25 Hz to accommodate continued testing. These tests were performed with the cutoff frequency set at 5 Hz at USC. The resulting measured responses for these tests are presented below.
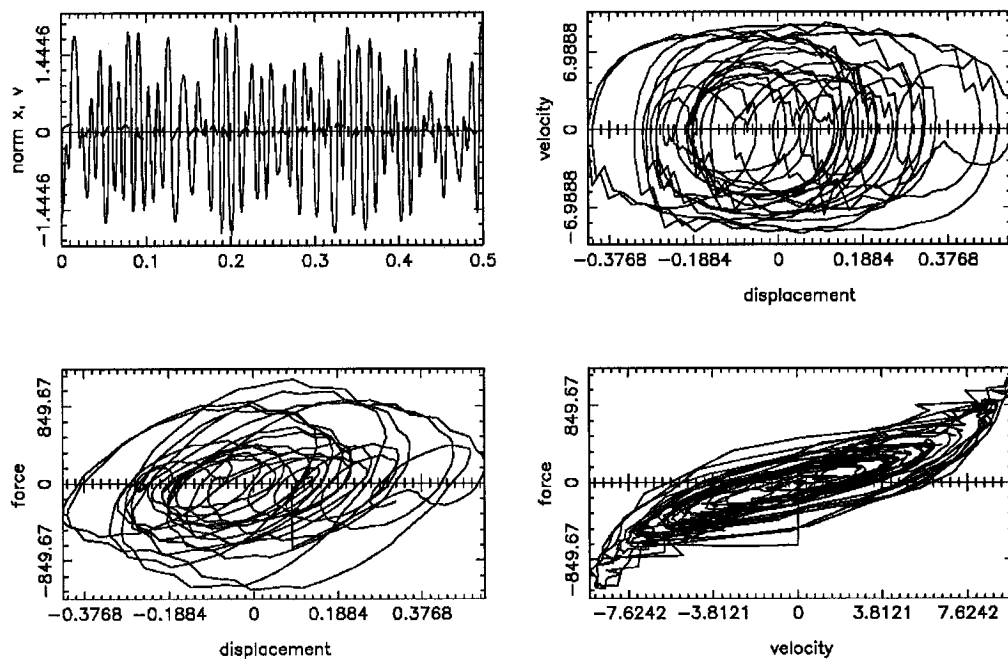
FIGURE 7.50. Damper response to broadband excitation, test #1
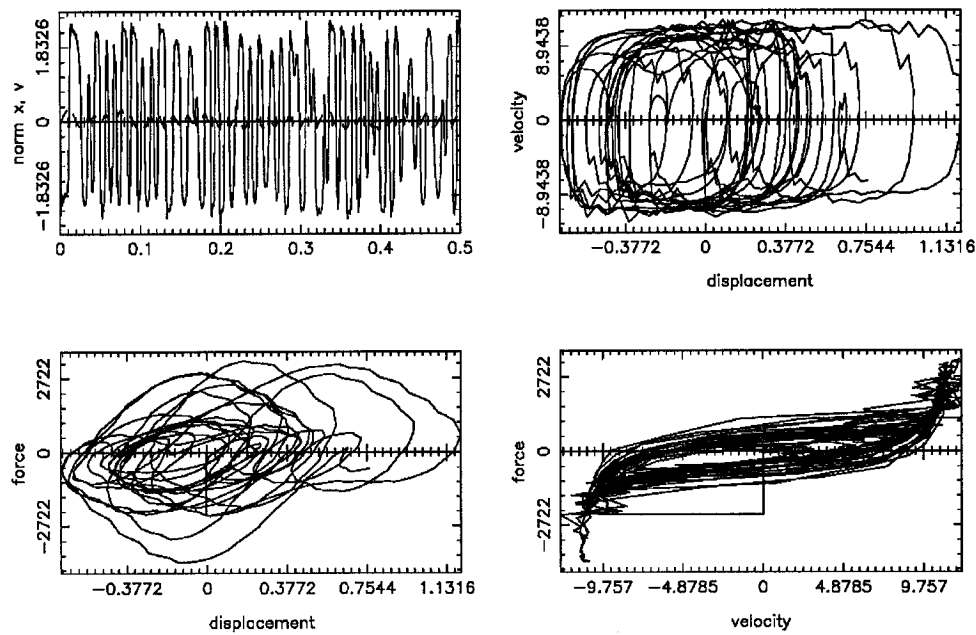
FIGURE 7.51. Damper response to broadband excitation, test #2

Chebyshev coefficients				
i/j	**1**	**2**	**3**	**4**
1	38.17	920.31	44.74	118.47
2	296.67	4.55	11.38	-17.19
3	-2.66	25.40	14.18	-26.54
4	-30.32	1.12	5.22	19.66
Power Series coefficients				
i/j	**1**	**2**	**3**	**4**
1	-35.75	46.26	0.33	0.71
2	833.23	41.19	-0.10	-0.64
3	11.22	131.87	3.10	-1.62
4	-1333.67	-237.60	2.65	3.58

TABLE 7.10. Identified damper coefficients, broadband excitation, test #1

280

Chebyshev coefficients				
i/j	1	2	3	4
1	322.43	2085.71	446.67	937.53
2	484.85	-51.98	-54.94	11.11
3	-209.43	-403.26	-229.84	-243.06
4	81.48	106.92	63.17	101.31
Power Series coefficients				
i/j	1	2	3	4
1	-212.89	-101.36	5.09	2.76
2	500.13	1.19	0.43	0.08
3	-82.03	122.87	-6.54	-1.98
4	126.42	-78.34	2.23	1.06

TABLE 7.11. Identified damper coefficients, broadband excitation, test #2
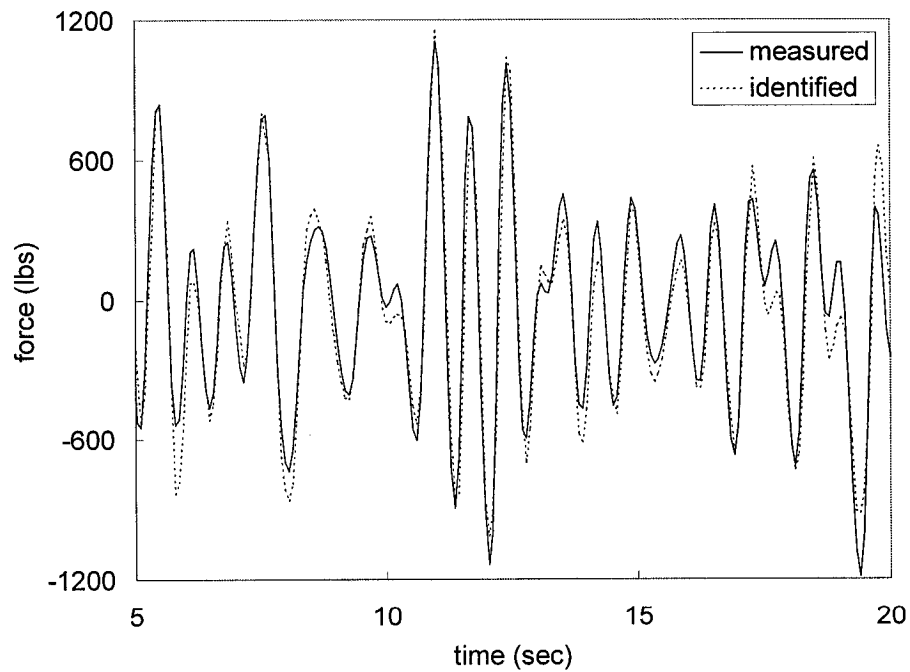
FIGURE 7.55. Measured versus identified force, broadband excitation, test #1

281
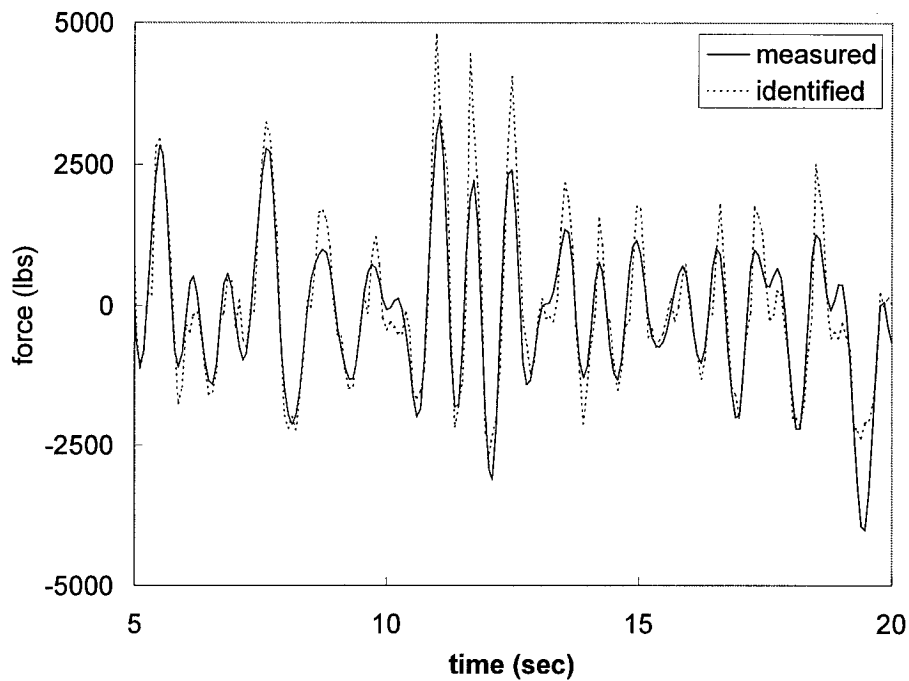
FIGURE 7.56. Measured versus identified force, broadband excitation, test #2

Note from the above results that the restoring force algorithm clearly tracks the system response. Data processing through the neural network and least squares recursive algorithm would yield similar results as noted in the simulation studies presented in Chapter 6.

The next step lies in developing threshold values for the system. There are two ways of approaching this problem; perform large sets of experiments to statistically quantify the system response and variability for a "healthy" damper, or physically introduce predefined damage to the system and excite the system to evaluate the response. Both methods require some initial investment to facilitate development of

282

valid thresholds describing the potential for system damage existing when crossed. Since it has been shown that any of the three algorithms is viable for detecting subtle system variations under noise pollution, damage detection thresholds can be developed for any of the three. Recall that the neural network results cannot be correlated to the physical system as can the restoring force and least squares method parameters. In any case, the physical system need not be modeled to determine damage.

7.7 Scaling effects

A concern held early in the development of the test plan for the scaled testing related to model scaling effects. The problem of model scaling has plagued researchers through the ages, particularly when full-scale testing was not feasible. It is shown through preliminary results from full-scale testing of similar dampers that these effects are inconsequential relative to the scaled model testing performed at the University of Southern California. The data presented in Figures 7.57 and 7.58 was drawn from cyclic testing performed at the SRMD research facility at the University of California, San Diego campus. Reviewing these results in conjunction with those reported in Section 7.6.1 reveals nearly identical system characteristics. Phase plane plots for each reveal similar nonlinear dynamic response to cyclic excitation. This result is powerful in that it refutes claims that scaling effects potentially invalidate results reported from the dynamic characterization, evaluation and determination of the effectiveness of identification algorithms utilizing a scaled model.

283
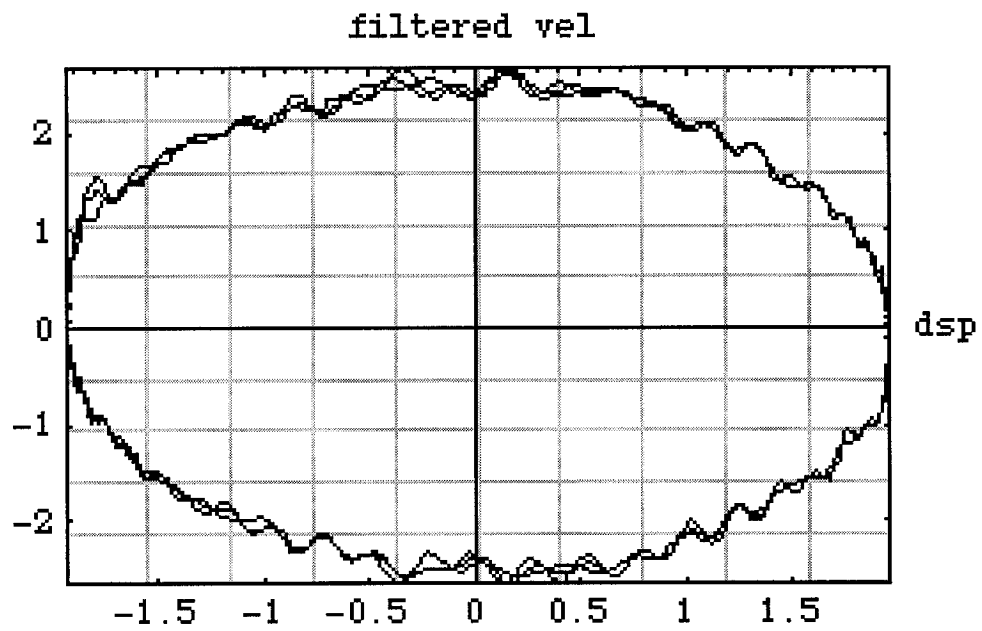
FIGURE 7.57. Full-scale damper test results; x versus v
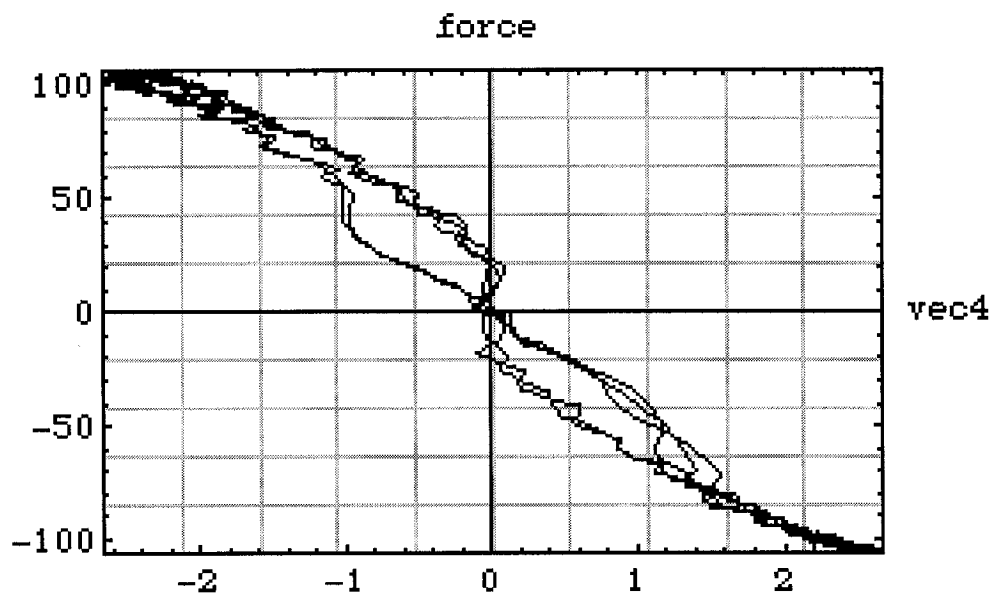
FIGURE 7.58. Full-scale damper test results; v versus f

284

8.0 Conclusion

The stated objective of this research was to develop an optimized set of analytical tools for in-field health monitoring of structural damper elements. In pursuit of this objective, a number of parametric and nonparametric health monitoring tools have been evaluated. Based on this evaluation, a subset of health monitoring tools has been optimized to enhance their error detection capabilities.

This analysis identified the restoring force and least squares recursive algorithms as the best means of *in-situ* error detection. Each of the analyzed algorithms showed success in replicating the system response to prescribed excitation, even under noise pollution.

In arriving at this conclusion, the research considered a number of health monitoring tools. The Chebyshev restoring force algorithm, Neural Network approach and the method of Chassiakos et al were selected for this research based on the successes portrayed in numerous publishings regarding their use. Monte Carlo statistical analysis of the simulation data was utilized to develop algorithm detection capabilities. Variability analysis was also introduced to determine the identification algorithm's ability to discern induced damage from manufacturing variances.

The author notes that a considerable amount of research on this subject had preceded this work. A key first step here, then, was to review the large body of literature

285

available on the subject. This was followed by selection from amongst those considered most well developed, based on simulation and actual experimental applications. The focus of this research was not in developing new identification algorithms, but in selecting and optimizing existing algorithms for *in-situ* real-time identification of damper elements. Thus, the algorithms studied herein were chosen based on existing tests and their ability to replicate nonlinear system response with low level computational effort. These tools were, then, subjected to rigorous analysis. This analysis employed simulation data as well as experimental data sets derived from a scaled version of dampers being implemented on the retrofit of the West Spans of the SFOBB.

The research efforts focused on the Chebyshev restoring force algorithm first. Several hundred thousand simulations were performed for varying degraded system states of linear and nonlinear models. The Chebyshev algorithm was chosen to process the resulting data to establish a baseline measure. Additionally, multiple levels of noise pollution were introduced to quantify algorithm discrimination capabilities. Selected simulations were then processed with the Neural Network and least squares recursive algorithms.

It was originally proposed that data from the prototype and proof tests of the dampers being employed on the SFOBB retrofit be compared to reduced-scale simulation studies conducted at the University of Southern California.

Unfortunately, due to construction schedule delays, the SFOBB dampers have not yet been tested. However, plans are in place to conduct full-scale damper testing and data acquisition, at either the newly constructed State-owned Seismic Response Modification Device (SRMD) facility at the University of California at San Diego or at Taylor's testing facilities in New York. Such testing is targeted for mid to late summer 2002. The results are expected to confirm those presented in this research as the tested damper was a similar device, only scaled from the actual dampers. The identification algorithms being employed, however, are immune to size effects, relying solely on the measured system response for identifying the system behavior.

Additional scaled model testing is underway at the campus of the University of California, Berkeley. Data from these tests, wherein actual damage levels are to be incorporated will be processed and analyzed through the above algorithms. These results are expected to further support the hypothesis that a detection system can be implemented in the field with only minor instrumentation needs. Online system quantification requires only a few transducers to provide velocity, displacement, force and temperature measurements. These transducers and the data acquisition system would be required to incorporate fairly high frequency response, with a data sampling rate of at least 1 kHz, and preferably 5 kHz. Identification can be performed on subsets of the real-time data stream. The advantages of such a system are a substantial reduction in periodic inspection and damper removal for testing, and subsequent reduction in handling damage potential. In the absence of direct

287

displacement and velocity measurements, integration of acceleration could be facilitated if the data set was acquired with anti-aliasing filtering. High fidelity integration schemes are being developed here at the University currently.

Further research efforts in this area should focus on actual testing of damaged states. This will require additional dampers and the ability to introduce stiffness and damping system changes. Some of this effort is underway at the University of California, Berkeley, as noted above.

In conclusion, the true engineering and research value of this effort is that it has been conclusively shown that identification algorithms can successfully discriminate system damage levels even under relatively high levels of noise pollution. System variability analysis was also analyzed, and it was shown that damage detection thresholds could be developed that allow for process variability while still discriminating damage at low levels. This is important in that it allows detection threshold analysis for a selected set of similar dampers only. Real applications will likely incorporate baseline system evaluation with detection thresholds applied as percentage standard deviations of measured state variables.

This research has moved industry closer to realizing significant gains in efficiency as well as reliability through *in-situ* health monitoring applications, by imparting the insight necessary to distill from the large body of extant research on system

288

identification and damage detection, optimizing those algorithms and providing the tools necessary to facilitate bridging the gap between academic study and real-life benefits. The proposed health monitoring system requires limited investment in terms of equipment and resources for implementation and maintenance, particularly when judged against the alternatives currently in place; that is, periodic system evaluation through physical testing, requiring removal, transport and reinstallation.

References

1. Abe, M., Fujino, Y., Kajimura, T., Yanagihara, M., and Sato, M., 1999, "Monitoring of a Long Span Suspension Bridge by Ambient Vibration Measurement", *Proceedings of the 2nd International Workshop on Structural Health Monitoring*, September 18-20, pp. 400-407.

2. Achenbach, J. D., Moran, B., and Zulfiqar, A., 1997, "Techniques and Instrumentation for Structural Diagnostics", *Proceedings of the 2nd International Workshop on Structural Health Monitoring, Current Status and Perspectives*, September 18-20, pp. 179-190.

3. Agrawal, A. K., 2000, "Semi-active Control Strategies for Buildings Subject to Near-field Earthquakes", *SPIE's 7th International Symposium on Smart Structures and Materials*, March, p. 159.

4. Aiken, I. D., 1998, "Testing of Seismic Isolators and Dampers – Considerations and Limitations", Structural Engineering World Wide, Elsevier Science Ltd., Oxford, England.

5. Aiken, I. D., and Kelley, J. M., 1995, "Pre-Qualification Testing of Viscous Dampers for the Golden Gate Bridge Seismic Rehabilitation Project", Earthquake Engineering Research Center Report No. EERC-STI/95-04.

6. Aiken, I. D., and Kelley, J. M., 1995, "Pre-Qualification Testing of Viscous Dampers for the Golden Gate Bridge Seismic Rehabilitation Project", Earthquake Engineering Research Center Report No. EERC-STI/95-02.

7. Aiken, I. D., and Kelley, J. M., 1996, "Cyclic Dynamic Testing of Fluid Viscous Dampers", Proceedings of the Fourth Caltrans Seismic Research Workshop, California Dept. of Transportation, Sacramento, CA.

8. Alampalli, S., and Cioara, T., 2000, "Selective Random Decrement Technique for Processing Bridge Vibration Data", *Structural Materials Technology IV, Nondestructive Testing Conference Proceedings*, March, pp. 75-80.

9. Al-Khalidy, A., Noori, M., Hou, Z., Yamamoto, S., Masuda, A., and Sone, A., 1997, "Health Monitoring Systems of Linear Structures Using Wavelet Analysis", *Proceedings of the 2nd International Workshop on Structural Health Monitoring, Current Status and Perspectives*, September 18-20, pp. 164-175.

290

10. Alvin, K. F., and Park, K. C., 1996, "Extraction of Substructural Flexibility from Measured Global Modes and Mode Shapes", *Proc. 1996 AIAA SDM Conference*, Paper No. AIAA 96-1297, Salt Lake City, Utah; submitted to AIAA Journal.

11. Atalla, M. J., and Inman, D. J., 1998, "On Model Updating Using Neural Networks", *Mechanical Systems & Signal Processing*, 12(1), pp. 135-161.

12. Blondet, M., 1993, "Dynamic Response of Two Viscoelastic Dampers", Report No. UCB/SEMM-94-01, Department of Civil Engineering, University of California, Berkeley, July.

13. Bolton, R. W., Stubbs, N., Park, S., Choi, S., and Sikorsky, C., 1999, "Field Measurements of Modal Parameters for Non-Destructive Damage Detection Algorithms", *Proceedings of the 2nd International Workshop on Structural Health Monitoring*, September 18-20, pp. 966-975.

14. Catbas, F. N., Grimmelsman, K. A., and Aktan, A. E., 2000, "Bridge Health-monitoring for Structural Performance", *Structural Materials Technology IV, Nondestructive Testing Conference Proceedings*, March, pp. 95-100.

15. Catbas, F. N., Grimmelsman, K. A., Barrish, R. A., Tsikos, C. J., and Aktan, A. E., 1999, "Structural Identification and Health Monitoring of a Long Span Bridge", *Proceedings of the 2nd International Workshop on Structural Health Monitoring*, September 18-20, pp. 417-429.

16. Chang, T. Y., Chang, C. C., and Xu, Y. G., 1999, "Updating Structural Parameters: An Adaptive Neural Network Approach", *Proceedings of the 2nd International Workshop on Structural Health Monitoring*, September 18-20, pp. 370-389.

17. Chassiakos, A. G., Masri, S. F., Smythe, A. W., and Caughey, T. K., 1998, "On-Line Identification of Hysteretic Systems", *ASME Journal of Applied Mechanics*, Vol. 65, March, pp. 194-203.

18. Chen, G., 2000, "Recent Developments in Structural Control Including Soil-structure Interaction Effect", *SPIE's 7th International Symposium on Smart Structures and Materials*, March, p. 150.

19. Choi, M., and Kwon, I., 2000, "Damage Detection System of a Real Steel Truss Bridge by Neural Networks", *SPIE's 7th International Symposium on Smart Structures and Materials*, March, p. 153.

20. Chong, K. P., 1997, "Health Monitoring of Civil Infrastructures", *Proceedings of the 2nd International Workshop on Structural Health Monitoring, Current Status and Perspectives*, September 18-20, pp. 339-350.

21. Constantinou, M. C., 1994, "Application of Fluid Viscous Dampers to Earthquake Resistant Design", Buffalo: National Center for Earthquake Engineering Research, September, pp. 73-80.

22. Constantinou, M. C., and Symans, M. D., 1992, "Experimental and Analytical Investigation of Seismic Response of Structures with Supplemental Fluid Viscous Dampers", Technical Report NCEER-92-0032, National Center for Earthquake Engineering Research, SUNY, Buffalo, December.

23. Doebling, S. W., Farrar, C. R., Prime, M. B., and Shevitz, D. W., 1996, "Damage Identification and Health Monitoring of Structural and Mechanical Systems from Changes in their Vibrations Characteristics: A Literature Review", Technical Report LA-13070-MS, Los Alamos National Laboratory, USA.

24. Doebling, S. W., and Hemez, F. M., 2001, "Overview of Uncertainty Assessment for Structural Health Monitoring", *Proceedings of the 3rd International Workshop on Structural Health Monitoring: The Demands and Challenges*, September 12-14, pp. 770-783.

25. Dowing, C. H., and Charles, E., 1999, "Measurement of Water Pressure and Deformation with Time Domain Reflectometry Cables", *Proc. SPIE.*, 2457, pp. 217-225.

26. Ehrgott, R. C., and Masri, S. F., 1992, "Modeling the Oscillatory Dynamic Behavior of Electrorheological Materials in Shear", IOP Publishing Ltd., pp. 275-285.

27. Farrar, C. R., and Doebling, S. W., 1997, "Lessons Learned from Applications of Vibration-Based Damage Identification Methods to a Large Bridge Structure", *Proceedings of the 2nd International Workshop on Structural Health Monitoring, Current Status and Perspectives*, September 18-20, pp. 351-370.

28. Fenves, G. L., Huang, W. H., Whittaker, A. S., Clark, P. W., and Mahin, S. A., 1998, "Modeling and Characterization of Seismic Isolation Bearings", U.S. Italy Workshop on Seismic Protective Systems for Bridges.

29. Fuchs, P. A., Washer, G. A., and Chase, S. B., 2000, "Large-scale Structural Monitoring Using a Scanning Laser Displacement Measurement Instrument", *Structural Materials Technology IV, Nondestructive Testing Conference Proceedings*, March, pp. 307-312.

30. Gaul, L., and Sachau, D., 1997, "Nonlinear Active Damping of Adaptive Space Structures", *Proceedings of the 2ⁿᵈ International Workshop on Structural Health Monitoring, Current Status and Perspectives*, September 18-20, pp. 208-219.

31. Hadjian, A. H., Masri, S. F., and Saud, A. F., 1987, "A Review of Methods of Equivalent Damping Estimation From Experimental Data", *ASME Journal of Applied Mechanics*, Vol. 109, May, pp. 236-243.

32. Hall, S. R., 1999, "The Effective Management and Use of Structural Health Data", *Proceedings of the 2ⁿᵈ International Workshop on Structural Health Monitoring*, September 18-20, pp. 265-275.

33. Hanagud, S., and Luo, H., 1997, "Damage Detection and Health Monitoring Based on Structural Dynamics", *Proceedings of the 2ⁿᵈ International Workshop on Structural Health Monitoring, Current Status and Perspectives*, September 18-20, pp. 715-726.

34. Haskell, G., and Lee, D., 19XX, " Fluid Viscous Damping as an Alternative to Base Isolation".

35. Helmicki, A., Hunt, V., Shell, M., Lenett, M., Turer, A., Dalal, V., and Aktan, A., 1999, "Mulidimensional Performance Monitoring of a Recently Constructed Steel-Stringer Bridge", *Proceedings of the 2ⁿᵈ International Workshop on Structural Health Monitoring*, September 18-20, pp. 408-416.

36. Herrmann, H. –G., and Streng, J., 1997, "Problem-Specific Neural Networks for Detecting Structural Damage", *Proceedings of the 2ⁿᵈ International Workshop on Structural Health Monitoring, Current Status and Perspectives*, September 18-20, pp. 267-278.

37. Hou, Z., and Noori, M., 1999, "Application of Wavelet Analysis for Structural Health Monitoring", *Proceedings of the 2ⁿᵈ International Workshop on Structural Health Monitoring*, September 18-20, pp. 946-955.

38. Housner, G. W., Bergman, L. A., Caughey, T. K., Chassiakos, A. G., Claus, R. O., Masri, S. F., Skelton, R. E., Soong, T. T., Spencer, B. F., and Yao, J. T. P., 1997, "Structural Control: Past, Present and Future", *Journal of Engineering Mechanics*, ASCE 123(9), September, pp. 897-971.

39. Hyland, D., and Fry, G., 1999, "A Neural-Genetic Hybrid Approach for Optimizing Structural Health Monitoring Systems", *Proceedings of the 2ⁿᵈ International Workshop on Structural Health Monitoring*, September 18-20, pp. 800-811.

40. Ibrahim, S. R., et al., 1977, "A Method for Direct Identification of Vibration Parameters from the Free Response", *Shock and Vibration Bulletin*, Vol. 47.

41. Ioannou, P., and Sun, J., 1996, "Robust Adaptive Control", Prentice Hall PTR, Upper Saddle River, New Jersey.

42. Jiao, L., 1996, "The Systematical Theory of Neural Networks", Xian, China: Xian University of Electrical Science and Technology press.

43. Katafygiotis, L. S., and Lam, H. F., 1997, "A Probabilistic Approach to Structural Health Monitoring Using Dynamic Data", *Proceedings of the 2nd International Workshop on Structural Health Monitoring, Current Status and Perspectives*, September 18-20, pp. 152-163.

44. Kreyszig, E., 1993, "Advanced Engineering Mathematics", 7th Edition, Wiley & Sons, New York.

45. Lee, G. C., and Liang, Z., 1999, "Development of a Bridge Monitoring System", *Proceedings of the 2nd International Workshop on Structural Health Monitoring*, September 18-20, pp. 349-358.

46. Levin, R. I., and Leven, N. A. J., 1998, "Dynamic Finite Element Model Updating Using Neural Networks", *Journal of Sound & Vibration*, 210(5), pp. 593-607.

47. Lihua, S., 1999, "Structural Damage Detection by ETDR Method and Wavelet Analysis of the Measured Signals", *Proceedings of the 2nd International Workshop on Structural Health Monitoring*, September 18-20, pp. 1029-1037.

48. Lihua, S., and Baoqi, T., 1997, "Identification of External Force Acting on a Plate Using Neural Networks", *Proceedings of the 2nd International Workshop on Structural Health Monitoring, Current Status and Perspectives*, September 18-20, pp. 229-237.

49. Liu, P. –L., and Sun, S. –C., 1997, "The Application of Artificial Neural Networks on the Health Monitoring of Bridges", *Proceedings of the 2nd International Workshop on Structural Health Monitoring, Current Status and Perspectives*, September 18-20, pp. 103-110.

50. Liu, P., S. Sana, and Rao, V. S., 1999, "Structural Damage Identification Using Time-Domain Parameter Estimation Techniques", *Proceedings of the 2nd International Workshop on Structural Health Monitoring*, September 18-20, pp. 812-820.

51. Lloid, G. M., and Wang, M. L., 1999, "Asymptotic Bias Correction for a Probabilistic Neural Network for Structural Health Monitoring", *Proceedings of the 2ⁿᵈ International Workshop on Structural Health Monitoring*, September 18-20, pp. 713-722.

52. Lopes Jr., V., Park, G., Cudney, H. H., and Inman, D. J., 1999, "Smart Structures Health Monitoring Using Artificial Neural Network", *Proceedings of the 2ⁿᵈ International Workshop on Structural Health Monitoring*, September 18-20, pp. 976-985.

53. Luo, H., and Hanagud, S., 1997, "Dynamic Learning Rate Neural Networks Training and Composite Structural Damage Detection", AIAA Journal, 35(9), pp. 1522-1527.

54. Makris, N., and Constantinou, M. C., 1990, "Viscous Dampers: Testing, Modeling, and Application in Vibration and Seismic Isolation", National Center for Earthquake Engineering Research, NCEER-90-0028, December.

55. Masri, S. F., and Caughey, T. K., 1979, "A Nonparametric Identification Technique for Nonlinear Systems", *ASME Journal of Applied Mechanics*, Vol. 46, No. 2, June, pp.433-447.

56. Masri, S. F., Chassiakos, A. G., and Caughey, T. K., 1993, "Identification of Nonlinear Dynamic Systems Using Neural Networks", *ASME Journal of Applied Mechanics*, Vol. 60, March, pp. 123-133.

57. Masri, S. F., Miller, R. K., Sassi, H., and Caughey, T. K., 1984, "A Method for Reducing the Order of Nonlinear Dynamic Systems", *Journal of Applied Mechanics*, Vol. 51, June, pp. 391-398.

58. Masri, S. F., Miller, R. K., Saud, A. F., and Caughey, T. K., 1987, "Identification of Nonlinear Vibrating Structures: Part I – Formulation", *ASME Journal of Applied Mechanics*, Vol. 54, December, pp. 918-922.

59. Masri, S. F., Miller, R. K., Saud, A. F., and Caughey, T. K., 1987, "Identification of Nonlinear Vibrating Structures: Part II – Applications", *ASME Journal of Applied Mechanics*, Vol. 54, December, pp. 923-929.

60. Masri, S. F., Miller, R. K., Traina, M. I., and Caughey, T. K., 1991, "Development of Bearing Friction Models from Experimental Measurements", *Journal of Sound and Vibration*, Vol. 148, No. 3., pp. 455-475.

61. Masri, S. F., Nakamura, M,. Chassiakos, A. G., and Caughey, T. K., 1996, "Neural Network Approach to Detection of Changes in Structural Parameters", *Journal of Engineering Mechanics*, April, pp. 350-360.

62. Masri, S. F., Smythe, A. W., and Chassiakos, A. G., 1998, "Detection of Structural Changes through Nonlinear System Identification Approaches", *Asia-Pacific Workshop on Seismic Design & Retrofit of Structures*, August, pp. 425-439.

63. Masri, S. F., Smythe, A. W., and Chassiakos, A. G., 1998, "Detection of Structural Changes through Nonlinear System Identification Approaches", *Asia-Pacific Workshop on Seismic Design & Retrofit of Structures*, August 10-12, pp. 425-439.

64. McClelland, W.S., and Pitts, W.H., 1943, "A logical calculus of the ideas immanent in nervous activity", *Bulletin of Mathematical Biophysics*, Vol. 5, pp. 115-133.

65. Mita, A., 1999, "Emerging Needs in Japan for Health Monitoring Technologies in Civil and Building Structures", *Proceedings of the 2nd International Workshop on Structural Health Monitoring*, September 18-20, pp. 56-67.

66. Narendra, K.S., and Parthasarathy, K., 1990, "Identification and control of dynamical systems using neural networks", *IEEE Trans. Neural Networks*, Vol. 1, pp. 4-27.

67. Papadimitriou, C., Katafygiotis, L. S., and Yuen, K. –V., 1999, "Optimal Instrumentation Strategies for Structural Health Monitoring Applications", *Proceedings of the 2nd International Workshop on Structural Health Monitoring*, September 18-20, pp. 543-552.

68. Park, G., Cudney, H. H., and Inman, D. G., 1999, "Impedance-Based Health Monitoring Technique for Civil Structures", *Proceedings of the 2nd International Workshop on Structural Health Monitoring*, September 18-20, pp. 523-532.

69. Park, K. C., and Reich, G. W., 1999, "Model-based Health Monitoring of Structural Systems: Progress, Potential, and Challenges", *Proceedings of the 2nd International Workshop on Structural Health Monitoring*, September 18-20, pp. 82-95.

70. Park, K. C., Reich, G. W., and Alvin, K. F., 1997, "Structural Damage Detection Using Localized Flexibilities", *Proceedings of the 2ⁿᵈ International Workshop on Structural Health Monitoring, Current Status and Perspectives*, September 18-20, pp. 125-139.

71. Reich, G. W., and Park, K. C., 1999, "On the Use of Substructural Transmission Zeros for Structural Health Monitoring", Center for Aerospace Structures, Report No. CU-CAS-99-10, University of Colorado, Boulder, CO.; submitted to AIAA Journal.

72. Reich, G. W., and Park, K. C., 2000, "Experimental Application of a Structural Health-monitoring Methodology", *SPIE's 7ᵗʰ International Symposium on Smart Structures and Materials*, March, p. 148.

73. Rossikhin, Y. A., and Shitikova, M. V., 2000, "Influence of Fractional Derivatives upon the Stability of Nonlinear Damped Vibrations of Suspension Bridges", *SPIE's 7ᵗʰ International Symposium on Smart Structures and Materials*, March, p. 171.

74. Shinozuka, M., and Rejaie, A., 2000, "Correlational Analysis of Remotely Sensed Pre- and Post- Disaster Images for Damage Detection", *SPIE's 7ᵗʰ International Symposium on Smart Structures and Materials*, March, p. 153.

75. Shuang, J., and Livingston, R. A., 2001, "Nonlinear Finite Element Modeling of the Woodrow Wilson Bridge for Structural Health Monitoring", *Proceedings of the 3ʳᵈ International Workshop on Structural Health Monitoring: The Demands and Challenges*, September 12-14, pp. 918-927.

76. Sikorsky, C., 1997, "Integrating Modal Based NDE Techniques and Bridge Management Systems Using Quality Management", *Smart Systems for Bridges, Structures and Highways*, San Diego, March 5-6, pp. 31-42.

77. Sikorsky, C., 1999, "Development of a Health Monitoring System for Civil Structures Using a Level IV Non-destructive Damage Evaluation Method", *Proceedings of the 2ⁿᵈ International Workshop on Structural Health Monitoring*, September 18-20, pp. 68-81.

78. Sikorsky, C., Stubbs, N., Bolton, R. W., Seible, F., 2001, "Performance Evaluation of a Composite Bridge using Structural Health Monitoring", *Proceedings of the 3ʳᵈ International Workshop on Structural Health Monitoring: The Demands and Challenges*, September 12-14, pp. 420-429.

79. Simula, O., Alhoniemi, E., Hollmen, J., and Vesanto, J., 1996, "Monitoring and Modeling of Complex Processes Using Hierarchical Self-Organizing Maps", ISCAS.

80. Soong, T. T., 1986-1994, "Seismic Applications of Viscoelastic Dampers", Research Accomplishments, The National Center for Earthquake Engineering Research, pp. 81-87.

81. Stubbs, N., and Kim, J. T., 1996, "Damage Localization in Structures without Baseline Modal Parameters", AIAA Journal Vol. 34, No. 9, September, pp. 1-6.

82. Stubbs, N., and Kim, J. T., 1996, "Damage Localization in Structures without Baseline Modal Parameters", *AIAA Journal*, 34(8), pp. 1644-1649.

83. Stubbs, N., Kim, J. T., and Topole, K., 1992, "An Efficeint and Robust Algorithm for Damage Localization in Offshore Platforms", *ASCE 10th Structures Congress '92*, San Antonio, Texas, pp. 543-546.

84. Stubbs, N., Kim, J. T., and Topole, K., 1992, "An Efficient and Robust Algorithm for Dmage Localization in Offshore Platforms", *ASCE 10th Structures Congress*, San Antonio, Texas, pp. 543-546.

85. Stubbs, N., Sikorsky, C., Park, S., Choi, S., and Bolton, R., 1999, "Verification of a Methodology to Nondestructively Evaluate the Structural Properties of Bridges", *Proceedings of the 2nd International Workshop on Structural Health Monitoring*, September 18-20, pp. 440-449.

86. Szewczyk, P. Z., and Hajela, P., 1994, "Damage Detection in Structures Based on Feature Sensitive Neural Networks", *ASCE Jouranl of Computing in Civil Engineering*, 8(2), pp. 163-178.

87. Taylor D., and Constantinou, M. C., 1994, "Testing Procedures for High Output Fluid Viscous Dampers Used in Building and Bridge Superstructures to Dissipate Seismic Energy", *Shock and Vibration*, Vol. 2, Issue 5, pp. 373-381.

88. Taylor, D. P., and Constantinou, M. C., 1994, "Fluid Dampers for Applications of Seismic Energy Dissipation and Seismic Isolation."

89. Tsopelas, P., and Constantinou, M. C., 1994, "Experimental and Analytical Study of a System Consisting of Sliding Bearings and Fluid Restoring Force/Damping Devices", Published as Report NCEER-94-0014 by the National Center for Earthquake Engineering Research, State University of New York at Buffalo.

298

90. Vanik, M. W., and Beck, J. L., 1997, "A Bayesian Probabilistic Approach to Structural Health Monitoring", *Proceedings of the 2nd International Workshop on Structural Health Monitoring, Current Status and Perspectives*, September 18-20, pp. 140-151.

91. Vecchio, A., and Auweraer, V. D., 2001, "An Experimental Validation of a Model-Based Approach in Damage Detection and Localization", *Proceedings of the 3rd International Workshop on Structural Health Monitoring: The Demands and Challenges*, September 12-14, pp. 957-966.

92. Wolfe, R. W., 1999, "USC Department of Civil Engineering Research Database User's Manual", unpublished reference manual.

93. Wolfe, R. W., 2000, "Three-dimensional Nonlinear Finite Element User's Manual", unpublished reference manual.

94. Wolfe, R. W., and Farran, H. J., 1996, "A Computer Analysis of the Vincent Thomas Suspension Bridge", *The Journal of Interdisciplinary Studies*, California State Polytechnic University Pomona, Vol. 9, pp. 81-86.

95. Wolfe, R. W., and Wahbeh, A. M., 2000, "Non-destructive Testing Challenges for the California Toll Bridge Seismic Retrofit Program", *Structural Materials Technology IV – An NDT Conference*, February 28 – March 3, pp. 165-170.

96. Wu, X., Ghaboussi, J., and Garrett, J. H., 1992, "Use of Neural Networks in Detection of Structural Damage", *Computers & Structures*, 42(4), pp. 649-659.

97. Yalla, S. K., Kareem, A., and Kantor, J. C., 2000, "Semi-active Variable Damping Liquid Column Dampers", *SPIE's 7th International Symposium on Smart Structures and Materials*, March, p. 145.

98. Yang, S. M., and Lee, G. S., 1997, "Structural Control by Integrating Neural Network and Experimental Design", *Proceedings of the 2nd International Workshop on Structural Health Monitoring, Current Status and Perspectives*, September 18-20, pp. 255-266.

99. Yao, J. T. P., and Wong, F. S., 1999, "Symptom Based Reliability and Structural Health Monitoring", *Proceedings of the 2nd International Workshop on Structural Health Monitoring*, September 18-20, pp. 743-753.

Appendices

Appendix 1

USC Department of Civil Engineering Research Database Users Manual

(Section 5.2.2)

301

USC

Department of Civil Engineering

Research Database

Users Manual

Raymond W. Wolfe

14 January, 1999

Preface

The purpose of this document is to define both the basic design parameters related to the USC Department of Civil Engineering Research database, as well as the user interface. The database is a tool intended to facilitate large-scale data storage resulting from the variety of research projects undertaken at the University. Data stored in a two-dimensional ASCII array is processed and stored efficiently in the database for future reference. The database is a compilation of the efforts of various graduate students through the years, dating back to the days of the VAX system. As such, when compiling the source code, it is imperative that the *–IV77* identifier is included in the compile command.

The benefits associated with the utilization of the database for the storage of research data are the ability to quickly and easily retrieve user defined segments of the data for analysis. In addition, a variety of data analysis tools are available to facilitate this endeavor, including integration codes and plotting routines. The data can also be retrieved and exported to external data analysis packages.

n-dimensional data arrays must be stored in ASCII format, but may be comma, space, or tab delimited. A parsing routine is included to preprocess the data for storage as one-dimensional vectors.

303

As you delve into the nuances of the following specifications, you will discover that the database is a powerful, but user-friendly tool, which will enable you to quickly maneuver data to serve the purposes of your research. Examples of data input, including a copy of the text input file and a brief description are included in Appendix A. Appendix B contains a sample ASCII two-dimensional data array. An explanation of the data storage scheme is detailed in Appendix C, and data retrieval examples are included in Appendix D.

304

Installation

The database must be installed on a UNIX platform. Once the source code is copied to the desired directory, it must be compiled. After the source code is compiled, you are ready to use the package. The executable file can be used for any size ASCII two-dimensional array by simply specifying the input parameters in a text file called *input* (reference Appendix A).

To install the database, follow these steps:

1. Copy the database subroutines to the desired directory on a UNIX server. The necessary subroutines and text files to compile successfully are as follows;

   - parse.f

   - MESG1.f

   - OPEN1.f

   - OPEN2.f

   - OPEN3.f

   - CHL14.f

   - CLOSE1.f

   - CPU.f

   - FLINF4.f

   - FLWRT5.f

   - FLRED5.f

305

- FILE01.TXT

- CB270A.TXT

- CB320.TXT

2. Compile the code by typing the following command at the UNIX

   command prompt:

   f77 - o datawrite.exe *.f -lV77

   Note the spaces between *f77*, *–o*, *datawrite.exe*, **.f*, and *-lV77*. This

   command line compiles all the *.f* files contained within the directory, then

   links them, creating the executable file *datawrite.exe*. The database code

   is now ready for usage.

General Usage

In general, the database can accommodate an *n*-dimensional array of data for

processing and storage. The data array must simply be saved in ASCII format to

facilitate the procedure. The name of the ASCII data array, the number of data

columns contained in the array, the database number to write to, the names of the

column vectors, and a 40-character maximum comment line are input in a text file

called *input* (reference Appendix A). There is a limitation of 20 data columns hard-

coded in the *main.f* source code. If this requires modification, the code will have to

be recompiled as described above prior to additional usage.

306

A compiled version of the database is easily utilized. The following is a general introductory procedure for new users.

1. Access the UNIX directory in which the database resides.

2. Copy the ASCII formatted *n*-dimensional array into the same directory.

3. Open the file, *input,* and change the parameters to correctly define the data array to be processed (reference Appendix A).

4. Type the name of the compiled source code at the UNIX command prompt. (This is *datawrite.exe* if the compile command line given above was followed).

The program then opens the *input* file and reads the input parameters. Next, it then opens the ASCII data file and parses the two-dimensional ASCII data into one-dimensional vector arrays derived from each column. The program proceeds to process the data into the database. Specifically, the command, **CALL FLWRT5( )**, begins this process.

The data is stored in the database as shown in Appendix C. Note that the data is referenced to vector names, date and time of entry, and vector length.

Data Extraction

Data is extracted from the database utilizing a routine called *extract*. This code simply requests that the user input the name of the vector and database number to

307

locate the data of interest (reference Appendix C). The code does require that this input follow the alphanumeric format specified for the argument *c14nam* as detailed in the "Important Notes" section of this manual. The user is then prompted for the name of the file to which the data is to be written. Next, the code extracts the vector data from the specified database. It is important to note that if several vectors with the same name are specified in the database, the *extract* routine will only extract from the most recent vector.

Important Notes

While the various subroutines utilized by this code are written in FORTRAN, and thus require strict adherence to rules related to text field size, spaces, and other characters, this has been accounted for in the specification of the variables defined in the file *input*. Thus, adherence to these rules is transparent to the user, unless parameters exceed the defined length, in which case the variables are truncated to proper length.

If the various subroutines are to be used separate from the executable, the user must carefully follow the variable length restrictions. Examples of importance are the CALL statements for the subroutines, *flwrt.f* and *flred5.f*. These subroutines require several variables in the argument, and these must follow strict rules as outlined herein.

308

SUBROUTINE FLWRT5(c14nam,length,V,c40cmt)

Specifically, for the subroutine, *flwrt.f*, the argument list is first a fourteen (14) character argument wherein the first six (6) characters define the data type; ie., TIME, DISPL, ACCEL, etc. The next character in this argument is a period, followed by a three (3) character file extension. A semi-colon follows as the eleventh (11th) character. Finally, the last three (3) characters of the fourteen (14) character argument are numeric, defining the database number wherein the data is to be written.

where:

C14nam: is a 14 character name as mentioned above, e.g. XDD1--.3NL;--1

> **NB:** the '-' characters should not actually be typed, they simply represent spaces!!

Length: is the length of the vector (integer) returned.

V: is the alpha vector name identifier.

C40cmt: is a 40-character text description input by the user.

SUBROUTINE FLRED5(c14nam,N1,N2,N3,NPICK,V)

where:

C14nam: is a 14 character name as mentioned above, e.g. XDD1--.3NL;--1

NB: the '–' characters should not actually be typed, they simply

represent spaces!!

N1: is the starting point (integer) to be extracted

N2: is the ending point (integer) to be extracted

N3: is the increment (integer) used to get from *N1* to *N2*.

NPICK: is returned (integer), and is the total number of points extracted

based on *N1*, *N2*, and *N3*

V: is the double precision vector, which is returned. This contains the `NPICK`

numerical data points extracted from the database.

The *flred5.f* subroutine can be included in any main program to extract data from the

FDR/RUF formatted databases.

Conclusion

The present code offers much flexibility, allowing the user to present the ASCII data

array file as a space, tab, or comma-delimited file. Additionally, the user can input a

forty (40) character descriptive text line to facilitate data definition for future

reference. The data array can be *n*-dimensional, given that *n* is specified as a

parameter in the input text file, *input*.

310

Appendix A – USC Database

The following is an example of an input file. Note that the executable code requires the input file to be named *input*. The parameters are entered on each line as follows;

1. The first line of the input file specifies the name of the file containing the two-dimensional ASCII data array to be processed into the database.

2. The second line specifies the database number to which the data is written. This can be any number from 1 to 999.

3. The third line denotes the number of columns contained in the two-dimensional ASCII data array to be processed into the database. (Note that this number must not exceed 20, unless the main program code is revised).

4. The next *n*-lines of input define the column vector names, which will be used to store the data in the database. Note that there must be as many lines of column headings as there are columns in the two-dimensional ASCII data array to be processed into the database. This is the number *n* specified in the third line. Thus, if *n* = 3 as shown in the example file below in the third line, column headings must be included in lines four through six. It is also important to note that the column headings defined below will be truncated at six characters. Hence, the column names denoted in the fifth and sixth lines of the example input file below will be stored in the database as x1disp and x1acce.

311

5. The last line in the input file is used to specify a 40-character comment to describe the data for future reference. Again, the comment line will be truncated at 40-characters.

```
test1.dat
1
3
time
x1accel
x1displ
revised code - datawrite.exe
```

FIGURE 1. Example input file

This appendix contains an example of a two-dimensional ASCII data array. Note that the data can be obtained from virtually any platform as long as it is saved in the ASCII format. Applications such as LabVIEW® and other data retrieval packages, PC applications such as Microsoft EXCEL®, as well as UNIX based applications allow the user to store the data array in ASCII format. Note that the data can be saved as either tab, space or comma delimited. In the example shown below, the data is comma delimited, and contains only three columns of data with two rows. This data file can be processed into the database using the input file delineated in Appendix A.

```
153.840,-245.000,-1.088
4156.80,2.000,0.093
```

FIGURE 2. Example data set for processing

313

This appendix contains an explanation and an example of the data storage in the
database. The user must understand the nuances of this appendix to fully appreciate
and utilize the database. A description of each column entry is included below.

```
2 1 1 time   .dat;  1   0  2  2  12- 2-99 10:28:40 first test of sdof
2 1 2 xlacce.dat;  1   2  2  4  12- 2-99 10:28:40 first test of sdof
2 1 3 xldisp.dat;  1   4  2  6  12- 2-99 10:28:40 first test of sdof
2 1 4 time   .dat;  1   6  2  8  12- 2-99 10:37:16 second test of sdof
2 1 5 xlacce.dat;  1   8  2 10  12- 2-99 10:37:17 second test of sdof
2 1 6 xldisp.dat;  1  10  2 12  12- 2-99 10:37:17 second test of sdof
2 1 7 time   .dat;  1  12  2 14  12- 2-99 10:44:55 third test of sdof
2 1 8 xlacce.dat;  1  14  2 16  12- 2-99 10:44:55 third test of sdof
2 1 9 xldisp.dat;  1  16  2 18  12- 2-99 10:44:55 third test of sdof
```

FIGURE 3. Screen capture of database ASCII file, Dxxx.FDR

1. The first column defines the data type, either single or double precision.
   A '2' denotes that the data is stored as double precision.

2. The second column defines the ?

3. The third column is a global counter. Note that it is incremented by one
   for each entry.

4. The fourth column contains the input argument *c14nam* as defined in the
   "Important Notes" section of the User's Manual. Note that the six-
   character column headers are included herein. The last three digits of this
   column denote the database number that the vector was written to.

314

5. The fifth column is a global counter defining the starting point of the data for each vector. Note that the first vector starts at zero.

6. The sixth vector describes the length of the vector as input. Note that the example ASCII data array depicted in Appendix B has only two rows, so that each of the three column vectors derived from said example would have a length of two.

7. The seventh column is also a global counter, used to define the ending point of the vector in the database. This number is simply the sum of the starting point and the vector length from the fifth and sixth columns.

8. The next column denotes the date that the data was written to the database, starting with the day, followed by the month, and then the year.

9. The ninth column denotes the time the data was written to the database in hours, minutes, and seconds. This is the data that is corrupted if the executable code was not compiled with the –IV77 statement, as described in the "Installation" section of this manual. This is because the time stamp call was originally written on the VAX system.

10. The final column contains the 40-character comment description, which was included in the last line of the input file (reference Appendix A).

315

Appendix D – USC Database

This appendix details several examples of the data retrieved from the database, given

the input described in the preceding appendices. First, a screen capture of the extract

routine is depicted, then the various outputs are shown. Note that data is the same as

that contained in the ASCII data array shown in Appendix B.

```
ENTER DATA FILE NAME (A14)
XXXXXX.DDD;NNN format
time .dat; 1
 Enter the name of the output file
Out1
samar.usc.edu(199): extract

ENTER DATA FILE NAME (A14)
XXXXXX.DDD;NNN format
x1disp.dat; 1
 Enter the name of the output file
out2
samar.usc.edu(200): extract

ENTER DATA FILE NAME (A14)
XXXXXX.DDD;NNN format
x1acce.dat; 1
 Enter the name of the output file
out3
samar.usc.edu(201):
```

FIGURE 4. Screen capture of *extract* routine

316

The data shown below is from the output file out1.dat, which is the data stored in the vector 'time .dat; 1'.

0.1538400E+03

0.4156800E+04

The data shown below is from the output file out2.dat, which is the data stored in the vector 'x1disp.dat; 1'.

-0.1088000E+01

0.9300000E-01

The data shown below is from the output file out2.dat, which is the data stored in the vector 'x1disp.dat; 1'.

-0.2450000E+03

0.2000000E+01

317

Appendix 2

Chebyshev polynomial coefficients for a linear system, revised algorithm

(Section 6.5.1.3)

318

Chebyshev 2-D polynomial coefficients, linear oscillator
(revised algorithm)

i/j	$T_0(\dot{x}')$	$T_1(\dot{x}')$	$T_2(\dot{x}')$	$T_3(\dot{x}')$	$T_4(\dot{x}')$	$T_5(\dot{x}')$	$T_6(\dot{x}')$	$T_7(\dot{x}')$	$T_8(\dot{x}')$	$T_9(\dot{x}')$
$T_0(x')$	-0.0648	0.99235	-0.1361	0.19174	0.03767	0.11236	-0.06522	0.02856	-0.07128	-0.02124
$T_1(x')$	7.59138	0.09213	-0.42173	0.18558	0.03059	0.12429	-0.12561	0.03764	-0.1586	-0.07189
$T_2(x')$	0.05413	0.09139	-0.03234	0.13463	0.11015	0.11061	-0.08191	0.00619	-0.08819	-0.04797
$T_3(x')$	-0.01106	-0.04959	-0.31367	0.07948	-0.02063	0.05709	-0.07046	0.02184	-0.0897	-0.0384
$T_4(x')$	0.13621	0.06315	0.16142	0.05296	0.09673	0.05513	-0.01914	-0.01052	-0.01642	-0.01575
$T_5(x')$	0.05545	-0.03039	-0.12898	0.02596	-0.01571	0.01235	-0.02142	0.01139	-0.03339	-0.01314
$T_6(x')$	0.01618	0.02176	0.01796	0.01383	0.01495	0.01707	-0.00795	-0.00289	-0.00606	-0.00318
$T_7(x')$	0.03844	-0.00425	-0.04215	0.01388	-0.00011	0.00747	-0.00948	0.0048	-0.01408	-0.0068
$T_8(x')$	0.02366	0.01118	0.03151	0.00972	0.01814	0.01291	-0.00517	-0.00116	-0.00424	-0.00313
$T_9(x')$	0.01076	-0.00891	-0.04829	0.00842	-0.0039	0.0026	-0.00897	0.00505	-0.01099	-0.00535
$T_{10}(x')$	0.01088	0.01032	0.01645	0.00619	0.01037	0.01007	-0.00401	-0.00335	-0.00082	-0.00243
$T_{11}(x')$	0.01564	-0.0047	-0.0187	0.00755	0.00249	0.00212	-0.00458	0.00367	-0.00628	-0.00385
$T_{12}(x')$	0.00836	0.00317	0.0068	0.00685	0.00603	0.00169	-0.00254	0.00147	-0.00301	-0.00296
$T_{13}(x')$	0.00397	-0.0023	-0.01574	0.00343	-0.00555	0.00287	-0.00374	0.00019	-0.00294	-0.00174
$T_{14}(x')$	0.01042	0.00407	0.00796	0.00629	0.00889	0.00134	-0.00111	0.00186	-0.00213	-0.00145
$T_{15}(x')$	0.00805	-0.0025	-0.01235	0.00146	-0.00156	0.00292	-0.002	0.00046	-0.00355	-0.00159
$T_{16}(x')$	0.00438	0.00434	0.00158	0.00121	0.00297	0.00314	-0.00197	0.00014	-0.00083	-0.00181
$T_{17}(x')$	0.00539	-0.00165	-0.01438	0.00363	0.00314	0.001	-0.00307	0.00241	-0.00321	-0.00258
$T_{18}(x')$	0.00529	0.00159	0.00799	0.00217	0.00492	0.0038	-0.00149	-0.00102	-0.00112	-0.0024
$T_{19}(x')$	0.00482	-0.00215	-0.00738	0.00211	-0.00094	-0.00057	-0.00355	0.00174	-0.00106	-0.00181

319

Chebyshev 2-D polynomial coefficients, linear oscillator (revised algorithm)

i/j	$T_{10}(\dot{x}')$	$T_{11}(\dot{x}')$	$T_{12}(\dot{x}')$	$T_{13}(\dot{x}')$	$T_{14}(\dot{x}')$	$T_{15}(\dot{x}')$	$T_{16}(\dot{x}')$	$T_{17}(\dot{x}')$	$T_{18}(\dot{x}')$	$T_{19}(\dot{x}')$
$T_0(x')$	-0.05403	0.00393	0.02199	0.06345	0.02124	0.03981	0.02549	-0.00949	-0.00883	-0.03436
$T_1(x')$	-0.07707	-0.00215	0.00491	0.1177	0.04518	0.03098	0.04864	0.00689	-0.02471	-0.0817
$T_2(x')$	-0.08172	-0.00506	0.04612	0.07845	0.03315	0.06142	0.03635	-0.02286	-0.00608	-0.05301
$T_3(x')$	-0.0343	0.00259	-0.01077	0.0628	0.02678	0.00027	0.02084	0.01375	-0.0187	-0.04753
$T_4(x')$	-0.03668	0.00013	0.03689	0.02363	0.01342	0.03536	0.01196	-0.01642	0.0051	-0.01706
$T_5(x')$	-0.0047	0.00125	-0.01194	0.02027	0.00967	-0.00858	0.00615	0.01387	-0.00695	-0.01804
$T_6(x')$	-0.01551	-0.00067	0.01184	0.00711	0.00282	0.01298	0.00319	-0.00662	0.00208	-0.00645
$T_7(x')$	-0.00291	-0.00057	-0.00422	0.01117	0.00574	-0.00079	0.00428	0.00362	-0.00334	-0.009
$T_8(x')$	-0.00787	-0.00132	0.00626	0.0046	0.00278	0.00884	0.00447	-0.00355	0.00085	-0.00252
$T_9(x')$	-0.00155	0.00048	-0.0042	0.00919	0.00544	-0.00406	0.00032	0.00335	-0.00412	-0.00569
$T_{10}(x')$	-0.00751	0.00095	0.00654	0.00313	0.00065	0.00684	0.00182	-0.00644	0.0006	-0.00005
$T_{11}(x')$	-0.00142	0.00017	-0.00117	0.00376	0.00135	-0.00179	0.00134	0.00396	-0.00039	-0.00346
$T_{12}(x')$	-0.00285	0.00114	0.00326	0.00309	0.00151	0.00086	-0.00033	-0.00006	0.0014	-0.00178
$T_{13}(x')$	-0.0035	0.00159	0.00057	0.00091	0.00029	0.00288	0.00143	-0.00104	0.00082	-0.00288
$T_{14}(x')$	-0.00129	-0.00043	-0.00029	-0.00001	0.0028	0.00334	0.00037	0.00199	0.00131	-0.00398
$T_{15}(x')$	-0.00093	0.00125	-0.00056	0.00092	0.00157	0.00131	-0.00056	-0.00188	-0.00009	-0.00004
$T_{16}(x')$	-0.00183	0.00086	0.0009	0.00129	0.00179	0.0029	0.00021	-0.00325	-0.00116	-0.00072
$T_{17}(x')$	-0.00054	0.00001	-0.00171	0.00198	0.00164	-0.00077	0.00068	0.00224	-0.00087	-0.00193
$T_{18}(x')$	-0.00229	0.00139	0.00319	0.00159	-0.00009	0.00153	0.00026	-0.00227	0.00121	0.00061
$T_{19}(x')$	-0.00057	0.00092	-0.00067	0.00203	0.00138	-0.001	0.00004	0.00096	-0.00001	-0.0019

320

Appendix 3

Chebyshev polynomial coefficients for a nonlinear system (Duffing oscillator), revised algorithm (Section 6.5.2.1.2)

321

Chebyshev 2-D polynomial coefficients, Duffing oscillator

i/j	$T_0(\dot{x}')$	$T_1(\dot{x}')$	$T_2(\dot{x}')$	$T_3(\dot{x}')$	$T_4(\dot{x}')$	$T_5(\dot{x}')$	$T_6(\dot{x}')$	$T_7(\dot{x}')$	$T_8(\dot{x}')$	$T_9(\dot{x}')$
$T_0(x')$	-0.21928	3.6181	-0.30222	0.33644	-0.12859	0.20588	-0.07025	0.10902	-0.00791	0.07247
$T_1(x')$	194.7364	-0.94413	-2.20378	-0.13017	-0.44777	-0.08981	-0.24377	-0.07707	-0.06102	-0.03021
$T_2(x')$	-0.35024	0.5906	-0.52343	0.29845	-0.24821	0.14631	-0.14428	0.03909	-0.02398	0.03056
$T_3(x')$	50.22016	-0.87634	-1.61958	-0.10535	-0.19773	-0.05957	-0.12486	-0.05979	-0.00282	-0.03448
$T_4(x')$	-0.16425	0.29374	-0.29967	0.07361	-0.16905	0.04215	-0.09968	0.01155	0.00113	0.03413
$T_5(x')$	-1.21821	-0.78721	-1.13891	-0.0915	-0.18581	-0.01599	-0.12845	0.0025	0.01339	0.00982
$T_6(x')$	-0.01433	0.40554	-0.07122	0.16744	-0.06568	0.10765	-0.0137	0.0596	0.05102	0.03943
$T_7(x')$	-0.79415	-0.66432	-0.71542	-0.08401	-0.1277	0.01193	-0.05204	0.03377	0.08131	0.01259
$T_8(x')$	0.02493	0.39563	-0.00837	0.09286	-0.0481	0.00817	-0.00044	-0.01916	0.04179	-0.01045
$T_9(x')$	-0.39557	-0.47417	-0.242	-0.04412	0.00515	0.04561	-0.00201	0.04341	0.06266	0.0136
$T_{10}(x')$	0.03482	0.30541	0.01103	-0.0014	-0.02216	-0.05423	-0.00363	-0.04419	0.02636	0.00299
$T_{11}(x')$	-0.16604	-0.28101	-0.02728	-0.01141	0.00115	0.03038	-0.04126	0.0226	0.00892	0.01154
$T_{12}(x')$	0.03772	0.19516	0.04285	-0.03926	0.01847	-0.06217	0.00093	-0.03554	0.01429	-0.00625
$T_{13}(x')$	-0.0868	-0.04652	-0.00559	0.04849	-0.03992	0.02457	-0.06069	-0.00564	-0.01492	0.02215
$T_{14}(x')$	0.00382	0.09624	0.01126	-0.05954	0.01143	-0.05487	-0.02515	-0.04933	0.00622	-0.02161
$T_{15}(x')$	-0.01583	0.07123	0.06597	0.06192	0.01529	0.00613	-0.0164	-0.05197	-0.01648	0.00987
$T_{16}(x')$	-0.01019	0.0695	0.00131	-0.0213	-0.00584	-0.00192	-0.03027	-0.03566	0.02049	-0.01457
$T_{17}(x')$	0.01908	0.06118	0.07151	0.04475	0.01822	0.00401	-0.00406	-0.04491	-0.01194	0.01869
$T_{18}(x')$	0.00057	0.04765	0.01994	0.01122	-0.00341	0.03668	-0.00319	0.00536	0.0339	0.00587
$T_{19}(x')$	0.01047	0.00433	0.01332	-0.00959	-0.02489	0.00479	-0.00433	-0.02162	0.00485	0.02485

322

Chebyshev 2-D polynomial coefficients, Duffing oscillator

i/j	$T_{10}(\dot{x}')$	$T_{11}(\dot{x}')$	$T_{12}(\dot{x}')$	$T_{13}(\dot{x}')$	$T_{14}(\dot{x}')$	$T_{15}(\dot{x}')$	$T_{16}(\dot{x}')$	$T_{17}(\dot{x}')$	$T_{18}(\dot{x}')$	$T_{19}(\dot{x}')$
$T_0(x')$	0.00943	0.02085	0.00298	0.03068	-0.00427	0.01443	-0.00161	0.01999	0.00914	0.02152
$T_1(x')$	-0.10201	-0.01567	-0.02265	0.02584	-0.04524	0.02871	-0.01143	0.03215	0.00509	0.01566
$T_2(x')$	0.01487	-0.02536	0.02078	0.00064	0.00995	-0.00204	0.01001	0.01415	0.02195	0.01621
$T_3(x')$	-0.08951	-0.02302	0.01663	0.00228	-0.00804	-0.00767	-0.02465	-0.00455	-0.00041	0.00652
$T_4(x')$	0.0251	-0.00839	0.01776	0.01081	0.00995	0.01228	-0.00775	0.02029	0.0137	0.01616
$T_5(x')$	-0.08934	0.0053	0.01704	0.0242	0.00221	0.00467	-0.01563	0.00202	-0.01379	0.00959
$T_6(x')$	0.03362	-0.02297	0.00619	-0.00309	-0.00645	-0.01786	-0.02136	-0.01104	0.0093	-0.02083
$T_7(x')$	-0.0406	-0.00994	0.04122	-0.00653	0.02078	-0.00461	-0.00106	-0.01782	-0.00287	-0.01244
$T_8(x')$	-0.00691	-0.02318	-0.00337	0.00447	0.00081	0.01009	-0.00621	0.01233	0.02309	-0.00063
$T_9(x')$	-0.06042	-0.01205	0.04801	-0.01144	0.00785	0.00269	-0.01183	-0.02084	0.00178	-0.00592
$T_{10}(x')$	-0.0255	0.0196	-0.00058	0.03188	0.00281	0.02525	0.0076	0.00516	0.02303	-0.01457
$T_{11}(x')$	-0.0302	-0.00451	0.07924	-0.00436	0.01527	0.01208	0.00707	-0.01709	0.01686	-0.0035
$T_{12}(x')$	-0.02807	0.0208	0.01156	0.027	-0.0156	-0.00147	0.01169	-0.01738	0.01601	-0.02084
$T_{13}(x')$	0.0004	0.01301	0.069	-0.01581	-0.02051	0.02094	0.00501	0.00218	0.0142	0.00562
$T_{14}(x')$	-0.03693	0.02973	0.01775	0.04066	-0.02284	0.0164	0.00988	0.01538	0.03325	0.0174
$T_{15}(x')$	-0.01937	0.0271	0.0245	-0.02978	-0.04592	0.0107	-0.00207	-0.00017	0.02194	0.01136
$T_{16}(x')$	-0.01668	0.04286	0.0304	0.03803	-0.02164	0.01299	0.02528	0.0061	0.0328	0.0011
$T_{17}(x')$	-0.02222	0.04471	0.00749	-0.01435	-0.02041	0.0017	0.01895	-0.0055	0.01529	0.01057
$T_{18}(x')$	0.00101	0.03808	0.02958	0.01751	-0.01918	-0.00615	0.00542	-0.00407	0.00494	-0.00362
$T_{19}(x')$	-0.00511	0.03696	-0.00578	-0.00654	-0.01409	0.01393	0.00882	0.00597	-0.0137	0.00418

323

Appendix 4

Chebyshev polynomial coefficients for a nonlinear system (Van der Pol oscillator), revised algorithm (Section 6.5.2.1.2)

324

Chebyshev 2-D polynomial coefficients, van der Pol oscillator

i\j	$T_0(\dot{x}')$	$T_1(\dot{x}')$	$T_2(\dot{x}')$	$T_3(\dot{x}')$	$T_4(\dot{x}')$	$T_5(\dot{x}')$	$T_6(\dot{x}')$	$T_7(\dot{x}')$	$T_8(\dot{x}')$	$T_9(\dot{x}')$
$T_0(x')$	-0.85622	42.83352	-1.24824	3.46646	-0.03566	1.20432	0.25999	0.38916	0.05118	0.22267
$T_1(x')$	0.17948	-5.0236	-7.6942	-2.05043	-1.37127	-0.40634	-0.09087	-0.48737	-0.22856	-0.21386
$T_2(x')$	-1.5693	41.55185	-2.27464	2.60972	-0.16503	1.07741	0.38124	0.15781	-0.01214	0.06641
$T_3(x')$	-0.23111	-4.28864	-0.54537	-1.28571	0.14124	-0.01812	0.25098	-0.19321	-0.00678	-0.0634
$T_4(x')$	-0.55295	-6.78466	-1.13819	-1.5671	-0.21887	-0.09938	0.14104	-0.27361	-0.18172	-0.1453
$T_5(x')$	2.0447	-2.76604	1.68873	-0.51991	0.15161	0.31256	0.28202	0.01128	-0.04588	0.00641
$T_6(x')$	0.65239	-4.80444	0.14923	-0.37915	-0.17888	0.39421	0.06064	0.03687	-0.15019	0.0452
$T_7(x')$	1.84421	-1.47529	1.26839	-0.01492	-0.10007	0.29141	0.21555	-0.01435	-0.06954	-0.0072
$T_8(x')$	0.87575	-2.69707	0.35811	0.33703	-0.22108	0.55502	0.02712	0.12128	-0.13359	0.08934
$T_9(x')$	1.257	-0.46361	0.8095	0.18836	-0.07067	0.13445	0.11268	-0.04577	-0.00823	0.02896
$T_{10}(x')$	0.36495	-1.61959	-0.07283	0.39438	-0.17951	0.29841	0.05282	0.0057	-0.05277	0.07082
$T_{11}(x')$	0.05348	-0.06938	-0.34714	0.02493	-0.08434	-0.06245	0.0786	-0.1106	0.02032	-0.02409
$T_{12}(x')$	-0.10334	-1.41098	-0.30091	0.18719	-0.0376	0.06909	0.0411	-0.04315	-0.02312	0.04676
$T_{13}(x')$	-0.1822	0.05731	-0.17834	-0.06871	0.27243	-0.09862	0.09621	-0.06057	0.01466	-0.00697
$T_{14}(x')$	-0.1632	-1.36676	-0.16887	0.0699	0.04753	-0.05078	-0.01234	-0.04482	-0.03941	-0.00935
$T_{15}(x')$	-0.37684	0.06394	-0.30266	-0.05224	0.24713	-0.06326	0.01939	-0.02485	0.04186	-0.01251
$T_{16}(x')$	-0.00949	-0.71081	0.04874	0.10793	0.02534	-0.14358	-0.03476	-0.0059	-0.02857	-0.02215
$T_{17}(x')$	-0.33046	0.08629	-0.29155	0.01205	0.09608	-0.03167	-0.00694	0.02388	0.05887	-0.01002
$T_{18}(x')$	0.01201	-0.34413	0.04164	0.18025	-0.07633	-0.11788	-0.08891	0.04195	-0.01344	-0.01514
$T_{19}(x')$	0.02908	-0.02214	-0.06682	-0.01811	-0.00414	-0.03406	0.03305	-0.00328	0.0813	-0.03307

325

Chebyshev 2-D polynomial coefficients, van der Pol oscillator

i/j	$T_{10}(\dot{x}')$	$T_{11}(\dot{x}')$	$T_{12}(\dot{x}')$	$T_{13}(\dot{x}')$	$T_{14}(\dot{x}')$	$T_{15}(\dot{x}')$	$T_{16}(\dot{x}')$	$T_{17}(\dot{x}')$	$T_{18}(\dot{x}')$	$T_{19}(\dot{x}')$
$T_0(x')$	0.04293	0.15307	0.0458	0.12537	0.06547	0.05703	0.00193	0.04098	0.01197	-0.00261
$T_1(x')$	0.00664	-0.11407	-0.02043	-0.08326	0.0167	-0.12885	-0.00301	0.00885	0.03801	-0.06155
$T_2(x')$	0.03819	0.07601	0.03941	0.12607	0.06924	0.0261	-0.03626	0.00565	0.01008	-0.04253
$T_3(x')$	0.11184	-0.03983	0.03107	0.00931	0.02978	-0.01593	-0.02366	0.04134	0.02527	-0.04014
$T_4(x')$	-0.02896	-0.09768	-0.01367	0.05072	0.0204	-0.01161	-0.07467	-0.0026	-0.00372	-0.06371
$T_5(x')$	0.11881	-0.01272	0.08733	0.07299	0.04951	0.02553	-0.05784	0.03802	0.00611	-0.00078
$T_6(x')$	0.0459	-0.02813	0.00822	0.11818	0.02661	0.06074	-0.07099	0.05656	-0.01039	-0.00574
$T_7(x')$	0.13767	-0.0525	0.07706	0.0541	0.06651	0.00627	-0.07767	-0.00344	-0.01097	-0.00099
$T_8(x')$	0.04861	0.00902	-0.01447	0.05151	0.03906	-0.0011	-0.06283	0.04335	-0.00435	0.00428
$T_9(x')$	0.11622	-0.05502	0.01771	0.02313	0.07372	0.00171	-0.07114	-0.00035	0.0006	0.0135
$T_{10}(x')$	0.03788	0.0012	-0.04106	0.00234	0.03635	-0.02209	-0.04965	0.03026	0.01196	0.0159
$T_{11}(x')$	0.09542	-0.03421	-0.04165	0.02581	0.03025	0.01703	-0.04772	0.01559	-0.01458	0.02331
$T_{12}(x')$	0.01166	-0.0312	-0.00496	0.00512	0.04611	-0.00119	-0.02193	0.02911	0.01099	0.00753
$T_{13}(x')$	0.02306	0.0171	-0.0632	0.0621	0.01297	0.02557	-0.03313	0.00682	-0.00185	-0.00452
$T_{14}(x')$	-0.03064	-0.01824	0.02472	0.0285	0.0302	0.02521	-0.02063	0.026	0.00052	-0.00577
$T_{15}(x')$	-0.00794	0.03322	-0.02524	0.036636	0.01445	0.02981	-0.02728	0.02072	-0.00292	-0.01169
$T_{16}(x')$	-0.05229	-0.00474	0.02135	0.00137	0.00894	0.01589	-0.02464	-0.00225	0.01204	-0.00318
$T_{17}(x')$	0.00026	0.02505	-0.02455	-0.03361	0.01297	-0.03831	-0.00364	0.00676	0.01829	-0.02239
$T_{18}(x')$	-0.04986	-0.03937	-0.00769	-0.03635	-0.02491	0.00493	-0.02884	-0.00671	0.01547	0.02277
$T_{19}(x')$	-0.02375	0.0273	-0.02172	-0.0256	0.00627	-0.02683	-0.01205	-0.00569	0.0205	-0.00992

326

Appendix 5

Uncertainty analysis – induced parameter variations with noise pollution –

linear model (Section 6.6.1.1)

327

8-Sep-2001 13:49

328
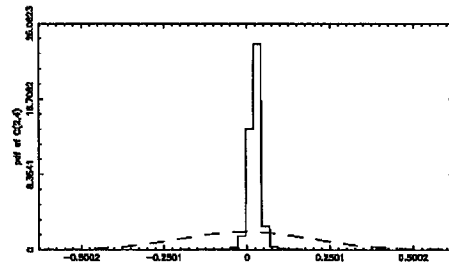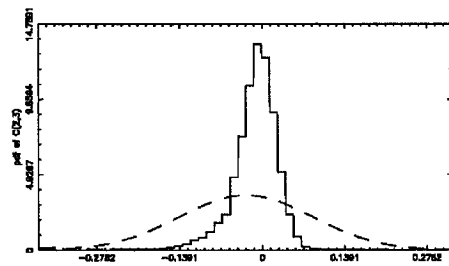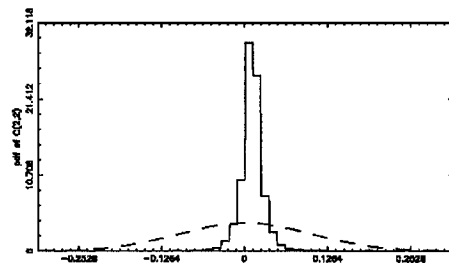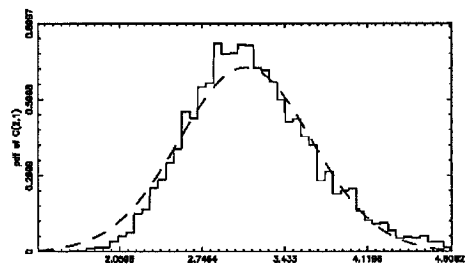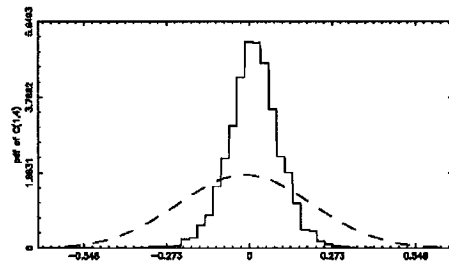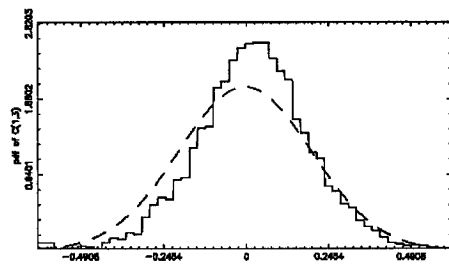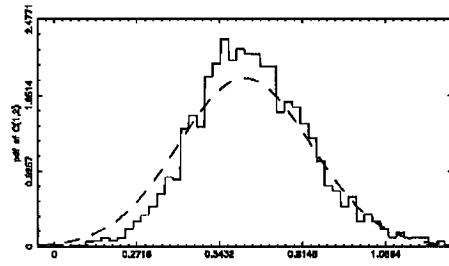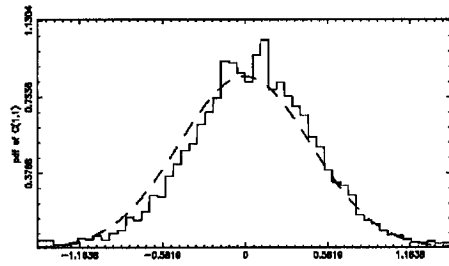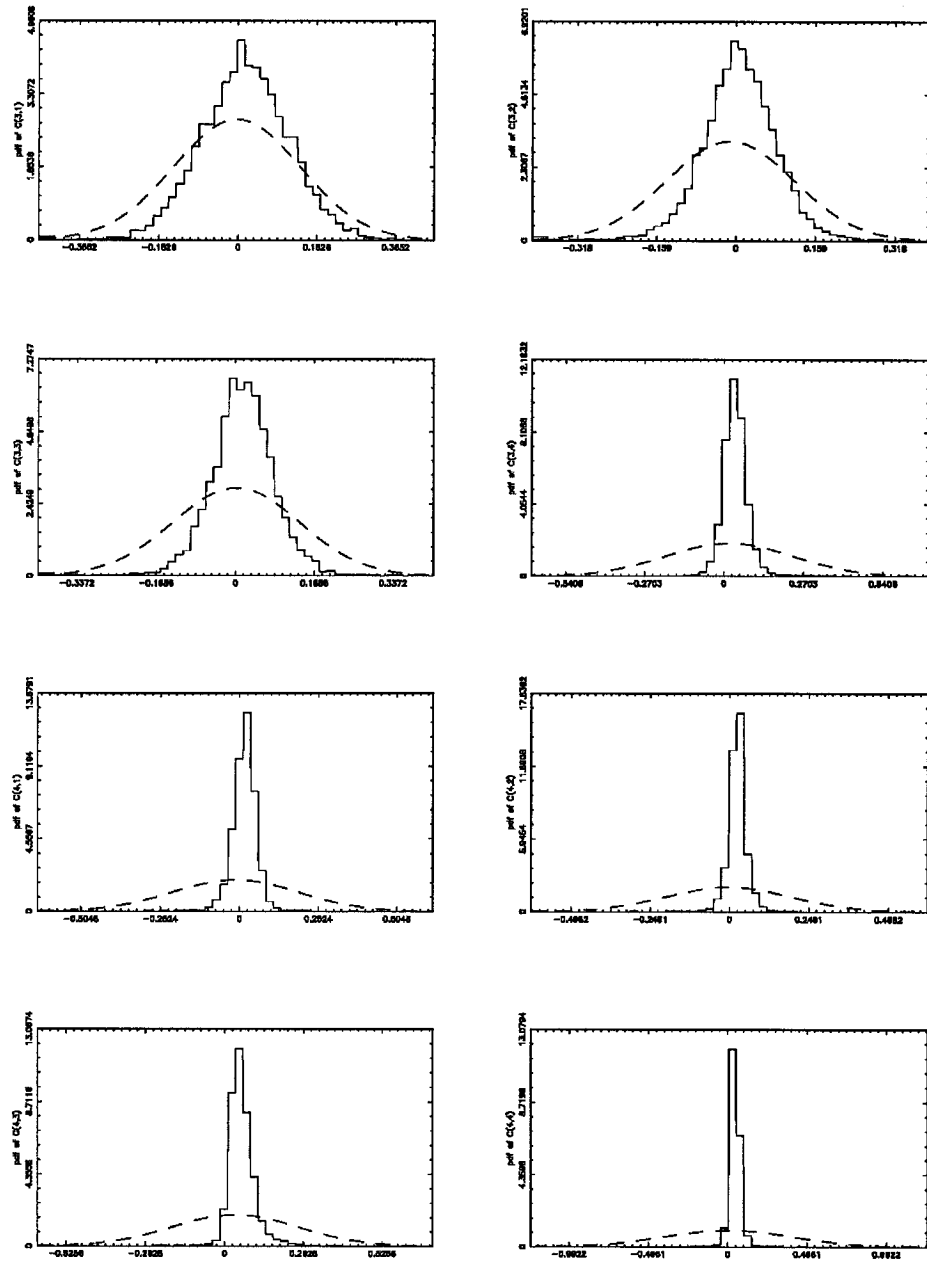
Appendix 6

Uncertainty analysis – induced parameter variations with noise pollution –

nonlinear model (Duffing oscillator) (Section 6.6.1.2)

330

28-Jun-2002 20:11

331

332
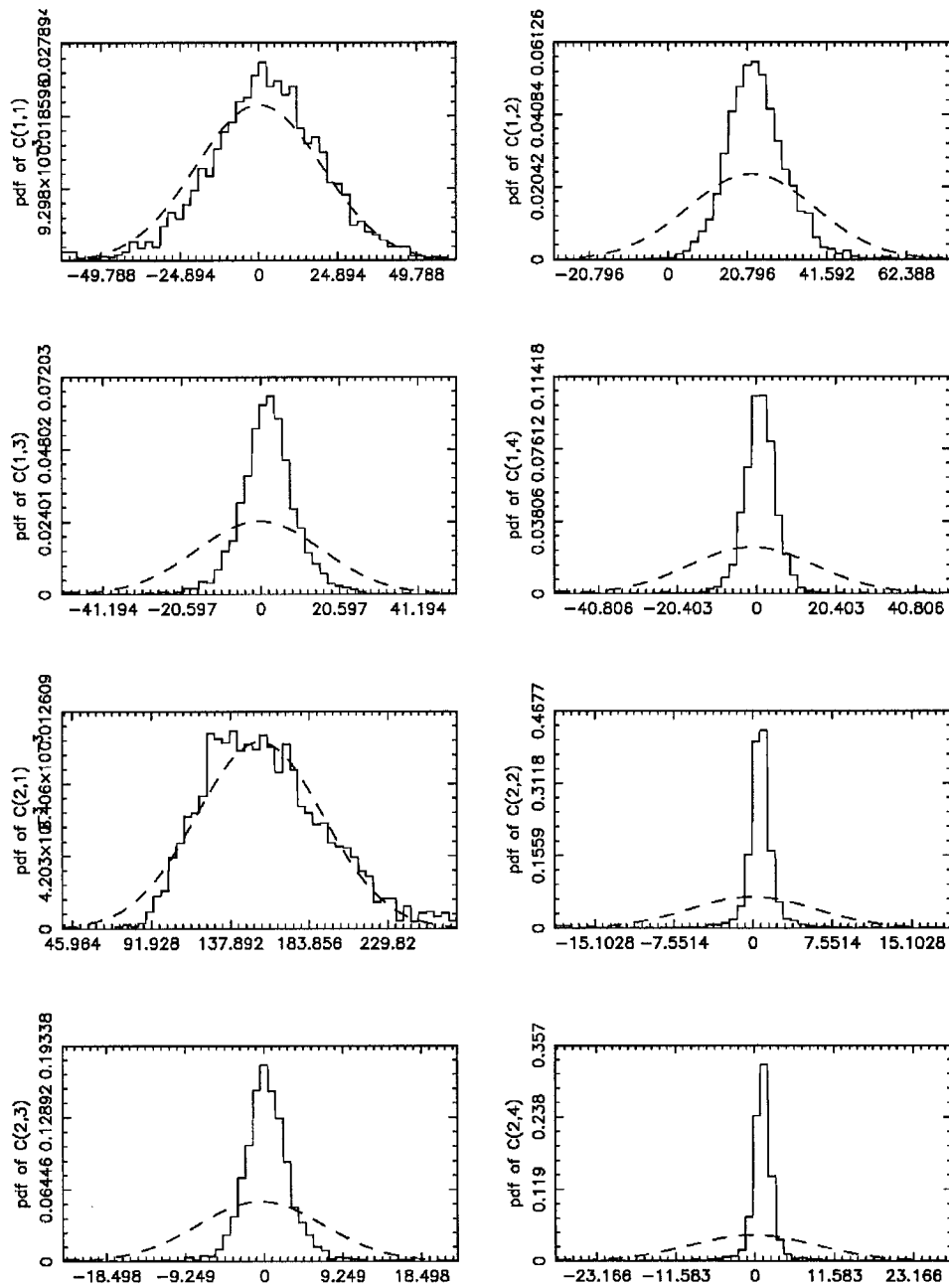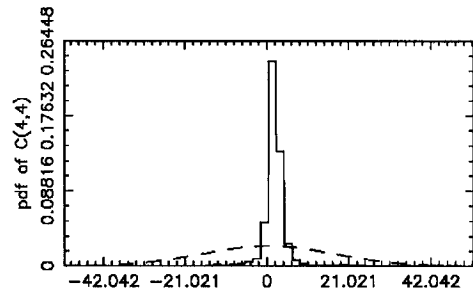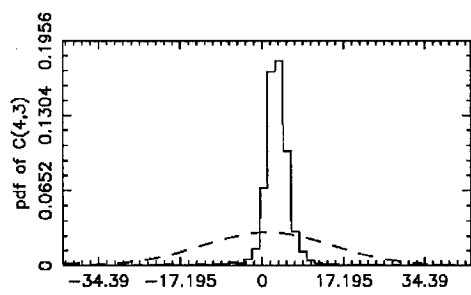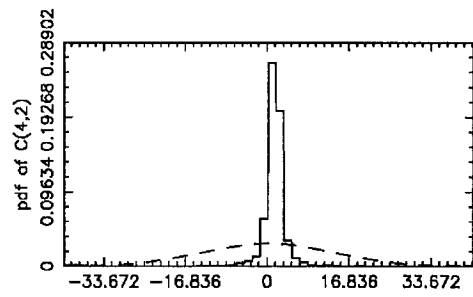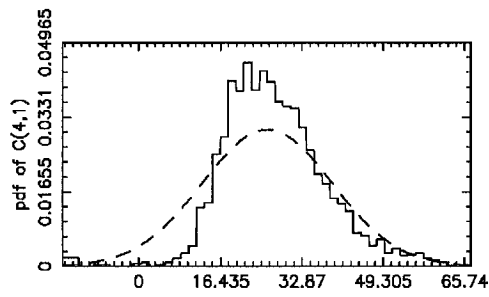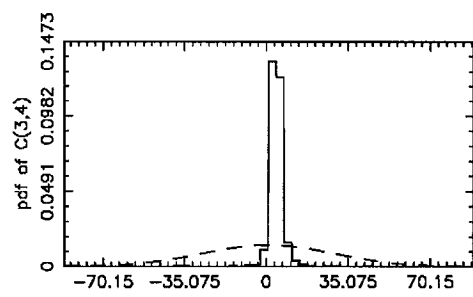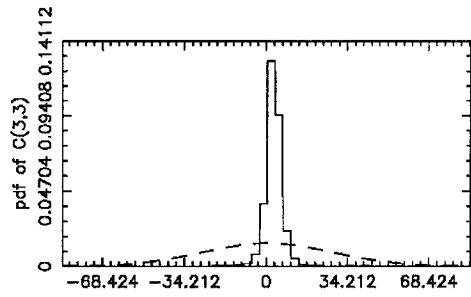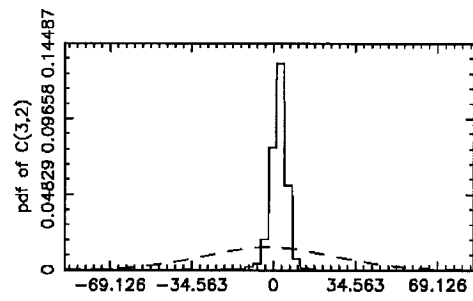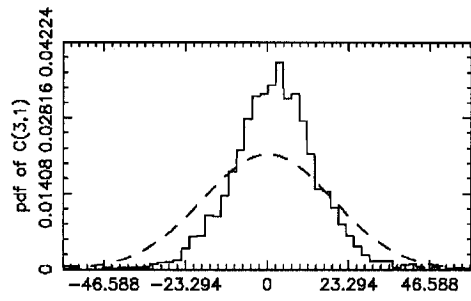
Appendix 7

Chebyshev to Power Series transformation (Mathematica output)

(Section 6.6.3)

Chebyshev to Power Series transformation (performed in Mathematica):

In[3]:= Expand[b1+b2*(a2*x-a1)+b3*(a4*y-a3)+b4*(a2*x-a1)^2+b5*(a4*y-a3)^2+b6*(a2*x-a1)*(a4*y-a3)+b7*(a4*y-a3)^3+b8*(a2*x-a1)^3+b9*(a2*x-a1)^2*(a4*y-a3)+b10*(a2*x-a1)*(a4*y-a3)^2+b11*(a2*x-a1)*(a4*y-a3)^3+b12*(a2*x-a1)^3*(a4*y-a3)+b13*(a2*x-a1)^2*(a4*y-a3)^2+b14*(a2*x-a1)^2*(a4*y-a3)^3+b15*(a2*x-a1)^3*(a4*y-a3)^2+b16*(a2*x-a1)^3*(a4*y-a3)^3]

$$
\begin{aligned}
\text{Out[3]}= & \; b1 - a1\,a3^2\,b10 + a1\,a3^3\,b11 + a1^2\,a3^3\,b12 + a1^2\,a3^2\,b13 - a1^2\,a3^3\,b14 - \\
& a1^3\,a3^2\,b15 + a1^3\,a3^3\,b16 - a1\,b2 - a3\,b3 + a1^2\,b4 + a3^2\,b5 + a1\,a3\,b6 - a3^3\,b7 - \\
& a1^3\,b8 - a1^2\,a3\,b9 + a2\,a3^2\,b10\,x - a2\,a3^3\,b11\,x - 3\,a1^2\,a2\,a3\,b12\,x - \\
& 2\,a1\,a2\,a3^2\,b13\,x + 2\,a1\,a2\,a3^3\,b14\,x + 3\,a1^2\,a2\,a3^2\,b15\,x - 3\,a1^2\,a2\,a3^3\,b16\,x + \\
& a2\,b2\,x - 2\,a1\,a2\,b4\,x - a2\,a3\,b6\,x + 3\,a1^2\,a2\,b8\,x + 2\,a1\,a2\,a3\,b9\,x + \\
& 3\,a1\,a2^2\,a3\,b12\,x^2 + a2^2\,a3^2\,b13\,x^2 - a2^2\,a3^3\,b14\,x^2 - 3\,a1\,a2^2\,a3^2\,b15\,x^2 + \\
& 3\,a1\,a2^2\,a3^3\,b16\,x^2 + a2^2\,b4\,x^2 - 3\,a1\,a2^2\,b8\,x^2 - a2^2\,a3\,b9\,x^2 - a2^3\,a3\,b12\,x^3 + \\
& a2^3\,a3^2\,b15\,x^3 - a2^3\,a3^3\,b16\,x^3 + a2^3\,b8\,x^3 + 2\,a1\,a3\,a4\,b10\,y - 3\,a1\,a3^2\,a4\,b11\,y - \\
& a1^3\,a4\,b12\,y - 2\,a1^2\,a3\,a4\,b13\,y + 3\,a1^2\,a3^2\,a4\,b14\,y + 2\,a1^3\,a3\,a4\,b15\,y - \\
& 3\,a1^3\,a3^2\,a4\,b16\,y + a4\,b3\,y - 2\,a3\,a4\,b5\,y - a1\,a4\,b6\,y + 3\,a3^2\,a4\,b7\,y + \\
& a1^2\,a4\,b9\,y - 2\,a2\,a3\,a4\,b10\,x\,y + 3\,a2\,a3^2\,a4\,b11\,x\,y + 3\,a1^2\,a2\,a4\,b12\,x\,y + \\
& 4\,a1\,a2\,a3\,a4\,b13\,x\,y - 6\,a1\,a2\,a3^2\,a4\,b14\,x\,y - 6\,a1^2\,a2\,a3\,a4\,b15\,x\,y + \\
& 9\,a1^2\,a2\,a3^2\,a4\,b16\,x\,y + a2\,a4\,b6\,x\,y - 2\,a1\,a2\,a4\,b9\,x\,y - 3\,a1\,a2^2\,a4\,b12\,x^2\,y - \\
& 2\,a2^2\,a3\,a4\,b13\,x^2\,y + 3\,a2^2\,a3^2\,a4\,b14\,x^2\,y + 6\,a1\,a2^2\,a3\,a4\,b15\,x^2\,y -
\end{aligned}
$$

Chebyshev to Power Series transformation (continued):

$$
\begin{aligned}
> \quad & 9\, a1\, a2^2\, a3^2\, a4\, b16\, x^2\, y + a2^2\, a4\, b9\, x^2\, y + a2^2\, a4\, b12\, x^3\, y - 2\, a2\, a3\, a4\, b15\, x^3\, y + \\[4pt]
> \quad & 3\, a2^3\, a3^2\, a4\, b16\, x^3\, y - a1\, a4\, b10\, y^2 + 3\, a1\, a3\, a4\, b11\, y^2 + a1\, a4^2\, b13\, y^2 - \\[4pt]
> \quad & 3\, a1^2\, a3\, a4\, b14\, y^2 - a1\, a4^2\, b15\, y^3 + 3\, a1\, a3\, a4^2\, b16\, y^2 + a4^2\, b5\, y^2 - \\[4pt]
> \quad & 3\, a3^2\, a4\, b7\, y^2 + a2\, a4\, b10\, x^2\, y^2 - 3\, a2\, a3\, a4\, b11\, x^2\, y^2 - 2\, a1\, a2\, a4\, b13\, x^2\, y^2 + \\[4pt]
> \quad & 6\, a1\, a2\, a3\, a4\, b14\, x^2\, y^2 + 3\, a1^2\, a2\, a4\, b15\, x^2\, y^2 - 9\, a1^2\, a2\, a3\, a4\, b16\, x^2\, y^2 + \\[4pt]
> \quad & a2^2\, a4^2\, b13\, x^2\, y^2 - 3\, a2^2\, a3\, a4\, b14\, x^2\, y^2 - 3\, a1\, a2\, a4^2\, b15\, x^2\, y^2 + \\[4pt]
> \quad & 9\, a1\, a2^2\, a3\, a4\, b16\, x^2\, y^2 + a2^2\, a4^2\, b15\, x^3\, y^2 - 3\, a2^2\, a3\, a4\, b16\, x^3\, y^2 - \\[4pt]
> \quad & a1\, a4^3\, b11\, y^3 + a1^2\, a4^3\, b14\, y^3 - a1^3\, a4\, b16\, y^3 + a4^3\, b7\, y^3 + a2\, a4\, b11\, x^3\, y^3 - \\[4pt]
> \quad & 2\, a1\, a2\, a4^3\, b14\, x^3\, y^3 + 3\, a1^2\, a2\, a4\, b16\, x^3\, y^3 + a2^2\, a4^3\, b14\, x^2\, y^3 - \\[4pt]
> \quad & 3\, a1\, a2^2\, a4\, b16\, x^2\, y^3 + a2^2\, a4^3\, b16\, x^3\, y^3
\end{aligned}
$$

Appendix 8

Damper experimental test plan – sinusoidal excitation (Section 7.0)

336

10-kip Damper Experimental Test Plan

Test No.	Ampl. (pk-pk, in)	Frequency	Test Date	Sample time	Sample rate	Filename
			Temp. Range = 70-80F			
1	1	0.5	1/18/02	60 sec	5kHz	a1w05t1_1
	2	0.5	1/18/02	60 sec	5kHz	a2w05t1_1
	4	0.5	1/18/02	60 sec	5kHz	a4w05t1_1
	6	0.5	1/18/02	60 sec	5kHz	a6w05t1_1
	1	1	1/18/02	60 sec	5kHz	a1w1t1_1
	2	1	1/18/02	60 sec	5kHz	a2w1t1_1
	4	1	1/19/02	60 sec	5kHz	a4w1t1_1
	1	5				
	2	5	xxx	xxx	xxx	xxx
2	1	0.5	1/19/02	60 sec	5kHz	a1w05t1_2
	2	0.5	1/19/02	60 sec	5kHz	a2w05t1_2
	4	0.5	1/19/02	60 sec	5kHz	a4w05t1_2
	6	0.5	1/20/02	60 sec	5kHz	a6w05t1_2
	1	1	1/20/02	60 sec	5kHz	a1w1t1_2
	2	1	1/20/02	60 sec	5kHz	a2w1t1_2
	4	1	1/21/02	60 sec	5kHz	a4w1t1_2
	1	5				
	2	5	xxx	xxx	xxx	xxx
3	1	0.5	1/19/02	60 sec	5kHz	a1w05t1_3
	2	0.5	1/19/02	60 sec	5kHz	a2w05t1_3
	4	0.5	1/19/02	60 sec	5kHz	a4w05t1_3
	6	0.5	1/20/02	60 sec	5kHz	a6w05t1_3
	1	1	1/20/02	60 sec	5kHz	a1w1t1_3
	2	1	1/21/02	60 sec	5kHz	a2w1t1_3
	4	1	1/21/02	60 sec	5kHz	a4w1t1_3
	1	5				
	2	5	xxx	xxx	xxx	xxx
4	1	0.5	1/20/02	60 sec	5kHz	a1w05t1_4
	2	0.5	1/20/02	60 sec	5kHz	a2w05t1_4
	4	0.5	1/20/02	60 sec	5kHz	a4w05t1_4
	6	0.5	1/20/02	60 sec	5kHz	a6w05t1_4
	1	1	1/20/02	60 sec	5kHz	a1w1t1_4
	2	1	1/21/02	60 sec	5kHz	a2w1t1_4
	4	1	1/21/02	60 sec	5kHz	a4w1t1_4
	1	5				
	2	5	xxx	xxx	xxx	xxx

337

10-kip Damper Experimental Test Plan

Test No.	Ampl. (pk-pk, in)	Frequency	Temp. Range = 70-80F Test Date	Sample time	Sample rate	Filename
	1	0.5	1/21/02	60 sec	5kHz	a1w05t1_5
	2	0.5	1/21/02	60 sec	5kHz	a2w05t1_5
	4	0.5	1/21/02	60 sec	5kHz	a4w05t1_5
	6	0.5	1/21/02	60 sec	5kHz	a6w05t1_5
5	1	1	1/21/02	60 sec	5kHz	a1w1t1_5
	2	1	1/21/02	60 sec	5kHz	a2w1t1_5
	4	1	1/23/02	60 sec	5kHz	a4w1t1_5
	1	5				
	2	5	xxx	xxx	xxx	xxx
	1	0.5	1/21/02	60 sec	5kHz	a1w05t1_6
	2	0.5	1/21/02	60 sec	5kHz	a2w05t1_6
	4	0.5	1/21/02	60 sec	5kHz	a4w05t1_6
	6	0.5	1/21/02	60 sec	5kHz	a6w05t1_6
6	1	1	1/21/02	60 sec	5kHz	a1w1t1_6
	2	1	1/21/02	60 sec	5kHz	a2w1t1_6
	4	1	1/24/02	60 sec	5kHz	a4w1t1_6
	1	5				
	2	5	xxx	xxx	xxx	xxx
	1	0.5	1/21/02	60 sec	5kHz	a1w05t1_7
	2	0.5	1/21/02	60 sec	5kHz	a2w05t1_7
	4	0.5	1/21/02	60 sec	5kHz	a4w05t1_7
	6	0.5	1/21/02	60 sec	5kHz	a6w05t1_7
7	1	1	1/21/02	60 sec	5kHz	a1w1t1_7
	2	1	1/21/02	60 sec	5kHz	a2w1t1_7
	4	1	1/24/02	60 sec	5kHz	a4w1t1_7
	1	5				
	2	5	xxx	xxx	xxx	xxx
	1	0.5	1/23/02	60 sec	5kHz	a1w05t1_8
	2	0.5	1/23/02	60 sec	5kHz	a2w05t1_8
	4	0.5	1/23/02	60 sec	5kHz	a4w05t1_8
	6	0.5	1/23/02	60 sec	5kHz	a6w05t1_8
8	1	1	1/23/02	60 sec	5kHz	a1w1t1_8
	2	1	1/23/02	60 sec	5kHz	a2w1t1_8
	4	1	1/28/02	60 sec	5kHz	a4w1t1_8
	1	5				
	2	5	xxx	xxx	xxx	xxx

10-kip Damper Experimental Test Plan

Test No.	Ampl. (pk-pk, in)	Frequency	Temp. Range = 70-80F			
			Test Date	Sample time	Sample rate	Filename
9	1	0.5	1/24/02	60 sec	5kHz	a1w05t1_9
	2	0.5	1/24/02	60 sec	5kHz	a2w05t1_9
	4	0.5	1/24/02	60 sec	5kHz	a4w05t1_9
	6	0.5	1/24/02	60 sec	5kHz	a6w05t1_9
	1	1	1/24/02	60 sec	5kHz	a1w1t1_9
	2	1	1/28/02	60 sec	5kHz	a2w1t1_9
	4	1	1/28/02	60 sec	5kHz	a4w1t1_9
	1	5				
	2	5	xxx	xxx	xxx	xxx
10	1	0.5	1/28/02	60 sec	5kHz	a1w05t1_10
	2	0.5	1/28/02	60 sec	5kHz	a2w05t1_10
	4	0.5	1/28/02	60 sec	5kHz	a4w05t1_10
	6	0.5	1/28/02	60 sec	5kHz	a6w05t1_10
	1	1	1/28/02	60 sec	5kHz	a1w1t1_10
	2	1	2/12/02	60 sec	5kHz	a2w1t1_10
	4	1	2/12/02	60 sec	5kHz	a4w1t1_10
	1	5				
	2	5	xxx	xxx	xxx	xxx

339

10-kip Damper Experimental Test Plan

Test No.	Ampl. (pk-pk, in)	Frequency	Temp. Range = 90-100F			
			Test Date	Sample time	Sample rate	Filename
1	1	0.5	1/18/02	60 sec	5kHz	a1w05t2_1
	2	0.5	1/18/02	60 sec	5kHz	a2w05t2_1
	4	0.5	1/18/02	60 sec	5kHz	a4w05t2_1
	6	0.5	1/18/02	60 sec	5kHz	a6w05t2_1
	1	1	1/18/02	60 sec	5kHz	a1w1t2_1
	2	1	1/18/02	60 sec	5kHz	a2w1t2_1
	4	1	1/19/02	60 sec	5kHz	a4w1t2_1
	1	5	1/19/02	30 sec	5kHz	a1w5t2_1
	2	5	xxx	xxx	xxx	xxx
2	1	0.5	1/19/02	60 sec	5kHz	a1w05t2_2
	2	0.5	1/19/02	60 sec	5kHz	a2w05t2_2
	4	0.5	1/19/02	60 sec	5kHz	a4w05t2_2
	6	0.5	1/19/02	60 sec	5kHz	a6w05t2_2
	1	1	1/19/02	60 sec	5kHz	a1w1t2_2
	2	1	1/19/02	60 sec	5kHz	a2w1t2_2
	4	1	1/19/02	60 sec	5kHz	a4w1t2_2
	1	5				
	2	5	xxx	xxx	xxx	xxx
3	1	0.5	1/19/02	60 sec	5kHz	a1w05t2_3
	2	0.5	1/19/02	60 sec	5kHz	a2w05t2_3
	4	0.5	1/19/02	60 sec	5kHz	a4w05t2_3
	6	0.5	1/19/02	60 sec	5kHz	a6w05t2_3
	1	1	1/19/02	60 sec	5kHz	a1w1t2_3
	2	1	1/19/02	60 sec	5kHz	a2w1t2_3
	4	1	1/19/02	60 sec	5kHz	a4w1t2_3
	1	5				
	2	5	xxx	xxx	xxx	xxx
4	1	0.5	1/20/02	60 sec	5kHz	a1w05t2_4
	2	0.5	1/20/02	60 sec	5kHz	a2w05t2_4
	4	0.5	1/20/02	60 sec	5kHz	a4w05t2_4
	6	0.5	1/20/02	60 sec	5kHz	a6w05t2_4
	1	1	1/20/02	60 sec	5kHz	a1w1t2_4
	2	1	1/20/02	60 sec	5kHz	a2w1t2_4
	4	1	1/20/02	60 sec	5kHz	a4w1t2_4
	1	5				
	2	5	xxx	xxx	xxx	xxx

10-kip Damper Experimental Test Plan

Test No.	Ampl. (pk-pk, in)	Frequency	Temp. Range = 90-100F			
			Test Date	Sample time	Sample rate	Filename
5	1	0.5	1/20/02	60 sec	5kHz	a1w05t2_5
	2	0.5	1/20/02	60 sec	5kHz	a2w05t2_5
	4	0.5	1/20/02	60 sec	5kHz	a4w05t2_5
	6	0.5	1/20/02	60 sec	5kHz	a6w05t2_5
	1	1	1/20/02	60 sec	5kHz	a1w1t2_5
	2	1	1/21/02	60 sec	5kHz	a2w1t2_5
	4	1	1/23/02	60 sec	5kHz	a4w1t2_5
	1	5				
	2	5	xxx	xxx	xxx	xxx
6	1	0.5	1/21/02	60 sec	5kHz	a1w05t2_6
	2	0.5	1/21/02	60 sec	5kHz	a2w05t2_6
	4	0.5	1/21/02	60 sec	5kHz	a4w05t2_6
	6	0.5	1/21/02	60 sec	5kHz	a6w05t2_6
	1	1	1/21/02	60 sec	5kHz	a1w1t2_6
	2	1	1/21/02	60 sec	5kHz	a2w1t2_6
	4	1	1/24/02	60 sec	5kHz	a4w1t2_6
	1	5				
	2	5	xxx	xxx	xxx	xxx
7	1	0.5	1/21/02	60 sec	5kHz	a1w05t2_7
	2	0.5	1/21/02	60 sec	5kHz	a2w05t2_7
	4	0.5	1/21/02	60 sec	5kHz	a4w05t2_7
	6	0.5	1/21/02	60 sec	5kHz	a6w05t2_7
	1	1	1/21/02	60 sec	5kHz	a1w1t2_7
	2	1	1/21/02	60 sec	5kHz	a2w1t2_7
	4	1	1/24/02	60 sec	5kHz	a4w1t2_7
	1	5				
	2	5	xxx	xxx	xxx	xxx
8	1	0.5	1/23/02	60 sec	5kHz	a1w05t2_8
	2	0.5	1/23/02	60 sec	5kHz	a2w05t2_8
	4	0.5	1/23/02	60 sec	5kHz	a4w05t2_8
	6	0.5	1/23/02	60 sec	5kHz	a6w05t2_8
	1	1	1/23/02	60 sec	5kHz	a1w1t2_8
	2	1	1/23/02	60 sec	5kHz	a2w1t2_8
	4	1	1/28/02	60 sec	5kHz	a4w1t2_8
	1	5				
	2	5	xxx	xxx	xxx	xxx

10-kip Damper Experimental Test Plan

Test No.	Ampl. (pk-pk, in)	Frequency	Temp. Range = 90-100F			
			Test Date	Sample time	Sample rate	Filename
9	1	0.5	1/23/02	60 sec	5kHz	a1w05t2_9
	2	0.5	1/23/02	60 sec	5kHz	a2w05t2_9
	4	0.5	1/23/02	60 sec	5kHz	a4w05t2_9
	6	0.5	1/23/02	60 sec	5kHz	a6w05t2_9
	1	1	1/23/02	60 sec	5kHz	a1w1t2_9
	2	1	1/23/02	60 sec	5kHz	a2w1t2_9
	4	1	1/28/02	60 sec	5kHz	a4w1t2_9
	1	5				
	2	5	xxx	xxx	xxx	xxx
10	1	0.5	1/28/02	60 sec	5kHz	a1w05t2_10
	2	0.5	1/28/02	60 sec	5kHz	a2w05t2_10
	4	0.5	1/28/02	60 sec	5kHz	a4w05t2_10
	6	0.5	1/28/02	60 sec	5kHz	a6w05t2_10
	1	1	1/28/02	60 sec	5kHz	a1w1t2_10
	2	1	2/12/02	60 sec	5kHz	a2w1t2_10
	4	1	2/12/02	60 sec	5kHz	a4w1t2_10
	1	5				
	2	5	xxx	xxx	xxx	xxx

342

10-kip Damper Experimental Test Plan

Test No.	Ampl. (pk-pk, in)	Frequency	Temp. Range = 110-120F Test Date	Sample time	Sample rate	Filename
	1	0.5	1/19/02	60 sec	5kHz	a1w05t3_1
	2	0.5	1/19/02	60 sec	5kHz	a2w05t3_1
	4	0.5	1/19/02	60 sec	5kHz	a4w05t3_1
	6	0.5	1/19/02	60 sec	5kHz	a6w05t3_1
1	1	1	1/19/02	60 sec	5kHz	a1w1t3_1
	2	1	1/19/02	60 sec	5kHz	a2w1t3_1
	4	1	xxx	xxx	xxx	xxx
	1	5	1/19/02	30 sec	5kHz	a1w5t3_1
	2	5	xxx	xxx	xxx	xxx
	1	0.5	1/19/02	60 sec	5kHz	a1w05t3_2
	2	0.5	1/19/02	60 sec	5kHz	a2w05t3_2
	4	0.5	1/19/02	60 sec	5kHz	a4w05t3_2
	6	0.5	1/19/02	60 sec	5kHz	a6w05t3_2
2	1	1	1/19/02	60 sec	5kHz	a1w1t3_2
	2	1	1/19/02	60 sec	5kHz	a2w1t3_2
	4	1	xxx	xxx	xxx	xxx
	1	5				
	2	5	xxx	xxx	xxx	xxx
	1	0.5	1/19/02	60 sec	5kHz	a1w05t3_3
	2	0.5	1/19/02	60 sec	5kHz	a2w05t3_3
	4	0.5	1/19/02	60 sec	5kHz	a4w05t3_3
	6	0.5	1/19/02	60 sec	5kHz	a6w05t3_3
3	1	1	1/19/02	60 sec	5kHz	a1w1t3_3
	2	1	1/19/02	60 sec	5kHz	a2w1t3_3
	4	1	xxx	xxx	xxx	xxx
	1	5				
	2	5	xxx	xxx	xxx	xxx
	1	0.5	1/20/02	60 sec	5kHz	a1w05t3_4
	2	0.5	1/20/02	60 sec	5kHz	a2w05t3_4
	4	0.5	1/20/02	60 sec	5kHz	a4w05t3_4
	6	0.5	1/20/02	60 sec	5kHz	a6w05t3_4
4	1	1	1/20/02	60 sec	5kHz	a1w1t3_4
	2	1	1/20/02	60 sec	5kHz	a2w1t3_4
	4	1	xxx	xxx	xxx	xxx
	1	5				
	2	5	xxx	xxx	xxx	xxx

343

10-kip Damper Experimental Test Plan

Test No.	Ampl. (pk-pk, in)	Frequency	Temp. Range = 110-120F			
			Test Date	Sample time	Sample rate	Filename
5	1	0.5	1/20/02	60 sec	5kHz	a1w05t3_5
	2	0.5	1/20/02	60 sec	5kHz	a2w05t3_5
	4	0.5	1/20/02	60 sec	5kHz	a4w05t3_5
	6	0.5	1/20/02	60 sec	5kHz	a6w05t3_5
	1	1	1/20/02	60 sec	5kHz	a1w1t3_5
	2	1	1/20/02	60 sec	5kHz	a2w1t3_5
	4	1	xxx	xxx	xxx	xxx
	1	5				
	2	5	xxx	xxx	xxx	xxx
6	1	0.5	1/21/02	60 sec	5kHz	a1w05t3_6
	2	0.5	1/21/02	60 sec	5kHz	a2w05t3_6
	4	0.5	1/21/02	60 sec	5kHz	a4w05t3_6
	6	0.5	1/21/02	60 sec	5kHz	a6w05t3_6
	1	1	1/21/02	60 sec	5kHz	a1w1t3_6
	2	1	1/21/02	60 sec	5kHz	a2w1t3_6
	4	1	xxx	xxx	xxx	xxx
	1	5				
	2	5	xxx	xxx	xxx	xxx
7	1	0.5	1/21/02	60 sec	5kHz	a1w05t3_7
	2	0.5	1/21/02	60 sec	5kHz	a2w05t3_7
	4	0.5	1/21/02	60 sec	5kHz	a4w05t3_7
	6	0.5	1/21/02	60 sec	5kHz	a6w05t3_7
	1	1	1/21/02	60 sec	5kHz	a1w1t3_7
	2	1	1/21/02	60 sec	5kHz	a2w1t3_7
	4	1	xxx	xxx	xxx	xxx
	1	5				
	2	5	xxx	xxx	xxx	xxx
8	1	0.5	1/23/02	60 sec	5kHz	a1w05t3_8
	2	0.5	1/23/02	60 sec	5kHz	a2w05t3_8
	4	0.5	1/23/02	60 sec	5kHz	a4w05t3_8
	6	0.5	1/23/02	60 sec	5kHz	a6w05t3_8
	1	1	1/23/02	60 sec	5kHz	a1w1t3_8
	2	1	1/23/02	60 sec	5kHz	a2w1t3_8
	4	1	xxx	xxx	xxx	xxx
	1	5				
	2	5	xxx	xxx	xxx	xxx

10-kip Damper Experimental Test Plan

Test No.	Ampl. (pk-pk, in)	Frequency	Test Date	Sample time	Sample rate	Filename
			Temp. Range = 110-120F			
9	1	0.5	1/23/02	60 sec	5kHz	a1w05t3_9
	2	0.5	1/23/02	60 sec	5kHz	a2w05t3_9
	4	0.5	1/23/02	60 sec	5kHz	a4w05t3_9
	6	0.5	1/23/02	60 sec	5kHz	a6w05t3_9
	1	1	1/23/02	60 sec	5kHz	a1w1t3_9
	2	1	1/23/02	60 sec	5kHz	a2w1t3_9
	4	1	xxx	xxx	xxx	xxx
	1	5				
	2	5	xxx	xxx	xxx	xxx
10	1	0.5	1/28/02	60 sec	5kHz	a1w05t3_10
	2	0.5	1/28/02	60 sec	5kHz	a2w05t3_10
	4	0.5	1/28/02	60 sec	5kHz	a4w05t3_10
	6	0.5	1/28/02	60 sec	5kHz	a6w05t3_10
	1	1	1/28/02	60 sec	5kHz	a1w1t3_10
	2	1	1/28/02	60 sec	5kHz	a2w1t3_10
	4	1	xxx	xxx	xxx	xxx
	1	5				
	2	5	xxx	xxx	xxx	xxx

345